TECHNISCHE UNIVERSITÄT WIEN
Vienna | Austria

DISSERTATION

MECHANOBIOLOGY AT THE MICROSCALE

ORGAN-ON-A-CHIP TECHNOLOGY AS A TOOL TO BOOST PRECLINICAL MODEL RELEVANCE

ausgeführt zum Zwecke der Erlangung des akademischen Grades einer Doktorin der technischen Wissenschaften unter der Leitung von

Univ. Prof. Dipl.-Ing. Dr. Peter Ertl
Institut für angewandte Synthesechemie (E163)
Institut für chemische Technologien und Analytik (E164)

eingereicht an der Technischen Universität Wien
Fakultät für technische Chemie

von

Dipl.-Ing. Barbara Eva Maria Bachmann, BSc
Mat.Nr.: 1007001

Date Signature

ACKNOWLEDGMENTS

First and foremost, I want to thank Prof. Peter Ertl for welcoming me into his group and introducing me to the big microworld of organs-on-a-chip. Thank you for your guidance, your challenges, and your mentorship in the last five years. Similarly, I want to express my gratitude to Prof. Heinz Redl for his unwavering trust in my abilities as a scientist and his embodiment of Claude Bernard's famous quote, "Art is I, science is we."

I want to thank all current and past Cell Chip Group members for the warm and enthusiastic scientific atmosphere, for the mutual constructive criticisms, and for many cheerful hours inside and out of the lab. I especially want to thank Sarah Spitz for agreeing to conduct her Master's thesis on my project many years ago and for all the lamina talks that followed. I also want to thank Christoph Eilenberger for his constructive comments on my projects' visual representations, fruitful discussions, and nutritious lunches, and Dr. Helene Zirath for continuous support on all scientific and administrative issues.

Special thanks to the Ludwig Boltzmann Institute for Experimental and Clinical Traumatology, particularly to Dr. Sylvia Nürnberger and Dr. Wolfgang Holnthoner, for sharing their labs and their biological expertise. Thank you to Michaela Stainer, Marian Fürsatz, Severin Mühleder, Karoline Pill, and Marianne Pultar for their assistance in cell isolation, cultivation, and analysis.

Last but not least, I want to thank Andreas Hanka for his immense support, his continuous loyalty, and for taking care of me and our furbabies. Thank you.

TABLE OF CONTENTS

ABSTRACT

Organ-on-a-chip technology provides precise control over vital biological, physical, and chemical parameters needed to recreate the physiological niche *in vitro*, thus fostering the establishment of organ models capable of recapitulating near-native tissue architectures and functions. These smallest functional units of human organs can now be subjected to dynamic (patho)physiological stimulation such as fluid flow, matrix stiffness, and nutrient diffusion. It is essential to highlight that any living tissue will react to changes in their respective environment, resulting in either maintaining healthy or displaying diseased phenotypes. Consequently, a deeper understanding of the cellular mechanisms that guide and regulate cell fate, including apoptosis, proliferation, differentiation, and migration in the presence of external biophysical stimuli, will ultimately open new insights into the onset, progression, and remission of diseases. This doctoral work clearly demonstrates that mechanobiological stimuli significantly improve physiologic relevance within vasculature-on-a-chip and cartilage-on-chip devices. The combinatorial effects of fluid perfusion, interstitial flow, and soluble compound delivery are instrumental in forming vasculature within large-sized vascularized tissue constructs and defining mechanisms in reciprocal signaling during vasculogenesis. This doctoral thesis also reports that directional interstitial fluid flow stimulation substantially contributes to establishing a blood-lymphatic capillary interface by initiating lymphatic sprout formation and guiding lymphatic vessel maturation. Similarly, replicating perichondral tissue elasticity and the directional nutrient gradient across cartilage tissue improved the redifferentiation capacity of primary chondrocytes on-chip. Chondrocytes cultivated under optimized conditions exhibited a striking similarity to native cartilage, including spherical

morphology, synthesized cartilage matrix, and arranged into superficial and deep zone cartilage. The microphysiological systems developed within this thesis are expected to foster the identification of novel drug delivery routes into the lymphatic system and decipher deregulatory disease mechanisms in cartilage anabolism and catabolism, thus providing a tool to boost the discovery of novel drug candidates.

KURZFASSUNG

Die „Organ-on-a-Chip“-Technologie ermöglicht die präzise Kontrolle über biologische, physikalische und chemische Parameter zur Nachahmung der physiologischen Nische eines Organes *in vitro*. Damit fördert sie die Etablierung von Organmodellen zur Nachbildung von nahezu nativen Gewebearchitekturen und -funktionen. Diese kleinsten funktionellen Einheiten menschlicher Organe können zusätzlich einer (patho-) physiologischen mechanischen Stimulation wie Fluss, Matrixfestigkeit, oder Nährstoffdiffusion unterzogen werden. Jedes Gewebe reagiert sensibel auf Veränderungen in ihrer jeweiligen Umgebung, was entweder dazu führt, dass gesundes Zellverhalten erhalten bleibt, oder, dass erkrankte Phänotypen auftreten. Folglich ermöglicht ein tieferes Verständnis der zellulären Mechanismen, die in Gegenwart externer biophysikalischer Reize das Zellschicksal steuern und regulieren, neue Einblicke in den Beginn, das Fortschreiten, und die Remission von Krankheiten. Diese Dissertation zeigt deutlich, dass dynamische mechanobiologische Reize wie interstitieller Fluss und Nährstoffgradienten die physiologische Relevanz in Blutgefäßen-am-Chip und Knorpel-am-Chip Systemen signifikant verbessern. Es wird gezeigt, dass der kombinatorische Effekt von Perfusion, interstitiellem Fluss, und Diffusion löslicher Moleküle einen positiven Effekt auf die Vaskularisierung von großen Gewebestücke hat und hilft, Mechanismen für die wechselseitige Signalübertragung während der Vaskulogenese zu definieren. Diese Doktorarbeit berichtet auch, dass direktionaler interstitieller Fluss wesentlich zur Bildung eines Blut-Lymph-Kapillarbetts im Chip beiträgt, indem er die Bildung von Lymphgefäßen initiiert. In ähnlicher Weise verbessert die Nachahmung der Elastizität des perichondralen Gewebes und des Nährstoffgradienten im Knorpelgewebe die

Redifferenzierungskapazität von primären Knorpelzellen. Unter optimierten Bedingungen kultivierte Knorpelzellen zeigen eine bemerkenswerte Ähnlichkeit mit nativem Knorpel, einschließlich sphärischer Morphologie, synthetisierter Knorpelmatrix und Anordnung in oberflächlichen und tiefen Zonenknorpel. Es wird erwartet, dass die im Rahmen dieser Arbeit entwickelten mikrophysiologischen Systeme die Identifizierung neuer Arzneimittelabgabewege in z. B. das Lymphsystem fördern sowie arthrotische Krankheitsprozesse entschlüsseln und so zur Entdeckung neuer Arzneimittelkandidaten beitragen.

AIMS AND THESIS HYPOTHESIS

This doctoral thesis is aimed at engineering various organ-on-a-chip systems to subject 3D cell cultures to dynamic stimulation resembling the native mechanobiological microenvironment as well as monitoring the corresponding cell and tissue responses. The development of microphysiological systems is accomplished by applying state-of-the-art rapid prototyping techniques, including casting, lithography, and xurography, which enable precise control over vital biophysical parameters, including fluid perfusion and interstitial fluid flow regimes, matrix elasticity, as well as nutrient diffusion, and compound gradients. It is essential to highlight that biomechanical stimuli in current *in vitro* 3D cell culture models are largely underrepresented in biomedical research. To close this scientific and technological gap, dynamic stimulation of 3D cell cultures via microfluidic technology is introduced to enhance physiologic biomimicry within organ-on-a-chip models. Only a more accurate depiction of the native tissue results in (1) a clear understanding of physiologic cell behavior, (2) advanced knowledge of pathological changes, and (3) increased predictability of drug benefits and side effects. In other words, this thesis follows a “home away from home” approach for mammalian cells by adding a dynamic, mechanical component through organ-on-a-chip technology to investigate cell behavior in health, disease, and treatment.

CHAPTER 1

INTRODUCTION

ORGAN-ON-A-CHIP AND MECHANOBIOLOGY

1. Problem and Motivation

Current preclinical models center around monolayer cell cultures and animal models that both fail to depict human biology accurately. Monolayer models cannot capture the dynamic, 3D environment of native tissues, while the complexity that animal models offer results in poor control of experimental parameters. Additional ethical concerns and interspecies differences between animals and humans dictate the increasing need for more physiologically relevant preclinical *in vitro* models in biomedical research.

Organ-on-a-chip technology is an emerging technique at the biology and engineering interface capable of bridging this gap between preclinical *in vitro* and *in vivo* models. Limitations of current technologies are overcome by employing microfluidic engineering and rapid prototyping techniques to replicate tissue environment and architecture while precisely controlling experimental parameters. Organ-on-a-chip systems achieve this by employing the lab-on-a-chip toolbox to accurately manipulate nano- and picolitres of fluids via carefully microfabricated channels, membrane deflections, and fluid pumping.

Adding these engineering technologies to the biological repertoire enables considering and replicating the dynamic, ever-changing physiologic tissue environment where cells constantly experience mechanical stimulation crucial for cell behavior and tissue development. Microfluidic rapid prototyping allows tailoring tissue architecture and spatiotemporally regulating molecule gradients vital for tissue function that other preclinical *in vitro* systems fail to replicate. At the same time, membrane deflection and fluid pumping can mimic mechanical forces within the human body like compression and blood flow.

This thesis applies these technologies to engineer mechanobiology-on-chip devices and demonstrates the importance of dynamic cultivation in vasculature-on-chip and cartilage-on-chip systems. Considering the mechanical environment not only results in superior cell behavior and differentiation but also provides a profound understanding of (patho)physiological processes in the human body that is vital for preclinical model accuracy and reliability.

2. NEW KID IN THE LAB: ORGAN-ON-A-CHIP TECHNOLOGY IN BIOMEDICAL RESEARCH

The central aim of biomedical research is to understand human physiology, identify disease mechanisms, and develop novel treatment options. To achieve this goal, scientists need to implement model systems mimicking their desired biological niche to circumvent human use in preclinical biomedical trials. Unfortunately, many of these efforts still rely on monolayers of cells in plastic dishes (*in vitro* models) or lab animals (*in vivo* models). Monolayer culture either uses tissue cells that are ripped out of their tissue matrix and forced to grow on rigid plastic surfaces or cancer cell lines that have been grown in the laboratory under unphysiologic conditions for decades. As a result of this artificial environment, cell monolayers might predict basic drug toxicity responses (e.g., if a drug destroys cancer cells or harms normal cells) but cannot capture complex human physiology, leading to unreliable results.[1]

In contrast to monolayer *in vitro* models, animal models capture the complex tissue architectures and multi-organ interaction of a whole organism. However, animal anatomy and physiology are fundamentally different from the human body. To overcome some of these shortcomings, scientists invented transgenic mouse models that artificially induce human-like diseases in lab animals. Some of these models might mimic human diseases, but the inability of animal models to accurately replicate human diseases is becoming increasingly evident.[2] As a consequence of this widespread use of unrepresentative *in vitro* and *in vivo* model systems, many drugs fail to show efficacy and safety when advancing from preclinical to clinical trials, and drug approval rates are declining despite better identification mechanisms to find candidates.[1]

Chip-based *in vitro* organ models offer a solution to the disadvantages of current biomedical models. Organ-on-a-chip systems combine microfabrication techniques with next-generation cell culture techniques to simulate complex human organ anatomy within a microfluidic device *in vitro*. Applying microfluidic techniques allows to design the desired cell environment flexibly and overcome monolayer cell culture constraints. In other words, scientists can now consider human tissue architecture and invent an individually tailored organ-on-a-chip system to arrange and stimulate tissue cells according to nature's blueprint. To fulfill the unmet need in biomedical research, organ-on-a-chip models need to consider (1) the three-dimensional architecture of tissues and (2) the dynamic environment of the human body. This doctoral work engineers organ-on-a-chip systems to recreate the dynamic 3D tissue microenvironment using dynamic inputs. As illustrated in Figure 1, the implementation of 3D cell culture in organ-on-a-chip technology is crucial for developing relevant model systems.[3]

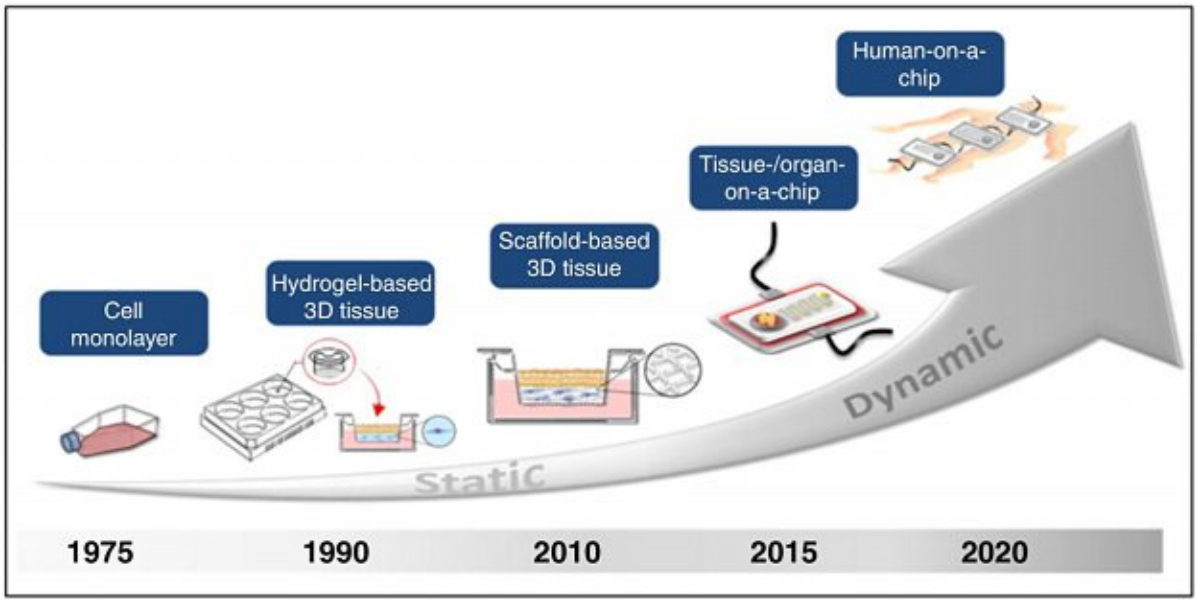

FIGURE 1: ADVANCEMENT OF CELL CULTURE SYSTEMS TO REPLICATE HUMAN ANATOMY FROM CELL MONOLAYERS TO 3D CELL CULTURES AND DYNAMIC ORGAN-ON-A-CHIP SYSTEMS. FROM PLANZ ET AL[3]. REPRINTED WITH PERMISSION FROM ELSEVIER.

In 3D cell culture, tissue cells are embedded within extracellular-matrix mimicking hydrogels that consider the surrounding tissue of the individual cell type (e.g., tissue elasticity, growth factor content, and other types of tissue-resident cells) instead of forcing the cells to grow in plastic dishes.[4] In addition to considering 3D tissue architecture, novel model systems in biomedical research need to subject the 3D *in vitro* tissues to dynamic inputs mimicking their mechanobiological bodily surrounding to recreate human physiology. This thesis's outcomes make a compelling case to implement dynamic inputs like fluid perfusion, interstitial flow, matrix elasticity, and directional nutrient diffusion into organ-on-a-chip systems to increase their significance as a biomedical research model. This chapter puts the importance of the work into context by detailing how microfabrication techniques can replicate biology, explaining why organ-on-a-chip is one of the top 10 emerging technologies[5], and introducing biosensing as a crucial factor to permit non-invasive monitoring of cells in microfluidic devices.

2.1. Rapid prototyping – how to engineer a biological niche

Organ-on-a-chip systems owe the "chip" part of their name to one of their parent technologies – microelectronic computer chips.[6] Microfluidic technology was developed by applying well-established micromachining processes from the semiconductor industry to fabricate initial microfluidic devices from glass and silicon. Microfluidic devices can down-scale chemical reactions to nanolitre volumes, providing an immense advantage for reactions requiring expensive, rare, or toxic chemicals. Due to the superior optical properties and ease-of-use, silicon was soon replaced with high-performance polymers like thermoplastics and poly-

dimethylsiloxane (PDMS).[7] Thermoplastics are polymers that are solid at room temperature but melt at higher temperatures, ideal for high-throughput production in the plastic industry. In contrast, PDMS, a silicone, is a heat-curable polymer that can be cast into molds at room temperature and solidifies at 70°C. PDMS is the most abundant polymer in lab-scale organ-on-a-chip systems due to its optical transparency, oxygen permeability, and biocompatibility.[8]

The replacement of silicon with plastics allowed microfluidic technology to move from elaborate manufacturing procedures requiring clean-room facilities to methods easily accessible with minimal equipment in any biomedical research laboratory.[7] Soft lithography, the most frequently used method, involves casting liquid PDMS onto a mold with the microfluidic structures' positive counterparts. The mold can be manufactured from a digital design via photolithography or 3D printing. Photolithography is an elaborate process but allows to achieve structures down to 100 µm even without clean-room facilities, while cheap and accessible 3D printing has a resolution of 1 mm. The easy accessibility of these techniques combined with their ability to produce molds of appropriate resolution facilitates rapid microfluidic device prototyping in biomedical research.

Figure 2 shows a microfluidic device manufacturing process using photolithography and replica molding, as applied within this thesis.[9] Figure 2a depicts the photolithography process where a mold is produced by coating a UV-curable material (photoresist) onto a silicon wafer before being overlayed by a photomask containing the microfluidic device structures. Subsequent UV-exposure then only solidifies the photoresist corresponding to the desired structures, yielding a positive replica of the desired microchannels after removing the remaining liquid photoresist. The mold is then used to manufacture the actual microfluidic

device from PDMS via replica molding, as shown in Figure 2b. To this end, heat-curable PDMS is cast on top of the mold, polymerized, and peeled off. After PDMS polymerization, the final microfluidic device is produced by back-end processing through punching in- and outlet ports and bonding the PDMS to a glass surface via oxygen plasma to generate sealed channels

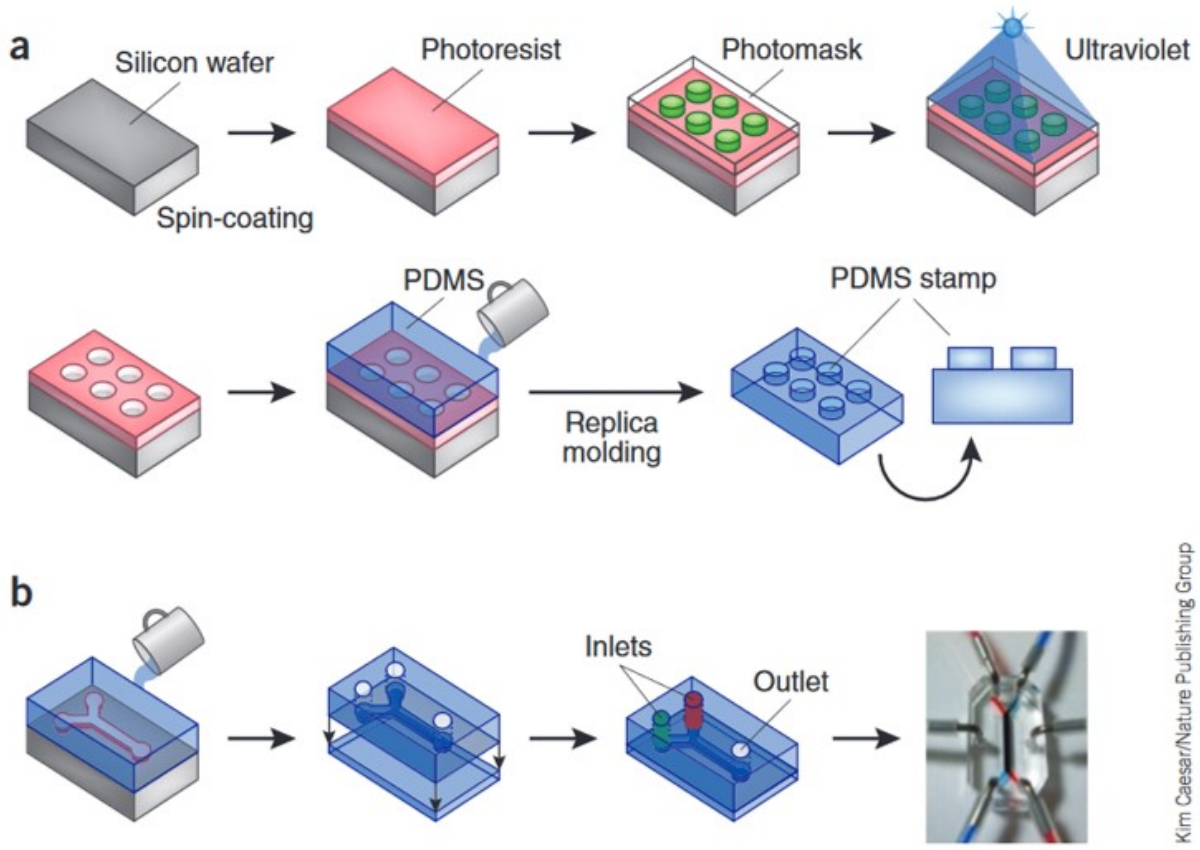

FIGURE 2: SOFT LITHOGRAPHY MICROFABRICATION TECHNIQUE. (A) PHOTOLITHOGRAPHY PRODUCES A POSITIVE REPLICA OF THE DESIRED MICROSTRUCTURES BY COATING A UV-CURABLE MATERIAL (PHOTORESIST) ONTO A SILICON WAFER AND CURING VIA UV-EXPOSURE. (B) REPLICA MOLDING OF PDMS YIELDS THE FINAL MICROFLUIDIC DEVICE VIA LIQUID POLYMER CASTING, CURING, AND BACK-END PROCESSING. IMAGE REPLICATED FROM BHATIA AND INGBER[10] WITH PERMISSION FROM SCIENCE NATURE PUBLISHING.

Alternative microfabrication procedures to soft lithography use thermoplastics for hot embossing or injection molding and are typically used when scaling up microfluidic device production for commercial purposes.[11] These methods utilize the thermoplastic properties of melting into liquid form at higher temperatures. Hot embossing melts a polymer plate's

surface and imprints it with microfluidic structures, while a liquid polymer solution is introduced into a mold and subsequently hardened in injection molding.

The intended purpose and available infrastructure determine the type of microfabrication method applied to manufacture organs-on-a-chip. In biomedical research, the microfabrication method needs to enable the microchannel features' rapid adjustment to facilitate design iterations based on biological experiments. In other words, microfluidic devices typically undergo multiple stages of design modifications and device development to become a functional organ-on-a-chip device. When designing an organ-on-a-chip device, the first steps are to determine (1) the functional characteristics and needed complexity, (2) the factors crucial for the research question, and (3) the required readouts.[12] These parameters, discussed within the next sections, include fluid and user handling, choice of cell and cultivation type(s), the implementation of on-line monitoring to facilitate readout or integration of dynamic stimulation.

2.2. From microfluidic devices to organs-on-a-chip

Lab-on-a-chip and organ-on-a-chip technology are based on microfluidic systems invented to analyze and manipulate small (10^{-9} to 10^{-18} liters) amounts of fluids in micrometer-sized channels.[6] Microfluidic systems utilize their small channel size to (1) minimize the amount and cost of reagents, (2) shorten reaction times, and (3) increase detection resolution and sensitivity in chemical reactions.[13] With the precise control of channel size and geometry, microfluidic chips can perform chemical reactions on a scale of mm^3 instead of cost-intensive

m^3-sized reactors. Flows in microfluidic devices are always laminar due to the small size of microfluidic channels, resulting in fluids flowing alongside one another without mixing. This phenomenon enables surface patterning without additional equipment and generates specific regions to capture antibodies or cells for facile result readout.

From initial devices with simple channels, microfluidic systems quickly evolved into lab-on-a-chip systems by adding automated fluid handling to perform reactions within one device that typically require multiple steps in a lab.[14,15] A lab-on-a-chip device typically includes multiple fluid inlets for samples and reagents, channels to separate, mix, or incubate the reagents, pumps to move the fluids, and sensor spots for analysis as shown in Figure 3.[15,16]

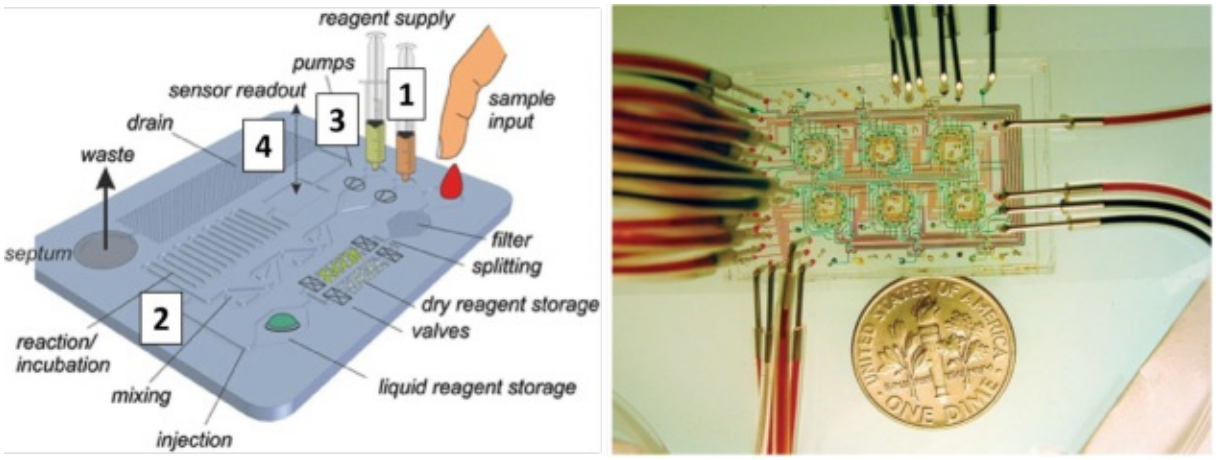

FIGURE 3: (LEFT) SCHEMATIC OF A TYPICAL LAB-ON-A-CHIP DEVICE CONTAINING (1) INPUTS FOR SAMPLE AND REAGENTS, (2) MICROFLUIDIC CHANNELS FOR FILTERING, SPLITTING, AND MIXING FLUIDS, (3) PUMPS AND VALVES TO MOVE THE FLUID AND (4) A SENSOR READOUT SPOT. (RIGHT) A PHOTOGRAPH OF A MICROFLUIDIC DEVICE WITH MULTIPLE FLUID INLETS (RED/YELLOW) AND VALVES FOR FLUID MANIPULATION (GREEN). CHANNELS ARE FILLED WITH INK FOR VISUALIZATION. ADAPTED FROM CASTILLO-LEÓN ET AL[15] AND BALAGADDÉ ET AL[16] WITH PERMISSION FROM SPRINGER AND SCIENCE NATURE PUBLISHING GROUPS.

The advantages of lab-on-a-chip systems to spatially control fluids while simultaneously reducing reagent consumption soon led to the application of microfluidics in cell-based lab-on-a-chip systems[11]. Conventional cell culture consumes large amounts of cells and expensive

growth media. However, physiologically relevant primary cells are often tricky to isolate due to tissue availability, do not retain their functionality in culture, and require multiple weeks to reach appropriate cell numbers. Additionally, many conventional cell-based assays lack reproducibility, reliability, and robustness leading to experimental inconsistencies.[17] Applying lab-on-a-chip technology to cell culture provides analysis tools to inexpensively grow and analyze small numbers of cells under reproducible measurement conditions. Microfluidic systems are the only technology capable of spatiotemporally controlling cell growth and simultaneously mimicking the complex tissue environment by regulating fluid and soluble factor transport using microfluidic channels.[18]

Early applications of cell-based lab-on-a-chip systems included manipulation of cells suspended in fluid for cell sorting and analysis or fractionation of tumor cells and platelets in blood samples.[19,20] One application of cell-based microfluidic systems to separate platelets, white blood cells, and circulating tumor cells is depicted in Figure 4.[21]

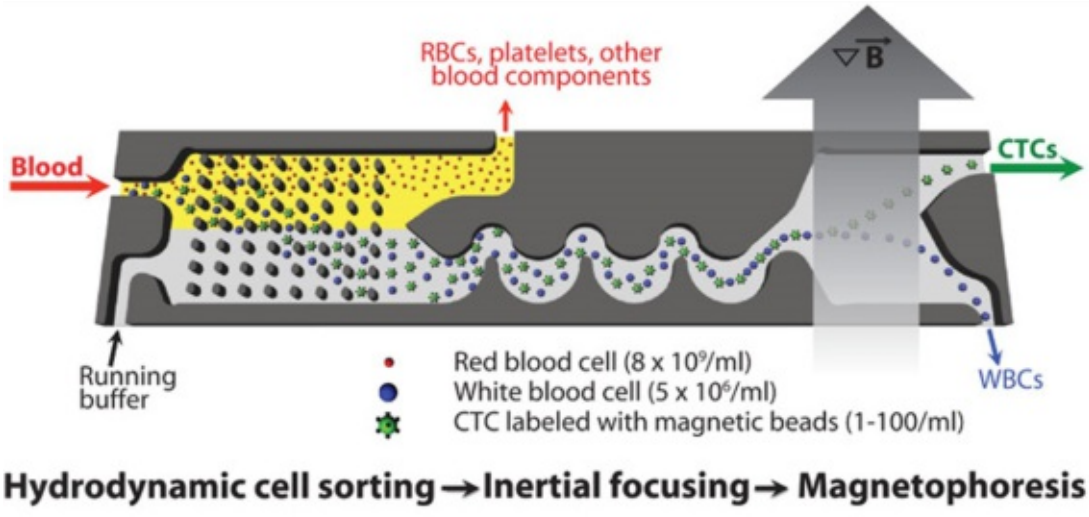

FIGURE 4: SCHEMATIC OF MICROFLUIDIC DEVICE TO SORT BLOOD COMPONENTS USING HYDRODYNAMIC CELL SORTING, INERTIAL FOCUSING, AND MAGNETOPHORESIS ON ONE DEVICE. CTC = CIRCULATING TUMOR CELL. IMAGE ADAPTED FROM OZKUMUR ET AL[21] AND REPRINTED WITH PERMISSION FROM SCIENCE TRANSLATIONAL MEDICINE.

Here, microfluidic technology is applied to first separate nucleated cells from other blood components before cell focusing and separation based on a magnetic label. Such microfluidic systems are tremendously useful for detecting and analyzing small amounts of tumor cells in cancer patients, facilitating diagnosis and prognosis, and demonstrating microfluidic technology applicability to cell-based assays.

As the next step towards building an organ-on-a-chip, microfluidic devices were used to cultivate adherent cell monolayers. Microfluidic technology opened the possibility of progress from conventional methods to study cell-cell signaling in Transwell® systems to individualized microfluidic chambers.[8] Transwell® systems consist of two spatially separated cell culture compartments divided by a permeable membrane, enabling cell-cell signaling through the shared cell culture medium while keeping the cells separate. However, it does not enable adjusting cell numbers or distances and is only suitable for monolayer culture of two different cell types. In contrast to Transwell® systems, cell-based microfluidic systems allow individualizing the number of cell types, cell amounts, distances, and cell cultivation setup. Figure 5 shows some examples of devices to study cell-cell interactions on-chip.[22] These microfluidic systems can account for physiologically relevant cell ratios, include more than two cell types at distances similar to *in vivo* and cultivate the cells as a monolayer or 3D cell culture depending on the individual physiological niche.

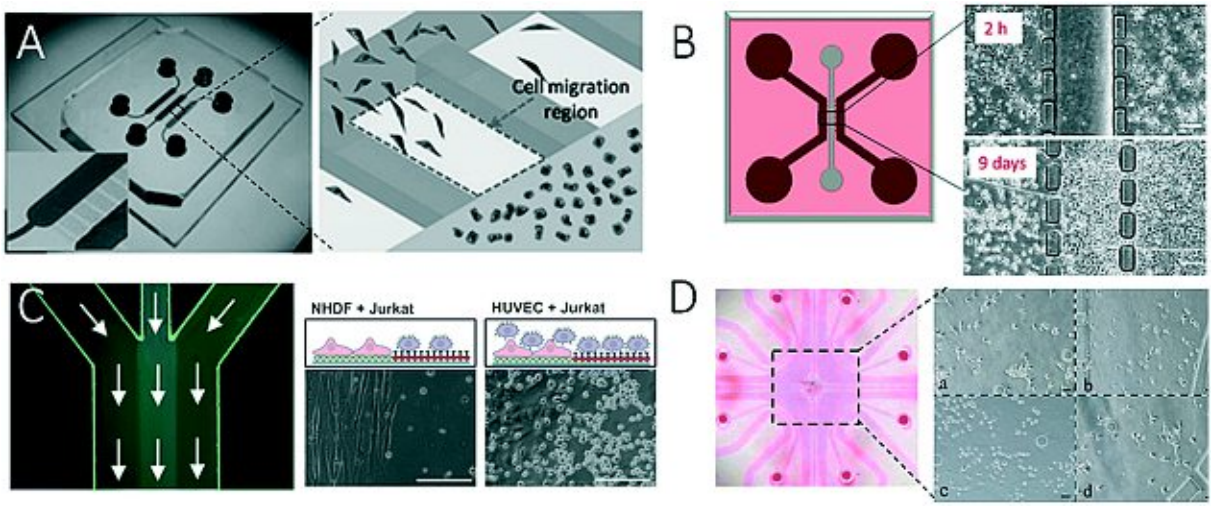

FIGURE 5: EXAMPLES OF MICROFLUIDIC DEVICES STUDYING CELL-CELL INTERACTION. (A) INTERACTIONS BETWEEN FIBROBLASTS AND TUMOUR CELLS. (B), CELL MIGRATION AND CELLULAR INTERACTION BETWEEN BONE MARROW STROMAL CELLS AND A LIVER TUMOUR CELLS, SCALE BAR 20 MM. (C) MICROFLUIDIC CHANNEL PATTERNING FOR CELL CAPTURE AND CULTIVATION, SCALE BAR 200 µm. (D) RECONSTRUCTING THE BLADDER MICROENVIRONMENT BY COCULTURE OF FOUR DIFFERENT CELL TYPES SEPARATED VIA HYDROGEL BARRIERS. ADAPTED FROM ROTHBAUER ET AL[22] - PUBLISHED BY THE ROYAL SOCIETY OF CHEMISTRY.

3D cell cultures, where cells are cultured within hydrogels or scaffolds, mimic tissue structure and are the first step towards creating more relevant *in vitro* models. Especially hydrogels, hydrophilic polymer networks that consist predominantly of water to form a jelly-like substance, can easily be integrated into cell-based microfluidic systems due to their polymerization behavior. Cells are resuspended and injected within the liquid hydrogel that subsequently polymerizes on-chip to form a 3D matrix as applied within this thesis. The union of microfluidic technology with advanced cell culture techniques gave rise to a new field of preclinical modeling in biomedical research – organ-on-a-chip.

Organ-on-a-chip systems are defined by the ability to recapitulate the smallest functional unit of an organ. This quest is achieved by carefully considering cell types, numbers, architecture, and the organ environment in question to stimulate the cells to function similarly to bodily tissues. In other words, each organ-on-a-chip system needs to replicate the signals directing

cells *in vivo* via *in vitro* engineering methods to gain native cell behavior.[10] Cells cultivated within organ-on-a-chip systems show cell differentiation, maturation, and organization replicating their target tissue. Figure 7 shows three different systems for liver, kidney, and lung-on-a-chip systems. These examples represent tissue barriers by downscaling the representative components to a cell-fluid interface and are capable of mimicking their organ parent's key parameters. For example, livers-on-a-chip absorb and metabolize drugs, kidneys-on-a-chip eliminate toxins, and lungs-on-a-chip react negatively to smoke exposure.[23–25] Table 1 additionally summarizes currently available organ-on-a-chip systems capable of predicting physiological cell behavior, disease phenotypes, and drug responses in a research setting.

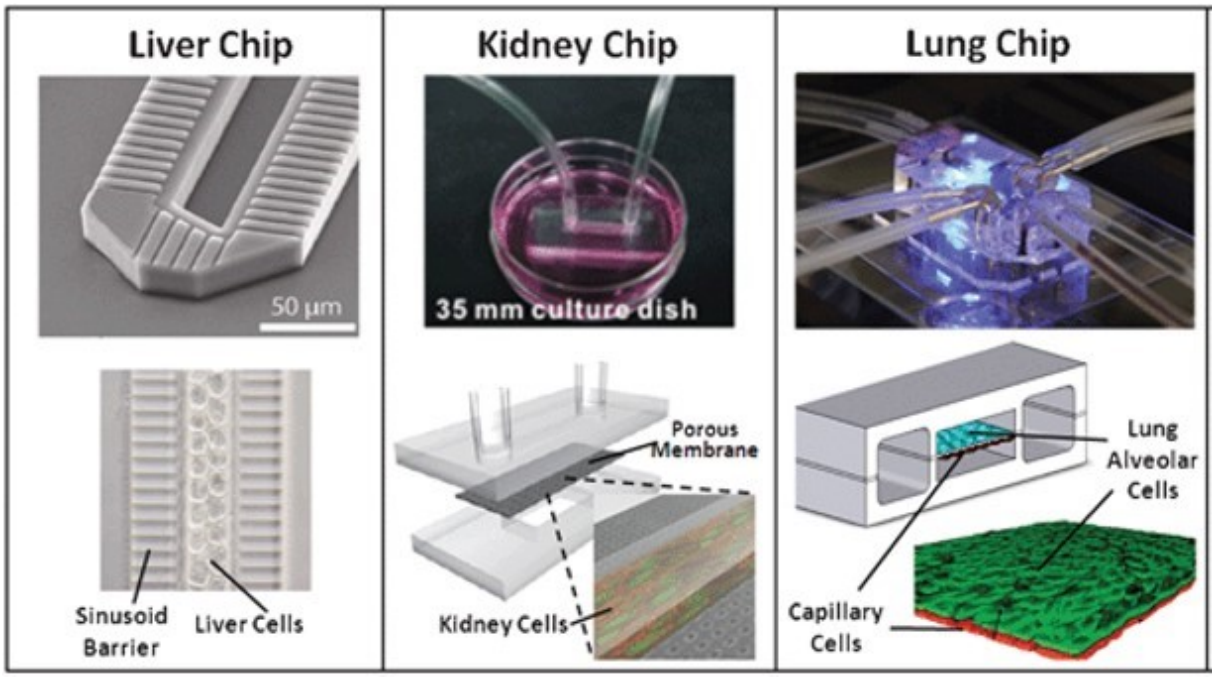

FIGURE 6: ORGAN-ON-A-CHIP SYSTEMS MIMICKING TISSUE–TISSUE AND ORGAN–ORGAN INTERFACES. LIVER CHIP: HEPATOCYTES SEPARATED FROM FLUID FLOW BY A MICROFABRICATED BARRIER MIMICKING A LIVER SINUSOID. KIDNEY CHIP: A SEMI-PERMEABLE MEMBRANE SEPARATES KIDNEY EPITHELIAL CELLS FROM A PERFUSED CHANNEL REPRESENTING URINE. LUNG CHIP: LUNG EPITHELIAL CELLS AND MICROVASCULAR ENDOTHELIAL CELLS SEPARATED BY, CULTIVATED ON, AND STRETCHED VIA A FLEXIBLE MEMBRANE REPRESENT THE ALVEOLAR-CAPILLARY INTERFACE. ADAPTED FROM HUH ET AL[22] WITH PERMISSION FROM THE ROYAL SOCIETY OF CHEMISTRY.

TABLE 1: OVERVIEW OF THE MOST STUDIED ORGAN-ON-A-CHIP SYSTEMS, ADAPTED FROM RONALDSON-BOUCHARD AND VUNJAK-NOVAKOVIC[12] WITH PERMISSION FROM CELL PRESS.

ORGAN TYPE (FUNCTIONAL UNIT)	DESIGN CONSIDERATIONS	READOUTS	REFERENCES
HEART	Contractility and electrical activity	Beat rate, excitation threshold, maximum capture rate, contractility	26–32
LUNG (ALVEOLI)	Air-liquid interface and pulmonary drug absorption	Cell imaging and dissolved gas concentration	33–35
LIVER (HEPATIC LOBULE)	Drug metabolism, cytochrome P450 interaction, and hepatocyte/fibroblast coculture	Albumin and urea production, cytochrome P450 enzymatic activity, metabolite conversion, and drug-induced liver injury (DILI)	36–45
KIDNEY (NEPHRON AND PROXIMAL TUBULE)	Drug clearance and proximal tubule epithelium exposed to shear stress	Filtration, reabsorption, urea concentration, epithelial cell polarization, alkaline phosphatase activity, and permeability glycoprotein efflux transporter	46–48
GUT	Drug absorption, villi and microvilli formation, mucosa barrier, and symbiotic bacteria present	Transepithelial transport, absorption, toxicity, cytochrome P450 3A4 isoform drug metabolism, and responses to bacteria	49–51
BRAIN/BBB	Selective drug penetration and interactions between cell types	Transendothelial resistance (TEER), permeability, and drug transport	52–57
SKIN	Air-liquid interface and dermal drug absorption	Transdermal transport, immunohistochemistry, and gene expression	58–60
VASCULATURE	Barrier functionality and thrombosis	Permeability, response to shear stress, TEER, and FITC-dextran assay	61–64

In summary, organ-on-a-chip systems have transformed biomedical research by providing an alternative to conventional models. This thesis advances the field by engineering novel organ-on-a-chip systems that rely on dynamic inputs to recapitulate human tissues, such as a microvasculature-on-chip system including lymphatic capillaries (**Manuscript #3**) and a cartilage-on-chip system mimicking native tissue architecture (**Manuscript #6**). To become a feasible alternative to animal testing in preclinical drug development, organ-on-a-chip systems need to include (1) biosensing strategies for in-line monitoring of cell behavior within the devices and (2) dynamic cell environments like fluid flow, native tissue elasticity, and directional nutrient gradients.

2.3. BIOSENSING METHODS – MONITORING CELL BEHAVIOR WITHIN MICROFLUIDIC DEVICES

In-line biosensors in microfluidic devices non-invasively monitor cell cultures and provide multiple advantages over conventional endpoint analysis methods such as ELISA or RT-qPCR that require cell harvesting. Biosensor-integrated microfluidic devices (1) allow to observe the cells continuously over prolonged periods, (2) enable to adjust experimental parameters accordingly, (3) remove the necessity of preparing multiple experimental replicas for different endpoint readouts, (4) require less cell culture material than conventional systems, and still (5) provide the ability to harvest the cells for traditional endpoint analysis.[65] As a result, overcoming the limitations of endpoint analysis by integrating biosensors to analyze cell metabolism, barrier functions, or cell activity via oxygen or other metabolites has been a central aim of microfluidic technology in the last five years.[66]

Dissolved oxygen tension directly links to cell behavior *in vitro* and *in vivo*, making it an excellent indicator to monitor the cellular environment in organ-on-a-chip systems. Oxygen sensors assess cell vitality and record metabolic changes in response to drugs or toxic compounds via oxygen consumption rates. This thesis reports a method to monitor oxygen levels using optical sensing non-invasively via integrated luminescent sensor spots (**Manuscript #1**).[67] In optical oxygen sensing, a luminescent oxygen sensor continuously measures dissolved oxygen tension based on an oxygen-sensitive dye. The liquid sensors easily integrate into the transparent microfluidic devices via subsequently dried sensor spots. Exemplary images of microfluidic devices containing non-invasive real-time oxygen sensors are shown in Figure 7.

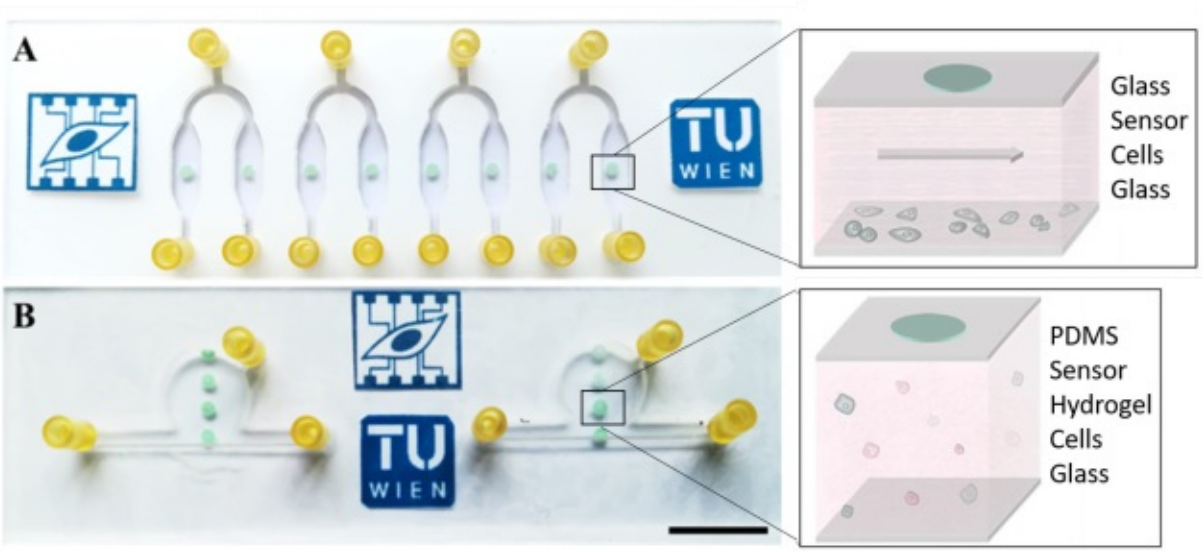

FIGURE 7: (A) MICROFLUIDIC DEVICE TO MONITOR OXYGEN LEVELS IN CELL MONOLAYERS WITH AN INCORPORATED LUMINESCENT OXYGEN SENSOR IN GREEN AND SCHEMATIC OF SENSOR SETUP WHERE THE SENSOR SPOTS SITS ABOVE THE CELL CULTURE. (B) MICROFLUIDIC DEVICE TO MONITOR OXYGEN CONCENTRATION AT DIFFERENT LOCATIONS WITHIN A 3D HYDROGEL-BASED CELL CULTURE VIA A SENSOR SPOT ARRAY (GREEN) AND SCHEMATIC OF SENSOR SETUP. ADAPTED FROM ZIRATH, SPITZ, ROTHBAUER & BACHMANN ET. AL.[67] WITH PERMISSION FROM FRONTIERS BY THE CREATIVE COMMONS ATTRIBUTION LICENSE.

Dissolved oxygen tension within the microfluidic cell culture gives information on (1) cell vitality, (2) cell metabolism, and (3) oxygen availability. This information can help assess physiologic conditions within the device, record changes resulting from pathologic alterations, or determine nanoparticle and drug toxicity. In other words, integrated oxygen sensors allow to monitor dynamic changes within the cell environment non-invasively and in real-time over prolonged culture periods.

Such cost-efficient and reliable sensing approaches are crucial to enable high-throughput drug testing in organ-on-a-chip systems needed for biomedical research and pharmaceutical development. However, to date, only a handful of sensing approaches have been combined with organ-on-a-chip systems. This thesis describes a novel approach for oxygen sensing in microfluidic cell cultures. Integrating in-line sensing methods in organ-on-a-chip systems will improve organ-on-a-chip technology prospects to become a viable alternative to conventional preclinical models. In addition to incorporating in-line sensing to accommodate high-throughput testing, organ-on-a-chip systems need to replicate the dynamic tissue environment by applying microfluidic engineering techniques. The next section will explain why this dynamic environment is crucial to attaining physiologic biomimicry *in vitro* and how this thesis employs organ-on-a-chip systems to subject 3D cell cultures to mechanical stimulation resembling the native microenvironment.

3. MECHANOBIOLOGY-ON-A-CHIP – CONSIDERING THE DYNAMIC HUMAN TISSUE ENVIRONMENT

Human tissues are continuously subjected to physical stress. It can be as evident as the heart pumping blood through the cardiovascular system and cartilage tissues compressed by walking, or as imperceptible as tissue elasticity and interstitial fluid flow. Mechanobiology describes how cells react to these mechanical inputs with a biological output, dictating physiological tissue maintenance or pathological changes. Dynamic stimuli substantially impact tissue development and functionality by directing cell migration, differentiation, and matrix synthesis. The *in vitro* replication of this ever-changing physiologic environment is crucial to gain a relevant biomedical research model.

Organ-on-a-chip systems can precisely mimic biological niches by adapting engineering techniques from lab-on-a-chip systems like electrochemical fluid separation, fluid perfusion, or valves with flexible membranes. Figure 8 shows the mechanobiological cell environment *in vivo* and how organs-on-a-chip can replicate it *in vitro* (**Manuscript #2**).[68] Tissue cells experience static mechanic stimulation like tissue topography and elasticity, flow-induced mechanical stimuli like shear stress and interstitial flow, and direct physical inputs like compression and stretch. Organ-on-a-chip technology presents an *in vitro* research model to recreate these stimuli while controlling the cell environment and monitoring cell behavior. Microfluidic pumps push fluid through the channels to mimic blood flow,[64,69,70] fluid reservoirs create hydrostatic pressure and interstitial flow similar to the capillary bed,[71–73] and flexible membranes imitate breathing,[33,74] gut peristalsis,[75,76] or cartilage compression[77] to yield cell behaviors that strikingly resemble *in vivo* phenomena.

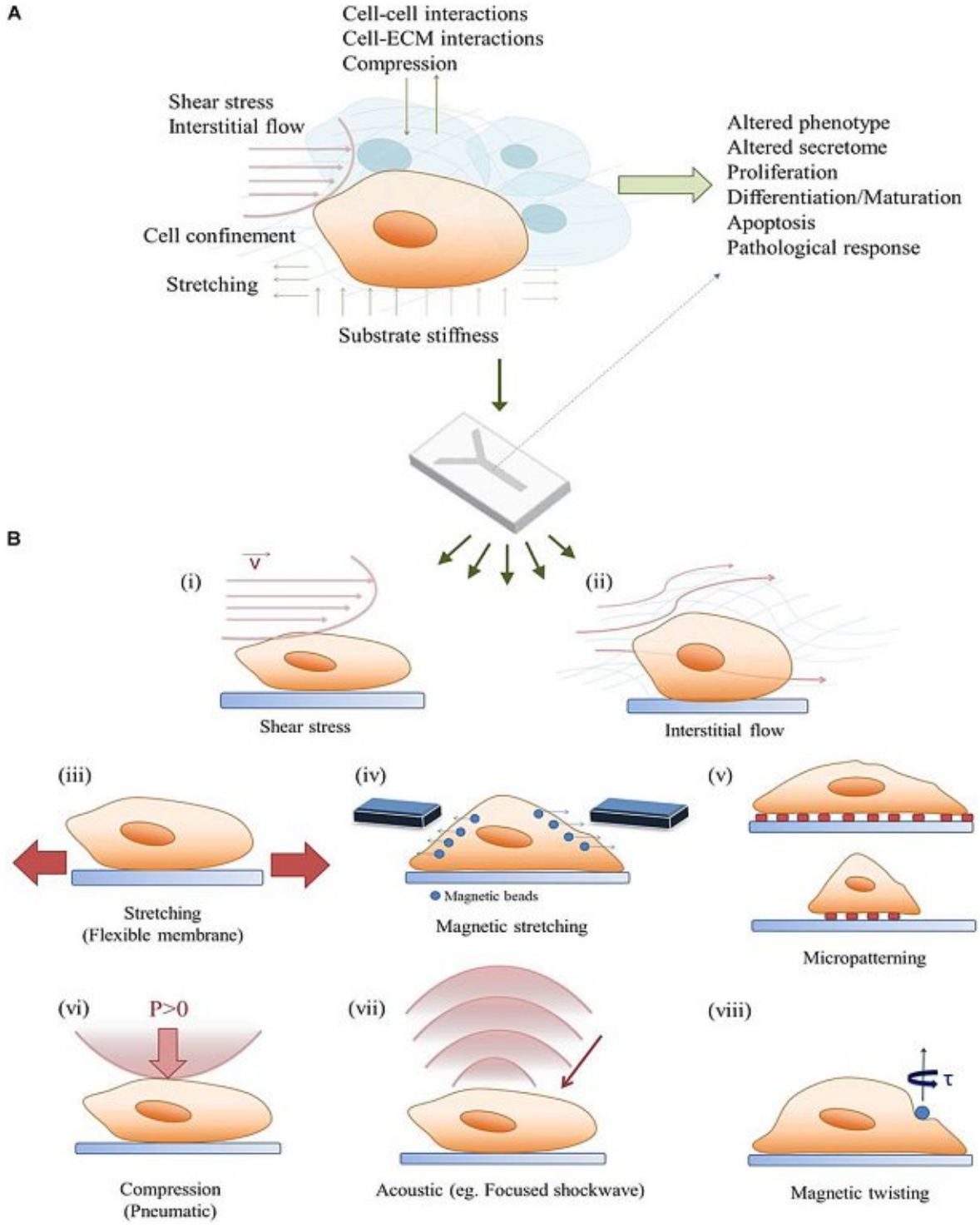

FIGURE 8: THE DYNAMIC CELL ENVIRONMENT AND METHODS TO REPLICATE IT USING ORGAN-ON-A-CHIP SYSTEMS. (A) **MECHANOBIOLOGICAL CUES IN THE CELLULAR ENVIRONMENT REGULATE CELL SIGNALING AND PHENOTYPE AND DICTATE PHYSIOLOGICAL AND PATHOLOGICAL TISSUE RESPONSE.** (B) **POTENTIAL ON-CHIP STIMULATION STRATEGIES FOR MICROFLUIDIC CELL CULTURES. ADAPTED FROM ERGIR & BACHMANN ET AL[68] UNDER PERMISSION FROM FRONTIERS BY THE CREATIVE COMMONS ATTRIBUTION LICENSE.**

Figure 9 illustrates specific engineering approaches to replicate heart and lung biology and design considerations to replicate the dynamic tissue environment.[12] To mimic heart tissue, a strip of human cardiomyocytes capable of beating motions is stimulated electromechanically and reacts with alternations in beating frequency and contraction intensity (Figure 9A-C). In contrast, a barrier of lung epithelial and endothelial cells on either side of a flexible membrane represents a human lung alveolus. In this model, mechanic stimulation via blood flow in the endothelial compartment combined with cyclic stretching of the membrane emulates blood flow and breathing motions to replicate organ-level lung functions (Figure 9D-F).[33] These examples demonstrate that mechanobiology-on-chip devices permit unprecedented replication of dynamic tissue environments within *in vitro* models, making them an ideal engineering tool to enhance preclinical model relevance.

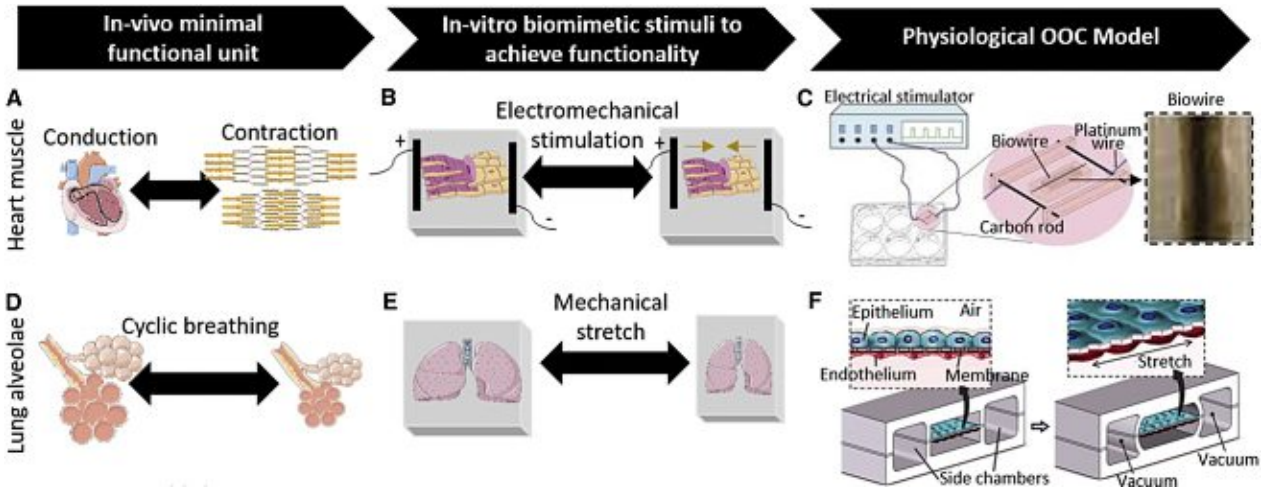

FIGURE 9: (A–C) STRIP OF CARDIAC TISSUE DEFINED AS THE MINIMAL FUNCTIONAL UNIT OF A HEART INVOLVING (A) CONDUCTION AND CONTRACTILITY AND (B) ELECTROMECHANICAL STIMULATION. (C) HEART-ON-CHIP DEVICE WITH HUMAN CARDIOMYOCYTES EMBEDDED IN A HYDROGEL THAT CAN BE ELECTROMECHANICALLY STIMULATED. (D–F) SINGLE ALVEOLUS AS THE MINIMAL FUNCTIONAL UNIT OF A LUNG MIMICKING (D) CYCLIC BREATHING USING (E) CYCLIC MECHANICAL STRETCH. (F) A LUNG-ON-CHIP DEVICE CONSISTING OF LAYERS OF EPITHELIUM AND ENDOTHELIUM ON TWO SIDES OF A STRETCHABLE MEMBRANE. REPRINTED FROM RONALDSON-BOUCHARD AND VUNJAK-NOVAKOVIC[12] WITH PERMISSION FROM ELSEVIER.

This section will detail how the organ-on-a-chip systems engineered within this thesis implemented mechanobiological stimulation to enhance the physiologic relevance of vasculature-on-chip and cartilage-on-chip models. Subjecting 3D cell cultures to physiologic perfusion, interstitial flow, matrix elasticity, and dynamic nutrient gradients results in a more accurate depiction of the native tissue niche.

3.1. Fluid flows – perfusion and interstitial flow in vascular models

Physiological models of the human vasculature need to include fluid flows to replicate anatomical and functional characteristics crucial for vascular biology and associated pathologies.[78] However, conventional *in vitro* replicas of vasculature predominantly rely on cell monolayers, where endothelial cells lining the inner side of blood vessels in the body are cultivated within plastic dishes representing neither the dynamic nor the 3D nature of vasculature. Organ-on-a-chip systems provide an alternative that can incorporate 3D capillary networks and emulate fluid flows to generate vasculature-on-chip systems for cardiovascular and lymphatic preclinical models.

Vasculature-on-chip devices incorporate hydrogels as a matrix for 3D vessel formation using two different methods - sacrificial molding or self-assembled vascularization.[78] Schematic devices and workflows of both methods are depicted in Figure 10. Sacrificial molding creates a single vessel within a hydrogel matrix by polymerizing the hydrogel around a needle that is subsequently removed before circumferential endothelial cell seeding. This method recreates vessels of 75 – 250 µm in diameter and is routinely employed in cardiovascular microfluidic

models to determine endothelial cell behavior[79] and barrier characteristics[80] in response to growth factor stimulation,[81,82] drug treatment,[83] and disease.[84,85] Since 2018, the repertoire includes first replicas of lymphatic vasculature alone[86] or in combination with blood vessels.[87]

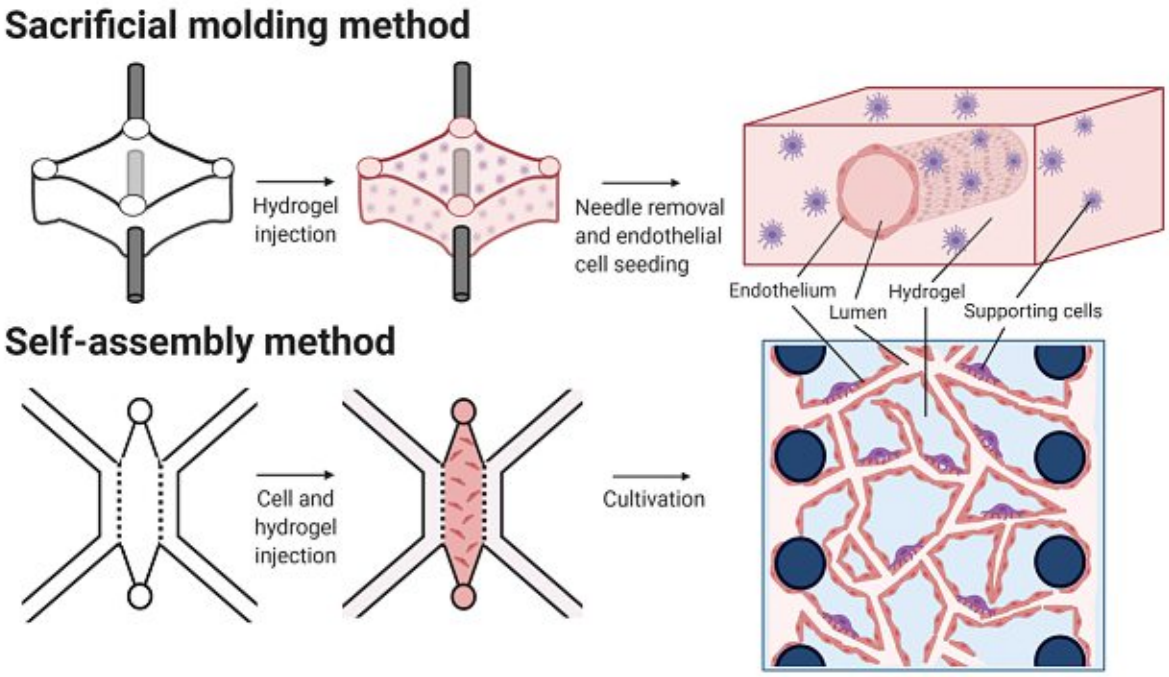

FIGURE 10: METHODS IN VASCULATURE-ON-CHIP DEVICES TO RECREATE A 3D ENVIRONMENT. SACRIFICIAL MOLDING CREATES ONE SINGLE VESSEL WITH AN OPEN LUMEN WHILE SELF-ASSEMBLY RELIES ON CAPILLARY FORMATION FROM A CELL SUSPENSION VIA VASCULOGENESIS. IMAGE CREATED USING BIORENDER.COM.

In contrast to sacrificial molding, self-assembly models utilize vasculogenesis from single cells to form interconnected networks. Hydrogel-embedded endothelial cells are injected into a central channel separated from two medium channels by micropillars. The method generates a replica of the capillary bed with vessel diameters of 5 – 50 µm where the medium supply channels represent an arteriole and venule. Mural cells in direct cell-cell contact or spatially separated chambers act as pericytes[64] or specific tissue cells.[88] These devices can generate fluid flows similar to *in vivo* capillaries, resulting in physiologic permeability values[89] to investigate cancer metastasis[88] and anti-angiogenic therapies.[90] Like in sacrificial molding

techniques, lymphatic vasculature models using self-assembly or simply hydrogel-embedded lymphatic endothelial cells are still scarce. The two existing studies report a physiologic reaction to growth factor and directional interstitial flow stimulation[73] and an involvement of LECs in the metastatic cascade.[91] This thesis reports the first self-assembly model that combines blood and lymphatic capillaries by recreating the capillary bed's physiologic fluid flows (**Manuscript #3**). Table 2 gives an overview of vasculature-on-chip systems reported since 2010 and existing lymphatic replicas to date.

TABLE 2: OVERVIEW OF VASCULATURE-ON-CHIP METHODS, VASCULATURE TYPES, AND OUTCOMES

METHOD	VASCULATURE	OUTCOME AND REFERENCE
SACRIFICIAL MOLDING	BLOOD	Essential proteins in regulating barrier function in inflammation[85]
		Identification of novel mechanosensory complex[79]
		Formation of stable arteriole and artery-like structures[92]
		Efficacy of low-intensity ultrasound treatment of tumors[93]
	LYMPH	Organotypic lymphatic function dependent on cell-cell signaling[86]
	BLOOD & LYMPH	Anti-angiogenic drug screening[87]
SELF ASSEMBLY	BLOOD	Angiogenesis dependent on IF and VEGF concentration[94]
		Direct cell-cell contact and reciprocal signaling are vital for vasculogenesis[64]
		On-chip recapitulation of physiologic permeability[72]
	LYMPH	Interstitial flow augments LEC sprouting in synergy with growth factors[73]
	BLOOD & LYMPH	LEC and BEC form viable vessels as a result of dynamic cultivation in a coculture setup resembling the capillary bed (**Manuscript #3**)

In contrast to conventional static culture methods, these vasculature-on-chip systems can produce physiologically relevant fluid flows using pumps or hydrostatic pressure. The applied method depends on the studied vascular biology and the intended flow velocity.[95] Fluid pumps connected to the microfluidic channels can generate flow velocities in the scale of cm/s to

mimic intraluminal blood flow. Exposing endothelial cells to this type of flow alters their behavior and can result in cell alignment and vascular network formation depending on microfluidic device design and flow setup, as shown in Figure 11 (**Manuscript #4**).[64]

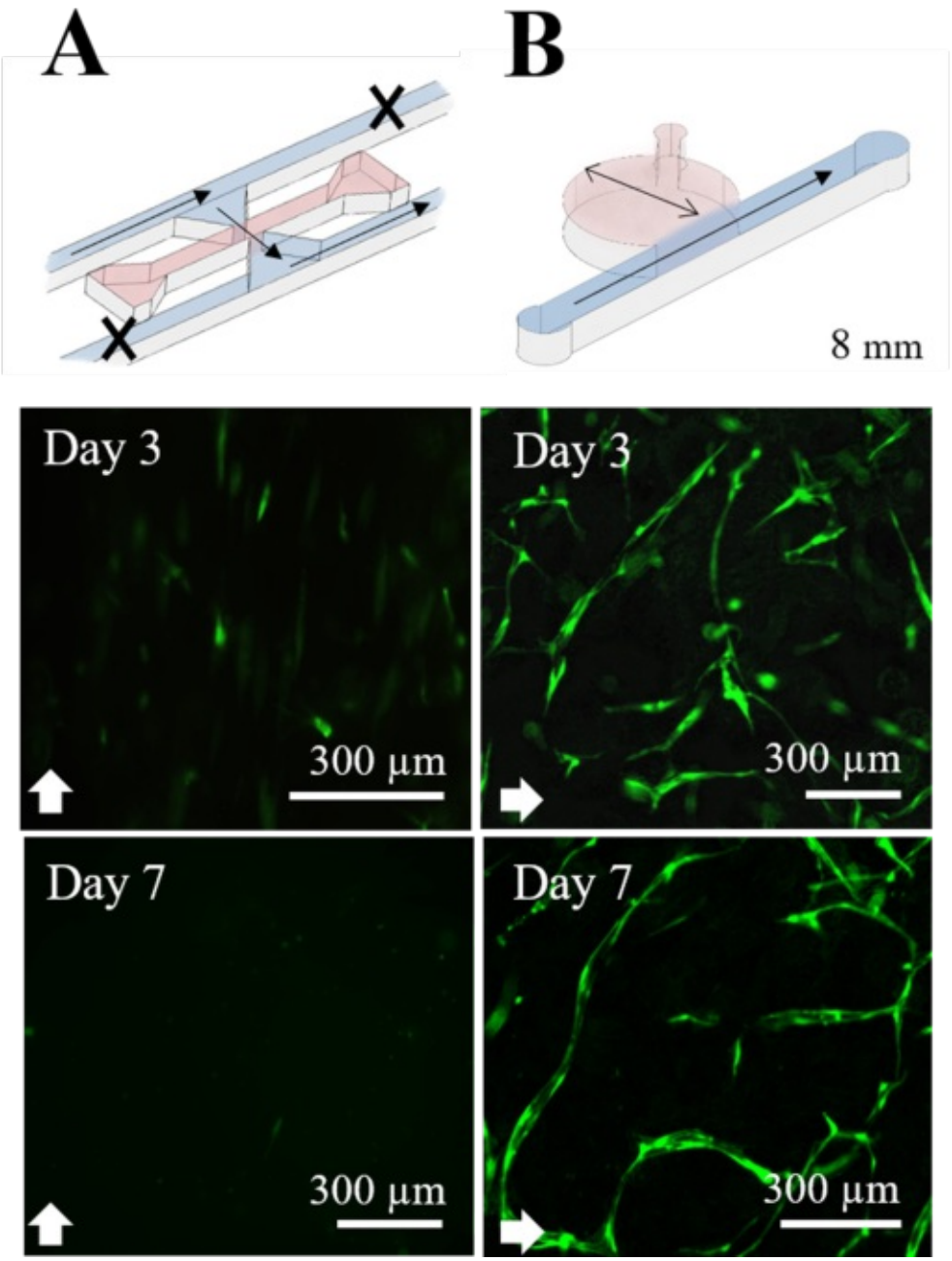

FIGURE 11: MICROFLUIDIC DEVICES TO INVESTIGATE ENDOTHELIAL CELL RESPONSES TO FLUID PERFUSION. ARROWS INDICATE FLOW DIRECTION. (A) DIRECT PERFUSION OF HYDROGEL-EMBEDDED VASCULAR CULTURES SHOWING LOSS OF CELL VIABILITY WITHIN 7 DAYS. (B) INDIRECT PERFUSION OF HYDROGEL-EMBEDDED VASCULAR CULTURES SHOWING FORMATION OF FUNCTIONAL VASCULAR NETWORKS WITHIN 7 DAYS. REPRODUCED FROM BACHMANN ET AL[96] WITH PERMISSION FROM AIP PUBLISHING.

Fluid perfusion through or next to hydrogel-embedded endothelial cell cultures directs endothelial cell behavior in microfluidic devices. Indirectly perfused cultures benefit from improved nutrient delivery and form vascular networks within seven days, while direct perfusion results in reciprocal signaling molecule elution and cell death.

In contrast to external fluid perfusion to generate flow velocities in the cm/s range, hydrostatic-pressure driven flow vasculature-on-chip devices operate with an interstitial-like fluid flow with velocities on the scale of µm/s. The flow is generated via gravity due to fluid column height differences between reservoirs on either side of the cell chamber. Figure 12 shows the generation of a hydrostatic pressure-driven flow in a self-assembly device with hydrogel compartments for blood and lymphatic vasculature (**Manuscript #3**).

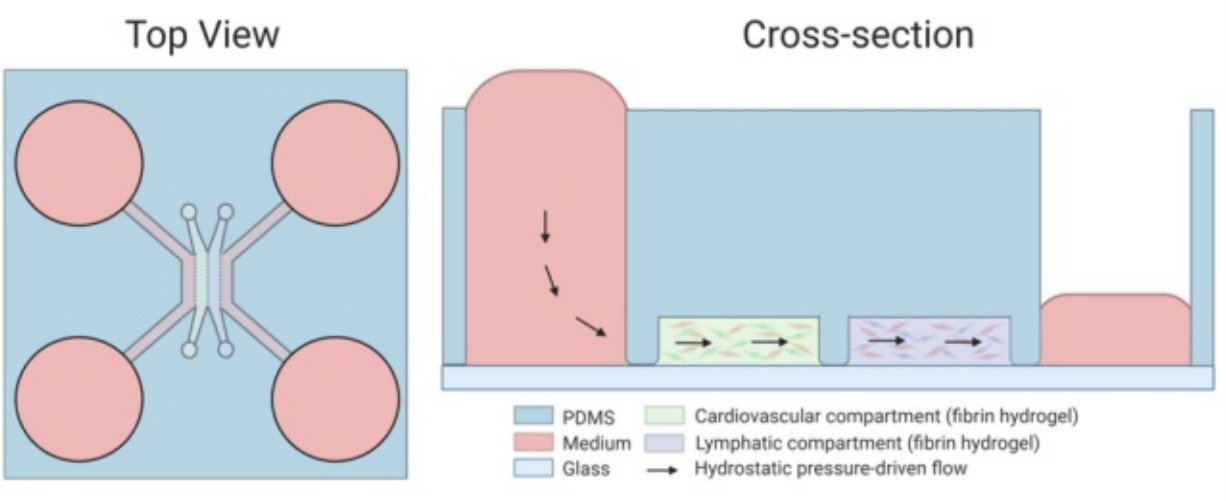

FIGURE 12: TOP VIEW AND CROSS-SECTION OF MICROFLUIDIC DEVICE MIMICKING THE CAPILLARY BED VIA HYDROSTATIC PRESSURE-DRIVEN FLOW. A FLUID COLUMN HEIGHT DIFFERENCE BETWEEN THE MEDIUM RESERVOIRS ON EITHER SIDE OF THE DEVICE GENERATES A FLUID FLOW OF 1 – 3 µm/s REPRESENTATIVE OF THE INTERSTITIAL FLOW WITHIN THE CAPILLARY BED. IMAGE CREATED USING BIORENDER.COM.

The device mimics interstitial fluid flow for mechanobiological stimulation and enhanced physiologic representation of the capillary bed. Interstitial fluid flow describes the fluid flow through tissues generated by a combination of transendothelial flow, the surrounding tissue's dynamic movement, and fluid pressure differences in the capillary bed, as depicted in Figure 13.

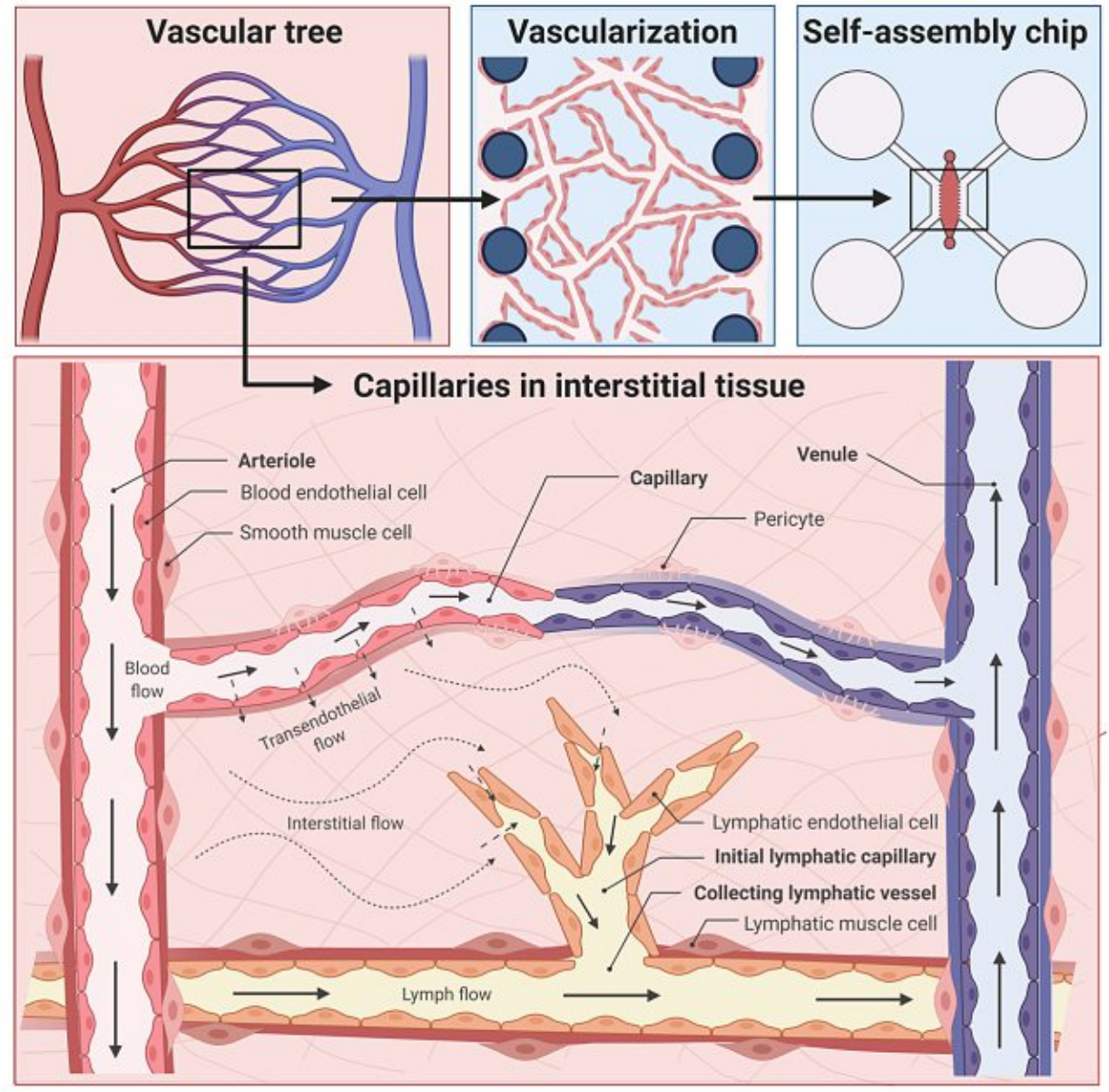

FIGURE 13: ANATOMY AND FLUID FLOW WITHIN THE CAPILLARY BED AND INTERSTITIAL TISSUE CONSISTING OF BLOOD AND LYMPHATIC VASCULATURE AND ENGINEERING OF CAPILLARIES WITHIN A VASCULATURE-ON-CHIP MICROPHYSIOLOGICAL SYSTEM. IMAGE CREATED USING BIORENDER.COM.

With flow velocities In the magnitude of 0.1 – 10 µm/s, interstitial flow is a slow but crucial unseen force in modulating cell behavior that stimulates cells through shear stress on the cell surface or by dynamically shaping pericellular molecule distribution.[97] Interstitial flow direction is vital in lymphatic development in embryos[98] and blood and lymphatic capillary formation in adults.[99] Vasculature-on-chip devices can replicate interstitial flow via hydrostatic-pressure driven flow. This thesis reports the successful establishment of a blood-lymph microvasculature interface-on-chip, depicted in Figure 14 (**Manuscript #3**).

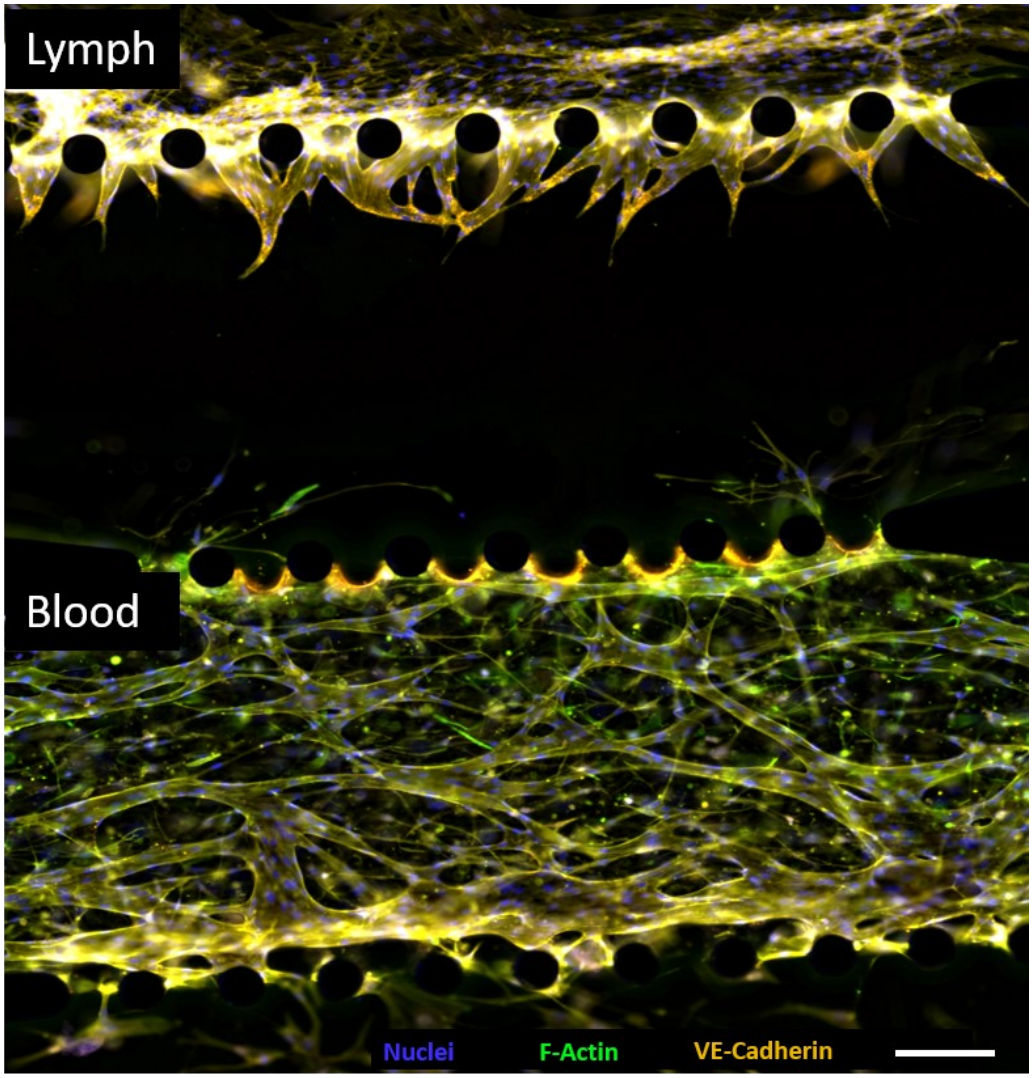

FIGURE 14: BLOOD-LYMPH CAPILLARY INTERFACE ENGINEERED USING MICROFLUIDIC TECHNOLOGY FOR MECHANOBIOLOGICAL FLOW STIMULATION. BOTH LYMPH (TOP) AND BLOOD (BOTTOM) ENDOTHELIAL CELLS FORM VIABLE CAPILLARY STRUCTURES EXPRESSING FUNCTIONAL ENDOTHELIAL CELL JUNCTIONS.

Microfluidic engineering techniques enable cocultivation of spatially separated 3D blood and lymphatic vessels under controlled, unidirectional interstitial fluid flow while allowing signaling molecule exchange similar to the *in vivo* situation. Dynamic, physiologically relevant, mechanobiological cultivation leads to increased vessel sprouting number, length, and morphological characteristics. This organ-on-a-chip system can elucidate drug delivery mechanisms into the lymphatic system, potentially leading to novel anti-inflammatory, anti-viral, and chemotherapeutic therapies by including physiologically relevant mechanobiology.

Dynamic cultivation of vasculature-on-chip is crucial to ensure the functional relevance of the cell-based assays in biomedical research. This thesis's original works show that intraluminal and interstitial flow can be replicated in vasculature-on-chip devices and lead to novel insights into endothelial cell behavior. The vasculature-on-chip models used demonstrate not only the importance of dynamic cultivation but also the crucial impact of considering the tissue environment of the specific cell culture. Endothelial cells only form functional capillary networks in pliable 3D matrices enabling cell migration and in coculture with supporting cells that secrete growth factors. Both of these components are state-of-the-art methods in vasculature-on-chip devices. However, research into the ideal culture conditions that provide native cell behavior within *in vitro* models is still in its infancy for other tissue systems. The next section will shed light on a different tissue, cartilage, and demonstrate the importance of considering mechanobiological stimulation via matrix elasticity and nutrient supply when reconstructing a biological niche *in vitro*.

3.2. A COMPLEX (T)ISSUE – MATRIX ELASTICITY AND MOLECULE GRADIENTS IN CARTILAGE-ON-CHIP

In contrast to the numerous on-chip approaches for vascular research described in section 3.1., the application of microfluidic technologies to replicate articular cartilage has only gained momentum since 2018. To date, there is no viable biomedical research model that recapitulates cartilage biology sufficiently to decipher the processes in cartilage re- and degeneration. A viable cartilage tissue model will need to consider the tissues' unique structure and functional properties.[100] Articular cartilage is a highly specialized, two to four-millimeter thick connective tissue covering the ends of bones in synovial joints. The tissue is characterized by (1) inhabitation by a single specialized cell type – the chondrocytes, (2) a unique composition and structure designed to withstand compressive forces, and (3) nutrient supply only via diffusion due to lack of innervation and vascularization.[101] These key characteristics mean that a cartilage tissue model needs to (1) incorporate articular chondrocytes, (2) resemble native tissue elasticity, and (3) supply nutrients via diffusion.

The first requirement, incorporation of chondrocytes, can be fulfilled by isolating primary chondrocytes from cartilage tissue. However, conventional culture methods need high cell numbers challenging to attain due to chondrocyte dedifferentiation during monolayer expansion. In short, chondrocytes cultivated in monolayer change their morphology and matrix synthesis drastically and no longer behave similarly to their *in vivo* counterparts.[102] Only the reintroduction of chondrocytes into a suitable 3D culture in an early passage can

restore chondrotypic behavior. A suitable 3D matrix stimulates the chondrocytes to regain their physiologic phenotype by resembling native tissue elasticity.

Matrix elasticity varies significantly throughout the body from soft brain tissue to stiff bone tissue. The Young's modulus defines matrix elasticity, where brain tissue has a Young's modulus of 0.1 – 1 kPa while a 15 kPa elasticity describes muscle tissue, and 30 kPa the perichondral environment in cartilage tissue.[103] Extracellular matrices mimicking host tissue elasticity direct stem cell differentiation towards the respective tissue cell type.[103] Chondrocytes need to be cultivated within matrices with elasticities similar to the perichondral matrix to regain chondrotypic morphology and synthesize cartilage matrix, as shown in Figure 15 (**Manuscript #5**).[104]

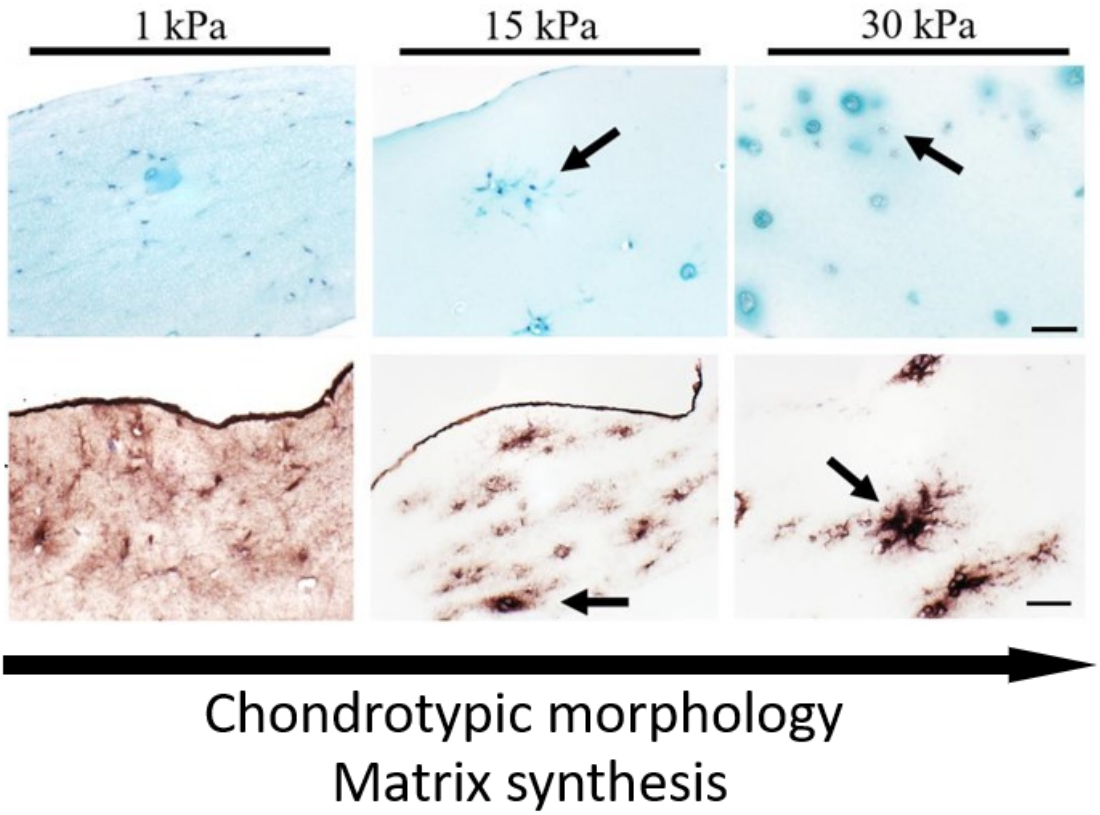

FIGURE 15: CHONDROCYTE RE-DIFFERENTIATION IN HYDROGELS OF 1 kPA, 15 kPA, AND 30 kPA YOUNG'S MODULUS. CHONDROCYTES CULTIVATED IN HIGH ELASTICITY HYDROGELS SHOW PHYSIOLOGICAL MORPHOLOGY AND MATRIX SYNTHESIS. ADAPTED FROM BACHMANN ET AL[104] FROM FRONTIERS UNDER UNDER THE TERMS OF THE CREATIVE COMMONS ATTRIBUTION LICENSE.

Chondrocytes react to an environment that mimics their native tissue by regaining a physiologic morphology and synthesizing cartilage-associated matrix molecules. In addition to cultivating chondrocytes in matrices of elasticity similar to native cartilage tissue, delivering nutrients via diffusion promotes this process. Cartilage lacks vascularization and innervation, meaning the synovial fluid supplies all nutrients to chondrocytes via diffusion. Microfluidic technology can recapitulate this unique anatomical property by designing cartilage-on-a-chip devices where hydrogel-embedded chondrocytes are nourished only via diffusion from an adjacent medium channel. Figure 16 shows the native environment of cartilage tissue and a schematic of a cartilage-on-chip device.

Native articular cartilage is organized into three distinct zones. Within the superficial zone adjacent to the joint space, elongated chondrocytes arrange parallel to the articular surface to protect underlying layers from excessive shear forces. In the middle zone that acts as a transitional space between the superficial zone and the underlying deep zone, spherical chondrocytes are sparsely distributed. In the last layer, the deep zone, chondrocytes arrange in columnar groups perpendicular to the joint surface. Chondrocytes are organized into units called chondrons, describing an individual or grouped chondrocytes surrounded by a perichondral matrix.[54] Cartilage-on-chip devices not only have the advantage of stimulating the chondrocytes via native directional nutrient gradients but also require significantly fewer cells than conventional approaches, thus avoiding prolonged *in vitro* expansion. The schematic in Figure 16 and experimental data depicted in Figure 17 show that microfluidic nutrient-gradient-based chondrocyte cultures can mirror *in vivo* articular cartilage physiology (**Manuscript #6**).[105]

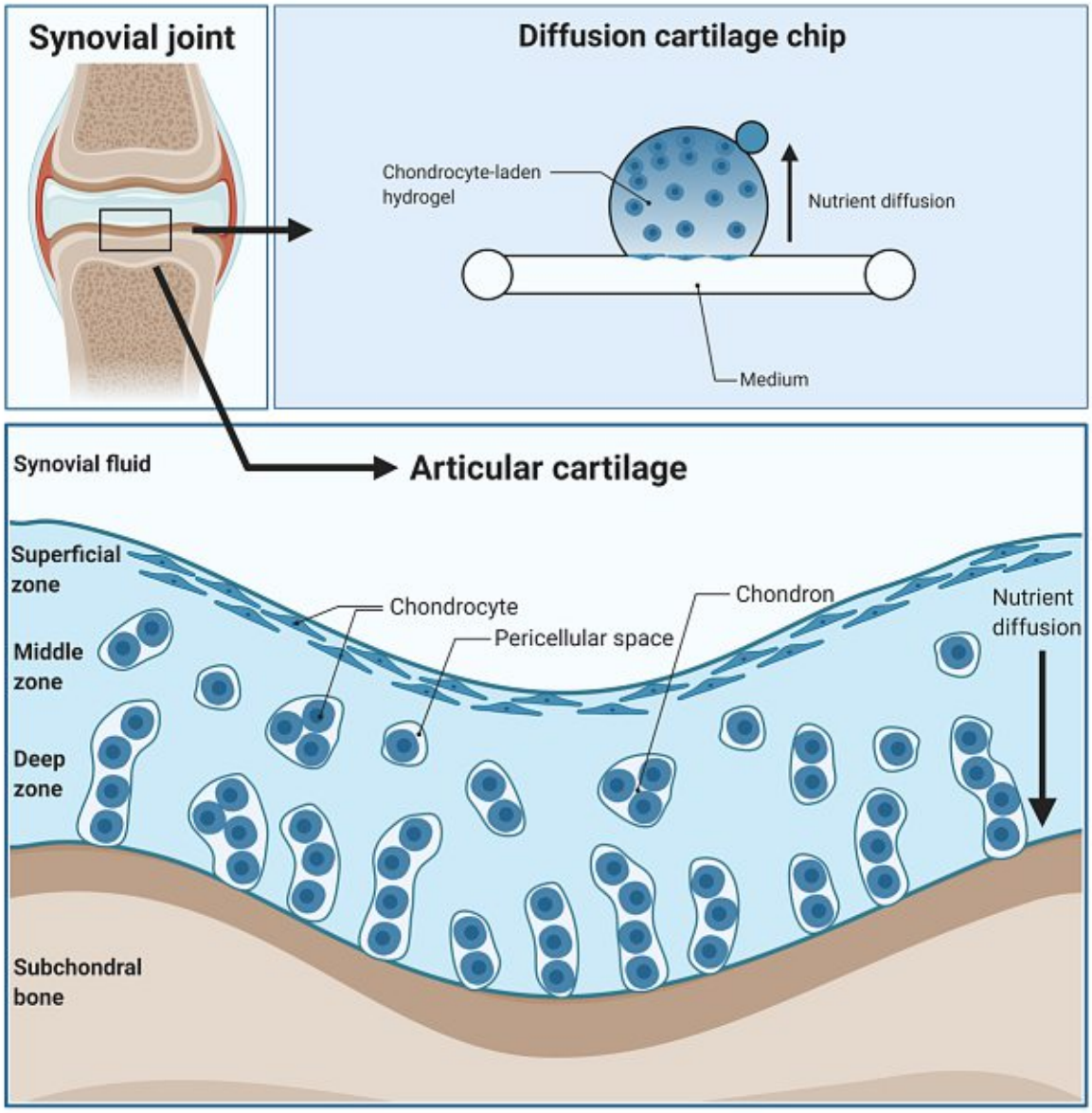

FIGURE 16: SCHEMATIC OF A SYNOVIAL JOINT SHOWING BONES, SYOVIUM AND ARTICULAR CARTILAGE, MAGIFICANTION OF ARTICULAR CARTILAGE DIVIDED INTO SUPERFICIAL, MIDDLE AND DEEP ZONE, AND REPRESENTATION OF A DIFFUSION BASED CARTILAGE-ON-CHIP MODEL REPLICATING TISSUE ARCHITECTURE. IMAGE CREATED USING BIORENDER.COM.

The cartilage-on-chip device supports chondrocyte redifferentiation hallmarks such as spherical cell morphology, low metabolic turnover, and collagen II expression. The nutrient diffusion incites the cells to arrange similarly to superficial zone cartilage along the medium-gel interface and arrange perpendicularly in hydrogel regions beyond the superficial zone.

Cartilage-on-chip cultures respond to inflammatory stimulation with an osteoarthritis-like phenotype of matrix degradation, which can be rescued with steroid treatment. The microfluidic device hosts six cartilage-on-chip chambers with volumes of 10 µL each that enable an implementation as a preclinical model for osteoarthritis with minimum cell and consumable requirements.

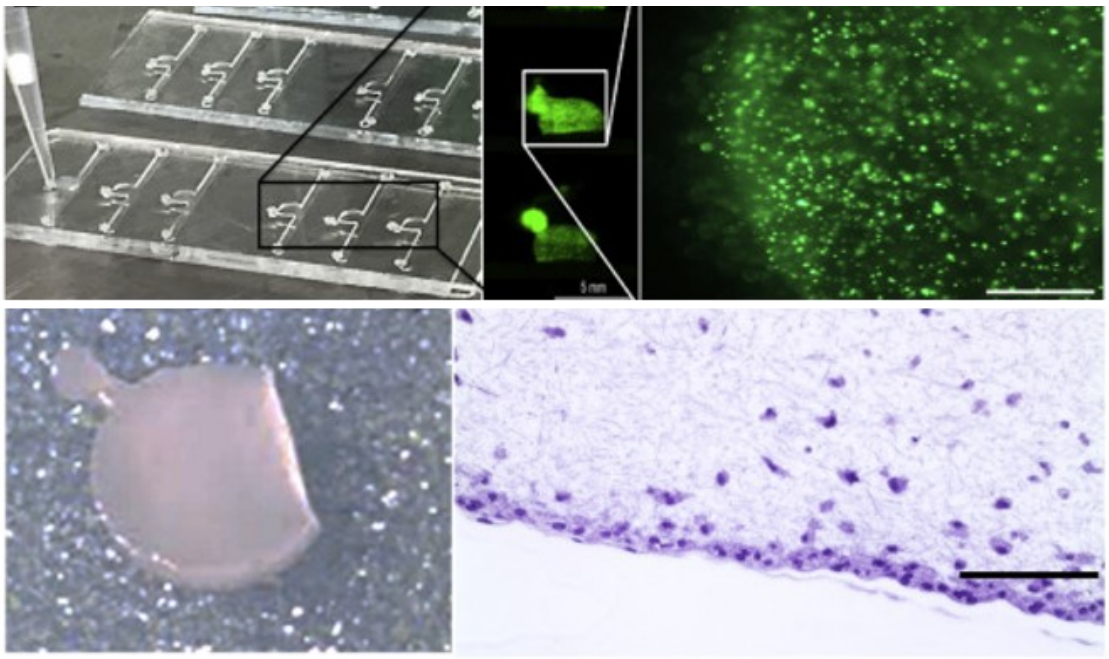

FIGURE 17: MICROFLUIDIC DIFFUSION BASED CHONDROCYTE CULTURES. (TOP LEFT) MICROFLUIDIC DEVICE WITH 6 CULTIVATION UNITS SUPPLYING CHONDROCYTE CULTURES VIA DIFFUSION. (TOP RIGHT) CHONDROCYTES REMAIN VIABLE OVER PROLONGED CULTIVATION PERIODS. (BOTTOM LEFT) HYDROGEL-EMBEDDED CHONDROCYTES RELEASED FROM DEVICE FOR POST PROCESSING. (BOTTOM RIGHT) CHONDROCYTES ARRANGE SIMILARLY TO SUPERFICIAL ZONE CARTILAGE ALONG GEL-MEDIUM INTERFACE. ADAPTED FROM ROSSER & BACHMANN ET AL.[105] WITH PERMISSION FROM ELSEVIER.

In contrast to the cartilage models described in this thesis that account for native cartilage matrix elasticity and nutrient supply, other current cartilage-on-chip models mainly consider compressive forces a critical factor regulating chondrocyte behavior. Microfluidic devices subjecting chondrocytes to compression comprise a cell cultivation layer and a pneumatic layer separated by a flexible membrane. By applying pressurized air within the pneumatic

layer, the membrane inflates towards the cell chamber, thereby compressing the cells within. Figure 18 shows an example of such a device as a representative of one of only five cartilage-on-chip models reported to date, including the work conducted within this thesis (**Manuscript #6).** The devices can either simultaneously compress multiple free-standing cell-laden hydrogel cylinders[106] or a single hydrogel structure[77,107] and simulate physiologic or pathologic scenarios by varying strain amplitude and frequency. The device depicted in Figure 18 exposes a chondrocyte-laden hydrogel to joint-mimicking directional shear stresses and compressive stress simultaneously, leading to enhanced ECM synthesis.[107]

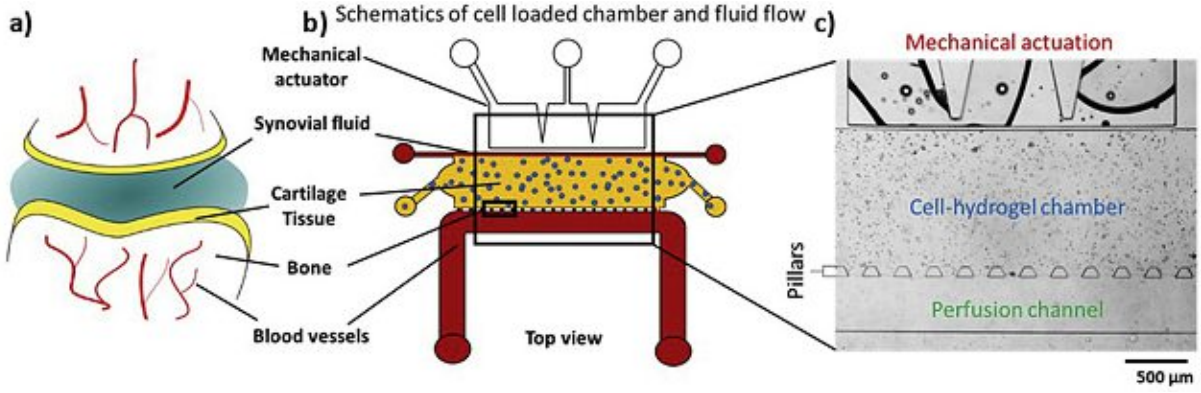

FIGURE 18: SCHEMATIC OF A KNEE JOINT (A), SCHEMATIC REPRESENTATION OF A CARTILAGE-ON-CHIP DEVICE (B) AND MICROGRAPH OF THE DEVICE STRUCTURE (C). THE DEVICE MECHANICALLY ACTUATES THE CELLS SIMILAR TO THE COMPRESSIVE FORCES WITHIN THE KNEE JOINT. REPRINTED FROM PAGGI ET AL[107] WITH PERMISSION FROM ELSEVIER.

Combining dynamic compression with a native cartilage microenvironment recapitulating matrix elasticities and gradient-based nutrient supply will result in a promising cartilage-on-a-chip model for biomedical research. Altogether, cartilage-on-chip technology has just begun to show its advantages in recreating cartilage tissue *in vitro.* In the future, cartilage-on-a-chip devices will be capable of engineering a viable *in vitro* cartilage model to understand physiologic cartilage synthesis, metabolic deregulation during osteoarthritis and explore viable treatment options.

CHAPTER 2

RESULTS, DISCUSSION, AND CONCLUSION

1. CONTRIBUTION OVERVIEW

Manuscript #1: Helene Zirath, Mario Rothbauer, Sarah Spitz, Barbara Bachmann, Christian Jordan, Bernhard Müller, Josef Ehgartner, Eleni Priglinger, Severin Mühleder, Heinz Redl, Wolfgang Holnthoner, Michael Harasek, Thorsten Mayr, and Peter Ertl; **Every Breath You Take: Non-invasive Real-Time Oxygen Biosensing in Two- and Three-Dimensional Microfluidic Cell Models** *Front. Physiol*., 03 July 2018, Volume 9, Article Number 815

Manuscript #2: Ece Ergir, Barbara Bachmann, Heinz Redl, Giancarlo Forte, and Peter Ertl; **Small Force, Big Impact: Next Generation Organ-on-a-Chip Systems Incorporating Biomechanical Cues**; *Front. Physiol.,* October 2018, Volume 9, Article Number 1417

Manuscript #3: Barbara Bachmann, Sarah Spitz, Christian Jordan, Patrick Schuller, Heinz Wanzenböck, Bahram Haddadi, Michael Harasek, Heinz Redl, Wolfgang Holnthoner, and Peter Ertl; **Microvasculature-on-a-Chip: Bridging the interstitial blood-lymph interface via mechanobiological stimuli;** Manuscript Draft

Manuscript #4: Barbara Bachmann, Sarah Spitz, Mario Rothbauer, Christian Jorden, Michaela Purtscher, Helene Zirath, Patrick Schuller, Christoph Eilenberger, Syed Faheem Ali, Severin Mühleder, Eleni Priglinger, Michael Harasek, Heinz Redl, Wolfgang Holnthoner, and Peter Ertl; **Engineering of three-dimensional pre-vascular networks within fibrin hydrogel constructs by microfluidic control over reciprocal cell signaling;** *Biomicrofluidics,* 2018, Volume 12

Manuscript #5: Barbara Bachmann, Sarah Spitz, Barbara Schädl, Andreas Teuschl, Heinz Redl, Sylvia Nürnberger, and Peter Ertl; **Stiffness Matters: Fine-Tuned Hydrogel Elasticity Alters Chondrogenic Redifferentiation;** *Front. Bioeng. Biotechnol*. April 2020, Volume 8, Article 373

Manuscript #6: Julie Rosser, Barbara Bachmann, Christian Jordan, Iris Ribitsch, Eva Haltmayer, Sinan Gültekin, Sini Junttila, Bence Galik, Attila Gyenesei, Bahram Haddadi, Michael Harasek, Monika Egerbacher, Peter Ertl, and Florien Jenner; **Microfluidic nutrient gradient-based three-dimensional chondrocyte culture-on-a-chip as an in vitro equine arthritis model**; *Materials Today Bio* Volume 4 (2019) Article Number 100023

2. RESEARCH ARTICLE SUMMARIES

EVERY BREATH YOU TAKE: NON-INVASIVE REAL-TIME OXYGEN BIOSENSING IN TWO- AND THREE-DIMENSIONAL MICROFLUIDIC CELL MODELS

Helene Zirath, Mario Rothbauer, Sarah Spitz, Barbara Bachmann, Christian Jordan, Bernhard Müller, Josef Ehgartner, Eleni Priglinger, Severin Mühleder, Heinz Redl, Wolfgang Holnthoner, Michael Harasek, Thorsten Mayr, and Peter Ertl

The integration of luminescent in-line oxygen sensors provides knowledge on the availability of dissolved oxygen inside microfluidic cell culture systems vital for recreating physiologically-relevant microenvironments and providing reliable and reproducible measurement conditions. Although several sensing approaches have been reported to monitor oxygen levels in cell monolayers, the oxygen demands of microfluidic three-dimensional cell cultures and spatiotemporal variations of oxygen concentrations in microfluidic cell culture systems are still mostly unknown. Two different microfluidic devices containing embedded sensor arrays to monitor local oxygen levels were engineered within this work. The devices were applied to investigate (i) oxygen consumption rates, (ii) oxygen gradients within cell culture chambers, and (iii) the influence of microfluidic material surface coatings, cell densities, and medium flow rate on the respiratory activities of four different cell types. Dynamic control of cyclic normoxic-hypoxic cell microenvironments is accomplished using programmable flow profiles employing both gas-impermeable and gas-permeable microfluidic biochips.

Small Force, Big Impact: Next Generation Organ-on-a-Chip Systems Incorporating Biomechanical Cues

Ece Ergir, Barbara Bachmann, Heinz Redl, Giancarlo Forte, and Peter Ertl

This review article gives an overview of how microfluidic lab-on-a-chip systems generate mechanical stresses, in what context these systems are currently used, and what knowledge gaps still need to be addressed. State-of-the-art organ-on-a-chip systems published since 2012 are described based on cultivation type and recreated biological stimulus. Monolayer microfluidic models integrating biophysical cues routinely utilize endothelial cells in a perfused channel to simulate a blood vessel to either determine endothelial cell behavior individually or emulate an organ barrier. In these barrier models, endothelial and epithelial cells of the respective organ are cultivated on either side of a flexible, porous membrane that is periodically stretched to simulate breathing or gut peristalsis. In contrast, 3D models imitate physiologic tissue structure by embedding cells within hydrogels. These models can employ interstitial flow to improve organoid viability or mimic pressure differences between blood and lymphatic capillaries. Alternatively, microfluidic systems similar to the barrier models mentioned above replicate rhythmic heartbeats or tissue compression via a flexible membrane. Even though organ-on-a-chip systems already employ mechanobiological stimuli, the models still need to be optimized to mimic the physiological niche accurately or translate to currently unstudied organ systems.

MICROVASCULATURE-ON-A-CHIP: BRIDGING THE INTERSTITIAL BLOOD-LYMPH INTERFACE VIA MECHANOBIOLOGICAL STIMULI

Barbara Bachmann, Sarah Spitz, Christian Jordan, Patrick Schuller, Heinz Wanzenböck, Bahram Haddadi, Michael Harasek, Heinz Redl, Wolfgang Holnthoner, and Peter Ertl

A microfluidic microvasculature-on-chip system is engineered by employing hydrostatic pressure between fluid reservoirs to mimic the pressure drop between blood and lymphatic capillaries *in vivo*. This hydrostatic pressure difference results in a directional interstitial fluid flow of 1 – 3 µm/s across a hydrogel compartment housing blood and lymphatic endothelial cultures. The microfluidic device design enables a cultivation setup that imitates interstitial tissue by forming blood capillaries from endothelial and stem cell cocultures via vascularization in one compartment and lymphatic sprouting into a cell-free hydrogel in the other. This cultivation setup replicates capillary anatomy by supplying the blood capillaries with stabilizing pericytes while allowing the formation of permeable initial lymphatics devoid of supportive cells. Subsequent mechanobiological stimulation via directional interstitial flow enhances the sprouting of lymphatic cells, increases capillary length, and supports the formation of lumenized lymphatic capillaries in addition to enabling the maintenance of a blood capillary network. This novel microvasculature-on-chip device supports the formation of both vasculatures within one device using mechanobiological stimulation via interstitial flow, which will serve as a platform to study lymph-specific drug delivery. Novel biomedical preclinical models need to consider and recreate the dynamic native tissue environment to gain a viable alternative to conventional models.

ENGINEERING OF THREE-DIMENSIONAL PRE-VASCULAR NETWORKS WITHIN FIBRIN HYDROGEL CONSTRUCTS BY MICROFLUIDIC CONTROL OVER RECIPROCAL CELL SIGNALING

Barbara Bachmann, Sarah Spitz, Mario Rothbauer, Christian Jorden, Michaela Purtscher, Helene Zirath, Patrick Schuller, Christoph Eilenberger, Syed Faheem Ali, Severin Mühleder, Eleni Priglinger, Michael Harasek, Heinz Redl, Wolfgang Holnthoner, and Peter Ertl

This work employs two different vasculature-on-chip setups to assess reciprocal signaling between endothelial and adipose-derived stem cells in the vascularization of tissue constructs. The microfluidic setups vary in cultivation strategy to generate dynamic spatiotemporal gradients and monitor resulting network formation. The work shows that vascular network formation diminishes at distances greater than four millimeters from the medium channel in static conditions, while dynamic medium perfusion results in enhanced endothelial sprouting but truncated network formation. These phenomena can be attributed to alterations in growth factor availability since 40 kDa-sized molecules fail to permeate deeper hydrogel regions in static cultures, as characterized by CFD simulation. In contrast, perfusion application results in molecule elution from hydrogel regions adjacent to the medium channel. A hybrid cultivation regime of three-day static and four-day perfusion culture led to improved vessel parameters by allowing the formation of premature cell-cell connections within the first three days and enhancing growth factor delivery to increase maturation in subsequent perfusion culture. Combining mechanical stimulation via perfusion and soluble cues such as size-dependent gradients is key in replicating tissues using organs-on-a-chip and will provide a better understanding of angiogenesis.

Stiffness Matters: Fine-Tuned Hydrogel Elasticity Alters Chondrogenic Redifferentiation

Barbara Bachmann, Sarah Spitz, Barbara Schädl, Andreas Teuschl, Heinz Redl, Sylvia Nürnberger, and Peter Ertl

In the engineering of cartilage *in vitro* models, selecting an appropriate hydrogel matrix is vital for chondrocytes to regain a differentiated phenotype. This article tested the ability of three different hydrogel matrices of three different elasticities each to elicit chondrogenic redifferentiation. The hydrogel compositions were adjusted to elasticities similar to brain tissue, muscle tissue, or the perichondral matrix using oscillatory rheology. Primary human articular chondrocytes were embedded within the hydrogels, and redifferentiation status after three weeks was assessed based on morphology, gene expression, and matrix synthesis. In two hydrogels, chondrocytes showed high viabilities and distinct differences in redifferentiation behavior dependent on hydrogel elasticity. While chondrocytes in matrices of low elasticity remained de-differentiated and produced limited amounts of cartilage matrix, chondrocytes cultivated in hydrogels mimicking perichondral tissue re-differentiated efficiently. High elasticity hydrogels supported chondrotypic spherical morphology, a high collagen type II to collagen type I ratio, and produced notable amounts of sGAGs characteristic of native cartilage tissue. These results clearly demonstrate that cartilage-on-chip models need to integrate 3D chondrocyte cultures within hydrogels of optimized elasticity to represent articular joint biology accurately.

MICROFLUIDIC NUTRIENT GRADIENT-BASED THREE-DIMENSIONAL CHONDROCYTE CULTURE-ON-A-CHIP AS AN IN VITRO EQUINE ARTHRITIS MODEL;

Julie Rosser, Barbara Bachmann, Christian Jordan, Iris Ribitsch, Eva Haltmayer, Sinan Gültekin, Sini Junttila, Bence Galik, Attila Gyenesei, Bahram Haddadi, Michael Harasek, Monika Egerbacher, Peter Ertl, and Florien Jenner

Directional nutrient gradients play a crucial role in replicating cartilage anatomy *in vitro*. A microfluidic device consisting of a circular hydrogel chamber with an adjacent medium channel elicits nutrient diffusion within a three-millimeter thick cartilage tissue replica driving physiologic cell behavior. Primary equine chondrocytes were embedded within a high elasticity hydrogel matrix to generate an *in vitro* osteoarthritis disease model. The cells remained viable for an extended culture time of three weeks and showed characteristic features of differentiated chondrocytes such as spherical morphology, low metabolic activity, and expression of ECM molecules. The microfluidic cultivation prompted the chondrocytes to form a superficial-like zone at the medium interface and a deep zone at increased hydrogel depths, demonstrated by a characteristic zone-dependent chondrocyte morphology. Upon inflammatory stimulation, the chondrocytes developed an OA-like phenotype, which was partially rescued by steroid treatment. This work demonstrates the ability to recreate a native cartilage microenvironment via microfluidic engineering. The presented cartilage-on-chip device supports anti-inflammatory drug candidate screening to identify individualized treatment for osteoarthritis patients in personalized medicine.

3. STATEMENT OF CONTRIBUTIONS

Manuscript #1: Helene Zirath and Peter Ertl conceptualized the research. Torsten Mayr, Bernhard Müller, and Josef Ehgartner developed oxygen sensors. Severin Mühleder and Eleni Priglinger isolated primary cells. Helene Zirath, Barbara Bachmann, and Sarah Spitz performed experiments. Barbara Bachmann, Sarah Spitz, and Helene Zirath analyzed data. Christian Jordan performed CFD simulations with input from Michael Harasek. Barbara Bachmann, Helene Zirath, Sarah Spitz, and Mario Rothbauer drafted the manuscript. Peter Ertl revised the manuscript with input from Heinz Redl and Wolfgang Holnthoner. All authors approved the final version of the manuscript.

Manuscript #2: Barbara Bachmann and Ece Ergir generated the manuscript idea. Barbara Bachmann researched the manuscript's theoretical framework, reviewed original articles discussing mechanobiology-on-chip in 2D cell systems, and wrote the respective sections. Ece Ergir reviewed original articles on mechanobiology-on-chip in 3D, developed manuscript conclusions, and drafted the respective sections. Peter Ertl, Giancarlo Forte, and Heinz Redl gave input on all sections. All authors approved the final version.

Manuscript #3: Wolfgang Holnthoner initiated the project together with Barbara Bachmann and Heinz Redl. Barbara Bachmann created the device design, performed rapid prototyping, conducted experiments, and analyzed data. Christian Jordan, Bahram Haddadi, and Michael Harasek performed CFD simulations of interstitial flow. Patrick Schuller and Heinz Wanzenböck fabricated photomasks. Barbara Bachmann drafted the manuscript with input from Sarah Spitz and Peter Ertl. Peter Ertl approved the publication as a manuscript draft.

Manuscript #4: Mario Rothbauer initiated the research with Barbara Bachmann. Severin Mühleder and Eleni Priglinger isolated cells. Barbara Bachmann, Sarah Spitz, and Michaela Purtscher performed experiments. Syed Faheem Ali manufactured microchips. Christian Jordan performed CFD simulations with input from Michael Harasek. Barbara Bachmann, Helene Zirath, and Christoph Eilenberger analyzed data. Barbara Bachmann drafted the manuscript with Sarah Spitz, Mario Rothbauer, and Peter Ertl. Heinz Redl and Wolfgang Holnthoner provided vascularization expertise. All authors approved the manuscript.

Manuscript #5: Barbara Bachmann initiated the research with Heinz Redl, Sylvia Nürnberger, and Peter Ertl. Sarah Spitz performed rheological measurements under the supervision of Barbara Bachmann. Andreas Teuschl provided silk fibroin and expertise. Barbara Bachmann and Sarah Spitz performed cell culture experiments. Barbara Schädl performed histological processing. Barbara Bachmann performed RT-qPCR measurements and analyzed histological sections. Barbara Bachmann drafted the manuscript with input from Sarah Spitz, Sylvia Nürnberger, and Peter Ertl. All authors approved the final manuscript.

Manuscript #6: Julie Rosser, Florien Jenner, and Peter Ertl conceptualized research. Julie Rosser, Barbara Bachmann, Iris Ribitsch, and Eva Haltmayer isolated chondrocytes. Barbara Bachmann performed cell culture experiments and analyzed data. Sinan Gueltekin performed RT-qPCR. Sini Junttila, Bence Galik, and Attila Gyenesei analyzed data. Christian Jordan and Bahram Haddadi performed CFD simulations with input from Michael Harasek. Monika Egerbacher performed histological processing. Julie Rosser drafted the manuscript. Barbara Bachmann and Peter Ertl revised the manuscript with input from Florien Jenner. All authors approved the final manuscript.

4. Conclusion and Scientific Value

This doctoral thesis set out to engineer organ-on-a-chip systems to subject 3D cell cultures to mechanical stimulation resembling the native microenvironment and monitor the corresponding mechanobiological response. The results demonstrate that microfluidic systems are ideal for achieving physiologic tissue replicas for biomedical research by recreating the dynamic tissue environment using fluid flow, matrix elasticity, and nutrient diffusion. Incorporating dynamic stimulation of 3D cell cultures via microfluidic technology enhances physiologic biomimicry within organ-on-a-chip models. Four such systems were engineered within this thesis's original works. They could demonstrate their scientific value by replicating intraluminal and interstitial flow in vasculature-on-chip models and perichondral matrix elasticity and nutrient diffusion in cartilage-on-chip models. Understanding angio- and vasculogenesis is crucial for engineering vascularized tissue constructs and improving drug efficacy through lymphatic targeting. Within this thesis, a novel microvasculature-on-chip device housing a blood-lymph microvascular interface could demonstrate that mechanical stimulation via directional interstitial fluid flow induces lymphatic sprouting (**Manuscript #3**). The system supports the formation and maintenance of both blood and lymphatic vasculature within one device. It will be crucial in deciphering transport processes across the lymphatic capillaries, where targeting the lymphatic system for drug delivery enhances the potency of vaccines and chemotherapeutics.[108] Besides drug delivery studies, successful vascularization is critical in supplying tissue constructs with oxygen and nutrients beyond diffusion limits.[109] As the results of this thesis show, the combinatorial effects of dynamic growth factor delivery, interstitial flow, and reciprocal signaling are vital

for endothelial cell sprouting and vascularization (**Manuscript #4**). This microfluidic system, in combination with the novel in-line oxygen sensing strategies developed (**Manuscript #1**), establishes a platform to (1) provide non-vascularized tissues with nutrients via perfusion, (2) simultaneously utilize interstitial flow to incite vascularization, and (3) monitor tissue viability using oxygen sensors. In other words, the platform can facilitate tissue engineering efforts by controlling and monitoring extracellular soluble cue delivery.

In addition to highlighting the importance of extracellular cues within vascular *in vitro* models, this thesis's results emphasize the need to replicate key cartilage tissue characteristics such as 3D cultivation, high matrix elasticity, and nutrient supply via diffusion in cartilage models. When engineering cartilage tissue *in vitro*, chondrocytes need to be introduced into a native microenvironment to regain a physiologic phenotype after monolayer expansion.[100] A vital element in this process is the reintroduction of the chondrocytes into a 3D environment. This thesis demonstrates that scaffold type and elasticity need to imitate native cartilage for successful redifferentiation. Mechanical stimulation by ECM elasticities mimicking the perichondral matrix elicits increased redifferentiation and matrix production, leading to *de novo* formation of cartilage tissue *in vitro* (**Manuscript #5**). This knowledge will help effectively engineer cartilage replicas for disease modeling of osteoarthritis, as demonstrated in **Manuscript #6**. The combination of high elasticity hydrogels with diffusion-based nutrient gradient generation within a microfluidic device elicits chondrocytes to arrange similarly to cartilage zonation and respond to inflammatory cues and steroid treatment. This successful development of an OA disease model will accelerate the identification of disease processes deregulating matrix resorption and the discovery of novel drug candidates.

In conclusion, this doctoral thesis clearly demonstrates that organ-on-a-chip technology needs to implement dynamic stimulation replicative of the physiologic environment to boost preclinical *in vitro* model relevance. The addition of a dynamic, mechanical component to preclinical models through organ-on-a-chip technology will foster a profound understanding of cell behavior in health, disease, and treatment.

5. BIBLIOGRAPHY

1. Rothbauer, M., Rosser, J. M., Zirath, H. & Ertl, P. Tomorrow today: organ-on-a-chip advances towards clinically relevant pharmaceutical and medical in vitro models. *Current Opinion in Biotechnology* (2019). doi:10.1016/j.copbio.2018.08.009
2. Benam, K. H. *et al.* Engineered in vitro disease models. *Annu. Rev. Pathol. Mech. Dis.* (2015). doi:10.1146/annurev-pathol-012414-040418
3. Planz, V., Lehr, C. M. & Windbergs, M. In vitro models for evaluating safety and efficacy of novel technologies for skin drug delivery. *J. Control. Release* (2016). doi:10.1016/j.jconrel.2016.09.002
4. Baker, B. M. & Chen, C. S. Deconstructing the third dimension – how 3D culture microenvironments alter cellular cues. *J. Cell Sci.* **125**, 3015–3024 (2012).
5. Cann, O. These are the top 10 emerging technologies of 2016. *World Econ. Forum* (2016).
6. Whitesides, G. M. The origins and the future of microfluidics. *Nature* (2006). doi:10.1038/nature05058
7. McDonald, J. C. *et al.* Fabrication of microfluidic systems in poly(dimethylsiloxane). *Electrophoresis* (2000). doi:10.1002/(SICI)1522-2683(20000101)21:1<27::AID-ELPS27>3.0.CO;2-C
8. Rothbauer, M., Zirath, H. & Ertl, P. Recent advances in microfluidic technologies for cell-to-cell interaction studies. *Lab on a Chip* (2018). doi:10.1039/c7lc00815e
9. Bhatia, S. N. & Ingber, D. E. Microfluidic organs-on-chips. *Nature Biotechnology* (2014). doi:10.1038/nbt.2989
10. Huh, D., Torisawa, Y. S., Hamilton, G. A., Kim, H. J. & Ingber, D. E. Microengineered physiological biomimicry: Organs-on-Chips. *Lab on a Chip* (2012). doi:10.1039/c2lc40089h
11. Rothbauer, M., Wartmann, D., Charwat, V. & Ertl, P. Recent advances and future applications of microfluidic live-cell microarrays Lab-on-a-chip Organ-on-a-chip Body-on-a-chip. *Biotechnol. Adv.* **33**, 948–961 (2015).
12. Ronaldson-Bouchard, K. & Vunjak-Novakovic, G. Organs-on-a-Chip: A Fast Track for Engineered Human Tissues in Drug Development. *Cell Stem Cell* (2018). doi:10.1016/j.stem.2018.02.011
13. Sommer, G. J. *et al.* Introduction to microfluidics. in *Microfluidics for Biological Applications* (2009). doi:10.1007/978-0-387-09480-9_1
14. Paegel, B. M., Blazej, R. G. & Mathies, R. A. Microfluidic devices for DNA sequencing: Sample preparation and electrophoretic analysis. *Current Opinion in Biotechnology* (2003). doi:10.1016/S0958-1669(02)00004-6
15. Castillo-León, J. & Svendsen, W. E. (Eds. . *Lab-on-a-Chip Devices and Micro-Total*

Analysis Systems: A Practical Guide. *Springer* (2015).

16. Balagaddé, F. K., You, L., Hansen, C. L., Arnold, F. H. & Quake, S. R. Microbiology: Long-term monitoring of bacteria undergoing programmed population control in a microchemostat. *Science (80-.).* (2005). doi:10.1126/science.1109173

17. Ertl, P., Sticker, D., Charwat, V., Kasper, C. & Lepperdinger, G. Lab-on-a-chip technologies for stem cell analysis. *Trends in Biotechnology* (2014). doi:10.1016/j.tibtech.2014.03.004

18. Rothbauer, M., Wartmann, D., Charwat, V. & Ertl, P. Recent advances and future applications of microfluidic live-cell microarrays. *Biotechnology Advances* (2015). doi:10.1016/j.biotechadv.2015.06.006

19. McClain, M. A., Culbertson, C. T., Jacobson, S. C. & Ramsey, J. M. Flow cytometry of Escherichia coli on microfluidic devices. *Anal. Chem.* (2001). doi:10.1021/ac010504v

20. Inglis, D. W. *et al.* Microfluidic device for label-free measurement of platelet activation. *Lab Chip* (2008). doi:10.1039/b800721g

21. Ozkumur, E. *et al.* Inertial focusing for tumor antigen-dependent and -independent sorting of rare circulating tumor cells. *Sci. Transl. Med.* (2013). doi:10.1126/scitranslmed.3005616

22. Rothbauer, M., Zirath, H. & Ertl, P. Recent advances in microfluidic technologies for cell-to-cell interaction studies. *Lab Chip* (2017). doi:10.1039/C7LC00815E

23. Yoon No, D., Lee, K. H., Lee, J. & Lee, S. H. 3D liver models on a microplatform: well-defined culture, engineering of liver tissue and liver-on-a-chip. *Lab Chip* (2015). doi:10.1039/c5lc00611b

24. Wilmer, M. J. *et al.* Kidney-on-a-Chip Technology for Drug-Induced Nephrotoxicity Screening. *Trends in Biotechnology* (2016). doi:10.1016/j.tibtech.2015.11.001

25. Shrestha, J. *et al.* Lung-on-a-chip: the future of respiratory disease models and pharmacological studies. *Critical Reviews in Biotechnology* (2020). doi:10.1080/07388551.2019.1710458

26. Agarwal, A., Goss, J. A., Cho, A., McCain, M. L. & Parker, K. K. Microfluidic heart on a chip for higher throughput pharmacological studies. *Lab Chip* (2013). doi:10.1039/c3lc50350j

27. Giacomelli, E. *et al.* Three-dimensional cardiac microtissues composed of cardiomyocytes and endothelial cells co-differentiated from human pluripotent stem cells. *Dev.* (2017). doi:10.1242/dev.143438

28. Hirt, M. N. *et al.* Functional improvement and maturation of rat and human engineered heart tissue by chronic electrical stimulation. *J. Mol. Cell. Cardiol.* (2014). doi:10.1016/j.yjmcc.2014.05.009

29. Mannhardt, I. *et al.* Human Engineered Heart Tissue: Analysis of Contractile Force. *Stem Cell Reports* (2016). doi:10.1016/j.stemcr.2016.04.011

30. Zhang, Y. S. *et al.* Bioprinting 3D microfibrous scaffolds for engineering endothelialized

myocardium and heart-on-a-chip. *Biomaterials* (2016). doi:10.1016/j.biomaterials.2016.09.003

31. Mathur, A. *et al.* Human iPSC-based cardiac microphysiological system for drug screening applications. *Sci. Rep.* (2015). doi:10.1038/srep08883

32. Nunes, S. S. *et al.* Biowire: A platform for maturation of human pluripotent stem cell-derived cardiomyocytes. *Nat. Methods* (2013). doi:10.1038/nmeth.2524

33. Huh, D. *et al.* Reconstituting organ-level lung functions on a chip. *Science (80-.).* **328**, 1662–1668 (2010).

34. Long, C. *et al.* Design optimization of liquid-phase flow patterns for microfabricated lung on a chip. *Ann. Biomed. Eng.* (2012). doi:10.1007/s10439-012-0513-8

35. Benam, K. H. *et al.* Human lung small airway-on-a-chip protocol. in *Methods in Molecular Biology* (2017). doi:10.1007/978-1-4939-7021-6_25

36. Schepers, A., Li, C., Chhabra, A., Seney, B. T. & Bhatia, S. Engineering a perfusable 3D human liver platform from iPS cells. *Lab Chip* (2016). doi:10.1039/c6lc00598e

37. Lee, P. J., Hung, P. J. & Lee, L. P. An artificial liver sinusoid with a microfluidic endothelial-like barrier for primary hepatocyte culture. *Biotechnol. Bioeng.* (2007). doi:10.1002/bit.21360

38. Cho, C. H. *et al.* Layered patterning of hepatocytes in co-culture systems using microfabricated stencils. *Biotechniques* (2010). doi:10.2144/000113317

39. Khetani, S. R. & Bhatia, S. N. Microscale culture of human liver cells for drug development. *Nat. Biotechnol.* (2008). doi:10.1038/nbt1361

40. Ramaiahgari, S. C. *et al.* A 3D in vitro model of differentiated HepG2 cell spheroids with improved liver-like properties for repeated dose high-throughput toxicity studies. *Arch. Toxicol.* (2014). doi:10.1007/s00204-014-1215-9

41. Rennert, K. *et al.* A microfluidically perfused three dimensional human liver model. *Biomaterials* (2015). doi:10.1016/j.biomaterials.2015.08.043

42. Ware, B. R., Berger, D. R. & Khetani, S. R. Prediction of drug-induced liver injury in micropatterned co-cultures containing iPSC-derived human hepatocytes. *Toxicol. Sci.* (2015). doi:10.1093/toxsci/kfv048

43. Bhise, N. S. *et al.* A liver-on-a-chip platform with bioprinted hepatic spheroids. *Biofabrication* **8**, (2016).

44. Hassell, B. A. *et al.* Human Organ Chip Models Recapitulate Orthotopic Lung Cancer Growth, Therapeutic Responses, and Tumor Dormancy In Vitro. *Cell Rep.* **21**, 508–516 (2017).

45. Kostadinova, R. *et al.* A long-term three dimensional liver co-culture system for improved prediction of clinically relevant drug-induced hepatotoxicity. *Toxicol. Appl. Pharmacol.* (2013). doi:10.1016/j.taap.2013.01.012

46. Jang, K. J. *et al.* Human kidney proximal tubule-on-a-chip for drug transport and

nephrotoxicity assessment. *Integr. Biol. (United Kingdom)* (2013). doi:10.1039/c3ib40049b

47. Kim, S. *et al.* Pharmacokinetic profile that reduces nephrotoxicity of gentamicin in a perfused kidney-on-a-chip. *Biofabrication* (2016). doi:10.1088/1758-5090/8/1/015021

48. Weinberg, E., Kaazempur-Mofrad, M. & Borenstein, J. Concept and computational design for a bioartificial nephron-on-a-chip. *Int. J. Artif. Organs* (2008). doi:10.1177/039139880803100606

49. Shah, P. *et al.* A microfluidics-based in vitro model of the gastrointestinal human-microbe interface. *Nat. Commun.* (2016). doi:10.1038/ncomms11535

50. Kim, H. J. & Ingber, D. E. Gut-on-a-Chip microenvironment induces human intestinal cells to undergo villus differentiation. *Integr. Biol. (United Kingdom)* (2013). doi:10.1039/c3ib40126j

51. Esch, M. B. *et al.* On chip porous polymer membranes for integration of gastrointestinal tract epithelium with microfluidic 'body-on-a-chip' devices. *Biomed. Microdevices* (2012). doi:10.1007/s10544-012-9669-0

52. Booth, R. & Kim, H. Characterization of a microfluidic in vitro model of the blood-brain barrier (μBBB). *Lab Chip* (2012). doi:10.1039/c2lc40094d

53. Brown, J. A. *et al.* Recreating blood-brain barrier physiology and structure on chip: A novel neurovascular microfluidic bioreactor. *Biomicrofluidics* **9**, (2015).

54. Griep, L. M. *et al.* BBB on CHIP: Microfluidic platform to mechanically and biochemically modulate blood-brain barrier function. *Biomed. Microdevices* (2013). doi:10.1007/s10544-012-9699-7

55. Lancaster, M. A. *et al.* Cerebral organoids model human brain development and microcephaly. *Nature* (2013). doi:10.1038/nature12517

56. Wang, Y. I., Abaci, H. E. & Shuler, M. L. Microfluidic blood–brain barrier model provides in vivo-like barrier properties for drug permeability screening. *Biotechnol. Bioeng.* (2017). doi:10.1002/bit.26045

57. Spitz, S. *et al.* Cultivation and characterization of human midbrain organoids in sensor integrated microfluidic chips. *bioRxiv* (2019). doi:10.1101/869701

58. Abaci, H. E., Gledhill, K., Guo, Z., Christiano, A. M. & Shuler, M. L. Pumpless microfluidic platform for drug testing on human skin equivalents. *Lab Chip* (2015). doi:10.1039/c4lc00999a

59. Gledhill, K. *et al.* Melanin transfer in human 3D skin equivalents generated exclusively from induced pluripotent stem cells. *PLoS One* (2015). doi:10.1371/journal.pone.0136713

60. Petrova, A. *et al.* 3D in vitro model of a functional epidermal permeability barrier from human embryonic stem cells and induced pluripotent stem cells. *Stem Cell Reports* (2014). doi:10.1016/j.stemcr.2014.03.009

61. Fernandez, C. E. *et al.* Human vascular microphysiological system for in vitro drug

screening. *Sci. Rep.* (2016). doi:10.1038/srep21579

62. Kurokawa, Y. K. *et al.* Human Induced Pluripotent Stem Cell-Derived Endothelial Cells for Three-Dimensional Microphysiological Systems. *Tissue Eng. - Part C Methods* (2017). doi:10.1089/ten.tec.2017.0133

63. Moya, M. L., Hsu, Y. H., Lee, A. P., Christopher, C. W. H. & George, S. C. In vitro perfused human capillary networks. *Tissue Eng. - Part C Methods* (2013). doi:10.1089/ten.tec.2012.0430

64. Bachmann, B. *et al.* Engineering of three-dimensional pre-vascular networks within fibrin hydrogel constructs by microfluidic control over reciprocal cell signaling. *Biomicrofluidics* **12**, (2018).

65. Adam Kratz, S. R., Höll, G., Schuller, P., Ertl, P. & Rothbauer, M. Latest trends in biosensing for microphysiological organs-on-a-chip and body-on-a-chip systems. *Biosensors* (2019). doi:10.3390/bios9030110

66. Ferrari, E., Palma, C., Vesentini, S., Occhetta, P. & Rasponi, M. Integrating Biosensors in Organs-on-Chip Devices: A Perspective on Current Strategies to Monitor Microphysiological Systems. *Biosensors* (2020). doi:10.3390/bios10090110

67. Zirath, H. *et al.* Every breath you take: Non-invasive real-time oxygen biosensing in two- and three-dimensional microfluidic cell models. *Front. Physiol.* (2018). doi:10.3389/fphys.2018.00815

68. Ergir, E., Bachmann, B., Redl, H., Forte, G. & Ertl, P. Small force, big impact: Next generation organ-on-a-chip systems incorporating biomechanical cues. *Front. Physiol.* **9**, (2018).

69. Rothbauer, M. *et al.* Monitoring transient cell-to-cell interactions in a multi-layered and multi-functional allergy-on-a-chip system. *Lab Chip* **19**, 1916–1921 (2019).

70. Charwat, V. *et al.* Combinatorial in Vitro and in Silico Approach To Describe Shear-Force Dependent Uptake of Nanoparticles in Microfluidic Vascular Models. *Anal. Chem.* acs.analchem.7b04788 (2018). doi:10.1021/acs.analchem.7b04788

71. Hsu, Y.-H., Moya, M. L., Hughes, C. C. W., George, S. C. & Lee, A. P. A microfluidic platform for generating large-scale nearly identical human microphysiological vascularized tissue arrays. *Lab Chip* (2013). doi:10.1039/c3lc50424g

72. Offeddu, G. S. *et al.* An on-chip model of protein paracellular and transcellular permeability in the microcirculation. *Biomaterials* (2019). doi:10.1016/j.biomaterials.2019.05.022

73. Kim, S., Chung, M. & Jeon, N. L. Three-dimensional biomimetic model to reconstitute sprouting lymphangiogenesis in vitro. *Biomaterials* (2016). doi:10.1016/j.biomaterials.2015.11.019

74. Huh, D. *et al.* A human disease model of drug toxicity-induced pulmonary edema in a lung-on-a-chip microdevice. *Sci. Transl. Med.* **4**, (2012).

75. Villenave, R. *et al.* Human gut-on-a-chip supports polarized infection of coxsackie B1

virus in vitro. *PLoS One* (2017). doi:10.1371/journal.pone.0169412

76. Kim, H. J., Li, H., Collins, J. J. & Ingber, D. E. Contributions of microbiome and mechanical deformation to intestinal bacterial overgrowth and inflammation in a human gut-on-a-chip. *Proc. Natl. Acad. Sci.* **113**, E7–E15 (2016).

77. Occhetta, P. *et al.* Hyperphysiological compression of articular cartilage induces an osteoarthritic phenotype in a cartilage-on-a-chip model. *Nat. Biomed. Eng.* (2019). doi:10.1038/s41551-019-0406-3

78. Haase, K. & Kamm, R. D. Advances in on-chip vascularization. *Regenerative Medicine* (2017). doi:10.2217/rme-2016-0152

79. Polacheck, W. J. *et al.* A non-canonical Notch complex regulates adherens junctions and vascular barrier function. *Nature* (2017). doi:10.1038/nature24998

80. Polacheck, W. J., Kutys, M. L., Tefft, J. B. & Chen, C. S. Microfabricated blood vessels for modeling the vascular transport barrier. *Nat. Protoc.* (2019). doi:10.1038/s41596-019-0144-8

81. Chrobak, K. M., Potter, D. R. & Tien, J. Formation of perfused, functional microvascular tubes in vitro. *Microvasc. Res.* (2006). doi:10.1016/j.mvr.2006.02.005

82. Piotrowski-Daspit, A. S., Tien, J. & Nelson, C. M. Interstitial fluid pressure regulates collective invasion in engineered human breast tumors via Snail, vimentin, and E-cadherin. *Integr. Biol.* (2016). doi:10.1039/C5IB00282F

83. Osaki, T., Sivathanu, V. & Kamm, R. D. Vascularized microfluidic organ-chips for drug screening, disease models and tissue engineering. *Current Opinion in Biotechnology* (2018). doi:10.1016/j.copbio.2018.03.011

84. Costa, P. F. *et al.* Mimicking arterial thrombosis in a 3D-printed microfluidic: In vitro vascular model based on computed tomography angiography data. *Lab Chip* (2017). doi:10.1039/c7lc00202e

85. Alimperti, S. *et al.* Three-dimensional biomimetic vascular model reveals a RhoA, Rac1, and N-cadherin balance in mural cell–endothelial cell-regulated barrier function. *Proc. Natl. Acad. Sci. U. S. A.* (2017). doi:10.1073/pnas.1618333114

86. Gong, M. M. *et al.* Human organotypic lymphatic vessel model elucidates microenvironment-dependent signaling and barrier function. *Biomaterials* (2019). doi:10.1016/j.biomaterials.2019.119225

87. Osaki, T., Serrano, J. C. & Kamm, R. D. Cooperative Effects of Vascular Angiogenesis and Lymphangiogenesis. *Regen. Eng. Transl. Med.* (2018). doi:10.1007/s40883-018-0054-2

88. Jeon, J. S. *et al.* Human 3D vascularized organotypic microfluidic assays to study breast cancer cell extravasation. *Proc. Natl. Acad. Sci.* (2015). doi:10.1073/pnas.1417115112

89. Offeddu, G. S. *et al.* Microcirculation-on-Chip: Application of Transmural Flow Across In Vitro Microvasculature Enables Direct Sampling of Interstitial Therapeutic Molecule Distribution (Small 46/2019). *Small* (2019). doi:10.1002/smll.201970247

90. Phan, D. T. T. *et al.* A vascularized and perfused organ-on-a-chip platform for large-scale

drug screening applications. *Lab Chip* (2017). doi:10.1039/c6lc01422d

91. Ungaro, F. *et al.* Lymphatic endothelium contributes to colorectal cancer growth via the soluble matrisome component GDF11. *Int. J. Cancer* (2019). doi:10.1002/ijc.32286

92. Tan, A., Fujisawa, K., Yukawa, Y. & Matsunaga, Y. T. Bottom-up fabrication of artery-mimicking tubular co-cultures in collagen-based microchannel scaffolds. *Biomater. Sci.* (2016). doi:10.1039/c6bm00340k

93. DeOre, B. J., Galie, P. A. & Sehgal, C. M. Fluid flow rate dictates the efficacy of low-intensity anti-vascular ultrasound therapy in a microfluidic model. *Microcirculation* (2019). doi:10.1111/micc.12576

94. Abe, Y. *et al.* Balance of interstitial flow magnitude and vascular endothelial growth factor concentration modulates three-dimensional microvascular network formation. *APL Bioeng.* (2019). doi:10.1063/1.5094735

95. Kim, S., Kim, W., Lim, S. & Jeon, J. S. Vasculature-on-a-chip for in vitro disease models. *Bioengineering* (2017). doi:10.3390/bioengineering4010008

96. Bachmann, B. *et al.* Engineering of three-dimensional pre-vascular networks within fibrin hydrogel constructs by microfluidic control over reciprocal cell signaling. *Biomicrofluidics* (2018). doi:10.1063/1.5027054

97. Rutkowski, J. M. & Swartz, M. A. A driving force for change: interstitial flow as a morphoregulator. *Trends in Cell Biology* (2007). doi:10.1016/j.tcb.2006.11.007

98. Rutkowski, J. M., Boardman, K. C. & Swartz, M. A. Characterization of lymphangiogenesis in a model of adult skin regeneration. *Am. J. Physiol. - Hear. Circ. Physiol.* (2006). doi:10.1152/ajpheart.00038.2006

99. Ng, C. P., Helm, C. L. E. & Swartz, M. A. Interstitial flow differentially stimulates blood and lymphatic endothelial cell morphogenesis in vitro. *Microvasc. Res.* (2004). doi:10.1016/j.mvr.2004.08.002

100. Camarero-Espinosa, S., Rothen-Rutishauser, B., Foster, E. J. & Weder, C. Articular cartilage: From formation to tissue engineering. *Biomaterials Science* (2016). doi:10.1039/c6bm00068a

101. Sophia Fox, A. J., Bedi, A. & Rodeo, S. A. The basic science of articular cartilage: Structure, composition, and function. *Sports Health* (2009). doi:10.1177/1941738109350438

102. Charlier, E. *et al.* Chondrocyte dedifferentiation and osteoarthritis (OA). *Biochemical Pharmacology* (2019). doi:10.1016/j.bcp.2019.02.036

103. Engler, A. J., Sen, S., Sweeney, H. L. & Discher, D. E. Matrix Elasticity Directs Stem Cell Lineage Specification. *Cell* **126**, 677–689 (2006).

104. Bachmann, B. *et al.* Stiffness Matters: Fine-Tuned Hydrogel Elasticity Alters Chondrogenic Redifferentiation. *Front. Bioeng. Biotechnol.* (2020). doi:10.3389/fbioe.2020.00373

105. Rosser, J. *et al.* Microfluidic nutrient gradient–based three-dimensional chondrocyte

culture-on-a-chip as an in vitro equine arthritis model. *Mater. Today Bio* (2019). doi:10.1016/j.mtbio.2019.100023

106. Lee, D., Erickson, A., You, T., Dudley, A. T. & Ryu, S. Pneumatic microfluidic cell compression device for high-throughput study of chondrocyte mechanobiology. *Lab Chip* (2018). doi:10.1039/c8lc00320c

107. Paggi, C. *et al.* Cartilage-on-chip: a multi-modal platform to study human chondrocyte's response to mechanical stimuli. *Osteoarthr. Cartil.* (2020). doi:10.1016/j.joca.2020.02.287

108. Trevaskis, N. L., Kaminskas, L. M. & Porter, C. J. H. From sewer to saviour-targeting the lymphatic system to promote drug exposure and activity. *Nature Reviews Drug Discovery* (2015). doi:10.1038/nrd4608

109. Rouwkema, J. & Khademhosseini, A. Vascularization and Angiogenesis in Tissue Engineering: Beyond Creating Static Networks. *Trends in Biotechnology* (2016). doi:10.1016/j.tibtech.2016.03.002

CHAPTER 3

ORIGINAL ARTICLES

MANUSCRIPT #1

EVERY BREATH YOU TAKE: NON-INVASIVE REAL-TIME OXYGEN BIOSENSING IN TWO- AND THREE-DIMENSIONAL MICROFLUIDIC CELL MODELS

Helene Zirath, Mario Rothbauer, Sarah Spitz, Barbara Bachmann, Christian Jordan, Bernhard Müller, Josef Ehgartner, Eleni Priglinger, Severin Mühleder, Heinz Redl, Wolfgang Holnthoner, Michael Harasek, Thorsten Mayr, and Peter Ertl

frontiers in Physiology

METHODS
published: 03 July 2018
doi: 10.3389/fphys.2018.00815

Every Breath You Take: Non-invasive Real-Time Oxygen Biosensing in Two- and Three-Dimensional Microfluidic Cell Models

Helene Zirath[1,2†], Mario Rothbauer[1,2*†], Sarah Spitz[1,2†], Barbara Bachmann[1,2,3†], Christian Jordan[1], Bernhard Müller[4], Josef Ehgartner[4], Eleni Priglinger[2,3], Severin Mühleder[2,3], Heinz Redl[2,3], Wolfgang Holnthoner[2,3], Michael Harasek[1], Torsten Mayr[4] and Peter Ertl[1,2]*

[1] Institute of Applied Synthetic Chemistry, Institute of Chemical Technologies and Analytics, Institute of Chemical, Environmental and Bioscience Engineering, Vienna University of Technology, Vienna, Austria, [2] Austrian Cluster for Tissue Regeneration, Vienna, Austria, [3] Ludwig Boltzmann Institute for Experimental and Clinical Traumatology, Allgemeine Unfallversicherungsanstalt (AUVA) Research Centre, Vienna, Austria, [4] Institute of Analytical Chemistry and Food Chemistry, Graz University of Technology, NAWI Graz, Graz, Austria

OPEN ACCESS

Edited by:
Alberto Rainer, Università Campus Bio-Medico, Italy

Reviewed by:
Christoffer Laustsen, Aarhus University, Denmark
Giovann Vozzi, Università degli Studi di Pisa, Italy

***Correspondence:**
Helene Zirath
helene.zirath@tuwien.ac.at
Mario Rothbauer
mario.rothbauer@tuwien.ac.at

† These authors have contributed equally to this work.

Specialty section:
This article was submitted to Integrative Physiology, a section of the journal Frontiers in Physiology

Received: *12 April 2018*
Accepted: *11 June 2018*
Published: *03 July 2018*

Citation:
Zirath H, Rothbauer M, Spitz S, Bachmann B, Jordan C, Müller B, Ehgartner J, Priglinger E, Mühleder S, Redl H, Holnthoner W, Harasek M, Mayr T and Ertl P (2018) Every Breath You Take: Non-invasive Real-Time Oxygen Biosensing in Two- and Three-Dimensional Microfluidic Cell Models. Front. Physiol. 9:815. doi: 10.3389/fphys.2018.00815

Knowledge on the availability of dissolved oxygen inside microfluidic cell culture systems is vital for recreating physiological-relevant microenvironments and for providing reliable and reproducible measurement conditions. It is important to highlight that *in vivo* cells experience a diverse range of oxygen tensions depending on the resident tissue type, which can also be recreated *in vitro* using specialized cell culture instruments that regulate external oxygen concentrations. While cell-culture conditions can be readily adjusted using state-of-the-art incubators, the control of physiological-relevant microenvironments within the microfluidic chip, however, requires the integration of oxygen sensors. Although several sensing approaches have been reported to monitor oxygen levels in the presence of cell monolayers, oxygen demands of microfluidic three-dimensional (3D)-cell cultures and spatio-temporal variations of oxygen concentrations inside two-dimensional (2D) and 3D cell culture systems are still largely unknown. To gain a better understanding on available oxygen levels inside organ-on-a-chip systems, we have therefore developed two different microfluidic devices containing embedded sensor arrays to monitor local oxygen levels to investigate (i) oxygen consumption rates of 2D and 3D hydrogel-based cell cultures, (ii) the establishment of oxygen gradients within cell culture chambers, and (iii) influence of microfluidic material (e.g., gas tight vs. gas permeable), surface coatings, cell densities, and medium flow rate on the respiratory activities of four different cell types. We demonstrate how dynamic control of cyclic normoxic-hypoxic cell microenvironments can be readily accomplished using programmable flow profiles employing both gas-impermeable and gas-permeable microfluidic biochips.

Keywords: microfluidics, 3D culture, biosensor, oxygen, oxygen gradient, organ-on-a-chip, lab-on-a-chip, hydrogel

INTRODUCTION

With the emergence of advanced cell-based *in vitro* models, which resemble the architecture and physiology of actual native tissue, the ability to control and manipulate cellular microenvironment has become an important aspect in microfluidic cell culture systems. Spatio-temporal control over the cellular microenvironment includes (i) physical forces such as shear stress, (ii) biological cues such as direct and indirect cell–cell interactions, and (iii) chemical signals such as pH, oxygenation, and nutrient supply. Among biochemical signals, oxygen plays a key role in regulating mammalian cell functions in human health and disease. It is also important to note that oxygen concentration varies tremendously throughout the human body ranging from 14% in lungs and vasculature down to 0.5% in less irrigated organs such as cartilage and bone marrow (Jagannathan et al., 2016). Despite the different demand of oxygen in different tissues, routine cell culture is predominantly conducted under atmospheric oxygen tension of 21%. This elevated levels of oxygen exposure of cells is referred to as hyperoxia and can lead to altered cell behavior (Gille and Joenje, 1992). For instance, studies have shown that physiologic oxygen tension modulates stem cell differentiation (Mohyeldin et al., 2010), neurogenesis (Zhang et al., 2011), and is involved in a number of cellular mechanisms needed to maintain tissue function (Pugh and Ratcliffe, 2003; Volkmer et al., 2008). In turn, prolonged oxygen deprivation in a hypoxic oxygen milieu can result in a variety of human pathologies including cancer (Pouysségur et al., 2006), tumor development (Harris, 2002), necrosis (Harrison et al., 2007), infection (Zinkernagel et al., 2007), and stroke (Hossmann, 2006). The importance of monitoring and control of oxygen levels in mammalian cell cultures has therefore led to the implementation of a wide variety of sensing strategies ranging from standard electrochemical electrodes (Nichols and Foster, 1994) and enzymatic sensors (Weltin et al., 2014) to fluorescent and luminescent optical biosensors (Wolfbeis Otto, 2015; Ehgartner et al., 2016b). Of these methods, optical detection based on oxygen-sensitive dyes that are embedded in a polymer matrix are ideally suited for the integration in lab-on-a-chip systems due to the facile integration of sensor spots in microfluidic channels, their long-term stability, reliability, and cost-effectiveness of the sensing probes (Wang and Wolfbeis, 2014; Lasave et al., 2015; Sun et al., 2015). Luminescent intensity as well as decay time of the phosphorescent indicator dye is affected by the amount of the surrounding molecular oxygen, thus providing information on the local oxygen concentration (Gruber et al., 2017). Especially porphyrin-based sensor dyes are well suited for oxygen monitoring in cell-based microfluidic devices due to their high sensitivity, biocompatibility, and reversible quenching behavior (Ungerbock et al., 2013; Ehgartner et al., 2014). Typically, time-resolved optical oxygen monitoring of microfluidic cell culture systems is performed using a measurement set-up consisting of the biochip, optical fibers, a read-out system, and a data acquisition device (Oomen et al., 2016; Gruber et al., 2017). As an example, a polydimethylsiloxane (PDMS) microfluidic chip with oxygen flow-through sensors at the inlet and outlet and an optical oxygen sensor in the cell culture chamber has been realized for a real-time monitoring of respiratory rates of mouse embryonic stem cell cultures and for Chinese hamster ovary cells in monolayers for several days of culture (Super et al., 2016). Oxygen sensor spots were also integrated into microfluidic reaction chambers made of glass and silicon for monitoring of biocatalytic transformations (Ehgartner et al., 2016b). To create a more accessible read-out strategy for a broader research audience, a color CCD-camera mounted to a fluorescent microscope was used for 2D sensing of oxygen distribution inside microfluidic microchannels (Ungerbock et al., 2013). An additional multi-parametric analysis setup was established for simultaneous detection of oxygen and pH using core-shell nanoparticles incorporating oxygen- and pH-sensitive dyes (Ehgartner et al., 2016a). Despite these recent advances, little is still known on spatio-temporal variations of oxygen concentrations inside microfluidic 2D and 3D cell culture systems.

In this method paper, we investigate the influence of cell numbers, extra-cellular matrix (ECM) surface coatings, different cell types, as well as oxygen permeability of chip materials to determine the key microfluidic parameters needed to reliably monitor and precisely control oxygen levels during 2D and 3D cell cultivation. To gain deeper insight into oxygen supply to and demand of 2D and 3D cell cultures, we have developed two different microfluidic devices containing embedded sensor arrays as shown in **Figures 1A,B**. Material selection in particular influences gas exchange through the bulk chip material, which therefore directly influences the ability to control oxygen within the microfluidic environment. Initially, we have established two protocols for oxygen monitoring; **Figure 1C** shows the general methodology that can be used for oxygen monitoring of cell cultures during seeding, adhesion, and long-term cultivation. Additionally, another protocol, referred to hereafter as "optimized protocol," is established for precise determination of oxygen consumption rates in 2D microfluidic cultures as shown in **Figure 1D**. Further, we have compared oxygen consumption of cells from epithelial, endothelial, and mesenchymal origin including cancer cells (A549 lung epithelial cells) and primary cells [e.g., normal human dermal fibroblasts (NHDF), adipose-derived stem cells (ASC), and human umbilical vein endothelial cells (HUVEC)]. The effect of a controlled oxygen gradient throughout fibrin hydrogels during vascular network formation over a 7-day culture period is demonstrated using a 3D vascular co-culture model based on HUVEC endothelial cells and ASC stem cells. A final practical application of the oxygen monitoring method involves the early identification of cell necrosis within hydrogel constructs, thus providing quality control information on 3D-cell-laden hydrogel and microtissue cultures.

RESULTS AND DISCUSSION

Non-invasive Oxygen Monitoring in 2D Microfluidic Cell Cultures

Prior to oxygen monitoring of 2D cell cultures, the influence of chip material permeability was evaluated based on the response

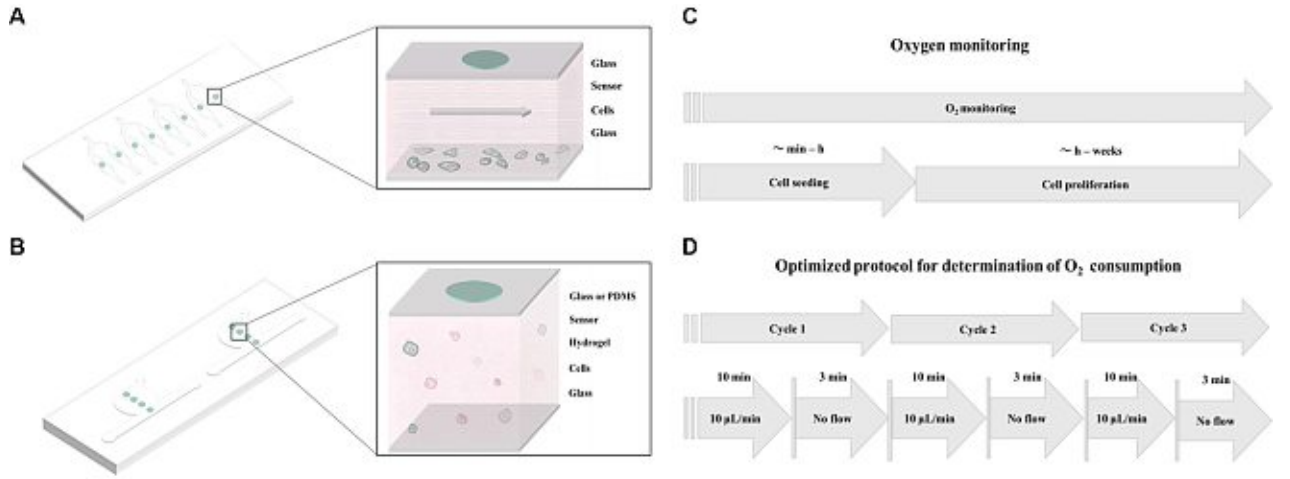

FIGURE 1 | Schematic overview of **(A)** monolayer culture chip and **(B)** 3D cell culture chip with integrated oxygen sensor spots immobilized on the top glass substrate. **(C)** Workflow of oxygen monitoring during cell seeding and cell proliferation studies. **(D)** Workflow of the optimized protocol for evaluation of oxygen consumption of 2D cell cultures.

of the oxygen-sensitive microparticle-based sensors. Therefore, gaseous oxygen content within sealed microchannels was monitored for microfluidic chips fabricated either from oxygen-permeable PDMS or impermeable glass (see **Supplementary Figure S1**). Both devices were simultaneously exposed to an oxygen environment of 2.5% for 20 min before re-oxygenation. As shown in **Figure 2A**, no sensor response was observable for gas-impermeable glass chips with no detectable decrease in partial oxygen pressure. Microfluidic chips made of gas-permeable PDMS showed a decrease in partial oxygen pressure from 176.4 to 15.4 hPa with a t_{90}-value of 15 min and a delay in full recovery to atmospheric oxygen after 87 min. These results demonstrate the importance of material selection during microfluidic chip fabrication. Differences in de- and re-oxygenation linked to material permeability offer the opportunity to either inhibit or allow external oxygen supply to the cell cultures. In turn, sensor-to-sensor variation was evaluated using oxygen concentrations ranging from 20 to 0.5% via small gas feeding by a CO_2/O_2 controller equipped with zirconium-based oxygen sensor, which was connected to the inlet ports of the microfluidic chips. As shown in **Figure 2B**, sensor-to-sensor variation among the individual sensor spots was 221.2 ± 1.3 hPa for 20%, 122.4 ± 0.3 for 10%, 61.9 ± 0.2 hPa for 5%, and 0.2 ± 0.1 hPa for 0.5% oxygen, respectively. These results show excellent reproducibility despite the manual dispensing of the sensor spots into the microfluidic devices.

In the next set of experiments, the impact of cell density on oxygen consumption was evaluated during cell seeding and for fully attached cell cultures. A549 lung epithelial cells were seeded in gas-impermeable microfluidic chips at initial cell seeding densities ranging from 1×10^4 to 1×10^5 cells/cm^2. **Figure 3A** shows a partial oxygen pressure around 200 hPa right after seeding, which accurately represents ambient oxygen levels in cell culture media at 37°C. Difference in partial oxygen pressure for increasing cell numbers was observable already 10 min after cell seeding, thus pointing at higher oxygen demand in the presence of larger cell numbers. Interestingly, while similar oxygen depletion values were observed in the first 40 min, rapid increase in oxygen consumption was found already after 50 min for 1.0×10^5 cells/cm^2 (see **Supplementary Figure S2**), which can be linked to completed cell adhesion and start of exponential cell growth (Rehberg et al., 2013). Cell densities of 1×10^4 and 2.5×10^4 cells/cm^2 resulted in moderate total oxygen depletion values of 13.4 ± 6.7 hPa and 31.1 ± 1.5 hPa, respectively. A more pronounced oxygen depletion was found for the highest cell density of 1×10^5 cells/cm^2 of 153.8 ± 16.7 hPa. Results of this study show that in the presence of high cell densities oxygen depletion occurs 3 h after cell seeding when using gas-impermeable glass microfluidic chips. Next, an optimized protocol was established for precise measurements of oxygen consumption rates (see **Figure 1D** for details). To ensure oxygen consumption measurements, a flow rate of 10 µL/min over period of 10 min prior to the measurements was introduced to maintain oxygenated conditions of around 200 hPa. Flow rates below this threshold did not show full oxygenation (data not shown). For the actual determination of oxygen consumption rates, flow was halted and the decrease in oxygen partial pressure was immediately recorded for 3 min in all chambers. **Figure 3B** shows decreasing oxygen levels over a period of 3 min (n = 3) in the presence of increasing numbers of fully attached A549 lung cells after 4 h of post-seeding, indicating that sufficient re-oxygenation prior to measurement markedly improves data quality. Calculated total oxygen consumption rates of 0.8 hPa/min for 1×10^4 cells/cm^2, 2.6 hPa/min for 2.5×10^4 cells/cm^2, and 4.6 hPa/min for 1×10^5 cells/cm^2. Overall, integration of sensor spots above the cell monolayer culture are sensitive enough to estimate oxygen availability and cell population oxygen demands in microfluidic cell cultivation chambers.

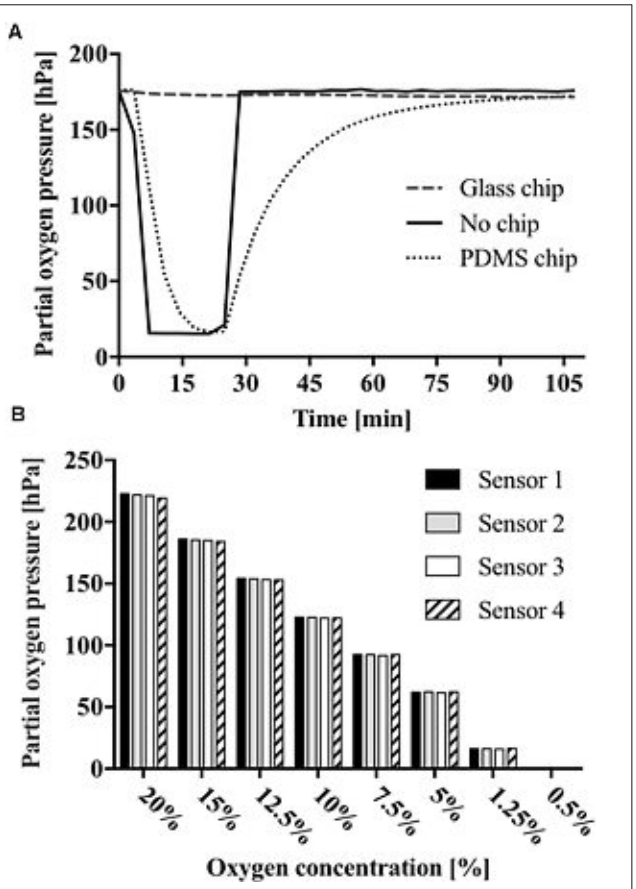

FIGURE 2 | (A) Partial oxygen pressures off- and on-chip fabricated from glass or PDMS. **(B)** Measurements presenting sensor-to-sensor variation and sensor response to declining oxygen concentration starting from 0.5 to 20%.

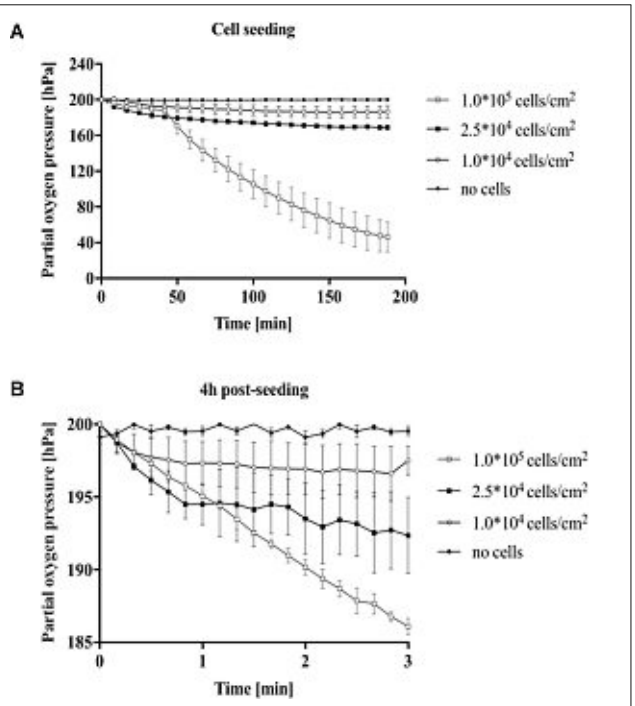

FIGURE 3 | Impact of cell density for A549 cells on oxygen consumption during cell seeding and after cell adhesion. **(A)** Partial oxygen pressure recorded during 3 h of cell seeding and **(B)** oxygen consumption 4 h post-seeding using the optimized oxygen consumption protocol.

Impact of Cell Type on Oxygen Consumption Rates

Differences in oxygen consumption rates between well-established primary cell types (Manning et al., 2015; Haase and Kamm, 2017; Zhang et al., 2017) and cancer cell lines (Cooper et al., 2016) were investigated to further evaluate the presented non-invasive microfluidic oxygen monitoring method. Partial oxygen pressure was monitored during cell seeding for cells from epithelial (A549), endothelial (HUVEC), and mesenchymal origin (NHDF and ASC) at the same initial seeding density of 2.5×10^4 cells/cm^2 corresponding to 5.5×10^3 cells per microchannel. As shown in **Figure 4A** the different cell types can be readily distinguished by cell type–specific variations in oxygen depletion during adhesion to the surface of the microfluidic channels. NHDF fibroblast cells showed highest oxygen depletion values leveling off at a partial oxygen pressure of 17 hPa, which corresponds to a total oxygen consumption of 183 ± 0.4 hPa oxygen in 3 h during cell adhesion. The oxygen consumption for the other cell types were lower with 104.2 hPa (n = 1) for A549 lung cells, 28.4 ± 0.4 hPa for HUVEC endothelial cells, and 59.4 ± 15.4 hPa for ASC stem cells, respectively. Next, oxygen consumption rates were determined using the optimized protocol as shown in **Figure 4B**. Oxygen consumption varied heavily between the different cell types exhibiting low cellular respiratory activity of 3.7 ± 1.2 hPa (1.2 ± 0.4 hPa/min) for A549 lung cells and 6.8 ± 2.1 hPa (2.3 ± 0.7 hPa/min) for HUVEC, 13.9 ± 1.6 hPa (4.7 ± 0.5 hPa/min) for ASC, and highest rates observable of 35.4 ± 2.5 hPa (11.8 ± 0.8 hPa/min) for fibroblast cells. Overall, these results correspond well with literature values the specific cell types demonstrating the good performance of the presented microfluidic oxygen sensing method (Heidemann et al., 1998; Powers et al., 2008; Abaci et al., 2010; Zhang et al., 2014). In addition, **Figure 4C** shows differences in both cell morphology and cell size with a cell size of 72.4 μm^2 for HUVEC endothelial cells, 71.6 μm^2 for A549, 232.9 μm^2 for NHDF fibroblast cells, and 125.3 μm^2 for ASC stem cells. Cell size directly correlates with oxygen consumption, (Wagner et al., 2011) which explains the high respiratory activity of fibroblast cells displaying the biggest cell size.

Impact of Cell Adhesion Promoters on Oxygen Consumption Rates

Since mammalian cells strongly interact and respond to surface properties such as the biocompatibility and functionalization of the interface, the influence of ECM surface promoters including 1% gelatin and collagen I was investigated on the respiratory activity of HUVEC endothelial cells during cell seeding and 3 h after attachment. As shown in **Figure 5A** already 3 min following the introduction of endothelial cells

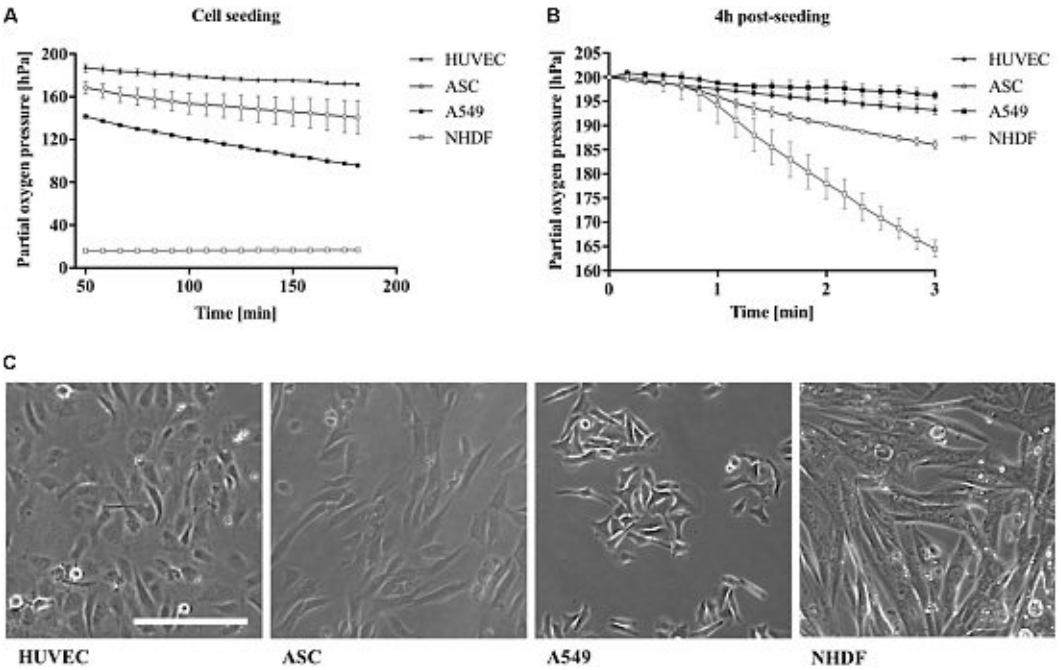

FIGURE 4 | Influence of cell type on partial oxygen pressure during **(A)** cell seeding and **(B)** 4 h post-seeding using the optimized oxygen consumption protocol (n = 6). **(C)** Cell morphology of different cell types seeded with same cell numbers per cm^2. Scale bar, 200 μm.

seeded on gelatin and collagen I-coated microchannels, a drop in partial oxygen pressure by 1 hPa was recorded. In contrast, partial oxygen pressure of 200 hPa remained in the absence of cells. In turn, after completion of cell attachment and establishment of endothelial cell monolayers, both adhesion promoters initiated elevated respiratory activities in the range of 130–150 hPa compared to untreated glass with partial oxygen pressure around 165.7 ± 5 hPa. **Figure 5B** shows that respiration of HUVEC endothelial cells further increased from 4 to 24 h post-seeding by 140% for collagen I coating and 170% for gelatin-coated microchannels. Even though respiratory activity of HUVEC endothelial cells cultured on untreated glass displayed highest relative increase of 250% after 24 h, however, absolute respiration rates were 20–40% lower than cells cultivated on ECM-like adhesion promoters. These findings can be explained by incomplete adhesion of cells on untreated surfaces, where 10% of the cells were only partially attached as shown in **Figure 5C**. In other words, our results demonstrate that our non-invasive on-chip oxygen detection method can also be applied for adhesion and biocompatibility studies, where metabolic assays as well as microscopic inspection of cell phenotype alone can result in overestimation of cellular activity.

Non-invasive Oxygen Monitoring in Three-Dimensional Microfluidic Cell Cultures

Since state-of-the-art *in vitro* models frequently employ 3D-hydrogel-based cell cultures, the integrated oxygen sensor array was evaluated using a well-established co-culture model of ASC stem cells with HUVEC endothelial cells (Muhleder et al., 2018). Here, an oxygen-permeable PDMS-based microfluidic biochip containing four spatially resolved sensor spots (see also **Figure 1B**) was seeded with a HUVEC/ASC cell co-culture. Oxygen monitoring was performed for medium supply channels (sensor #1) as well as at 2 to 7 mm within the fibrin hydrogel (sensors #2–4). On the first day of culture, cell co-cultures settled and established direct cell-cell contacts and reciprocal exchange of pro-angiogenic factors using a static stop-flow cultivation period over 24 h. **Figure 6A** (left panel) shows that after 45 min of hydrogel polymerization, partial oxygen pressure of the feeding channel stayed constant around 169.0 ± 1.1 hPa for the first day of culture. In contrast, within the hydrogel construct oxygen levels slowly decreased over time to around 132.4 ± 5.4 hPa independent of diffusion distance through the hydrogel with an average oxygen decrease of 2.5 hPa/h. After the first day of culture, continuous medium supply was initiated at a flow rate of 2 μL/min for the next 5 days of culture. **Figure 6A** (right panel) shows that at day 6 of vascular network formation, an oxygen gradient was established starting at steady atmospheric partial oxygen pressure of around 198.4 hPa for sensor #1 at the medium feeding channel, and linear decreasing values of 176.3 hPa for sensor #2 at 2 mm, 152.1 hPa for sensor #3 at 4.5 mm, and 140.9 hPa for sensor #4 at 7 mm distance from the feeding channel. Overall, average decrease of partial oxygen pressure of 10 hPa per day was observed for the deepest regions of the hydrogel construct. **Figure 6B** shows that even though a linear oxygen gradient was established, vascular network formation with interconnecting endothelial tubes started at a

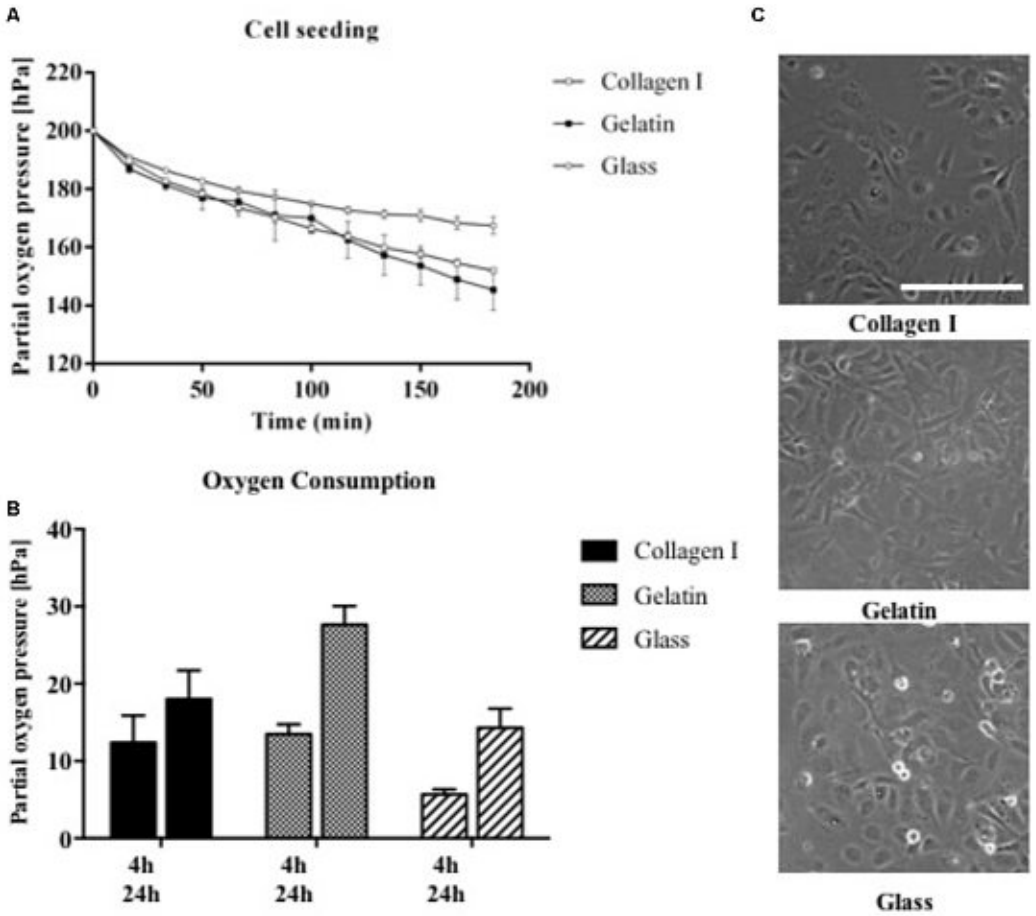

FIGURE 5 | (A) Influence of cell adhesion promoters on partial oxygen pressure during cell seeding for surfaces treated with collagen I and gelatin in comparison to untreated glass (n = 6). **(B)** Oxygen consumption rates of HUVEC endothelial cells on treated and untreated glass surfaces recorded after 4 and 24 h using the optimized oxygen consumption protocol (n = 6). **(C)** Morphology of HUVEC endothelial cells on treated and untreated glass surfaces 4 h post-seeding. Scale bar, 200 μm.

distance of 4.5 mm from the feeding channel. This means that a reduction of partial oxygen pressure by 70 hPa does not affect vascular network formation. In turn, similar vascularization experiments were performed for oxygen-impermeable glass-based microfluidics to generate stronger oxygen gradients. Due to limited oxygen supply from the humidified incubator atmosphere through the bulk chip material, oxygen can exclusively be controlled by adjustment of medium flow rate, thus amount of dissolved oxygen fed to the HUVEC/ASC cell co-culture. To elucidate this mechanism, *in silico* experiments performed using finite volume CFD simulations (Ansys FLUENT® 6.3.26) of oxygen distribution in fibrin hydrogel in the absence of cellular respiratory load were conducted to determine the oxygen saturation within the fibrin hydrogel by medium supply exclusively. **Supplementary Figure S3** shows that already during the first 60 min of medium perfusion, 50% of the supplied oxygen diffuses 2 mm into the hydrogel chamber. Rapid oxygen diffusion then results in a supply of 75% of dissolved oxygen into the depth of the chamber after 6 h and complete oxygen saturation of the chamber within 12 h after initiation of perfusion with the theoretical assumption of oxygen-free conditions at time point zero. **Figure 7A** (left panel) shows that during perfused hydrogel culture within oxygen-impermeable microfluidics right after 45 min of hydrogel polymerization, at a flow rate of 2 μL/min oxygen saturation at a partial oxygen pressure of 197.1 ± 3.2 hPa was observable for the medium feeding channel as well as up to 2 mm into the hydrogel construct. At distances between 4.5 and 7 mm, partial oxygen pressures decreased to 161.2 ± 9.5 hPa with a mean oxygen depletion rate of 5 hPa/h, which is twofold higher compared to the rate found with oxygen-permeable microfluidic chips. In turn, **Figure 7A** (right panel) shows that the combination of impermeable microfluidic biochips with optical in-line oxygen monitoring can be used to control oxygen within microfluidic cultures. By exploiting the respiratory activity of cells within the 3D hydrogel construct, this method can be used to control oxygen levels during long-term cultivation of 3D cells cultures without the need for external oxygen controllers such as CO_2/O_2 incubators, gas controls units for gas mixing, as well as nitrogen gas- or oxygen-scavenging chemicals for oxygen depletion. A pre-programmed flow profile

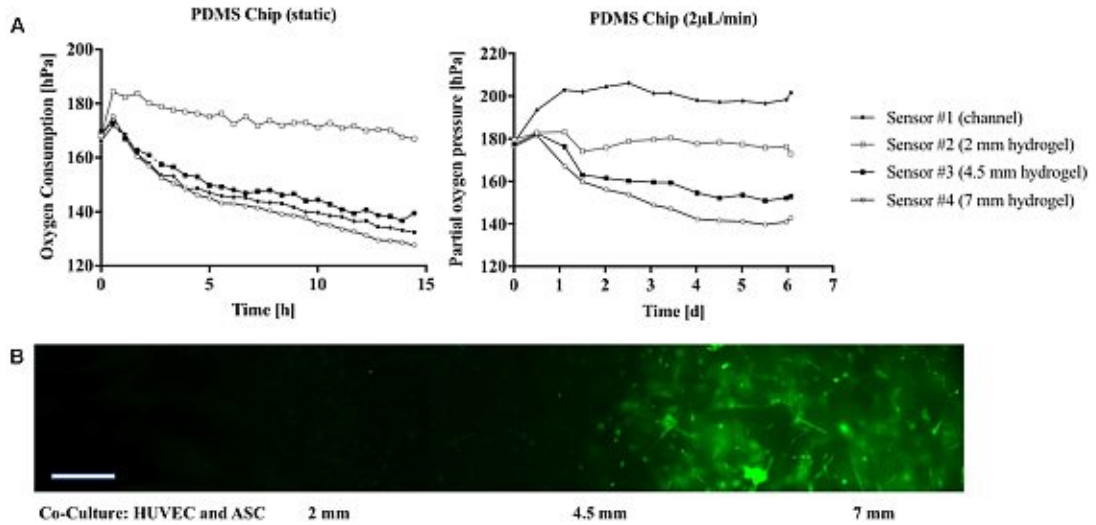

FIGURE 6 | (A) Partial oxygen pressure during cultivation of vascular co-cultures in gas-permeable PDMS microfluidic recorded 14 h post-seeding (no flow conditions; Left) followed by a dynamic cultivation period of 6 days (flow rate 2 µL/min; Right). **(B)** Morphology of the vascular network in glass chips in the presence of flow at 5 µL/min at day 6 post-seeding. GFP-HUVEC endothelial cells are displayed green. Scale bar, 50 µm.

in the range of 0–2 µL/min was used to expose cells to alternating cycles of normoxic and hypoxic culture conditions with peak-to-peak values for partial oxygen pressure of max. 200 hPa down to min. 17 hPa and an average cycle time around 2.5 h over several days for 3D cell culture. **Figure 7A** (bottom panel) shows that due to the cycling of normoxic and hypoxic conditions, formation of a vascular network with decreased length and thickness of vascular sprouts was observable; however, more even distribution of the network was observable starting already at 2 mm distance from the medium feeding channel. In a final set of experiments, we demonstrated how the presented non-invasive microfluidic oxygen monitoring method can be applied not only for oxygen control, but also for evaluation of cell health status during oxygen- and nutrient-dependent limitation of three-dimensional cultures in the absence of medium perfusion. As shown in **Figure 7B** (top panel) an oxygen gradient was established in the absence of medium perfusion due to the respiratory activity of intact cell co-cultures until day 3 post-seeding corresponding to vascular network formation (see **Figure 7B** bottom left image). Over the course of 36 h of nutrient and oxygen limitation, partial oxygen pressure gradually recovered to fully oxygenated conditions around 200 hPa, which is the result of cell death by nutrient and oxygen depletion over 6 days. **Figure 7B** shows a residual pattern of GFP-containing cell remnants (visible in the bottom center image) that resembles the vascular network morphology from day 3. These patterns were not observable for cell co-cultures closest to the medium feeding channel, which did not form vascular networks (bottom right image).

CONCLUSION

In this method paper, we demonstrate the ability to reliably and reproducibly detect dissolved oxygen levels and cellular oxygen demands in 2D and 3D microfluidic cell culture systems. The integration of oxygen-sensitive microparticle-based sensor spots enables time-resolved monitoring of partial oxygen pressures, thus allowing the estimation of cellular oxygen consumption rates of cell monolayers in the presence of increasing flow rates, varying cell numbers, cell types, and ECM-coatings. The total oxygen consumption observed for the different cell densities increased linearly. This means that the presented measurement method has the potential to be used for indirect monitoring of cell viability in toxicological screening studies. Additionally, we show that metabolic evaluation of complex 3D tissue-engineered constructs can be accomplished using biologically relevant co-cultures. The ability to monitor complex 3D physiological cellular microenvironments further highlights the benefits of sensor integration in microfluidic systems to control, mitigate, and accurately predict cell behavior (Charwat et al., 2013, 2014; Ertl et al., 2014; Mahto et al., 2015; Rothbauer et al., 2015a,b). The presented on-chip-integrated oxygen-sensing method is well suited for applications in advanced organ-on-a-chip systems, because it enables non-invasive, real-time, label-free, *in situ* monitoring of oxygen demands, metabolic activity, oxygen uptake rates, and cell viability. We believe that the integration of cost-efficient and reliable sensor technology in microfluidic devices holds great promise for the reliable establishment of physiologic or pathologic tissue conditions, thus opening new avenues in biomedical research and pharmaceutical development.

MATERIALS AND METHODS

Preparation of the Oxygen Sensor

Amine-functionalized polystyrene beads (500 µL of a 50 mg/mL stock solution, micromer® product code 01-01-303, micromod,

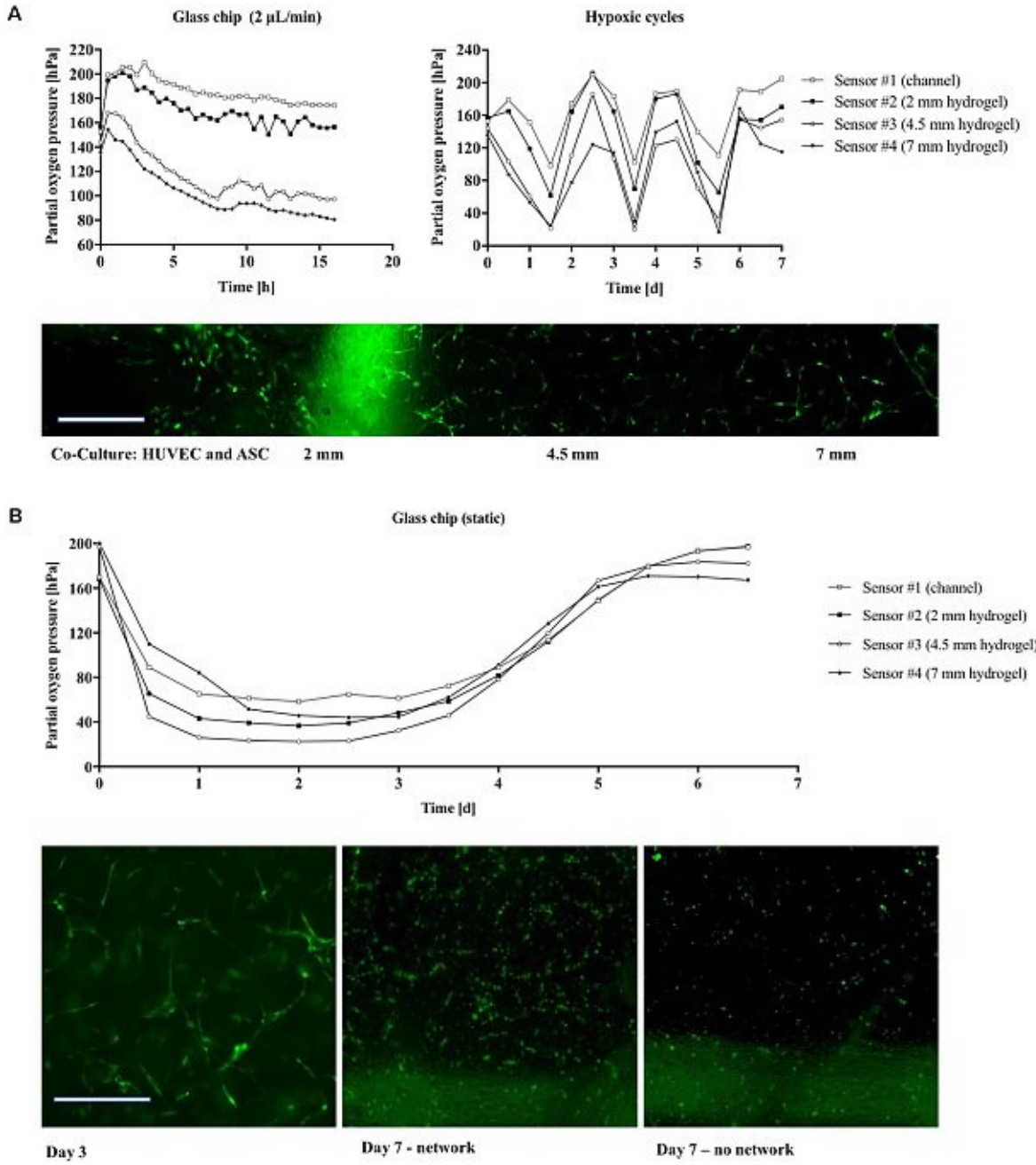

FIGURE 7 | (A) Partial oxygen pressure during cultivation of vascular co-cultures in gas-impermeable glass device recorded during the first 16 h (Left) and during long-term cultivation for 6 days (Right). **(B)** Morphology of the vascular network in glass chips in the absence of nutrient and oxygen supply. GFP-HUVEC endothelial cells are displayed green. Scale bar, 50 µm.

Germany) were diluted with water (2 mL) and THF (200 µL). This dispersion was stirred for 30 min at room temperature. Afterward, an oxygen indicator solution [188 µL of a THF solution containing 2 mg/mL platinum (II) meso-tetra (4-fluorophenyl) tetrabenzoporphyrin (PtTPTBPF)] was added dropwise, the dispersion was sonicated for 30 min, centrifuged at a relative centrifugation force of 6200, and the supernatant was decanted. The particles were purified using multiple washing, centrifugation, and decantation steps. The purification process was repeated with water (1–2 times) at the beginning, followed by ethanol (3–5 times) and finished with water (1–2 times). After the final decantation step the particles were diluted with water to a particle concentration of approx. 50 mg/mL. Characterization and calibration of oxygen sensor was performed as described previously (Ehgartner et al., 2016b).

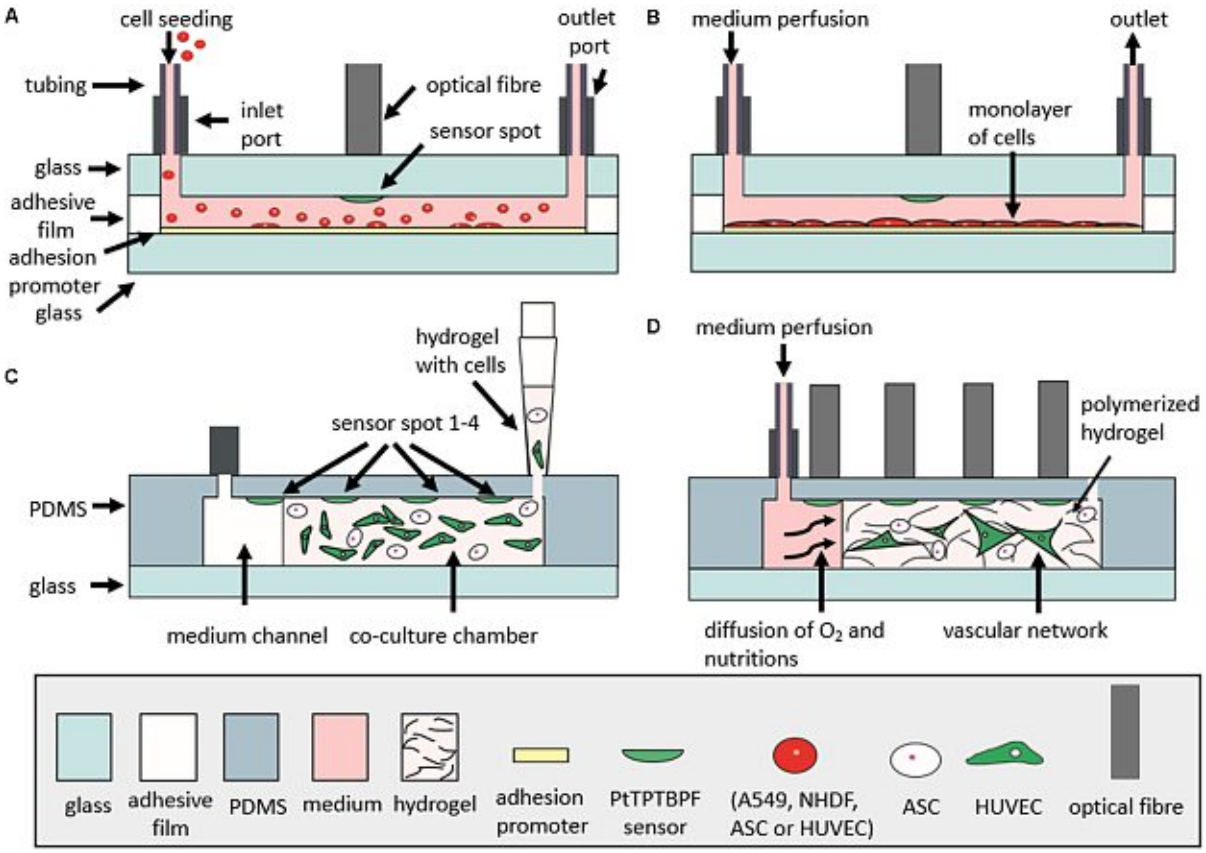

FIGURE 8 | Schematic illustration of microfluidic chips in cross section during cell seeding and cell culturing. **(A)** Monitoring of oxygen consumption during seeding of cells in microfluidic monolayer culture chip. **(B)** Measurement of oxygen consumption rates during the optimized protocol. **(C)** Seeding of cells and hydrogel into gas-permeable 3D cell culture chip. **(D)** Monitoring of oxygen consumption during vascular network formation in 3D cell culture chip with a continuous perfusion of medium. For the gas-impermeable 3D cell culture chip, the upper layer is made of glass and is bonded to the lower glass substrate with adhesive film (not shown in figure).

Microfluidic Chips and Sensor Integration

The microdevices for monolayer cultures were comprised of two glass substrates (VWR) bonded together with adhesive film containing the fluidic structure. Microfluidic chambers and channels were designed with CAD (AutoCAD 2017) and cut into the adhesive film (ARcare 8259 and ARseal 90880, Adhesive Research, Ireland) with a desktop vinyl cutter (GS-24 Desktop Cutter, Roland DGA Corporation, Germany). Three layers of adhesive film were used to obtain a chamber height of 460 μm. The chip contained 8 cell-culture chambers of 0.22 cm^2 (10 μL volume) with one inlet connected to two chambers with a 400 μm wide channel (**Figure 1A**). Holes for inlets and outlets were drilled into the upper glass substrate before integration of sensor particles. Oxygen sensor microparticles were applied by pipetting directly to the glass substrate. After drying for 2 h at room temperature, the microparticles were immobilized to the glass substrate and the fluidic structures were sealed with adhesive film via pressure activation. Devices for three-dimensional (3D) hydrogel cultures had a circular hydrogel chamber (65 μL volume) adjacent to a medium channel (see **Figure 1B**). Microstructures were either fabricated by soft lithography using PDMS (Sylgard® 184 Silicone Elastomer Kit, Down Corning, Germany) from 3D-printed molds (immaterialize, Denmark) or sandblasted into glass slides. Oxygen-sensitive conjugated microparticles were again applied via pipetting directly to the glass substrate and immobilized after 2 h of drying. PDMS devices were sealed by plasma bonding to glass slides using air plasma (Harrick Plasma, High Power, 2 min) and glass devices were sealed using adhesive film (ARseal 90880, Adhesive Research, Ireland).

Cell Culture

A549 human lung carcinoma epithelial-like cell line (ATCC) were cultured in RPMI 1640 Medium (Gibco) supplemented with 10% fetal bovine serum, L-glutamine, and 1% antibiotic/antimycotic solution. NHDF (Lonza) were cultured in high glucose Dulbecco's modified Eagle's medium (DMEM, Sigma Aldrich) supplemented with 10% fetal bovine serum, 2 mM glutamine, and 1% antibiotic-antimycotic solution. Primary human ASC and HUVEC were isolated as previously described (Petzelbauer et al., 1993; Wolbank et al., 2007; Priglinger et al., 2017)

and maintained in fully supplemented endothelial cell growth medium 2 (EGM-2, PromoCell) with 5% fetal calf serum until passage 5–9. GFP-labeled endothelial cells were prepared as previously described (Knezevic et al., 2017; Muhleder et al., 2018) All cell cultures were maintained in a humidified atmosphere at 37°C and 5% CO_2. Cell culture media used during perfusion of the microfluidic monolayer chambers was supplemented with 0.5% HEPES (Sigma Aldrich). Prior to cell seeding, microfluidic tubing and valves were sterilized with 70% ethanol and rinsed thoroughly with PBS (Sigma Aldrich) and cell culture medium. The assembled microfluidic biochips were disinfected using 70% ethanol and rinsed with sterile PBS prior to coating with 5% collagen I solution (Sigma Aldrich, Austria).

On-Chip Oxygen Monitoring

Oxygen monitoring was carried out at a sampling frequency of 1 Hz using a FireStingO2 optical oxygen meter (Pyroscience, Germany[1]) connected to optical fibers (length 1 m, outer diameter 2.2 mm, fiber diameter 1 mm). Integrated sensors were calibrated using a CO_2/O_2 oxygen controller (CO_2-O_2-Controller 2000, Pecon GmbH, Germany) equipped with integrated zirconium oxide oxygen sensors. Oxygen measurements were initiated directly after injection of cell solutions and partial oxygen pressure was monitored up to a maximum duration of 7 days. To evaluate the influence of cell number on oxygen consumption, A549 lung cells were seeded at concentrations of 1×10^4 cells/cm^2 (2.2×10^3 cells/chamber), 2.5×10^4 cells/cm^2 (5.5×10^3 cells/chamber), and 1.0×10^5 cells/cm^2 (22×10^3 cells/chamber). For oxygen monitoring of different cell types, A549 lung epithelial cells, NHDF fibroblast cells, HUVEC endothelial cells, and ASC stem cells were seeded at a concentration of 2.5×10^4 cells/cm^2 (5.5×10^3 cells/chamber) To investigate the influence of adhesion promoters on oxygen consumption, HUVEC endothelial cells were seeded at a concentration of 2.5×10^4 HUVEC/cm^2 (5.5×10^3 cells/chamber) on different surfaces including untreated glass 5% collagen I and 1% gelatin. For oxygen monitoring of 3D fibrin hydrogels, ASC stem cells and HUVEC endothelial cells were mixed at a cell density of 5×10^5 cells/mL (32.5×10^3 cells/chamber, 65 µL chamber volume) per cell type in fibrinogen and thrombin (TISSEEL®, Baxter, Austria) to obtain a final concentration of 2.5 mg/mL fibrinogen and 1 U/mL thrombin. The hydrogel was loaded into the hydrogel chambers of the microfluidic chip and allowed to polymerize for 45 min before the addition of fully supplemented EGM-2 culture medium. Thereafter, vascular 3D cell cultures were maintained at a flow rate of 2 µL/min. In **Figures 8A–D**, schematic illustrations depict the cell seeding and measurement setup of monolayer culture chips (A–B) and 3D culture chips (C–D).

Optimized Protocol for On-Chip Oxygen Consumption Measurements

For determination of oxygen consumption, an optimized protocol was established recording three consecutive measuring cycles. Each cycle comprised of an oxygen saturation phase of 10 µL/min for 10 min followed by a recording phase under stop-flow conditions for 3 min.

CFD Simulation of Oxygen

Oxygen saturation was simulated using a multipurpose finite volume CFD simulation (Ansys FLUENT®, v6.3.26). The hydrogel region was approximated as a porous zone with a porosity of $\varepsilon = 0.99$ and isotropic viscous resistances of $R = 6.67 * 10^{-12}$ 1/m^2. Simulations were performed using an oxygen diffusion coefficient of 2×10^{-9} m^2/s.

AUTHOR CONTRIBUTIONS

HZ, MR, SS, BB, and PE conceived the project and designed the experimental outline. HZ, MR, SS, and BB performed the microfluidic experiments and analyzed the data. CJ and MH conceived and performed finite volume CFD simulations. BM, JE, and TM prepared the optical sensors for oxygen biosensing. EP, SM, WH, and HR isolated and transfected the primary endothelial and adipose-derived stem cell cultures and shared their expertise in vascular tissue engineering. HZ, MR, SS, and BB drafted the manuscript. All authors contributed to and revised the final manuscript.

FUNDING

This work was funded by the European Union's Horizon 2020 research and innovation programme (685817) and the Austrian Research Promotion Agency (FFG; 849791). The authors acknowledge the TU Wien University Library for financial support through its Open Access Funding Program.

ACKNOWLEDGMENTS

The authors acknowledge the band "The Police" for their fundamental contribution to the title and Christoph Eilenberger for image analysis and fruitful discussions.

SUPPLEMENTARY MATERIAL

The Supplementary Material for this article can be found online at: https://www.frontiersin.org/articles/10.3389/fphys.2018.00815/full#supplementary-material

FIGURE S1 | Images of microfluidic devices. **(A)** Microfluidic glass chip (76 mm × 26 mm × 2.3 mm) for monolayer culture containing eight chambers with a sensor spot centralized in each chamber. **(B)** Microfluidic glass chip (76 mm × 26 mm × 4.4 mm) for three-dimensional (3D) hydrogel cultures with four sensor spots in each chamber. Scale bar represent 10 mm.

FIGURE S2 | Partial oxygen pressure recorded during 3 h of cell seeding zoomed in to the first 50 min of oxygen monitoring.

FIGURE S3 | Finite volume simulation of oxygen distribution in 3D hydrogel after **(A)** 1 h, **(B)** 6 h, and **(C)** 12 h of medium perfusion without cells showing complete saturation of hydrogel with oxygen within 12 h.

[1] www.pyro-science.com

REFERENCES

Abaci, H. E., Truitt, R., Luong, E., Drazer, G., and Gerecht, S. (2010). Adaptation to oxygen deprivation in cultures of human pluripotent stem cells, endothelial progenitor cells, and umbilical vein endothelial cells. *Am. J. Physiol. Cell Physiol.* 298, C1527–C1537. doi: 10.1152/ajpcell.00484.2009

Charwat, V., Joksch, M., Sticker, D., Purtscher, M., Rothbauer, M., and Ertl, P. (2014). Monitoring cellular stress responses using integrated high-frequency impedance spectroscopy and time-resolved ELISA. *Analyst* 139, 5271–5282. doi: 10.1039/c4an00824c

Charwat, V., Rothbauer, M., Tedde, S. F., Hayden, O., Bosch, J. J., Muellner, P., et al. (2013). Monitoring dynamic interactions of tumor cells with tissue and immune cells in a lab-on-a-chip. *Anal. Chem.* 85, 11471–11478. doi: 10.1021/ac403 3406

Cooper, J. R., Abdullatif, M. B., Burnett, E. C., Kempsell, K. E., Conforti, F., Tolley, H., et al. (2016). Long term culture of the A549 cancer cell line promotes multilamellar body formation and differentiation towards an alveolar type II pneumocyte phenotype. *PLoS One* 11:e0164438. doi: 10.1371/journal.pone. 0164438

Ehgartner, J., Strobl, M., Bolivar, J. M., Rabl, D., Rothbauer, M., Ertl, P., et al. (2016a). Simultaneous determination of oxygen and pH inside microfluidic devices using core-shell nanosensors. *Anal. Chem.* 88, 9796–9804.

Ehgartner, J., Sulzer, P., Burger, T., Kasjanow, A., Bouwes, D., Krühne, U., et al. (2016b). Online analysis of oxygen inside silicon-glass microreactors with integrated optical sensors. *Sens. Actuators B Chem.* 228, 748–757. doi: 10.1016/ j.snb.2016.01.050

Ehgartner, J., Wiltsche, H., Borisov, S. M., and Mayr, T. (2014). Low cost referenced luminescent imaging of oxygen and pH with a 2-CCD colour near infrared camera. *Analyst* 139, 4924–4933. doi: 10.1039/c4an00783b

Ertl, P., Sticker, D., Charwat, V., Kasper, C., and Lepperdinger, G. (2014). Lab-on-a-chip technologies for stem cell analysis. *Trends Biotechnol.* 32, 245–253. doi: 10.1016/j.tibtech.2014.03.004

Gille, J. J., and Joenje, H. (1992). Cell culture models for oxidative stress: superoxide and hydrogen peroxide versus normobaric hyperoxia. *Mutat. Res.* 275, 405–414. doi: 10.1016/0921-8734(92)90043-O

Gruber, P., Marques, M. P. C., Szita, N., and Mayr, T. (2017). Integration and application of optical chemical sensors in microbioreactors. *Lab Chip* 17, 2693–2712. doi: 10.1039/c7lc00538e

Haase, K., and Kamm, R. D. (2017). Advances in on-chip vascularization. *Regen. Med.* 12, 285–302. doi: 10.2217/rme-2016-0152

Harris, A. L. (2002). Hypoxia — a key regulatory factor in tumour growth. *Nat. Rev. Cancer* 2, 38–47. doi: 10.1038/nrc704

Harrison, B. S., Eberli, D., Lee, S. J., Atala, A., and Yoo, J. J. (2007). Oxygen producing biomaterials for tissue regeneration. *Biomaterials* 28, 4628–4634. doi: 10.1016/j.biomaterials.2007.07.003

Heidemann, R., Lütkemeyer, D., Büntemeyer, H., and Lehmann, J. (1998). Effects of dissolved oxygen levels and the role of extra- and intracellular amino acid concentrations upon the metabolism of mammalian cell lines during batch and continuous cultures. *Cytotechnology* 26, 185–197. doi: 10.1023/A: 1007917409455

Hossmann, K.-A. (2006). Pathophysiology and therapy of experimental stroke. *Cell. Mol. Neurobiol.* 26, 1055–1081. doi: 10.1007/s10571-006-9008-1

Jagannathan, L., Cuddapah, S., and Costa, M. (2016). Oxidative stress under ambient and physiological oxygen tension in tissue culture. *Curr. Pharmacol. Rep.* 2, 64–72. doi: 10.1007/s40495-016-0050-5

Knezevic, L., Schaupper, M., Muhleder, S., Schimek, K., Hasenberg, T., Marx, U., et al. (2017). Engineering blood and lymphatic microvascular networks in fibrin matrices. *Front. Bioeng. Biotechnol.* 5:25. doi: 10.3389/fbioe.2017. 00025

Lasave, L. C., Borisov, S. M., Ehgartner, J., and Mayr, T. (2015). Quick and simple integration of optical oxygen sensors into glass-based microfluidic devices. *RSC Adv.* 5, 70808–70816. doi: 10.1039/C5RA15591F

Mahto, S. K., Charwat, V., Ertl, P., Rothen-Rutishauser, B., Rhee, S. W., and Sznitman, J. (2015). Microfluidic platforms for advanced risk assessments of nanomaterials. *Nanotoxicology* 9, 381–395. doi: 10.3109/17435390.2014.94 0402

Manning, C. N., Martel, C., Sakiyama-Elbert, S. E., Silva, M. J., Shah, S., Gelberman, R. H., et al. (2015). Adipose-derived mesenchymal stromal cells modulate tendon fibroblast responses to macrophage-induced inflammation in vitro. *Stem Cell Res. Ther.* 6:74. doi: 10.1186/s13287-015-0059-4

Mohyeldin, A., Garzón-Muvdi, T., and Quiñones-Hinojosa, A. (2010). Oxygen in stem cell biology: a critical component of the stem cell niche. *Cell Stem Cell* 7, 150–161. doi: 10.1016/j.stem.2010.07.007

Muhleder, S., Pill, K., Schaupper, M., Labuda, K., Priglinger, E., Hofbauer, P., et al. (2018). The role of fibrinolysis inhibition in engineered vascular networks derived from endothelial cells and adipose-derived stem cells. *Stem Cell Res. Ther.* 9:35. doi: 10.1186/s13287-017-0764-2

Nichols, M. G., and Foster, T. H. (1994). Oxygen diffusion and reaction kinetics in the photodynamic therapy of multicell tumour spheroids. *Phys. Med. Biol.* 39, 2161–2181. doi: 10.1088/0031-9155/39/12/003

Oomen, P. E., Skolimowski, M. D., and Verpoorte, E. (2016). Implementing oxygen control in chip-based cell and tissue culture systems. *Lab Chip* 16, 3394–3414. doi: 10.1039/c6lc00772d

Petzelbauer, P., Bender, J. R., Wilson, J., and Pober, J. S. (1993). Heterogeneity of dermal microvascular endothelial cell antigen expression and cytokine responsiveness in situ and in cell culture. *J. Immunol.* 151, 5062–5072.

Pouysségur, J., Dayan, F., and Mazure, N. M. (2006). Hypoxia signalling in cancer and approaches to enforce tumour regression. *Nature* 441, 437–443. doi: 10.1038/nature04871

Powers, D. E., Millman, J. R., Huang, R. B., and Colton, C. K. (2008). Effects of oxygen on mouse embryonic stem cell growth, phenotype retention, and cellular energetics. *Biotechnol. Bioeng.* 101, 241–254. doi: 10.1002/bit. 21986

Priglinger, E., Schuh, C., Steffenhagen, C., Wurzer, C., Maier, J., Nuernberger, S., et al. (2017). Improvement of adipose tissue-derived cells by low-energy extracorporeal shock wave therapy. *Cytotherapy* 19, 1079–1095. doi: 10.1016/ j.jcyt.2017.05.010

Pugh, C. W., and Ratcliffe, P. J. (2003). Regulation of angiogenesis by hypoxia: role of the HIF system. *Nat. Med.* 9, 677–684. doi: 10.1038/nm0603-677

Rehberg, M., Ritter, J. B., Genzel, Y., Flockerzi, D., and Reichl, U. (2013). The relation between growth phases, cell volume changes and metabolism of adherent cells during cultivation. *J. Biotechnol.* 164, 489–499. doi: 10.1016/j. jbiotec.2013.01.018

Rothbauer, M., Praisler, I., Docter, D., Stauber, R. H., and Ertl, P. (2015a). Microfluidic impedimetric cell regeneration assay to monitor the enhanced cytotoxic effect of nanomaterial perfusion. *Biosensors* 5, 736–749. doi: 10.3390/ bios5040736

Rothbauer, M., Wartmann, D., Charwat, V., and Ertl, P. (2015b). Recent advances and future applications of microfluidic live-cell microarrays. *Biotechnol. Adv.* 33, 948–961. doi: 10.1016/j.biotechadv.2015.06.006

Sun, S., Ungerbock, B., and Mayr, T. (2015). Imaging of oxygen in microreactors and microfluidic systems. *Methods Appl. Fluoresc.* 3:034002. doi: 10.1088/2050-6120/3/3/034002

Super, A., Jaccard, N., Cardoso Marques, M. P., Macown, R. J., Griffin, L. D., Veraitch, F. S., et al. (2016). Real-time monitoring of specific oxygen uptake rates of embryonic stem cells in a microfluidic cell culture device. *Biotechnol. J.* 11, 1179–1189. doi: 10.1002/biot.201500479

Ungerbock, B., Charwat, V., Ertl, P., and Mayr, T. (2013). Microfluidic oxygen imaging using integrated optical sensor layers and a color camera. *Lab Chip* 13, 1593–1601. doi: 10.1039/c3lc41315b

Volkmer, E., Drosse, I., Otto, S., Stangelmayer, A., Stengele, M., Kallukalam, B. C., et al. (2008). Hypoxia in static and dynamic 3D culture systems for tissue engineering of bone. *Tissue Eng. Part A* 14, 1331–1340. doi: 10.1089/ten.tea. 2007.0231

Wagner, B. A., Venkataraman, S., and Buettner, G. R. (2011). The rate of oxygen utilization by cells. *Free Radic. Biol. Med.* 51, 700–712. doi: 10.1016/j. freeradbiomed.2011.05.024

Wang, X. D., and Wolfbeis, O. S. (2014). Optical methods for sensing and imaging oxygen: materials, spectroscopies and applications. *Chem. Soc. Rev.* 43, 3666–3761. doi: 10.1039/c4cs00039k

Weltin, A., Slotwinski, K., Kieninger, J., Moser, I., Jobst, G., Wego, M., et al. (2014). Cell culture monitoring for drug screening and cancer research: a transparent, microfluidic, multi-sensor microsystem. *Lab Chip* 14, 138–146. doi: 10.1039/ c3lc50759a

Wolbank, S., Peterbauer, A., Fahrner, M., Hennerbichler, S., van Griensven, M., Stadler, G., et al. (2007). Dose-dependent immunomodulatory effect of human

stem cells from amniotic membrane: a comparison with human mesenchymal stem cells from adipose tissue. *Tissue Eng.* 13, 1173–1183. doi: 10.1089/ten.2006.0313

Wolfbeis Otto, S. (2015). Luminescent sensing and imaging of oxygen: fierce competition to the clark electrode. *Bioessays* 37, 921–928. doi: 10.1002/bies.201500002

Zhang, J., Wei, X., Zeng, R., Xu, F., and Li, X. (2017). Stem cell culture and differentiation in microfluidic devices toward organ-on-a-chip. *Future Sci. OA* 3:FSO187. doi: 10.4155/fsoa-2016-0091

Zhang, K., Zhu, L., and Fan, M. (2011). Oxygen, a key factor regulating cell behavior during neurogenesis and cerebral diseases. *Front. Mol. Neurosci.* 4:5. doi: 10.3389/fnmol.2011.00005

Zhang, L., Marsboom, G., Glick, D., Zhang, Y., Toth, P. T., Jones, N., et al. (2014). Bioenergetic Shifts during transitions between stem cell states (2013 Grover Conference series). *Pulm. Circ.* 4, 387–394. doi: 10.1086/677353

Zinkernagel, A. S., Johnson, R. S., and Nizet, V. (2007). Hypoxia inducible factor (HIF) function in innate immunity and infection. *J. Mol. Med.* 85, 1339–1346. doi: 10.1007/s00109-007-0282-2

Conflict of Interest Statement: The authors declare that the research was conducted in the absence of any commercial or financial relationships that could be construed as a potential conflict of interest.

MANUSCRIPT #2

SMALL FORCE, BIG IMPACT: NEXT GENERATION ORGAN-ON-A-CHIP SYSTEMS INCORPORATING BIOMECHANICAL CUES

Ece Ergir, Barbara Bachmann, Heinz Redl, Giancarlo Forte, and Peter Ertl

frontiers in Physiology

MINI REVIEW
published: 09 October 2018
doi: 10.3389/fphys.2018.01417

Small Force, Big Impact: Next Generation Organ-on-a-Chip Systems Incorporating Biomechanical Cues

Ece Ergir[1,2†], Barbara Bachmann[2,3,4,5†], Heinz Redl[3,4,5], Giancarlo Forte[1,6,7] and Peter Ertl[2,4,5*]*

[1] Center for Translational Medicine, International Clinical Research Center, St. Anne's University Hospital, Brno, Czechia, [2] Faculty of Technical Chemistry, Institute of Applied Synthetic Chemistry and Institute of Chemical Technologies and Analytics, Vienna University of Technology, Vienna, Austria, [3] AUVA Research Centre, Ludwig Boltzmann Institute for Experimental and Clinical Traumatology, Vienna, Austria, [4] Austrian Cluster for Tissue Regeneration, Vienna, Austria, [5] Kompetenzzentrum für MechanoBiologie (INTERREG V-A Austria – Czech Republic Programme, ATCZ133), Vienna, Austria, [6] Competence Center for Mechanobiology (INTERREG V-A Austria – Czech Republic Programme, ATCZ133), Brno, Czechia, [7] Department of Biomaterials Science, Institute of Dentistry, University of Turku, Turku, Finland

Edited by:
Leonardo Alexandre Peyré-Tartaruga, Universidade Federal do Rio Grande do Sul (UFRGS), Brazil

Reviewed by:
Khashayar Khoshmanesh, RMIT University, Australia
Irena Levitan, University of Illinois at Chicago, United States
T. Alexander Quinn, Dalhousie University, Canada

****Correspondence:***
Giancarlo Forte
giancarlo.forte@fnusa.cz
Peter Ertl
peter.ertl@tuwien.ac.at

† These authors have contributed equally to this work

Specialty section:
This article was submitted to Integrative Physiology, a section of the journal Frontiers in Physiology

Received: *01 April 2018*
Accepted: *18 September 2018*
Published: *09 October 2018*

Citation:
Ergir E, Bachmann B, Redl H, Forte G and Ertl P (2018) Small Force, Big Impact: Next Generation Organ-on-a-Chip Systems Incorporating Biomechanical Cues. Front. Physiol. 9:1417. doi: 10.3389/fphys.2018.01417

Mechanobiology-on-a-chip is a growing field focusing on how mechanical inputs modulate physico-chemical output in microphysiological systems. It is well known that biomechanical cues trigger a variety of molecular events and adjustment of mechanical forces is therefore essential for mimicking *in vivo* physiologies in organ-on-a-chip technology. Biomechanical inputs in organ-on-a-chip systems can range from variations in extracellular matrix type and stiffness and applied shear stresses to active stretch/strain or compression forces using integrated flexible membranes. The main advantages of these organ-on-a-chip systems are therefore (a) the control over spatiotemporal organization of *in vivo*-like tissue architectures, (b) the ability to precisely control the amount, duration and intensity of the biomechanical stimuli, and (c) the capability of monitoring in real time the effects of applied mechanical forces on cell, tissue and organ functions. Consequently, over the last decade a variety of microfluidic devices have been introduced to recreate physiological microenvironments that also account for the influence of physical forces on biological functions. In this review we present recent advances in mechanobiological lab-on-a-chip systems and report on lessons learned from these current mechanobiological models. Additionally, future developments needed to engineer next-generation physiological and pathological organ-on-a-chip models are discussed.

Keywords: microfluidics, mechanobiology, organ-on-a-chip, lab-on-a-chip, *in vitro* organ models, mechanical cell actuation

INTRODUCTION

Conventional mammalian cell culture systems are predominantly based on two-dimensional (2D) monolayer cultures to study cellular mechanisms in pharmaceutical research, toxicology and biomedicine. Even though 2D cell culture models are routinely used, they fail to recapitulate the spatiotemporal dynamics that cells encounter *in vivo*. The discrepancy between *in vitro*

monolayers and native tissue structures leads in many cases to altered phenotype, cell morphology and behavior, thus rendering results from 2D cell-based assays questionable (Baker and Chen, 2012). To overcome the drawbacks associated with 2D monocultures, recent cell cultivation setups aim to re-engineer the physiological cellular microenvironment of native tissues. This can be accomplished by moving toward three-dimensional (3D) culture systems through cultivating cells in hydrogels, scaffolds or aggregates (Chen et al., 2002; Drury and Mooney, 2003; Griffith and Swartz, 2006; Fennema et al., 2013). The implementation of 3D cell culture systems by itself allows for indirect mechanical stimulation by controlling the rigidity and stiffness of the extracellular matrix, which has shown to modulate cellular responses (Engler et al., 2006; Kumar, 2014). Additionally, 3D-tissue models can be further subjected to dynamic mechanical stimuli including fluid flow, stretch/strain and compression. The application of indirect and/or direct mechanical stimuli in tissue cultures has become a rapidly growing research field that is commonly known as mechanobiology (Eyckmans et al., 2011). It is important to highlight that almost every tissue of a human body is subjected to either constant or temporary mechanical stimuli. This means that the application of mechanobiological forces represents a vital step toward the establishment of physiological microenvironments *in vitro* (Wang and Thampatty, 2006; Jansen et al., 2015). To date a variety of mechanobiological forces, shown in **Figure 1A**, have been employed in 2D and 3D *in vitro* cultures including (a) matrix stiffness that mimic the respective Young's moduli of native tissue, (b) fluid flow in vascular systems and interstitial tissue, (c) stretch/strain mechanisms in the lung, heart and gastrointestinal tract as well as (d) compression in the musculoskeletal system (Lovett et al., 2009; Riehl et al., 2012; Shachar et al., 2012; Ahearne, 2014). These mechanobiological systems demonstrated improved cell-to-cell and cell-to-matrix interactions resulting in significant progress in recapitulating physiological microenvironments *in vitro*. Although these tissue models led to substantial advances in understanding mechanobiology on a macroscale, common tissue engineering-based approaches require sizeable amounts of cells as well as reagents but lack precise control over location and amount of the stimulus. A commonly accepted solution in fostering our understanding of biomechanical effects is taking the tissue to the microscale. This can be accomplished by mimicking cellular microenvironments in microfluidic devices, which not only offer a decrease in cell numbers and consumables but also allow precise control over spatio-temporal stiffness and growth factor gradients as well as mechanical stimulus type, amount and location (Huh et al., 2011; Bhatia and Ingber, 2014; Rothbauer et al., 2015; van Duinen et al., 2015). In other words, microdevices can be used to investigate contractility, cell confinement and micropatterning, all of which are crucial in gaining deeper insights into mechanobiological phenomena. Moreover, microfluidic chips are compatible with high resolution microscopy for cell observation and also allow the integration of actuators and sensors, which provides the opportunity to trigger and monitor cellular behavior *in situ*. Overall this review focuses on emerging physiologically relevant micro-tissue models in mechanobiology-on-a-chip setups in both culture environments since 2012, shortly summarized in **Table 1**.

MICROFLUIDIC MECHANOBIOLOGY IN MONOLAYERS AND BARRIER MODELS

Shear Stress

Microfluidic devices with their laminar flow regimes have widely been used to expose cells to fluid flow induced shear stress. This has led to substantial improvements in understanding the mechanobiological effect of shear stress variations on endothelial cells in vascular models but also in osteocyte, cardiomyocyte and epithelial cell biology. In particular, fluid flow plays a major role in vascular biology as the endothelial cell lining layer inside blood vessels is constantly exposed to pulsatile blood flow (Baratchi et al., 2017). Subjecting endothelial cells to physiological unidirectional or disturbed shear stress patterns has been shown to significantly alter cell morphology and phenotype. For example, it has been shown that shear stress influences nanoparticle uptake of endothelial cells where higher flow rates led to reduced uptake. Using an *in vitro* as well as *in silico* approach, Charwat et al. (2018) found that clathrin-mediated uptake of nanoparticles is drastically reduced when exceeding shear forces of 1.8 dyn/cm^2, implying an important role of shear stress when investigating *in vitro* nanoparticle uptake. Another study, published by Griep et al. (2013), successfully recreated the smallest unit of the blood brain barrier using immortalized brain endothelial cells to study barrier integrity in the presence of physiological shear force. While unidirectional shear stress plays an important role in assessing healthy vessel physiology, microfluidic devices can also be utilized to create bi- and multidirectional flow patterns for mimicking endothelial pathology. Such disturbed flow patterns allow for flow type-dependent gene expression profiling of endothelial cells (Zheng et al., 2017) as well as observation of leucocyte – endothelial cell interactions (Venugopal Menon et al., 2018) and the role of glucose uptake in endothelial dysfunction (Patibandla et al., 2014) for modeling inflammation and hyperglycemia in atherosclerosis. The effect of shear stress on endothelial cells and microfluidic technologies have recently been extensively reviewed elsewhere (Smith and Gerecht, 2014; Haase and Kamm, 2017; Kim et al., 2017). Furthermore, microfluidic devices have also been used outside of endothelial research to record phenotypic transformations of aortic valve interstitial cells during applied shear stress and to monitor morphological changes of osteocytes during application of flow. Additionally, Middleton et al. (2017a) showed that in the presence of shear stress, cell to cell interactions of osteocytes co-cultured with osteoclast are enhanced, leading to the improved mechanical response of bone cells. A more detailed review on monitoring cell-cell interaction using microfluidic devices was recently published by Rothbauer et al. (2017). Altogether, microfluidic devices are an important tool to study shear stress, but while the effects on endothelial cells have been studied extensively, other cell types

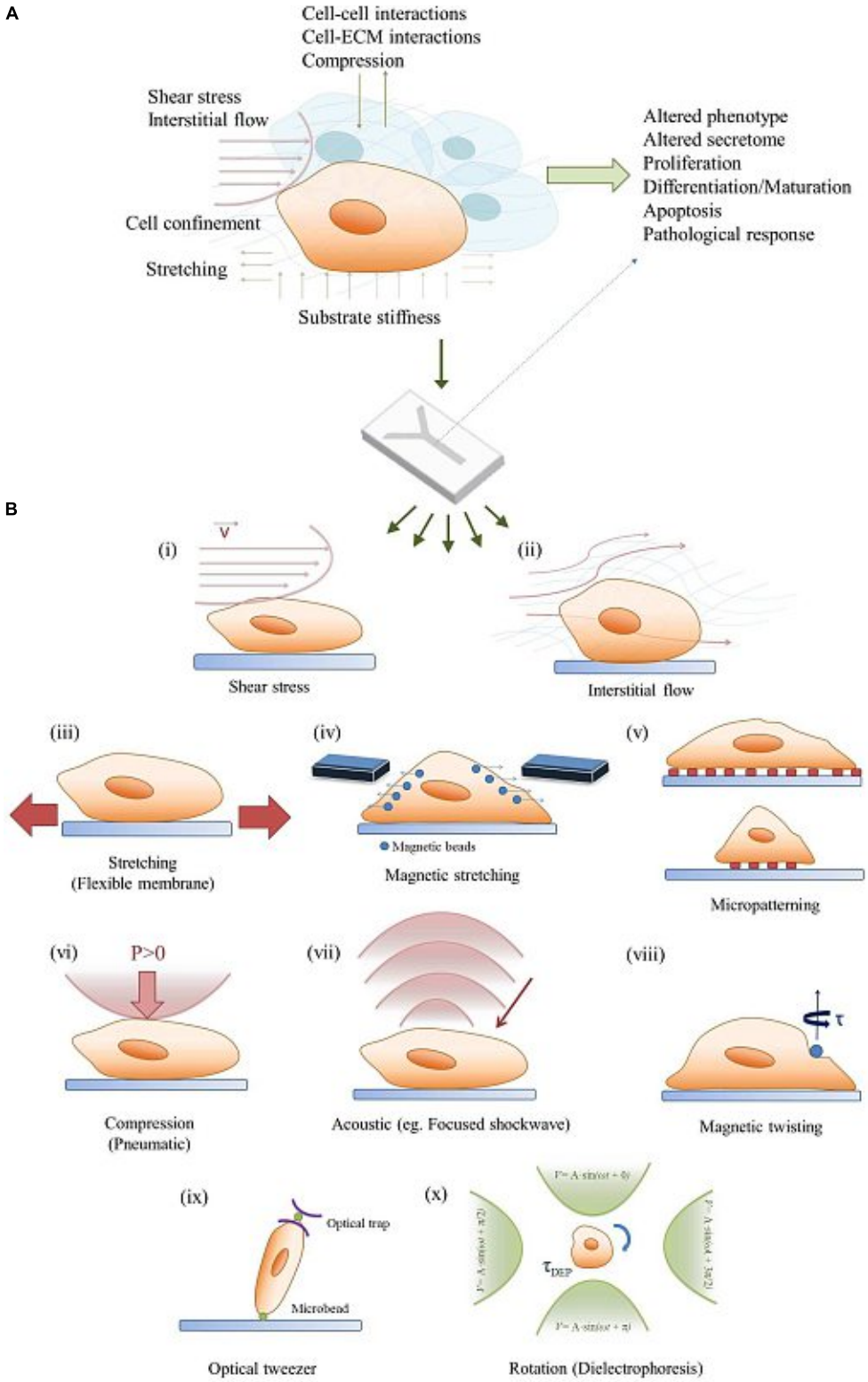

FIGURE 1 | Bridging the *in vivo/in vitro* gap in mechanobiology. **(A)** A combination of mechanobiological cues in the microenvironment can regulate cell signaling and phenotype as well as physiological and pathological tissue response. **(B)** A simplified demonstration of a mechanobiology-on-a-chip, and potential on-chip stimulation strategies for microfluidic 2D/3D cell cultures: (i) Shear stress, (ii) Interstitial flow, (iii) Stretching, (iv) Magnetic stimulation, (v) Micropatterning, (vi) Compression, (vii) Acoustic stimulation, (viii) Magnetic twisting, (ix) Optical tweezers, and (x) Rotation (dielectrophoresis).

TABLE 1 | Summary on recent reports on mechanobiological approaches for cell manipulation in microfluidic devices.

Biomechanical stimulus	Organ culture	Cell type	Environment	Reference
Interstitial flow	Vasculature	Primary	3D	Hsu et al., 2013; Jeon et al., 2014; Kim S. et al., 2016
Interstitial flow	Brain	Primary	3D	Park et al., 2015; Wang et al., 2018
Interstitial flow	Liver	Primary	3D	Lee et al., 2013
Substrate stiffness	–	Cell line	2D	García et al., 2015
Electromechanical	–	Primary	2D	Pavesi et al., 2015
Shear stress	Vasculature	Primary	2D	Charwat et al., 2018
Shear stress	–	Cell line	2D	Soffe et al., 2017
Shear stress	Blood brain barrier	Cell line	2D	Griep et al., 2013
Shear stress	Aortic valve	Primary	2D	Wang et al., 2017
Shear stress	Blood brain barrier	Primary	2D/3D	Brown et al., 2015
Shear stress	Blood brain barrier	Cell line	2D/3D	Sellgren et al., 2015
Shear stress	Extravasation	Primary	3D	Jeon et al., 2015
Shear stress	Vasculature	Primary	3D	Kim et al., 2013
Shear stress	Bone	Cell line	2D	Middleton et al., 2017a,b
Shear stress	Bone	Primary	3D	Altmann et al., 2014
Shear stress	Vasculature	Primary	2D	Zheng et al., 2017
Shear stress	Vasculature	Primary	2D	Venugopal Menon et al., 2018
Shear stress	Vasculature	Primary	2D	Patibandla et al., 2014
Stretching	Lung	Primary and cell line	2D	Huh et al., 2010, 2012; Benam et al., 2016; Hassell et al., 2017; Jain et al., 2018
Stretching	Gut	Primary and cell line	2D	Kim H.J. et al., 2016; Villenave et al., 2017
Stretching	Heart	Primary	2D	Ugolini et al., 2016, 2017
Stretching	Muscle	Primary and cell line	2D	Michielin et al., 2015
Stretching	Vasculature	Primary	2D	Zhou and Niklason, 2012
Stretching	–	Primary	3D	Liu et al., 2016
Stretching	Heart	Primary	3D	Marsano et al., 2016; Occhetta et al., 2018
Stretching	–	Cell line	3D	Li et al., 2016
Stretching	–	–	2D/3D	Gizzi et al., 2017
Stretching	Artery	Primary	2D	van Engeland et al., 2018
Compression	Bone	Primary	2D	Park et al., 2012
Compression	Vasculature	Primary	2D	Sticker et al., 2017

The dashes (–) identify studies with devices without a defined target organ, tissue or cell culture.

and different co-culture models would certainly benefit from further research.

Stretching

In contrast to shear-dependent mechanobiological effects, microfluidic devices have recently come into focus for their ability to engineer miniaturized functional barrier units. Different from the aforementioned models where cells are grown in monolayer in microchannels, these systems aim to recreate the smallest possible unit of an organ by mimicking the barrier between two monolayers. An overview of such a microfluidic device including the respective cell actuation can be found in **Figure 1B**. The cells are cultivated back-to-back on cyclically stretched flexible membranes emulating organotypic movements. With the most famous example still being the Lung-on-a-Chip published by Huh et al. (2010), a number of similar systems have since been used to investigate a variety of different barrier models. For example, using the same microdevice containing a flexible membrane that is stretched by applying vacuum to two air channels on either side of the cultivation chamber, different pathological scenarios have been recapitulated, including pulmonary edema (Huh et al., 2012), small-airway inflammation (Benam et al., 2016), orthotopic lung cancer extravasation, growth and therapy (Hassell et al., 2017) and intravascular thrombosis assessment (Jain et al., 2018). A similar device has also been used to mimic bacterial overgrowth, inflammatory bowel disease (Kim H.J. et al., 2016) and virus infection (Villenave et al., 2017) in a gut-on-a-chip system and to study the effect of cyclic strain on proliferation and adaptive responses of cardiac fibroblasts (Ugolini et al., 2016, 2017) and to study endothelial cell and smooth muscle cell signaling under hemodynamic loading (van Engeland et al., 2018). A different design approach to exert stretch/strain forces in microfluidic cell cultures employ pressurized air to deflect a membrane on which cells are cultured. Cyclic mechanical actuation of a myoblast cell line and primary myoblasts using such a device is demonstrated in a muscular dystrophy model (Michielin et al., 2015) and to recreate the cyclic strain of blood vessels (Zhou and Niklason, 2012). While most examples in the literature focus on uniaxial stretching, a computationally informed, vacuum-actuated multi-axial microfluidic chip device has recently been developed that allows programmable actuation

along different directions (Gizzi et al., 2017), further advancing the opportunities for mechanobiological on-chip investigations from the broadly used uniaxial strain barrier model devices.

Compression and Other Novel Methods

A relatively new approach for mechanobiological stimulation in microfluidic devices is cellular compression. Even though this has been shown to stimulate the osteogenic differentiation of stem cells (Park et al., 2012) and used to investigate wound healing (Sticker et al., 2017), further studies need to be conducted to improve our understanding of compression-based biomechanical stimuli. Other methods to incorporate mechanobiological signals in microchips exploit the fact that microfluidics is ideally suited to create and monitor spatiotemporal gradients. For example, Soffe et al. (2017) showed that human embryonic kidney cells respond to shear stress gradients using trapezoid microchannel geometries, while García et al. (2015) investigated the effects of substrate stiffness gradients on cell behavior (Soffe et al., 2017). A sophisticated approach is reported by Pavesi et al. (2015): cells were subjected to multiple mechanical stimuli by adding the possibility of simultaneous electrical stimulation. The dual-stimulation strategy led to morphological and phenotypical cellular changes as well as altered cytoskeletal fiber orientation in mesenchymal stem cells. Nonetheless, while all the mentioned studies report an increase in physiological behavior of the cultured cells upon the exposure to mechanobiological cues, recreating of physiological microenvironment in a two-dimensional cultivation setup remains challenging.

MICROFLUIDIC MECHANOBIOLOGY IN THE THIRD DIMENSION

Even though the above described microfluidic 2D models seem suitable for recreating lining layers and barrier models, they still do not resemble physiological tissue architecture since most cells reside in a three-dimensional tissue matrix in their native environment. Hence, the third dimension remains an important issue that needs to be considered when aiming to re-engineer organ models *in vitro*. It is important to note that the physiological tissue microenvironment is composed of a variety of complex physical properties ranging from cell-cell interactions to the extracellular matrix composition and biomechanical stimuli such as dynamic stretching and compression. This biological complexity, to date, poses a significant challenge, since only a limited number of studies incorporating 3D mechanobiology on microfluidic chips have been reported.

Interstitial Flow

Additional to utilizing microfluidic devices in endothelial biology for investigating the effect of shear stress on monolayers, microchips are routinely used to determine the effects of interstitial flow on 3D vasculo- and angiogenesis. One approach involves the combination of vasculature with fluid flow where endothelial cells are co-cultured with supporting mural cells in hydrogels to generate blood vessels via vasculogenesis or angiogenesis. Hsu et al. (2013) developed a microfluidic device that is based on a resistive circuit concept to create an array of vascularized microtissue chambers. Interstitial fluid flow in the physiological range of 0.5 to 10 μm/s showed enhanced vessel-like structure formation corroborating similar studies from Jeon et al. (2014) for blood angiogenesis and from Kim S. et al. (2016) for lymphangiogenesis (Hsu et al., 2013). A more detailed review of recent advances in on-chip vascularization was recently published by Haase and Kamm (2017). However, microfluidics not only provides the perfect tool for exploring the importance of interstitial flow in endothelial cell biology but also for bone and brain organ-on-a-chip devices. In a recent study by Altmann et al. (2014), the morphogenesis of 3D cultured human primary alveolar bone osteoblasts under static and microfluidic growth conditions was compared. The cells were allowed to form aggregates in 300 μm cavities with fibronectin coating in poly (methyl methacrylate)-based chips and exposed to perfusion of 15, 30, and 60 μl/min flow rates. It was found that fluid flow lead to more distinct morphogenesis and more bone-specific gene expression and extracellular matrix formation after 7 days of culture. Additionally, Park et al. (2015) reported the design of a microfluidic chip-based 3D neurospheroid culture consisting in concave microwell arrays in which interstitial flow was generated by an osmotic micropump system. The results of the study showed that when neurospheroids are cultured under flow conditions, larger and more complex neural networks were formed compared to static culture. In a more recent 3D brain model, human induced pluripotent stem cell derived organoids were integrated into a microdevice using three-dimensional Matrigel. The on-chip cultured organoids showed improved neural differentiation and cortical organization under perfusion culture as well as enhanced expression of cortical layer markers, thus demonstrating the importance of 3D culture and mechanical fluid flow in enhancing brain organogenesis (Wang et al., 2018). Furthermore, Brown et al. (2015) created a complex physiologically relevant blood-brain-barrier model based on a back-to-back culture of endothelial cells that mimic blood vasculature with a co-culture of astrocytes, pericytes and hydrogel-embedded neurons that showed improved tight-junction formation under fluid flow conditions. These examples show that interstitial flow plays a crucial role for recreating physiological microenvironments and call for further research including a variety of other organ models.

Stretching and Compression in 3D

Other than the sophisticated stretch/strain devices for monolayer barrier models, compression and stretching of 3D microfluidic organ models is still in its infancy. One of the first applications involve a 3D cell construct that is exposed to cyclic mechanical strain to develop a beating heart-on-a-chip (Marsano et al., 2016). In this study, human induced pluripotent stem cell-derived cardiomyocytes were embedded in a fibrin gel prior to injection into the microdevices, and subsequently exposed to mechanical stimulation using a deformable PDMS (Polydimethylsiloxane) membrane (10% uniaxial strain, 1 Hz frequency). Interestingly, the mechanically stimulated constructs showed similar gene

expression levels of cardiac markers when compared to non-actuated controls. However, the mechanical stimulus resulted in decreased expression of MYH6 (a marker for less developed phenotype), thus indicating superior cardiac maturity compared to static conditions. Furthermore, elongated cardiac-like morphology was observed in the mechanically stimulated constructs. Recently, the same group employed a similar concept to propose a model of cardiac fibrosis by applying cyclic mechanical stretch to cardiac fibroblasts embedded in a 3D fibrin hydrogel. By exploiting this strategy, the authors claim to be able to mimic some of the key steps of cardiac fibrosis onset in a timely fashion: early fibroblast proliferation, their phenotype switch into myofibroblasts, extracellular matrix deposition and its final stiffening (Occhetta et al., 2018). An alternative microfluidic device containing deformable membranes was developed to investigate differentiation associated matrix production using a real-time stiffness sensor. The authors showed that mesenchymal stromal cells embedded in hydrogels and subjected to dynamic mechanical stimulation undergo myofibroblast differentiation and synthesize collagen, leading to gel stiffening (Liu et al., 2016). In another study, 3D responses of cells were quantified in the presence of extreme strain within 3D hydrogel matrices. Here, micro-magnetically actuated synthetic tissue cultures were developed and consisted of a polyethylene glycol dimethacrylate hydrogel layer containing iron microspheres, and a stiffness tunable gelatin methacryloyl hydrogel containing a population of fibroblasts. Using this magnetic field focusing device, strain-dependent proliferation, spreading, polarization, differentiation, and matrix adhesion was studied (Li et al., 2016). Although the system can be used to readily adjust mechanical strain within 3D hydrogel cell cultures, some limitations remain concerning extracellular matrix porosity and non-fibrous matrices not being representative of the cell environment in a real tissue. **Table 1** lists currently available technologies according to applied stimuli, organ culture and cell type using microfluidic 2D as well as 3D cell culture systems.

CONCLUDING REMARKS AND FURTHER PERSPECTIVES

The combination of microfabrication-based technologies with complex biology has enabled the development of advanced *in vitro* models capable of culturing and analyzing cell and tissue constructs under physiologically relevant conditions (Ertl, 2015; Rothbauer et al., 2015, 2017). While microfluidic models for 2D mechanical stimulation involving stretch and strain has been widely investigated, the application of physiologically relevant axial strain in 3D cell culture systems is still in its infancy. To date only few microdevices have been developed that are capable of recreating mechanobiological relevant three-dimensional cellular microenvironments. Current mechanobiology-on-a-chip advances are hindered by both technological shortcomings and the limited reliability of current *in vitro* 3D cell culture systems. One possible solution to improve fabrication speed, precision, material selection, and (bio)compatibility could be stereolithography, which already enables (a) additive manufacturing of microchannels down to 300 μm and (b) the integration of pneumatic valves for automated cell handling and manipulation of complex biological structures on chip. Next generation microfluidic devices will need to contain computer-controlled valves and micropumps for fluid-mechanical stimulation of cells (Rogers et al., 2015; Chen et al., 2016) and integrated actuators to reliably regulate and modify mechanical forces on tissue constructs. Furthermore, future microfluidic devices will need to address current limitations in microdevice operation to minimize the need for bulky off-chip equipment such as pumps, heaters, microscope, gas-supply, and connectors. While the incorporation of micropumps and -valves or alternative approaches for on-chip fluid handling have already been demonstrated in state-of-the-art devices (Sung et al., 2010; Kim et al., 2012; Hasenberg et al., 2015), integrated sensing solutions that replace off-chip detection methods are still scarce. The integration of micro- and nanosensors will ultimately enable the investigation of dynamic cellular responses to any imaginable physical, chemical and biological stimuli, thus providing detailed information on tissue behavior down to the molecular level. In conclusion, given the complexity of *in vivo* biological architectures of tissues and organs, next generation mechanobiology-on-a-chip systems will need to significantly increase the similarity of *in vitro* 3D biologically inspired constructs using highly integrated, fully automated and miniaturized cell analysis systems.

AUTHOR CONTRIBUTIONS

EE and BB conceived the general structure of the review, revised the existing literature, and drafted the manuscript. HR, GF, and PE revised the text and contributed to the final manuscript.

FUNDING

This work was funded by the European Union's INTERREG V-A AT-CZ program (ATCZ133), the European Social Fund and European Regional Development Fund–Project MAGNET (No. CZ.02.1.01/0.0/0.0/15_003/0000492).

REFERENCES

Ahearne, M. (2014). Introduction to cell-hydrogel mechanosensing. *Interface Focus* 4:20130038. doi: 10.1098/rsfs.2013.0038

Altmann, B., Löchner, A., Swain, M., Kohal, R. J., Giselbrecht, S., Gottwald, E., et al. (2014). Differences in morphogenesis of 3D cultured primary human osteoblasts under static and microfluidic growth conditions. *Biomaterials* 35, 3208–3219. doi: 10.1016/j.biomaterials.2013.12.088

Baker, B. M., and Chen, C. S. (2012). Deconstructing the third dimension – how 3D culture microenvironments alter cellular cues. *J. Cell Sci.* 125, 3015–3024. doi: 10.1242/jcs.079509

Baratchi, S., Khoshmanesh, K., Woodman, O. L., Potocnik, S., Peter, K., and McIntyre, P. (2017). Molecular sensors of blood flow in endothelial cells. *Trends Mol. Med.* 23, 850–868. doi: 10.1016/j.molmed.2017.07.007

Benam, K. H., Villenave, R., Lucchesi, C., Varone, A., Hubeau, C., Lee, H.-H., et al. (2016). SL Small airway-on-a-chip enables analysis of human lung inflammation and drug responses *in vitro*. *Nat. Methods* 13, 151–157. doi: 10.1038/nmeth.3697

Bhatia, S. N., and Ingber, D. E. (2014). Microfluidic organs-on-chips. *Nat. Biotechnol.* 32, 760–772. doi: 10.1038/nbt.2989

Brown, J. A., Pensabene, V., Markov, D. A., Allwardt, V., Diana Neely, M., Shi, M., et al. (2015). Recreating blood-brain barrier physiology and structure on chip: a novel neurovascular microfluidic bioreactor. *Biomicrofluidics* 9:054124. doi: 10.1063/1.4934713

Charwat, V., Olmos Calvo, I., Rothbauer, M., Kratz, S. R. A., Jungreuthmayer, C., Zanghellini, J., et al. (2018). Combinatorial in Vitro and in silico approach to describe shear-force dependent uptake of nanoparticles in microfluidic vascular models. *Anal. Chem.* 90, 3651–3655. doi: 10.1021/acs.analchem.7b04788

Chen, C., Mehl, B. T., Munshi, A. S., Townsend, A. D., Spence, D. M., and Martin, R. S. (2016). 3D-printed microfluidic devices: fabrication, advantages and limitations—a mini review. *Anal. Methods* 8, 6005–6012. doi: 10.1039/C6AY01671E

Chen, G., Ushida, T., and Tateishi, T. (2002). Scaffold design for tissue engineering. *Macromol. Biosci.* 2, 67–77.

Drury, J. L., and Mooney, D. J. (2003). Hydrogels for tissue engineering: scaffold design variables and applications. *Biomaterials* 24, 4337–4351. doi: 10.1016/S0142-9612(03)00340-5

Engler, A. J., Sen, S., Sweeney, H. L., and Discher, D. E. (2006). Matrix elasticity directs stem cell lineage specification. *Cell* 126, 677–689. doi: 10.1016/j.cell.2006.06.044

Ertl, P. (2015). Recent advances of biologically inspired 3D microfluidic hydrogel cell culture systems. *Cell Biol. Cell Metab.* 2:005. doi: 10.24966/CBCM-1943/100005

Eyckmans, J., Boudou, T., Yu, X., and Chen, C. S. (2011). A hitchhiker's guide to mechanobiology. *Dev. Cell* 21, 35–47. doi: 10.1016/j.devcel.2011.06.015

Fennema, E., Rivron, N., Rouwkema, J., van Blitterswijk, C., and de Boer, J. (2013). Spheroid culture as a tool for creating 3D complex tissues. *Trends Biotechnol.* 31, 108–115. doi: 10.1016/j.tibtech.2012.12.003

García, S., Sunyer, R., Olivares, A., Noailly, J., Atencia, J., and Trepat, X. (2015). Generation of stable orthogonal gradients of chemical concentration and substrate stiffness in a microfluidic device. *Lab Chip* 15:12. doi: 10.1039/C5LC00140D

Gizzi, A., Giannitelli, S. M., Trombetta, M., Cherubini, C., Filippi, S., De Ninno, A., et al. (2017). Computationally informed design of a multi-axial actuated microfluidic chip device. *Sci. Rep.* 7:5489. doi: 10.1038/s41598-017-05237-9

Griep, L. M., Wolbers, F., De Wagenaar, B., Ter Braak, P. M., Weksler, B. B., Romero, I. A., et al. (2013). BBB on CHIP: microfluidic platform to mechanically and biochemically modulate blood-brain barrier function. *Biomed. Microdev.* 15, 145–150. doi: 10.1007/s10544-012-9699-7

Griffith, L. G., and Swartz, M. A. (2006). Capturing complex 3D tissue physiology in vitro. *Nat. Rev. Mol. Cell Biol.* 7, 211–224. doi: 10.1038/nrm1858

Haase, K., and Kamm, R. D. (2017). Advances in on-chip vascularization. *Regen. Med.* 12, 285–302. doi: 10.2217/rme-2016-0152

Hasenberg, T., Mühleder, S., Dotzler, A., Bauer, S., Labuda, K., Holnthoner, W., et al. (2015). Emulating human microcapillaries in a multi-organ-chip platform. *J. Biotechnol.* 216, 1–10. doi: 10.1016/j.jbiotec.2015.09.038

Hassell, B. A., Goyal, G., Lee, E., Sontheimer-Phelps, A., Levy, O., Chen, C. S., et al. (2017). Human organ chip models recapitulate orthotopic lung cancer growth, therapeutic responses, and tumor dormancy in Vitro. *Cell Rep.* 21, 508–516. doi: 10.1016/j.celrep.2017.09.043

Hsu, Y.-H., Moya, M. L., Hughes, C. C. W., George, S. C., and Lee, A. P. (2013). A microfluidic platform for generating large-scale nearly identical human microphysiological vascularized tissue arrays. *Lab Chip* 13, 2990–2998. doi: 10.1039/c3lc50424g

Huh, D., Hamilton, G. A., and Ingber, D. E. (2011). From 3D cell culture to organs-on-chips. *Trends Cell Biol.* 21, 745–754. doi: 10.1016/j.tcb.2011.09.005

Huh, D., Leslie, D. C., Matthews, B. D., Fraser, J. P., Jurek, S., Hamilton, G. A., et al. (2012). A human disease model of drug toxicity-induced pulmonary edema in a lung-on-a-chip microdevice. *Sci. Transl. Med.* 4:159ra147. doi: 10.1126/scitranslmed.3004249

Huh, D., Matthews, B. D., Mammoto, A., Montoya-Zavala, M., Hsin, H. Y., and Ingber, D. E. (2010). Reconstituting organ-level lung functions on a chip. *Science* 328, 1662–1668. doi: 10.1126/science.1188302

Jain, A., Barrile, R., van der Meer, A. D., Mammoto, A., Mammoto, T., De Ceunynck, K., et al. (2018). Primary human lung alveolus-on-a-chip model of intravascular thrombosis for assessment of therapeutics. *Clin. Pharmacol. Ther.* 103, 332–340. doi: 10.1002/cpt.742

Jansen, K. A., Donato, D. M., Balcioglu, H. E., Schmidt, T., Danen, E. H. J., and Koenderink, G. H. (2015). A guide to mechanobiology: where biology and physics meet. *Biochim. Biophys. Acta Mol. Cell Res.* 1853, 3043–3052. doi: 10.1016/j.bbamcr.2015.05.007

Jeon, J. S., Bersini, S., Gilardi, M., Dubini, G., Charest, J. L., Moretti, M., et al. (2015). Human 3D vascularized organotypic microfluidic assays to study breast cancer cell extravasation. *Proc. Natl. Acad. Sci. U.S.A.* 112, 214–219. doi: 10.1073/pnas.1417115112

Jeon, J. S., Bersini, S., Whisler, J. A., Chen, M. B., Dubini, G., Charest, J. L., et al. (2014). Generation of 3D functional microvascular networks with mural cell-differentiated human mesenchymal stem cells in microfluidic vasculogenesis systems. *Integr. Biol.* 6, 555–563. doi: 10.1039/c3ib40267c

Kim, H. J., Li, H., Collins, J. J., and Ingber, D. E. (2016). Contributions of microbiome and mechanical deformation to intestinal bacterial overgrowth and inflammation in a human gut-on-a-chip. *Proc. Natl. Acad. Sci. U.S.A.* 113, E7–E15. doi: 10.1073/pnas.1522193112

Kim, S., Chung, M., and Jeon, N. L. (2016). Three-dimensional biomimetic model to reconstitute sprouting lymphangiogenesis in vitro. *Biomaterials* 78, 115–128. doi: 10.1016/j.biomaterials.2015.11.019

Kim, J., Kang, M., Jensen, E. C., and Mathies, R. A. (2012). Lifting gate polydimethylsiloxane microvalves and pumps for microfluidic control. *Anal. Chem.* 84, 2067–2071. doi: 10.1021/ac202934x

Kim, S., Kim, W., Lim, S., and Jeon, J. (2017). Vasculature-On-A-Chip for In vitro disease models. *Bioengineering* 4:E8. doi: 10.3390/bioengineering4010008

Kim, S., Lee, H., Chung, M., and Jeon, N. L. (2013). Engineering of functional, perfusable 3D microvascular networks on a chip. *Lab Chip* 13:1489. doi: 10.1039/c3lc41320a

Kumar, S. (2014). Cellular mechanotransduction: stiffness does matter. *Nat. Mater.* 13, 918–920. doi: 10.1038/nmat4094

Lee, S.-A., No, D. Y., Kang, E., Ju, J., Kim, D.-S., and Lee, S.-H. (2013). Spheroid-based three-dimensional liver-on-a-chip to investigate hepatocyte–hepatic stellate cell interactions and flow effects. *Lab Chip* 13:3529. doi: 10.1039/c3lc50197c

Li, Y., Huang, G., Li, M., Wang, L., Elson, E. L., Jian Lu, T., et al. (2016). An approach to quantifying 3D responses of cells to extreme strain. *Sci. Rep.* 6:19550. doi: 10.1038/srep19550

Liu, H., Simmons, C. A., and Sun, Y. (2016). A microfabricated platform with on-chip strain sensing and hydrogel arrays for 3D mechanical stimulation of cells. *Proc. IEEE Int. Conf. Micro Electro Mech. Syst.* 4, 267–270. doi: 10.1109/MEMSYS.2016.7421611

Lovett, M., Lee, K., Edwards, A., and Kaplan, D. L. (2009). Vascularization strategies for tissue engineering. *Tissue Eng. Part B Rev.* 15, 353–370. doi: 10.1089/ten.teb.2009.0085

Marsano, A., Conficconi, C., Lemme, M., Occhetta, P., Gaudiello, E., Votta, E., et al. (2016). Beating heart on a chip: a novel microfluidic platform to generate functional 3D cardiac microtissues. *Lab Chip* 16, 599–610. doi: 10.1039/C5LC01356A

Michielin, F., Serena, E., Pavan, P., and Elvassore, N. (2015). Microfluidic-assisted cyclic mechanical stimulation affects cellular membrane integrity in a human muscular dystrophy in vitro model. *RSC Adv.* 5, 98429–98439. doi: 10.1039/C5RA16957G

Middleton, K., Al-Dujaili, S., Mei, X., Günther, A., and You, L. (2017a). Microfluidic co-culture platform for investigating osteocyte-osteoclast signalling during fluid shear stress mechanostimulation. *J. Biomech.* 59, 35–42. doi: 10.1016/j.jbiomech.2017.05.012

Middleton, K., Kondiboyina, A., Borrett, M., Cui, Y., Mei, X., and You, L. (2017b). Microfluidics approach to investigate the role of dynamic similitude in osteocyte mechanobiology. *J. Orthop. Res.* 36, 663–671. doi: 10.1002/jor.23773

Occhetta, P., Isu, G., Lemme, M., Conficconi, C., Oertle, P., Räz, C., et al. (2018). A three-dimensional in vitro dynamic micro-tissue model of cardiac scar formation. *Integr. Biol.* 10, 174–183. doi: 10.1039/C7IB00199A

Park, J., Lee, B. K., Jeong, G. S., Hyun, J. K., Lee, C. J., and Lee, S.-H. (2015). Three-dimensional brain-on-a-chip with an interstitial level of flow and its application as an in vitro model of Alzheimer's disease. *Lab Chip* 15, 141–150. doi: 10.1039/C4LC00962B

Park, S.-H., Sim, W. Y., Min, B.-H., Yang, S. S., Khademhosseini, A., and Kaplan, D. L. (2012). Chip-based comparison of the osteogenesis of human bone marrow- and adipose tissue-derived mesenchymal stem cells under mechanical stimulation. *PLoS One* 7:e46689. doi: 10.1371/journal.pone.0046689

Patibandla, P. K., Rogers, A. J., Giridharan, G. A., Pallero, M. A., Murphy-Ullrich, J. E., and Sethu, P. (2014). Hyperglycemic arterial disturbed flow niche as an in vitro model of atherosclerosis. *Anal. Chem.* 86, 10948–10954. doi: 10.1021/ac503294p

Pavesi, A., Adriani, G., Rasponi, M., Zervantonakis, I. K., Fiore, G. B., and Kamm, R. D. (2015). Controlled electromechanical cell stimulation on-a-chip. *Sci. Rep.* 5:11800. doi: 10.1038/srep11800

Riehl, B. D., Park, J.-H., Kwon, I. K., and Lim, J. Y. (2012). Mechanical stretching for tissue engineering: two-dimensional and three-dimensional constructs. *Tissue Eng. Part B Rev.* 18, 288–300. doi: 10.1089/ten.teb.2011.0465

Rogers, C. I., Qaderi, K., Woolley, A. T., and Nordin, G. P. (2015). 3D printed microfluidic devices with integrated valves. *Biomicrofluidics* 9:16501. doi: 10.1063/1.4905840

Rothbauer, M., Wartmann, D., Charwat, V., and Ertl, P. (2015). Recent advances and future applications of microfluidic live-cell microarrays. *Biotechnol. Adv.* 33(Pt 1), 948–961. doi: 10.1016/j.biotechadv.2015.06.006

Rothbauer, M., Zirath, H., and Ertl, P. (2017). Recent advances in microfluidic technologies for cell-to-cell interaction studies. *Lab Chip* 10:1. doi: 10.1039/C7LC00815E

Sellgren, K. L., Hawkins, B. T., and Grego, S. (2015). An optically transparent membrane supports shear stress studies in a three- dimensional microfluidic neurovascular unit model An optically transparent membrane supports shear stress studies in a three-dimensional microfluidic neurovascular unit model. *Biomicrofluidics* 9:061102. doi: 10.1063/1.4935594

Shachar, M., Benishti, N., and Cohen, S. (2012). Effects of mechanical stimulation induced by compression and medium perfusion on cardiac tissue engineering. *Biotechnol. Prog.* 28, 1551–1559. doi: 10.1002/btpr.1633

Smith, Q., and Gerecht, S. (2014). Going with the flow: microfluidic platforms in vascular tissue engineering. *Curr. Opin. Chem. Eng.* 3, 42–50. doi: 10.1016/j.coche.2013.11.001

Soffe, R., Baratchi, S., Nasabi, M., Tang, S. Y., Boes, A., McIntyre, P., et al. (2017). Lateral trapezoid microfluidic platform for investigating mechanotransduction of cells to spatial shear stress gradients. *Sensors Actuat. B Chem.* 251, 963–975. doi: 10.1016/j.snb.2017.05.145

Sticker, D., Lechner, S., Jungreuthmayer, C., Zanghellini, J., and Ertl, P. (2017). Microfluidic migration and wound healing assay based on mechanically induced injuries of defined and highly reproducible areas. *Anal. Chem.* 89, 2326–2333. doi: 10.1021/acs.analchem.6b03886

Sung, J. H., Kam, C., and Shuler, M. L. (2010). A microfluidic device for a pharmacokinetic-pharmacodynamic (PK-PD) model on a chip. *Lab Chip* 10, 446–455. doi: 10.1039/B917763A

Ugolini, G. S., Pavesi, A., Rasponi, M., Fiore, G. B., Kamm, R., and Soncini, M. (2017). Human cardiac fibroblasts adaptive responses to controlled combined mechanical strain and oxygen changes in vitro. *eLife* 6:e22847. doi: 10.7554/eLife.22847

Ugolini, G. S., Rasponi, M., Pavesi, A., Santoro, R., Kamm, R., Fiore, G. B., et al. (2016). On-chip assessment of human primary cardiac fibroblasts proliferative responses to uniaxial cyclic mechanical strain. *Biotechnol. Bioeng.* 113, 859–869. doi: 10.1002/bit.25847

van Duinen, V., Trietsch, S. J., Joore, J., Vulto, P., and Hankemeier, T. (2015). Microfluidic 3D cell culture: from tools to tissue models. *Curr. Opin. Biotechnol.* 35, 118–126. doi: 10.1016/j.copbio.2015.05.002

van Engeland, N. C. A., Pollet, A. M. A. O., den Toonder, J. M. J., Bouten, C. V. C., Stassen, O. M. J. A., and Sahlgren, C. M. (2018). A biomimetic microfluidic model to study signalling between endothelial and vascular smooth muscle cells under hemodynamic conditions. *Lab Chip* 18, 1607–1620. doi: 10.1039/c8lc00286j

Venugopal Menon, N., Tay, H. M., Pang, K. T., Dalan, R., Wong, S. C., Wang, X., et al. (2018). A tunable microfluidic 3D stenosis model to study leukocyte-endothelial interactions in atherosclerosis. *APL Bioeng.* 2:16103. doi: 10.1063/1.4993762

Villenave, R., Wales, S. Q., Hamkins-Indik, T., Papafragkou, E., Weaver, J. C., Ferrante, T. C., et al. (2017). Human gut-on-a-chip supports polarized infection of coxsackie B1 virus in vitro. *PLoS One* 12:e0169412. doi: 10.1371/journal.pone.0169412

Wang, J. H.-C., and Thampatty, B. P. (2006). An introductory review of cell mechanobiology. *Biomech. Model. Mechanobiol.* 5, 1–16. doi: 10.1007/s10237-005-0012-z

Wang, X., Lee, J., Ali, M., Kim, J., and Lacerda, C. M. R. (2017). Phenotype transformation of aortic valve interstitial cells due to applied shear stresses within a microfluidic chip. *Ann. Biomed. Eng.* 45, 2269–2280. doi: 10.1007/s10439-017-1871-z

Wang, Y., Wang, L., Guo, Y., Zhu, Y., and Qin, J. (2018). Engineering stem cell-derived 3D brain organoids in a perfusable organ-on-a-chip system. *RSC Adv.* 8, 1677–1685. doi: 10.1039/C7RA11714K

Zheng, C., Zhang, X., Li, C., Pang, Y., and Huang, Y. (2017). Microfluidic device for studying controllable hydrodynamic flow induced cellular responses. *Anal. Chem.* 89, 3710–3715. doi: 10.1021/acs.analchem.7b00013

Zhou, J., and Niklason, L. E. (2012). Microfluidic artificial "vessels" for dynamic mechanical stimulation of mesenchymal stem cells. *Integr. Biol.* 4, 1487–1497. doi: 10.1039/c2ib00171c

Conflict of Interest Statement: The authors declare that the research was conducted in the absence of any commercial or financial relationships that could be construed as a potential conflict of interest.

MANUSCRIPT #3

MICROVASCULATURE-ON-A-CHIP: BRIDGING THE INTERSTITIAL BLOOD-LYMPH INTERFACE VIA MECHANOBIOLOGICAL STIMULI

Barbara Bachmann, Sarah Spitz, Christian Jordan, Patrick Schuller, Heinz Wanzenböck, Bahram Haddadi, Michael Harasek, Heinz Redl, Wolfgang Holnthoner, and Peter Ertl

Microvasculature-on-a-Chip: Bridging the interstitial blood-lymph interface via mechanobiological stimuli

Barbara Bachmann[1,2,3,4], Sarah Spitz[1,4], Christian Jordan[5], Patrick Schuller[6], Heinz Wanzenböck[6], Bahram Haddadi[5], Michael Harasek[5], Heinz Redl[2,3,4], Wolfgang Holnthoner[2,3,4] and Peter Ertl[* 1,3,4]

[1] Faculty of Technical Chemistry, Institute of Applied Synthetic Chemistry and Institute of Chemical Technologies & Analytics, Vienna University of Technology, 1060 Vienna, Austria

[2] AUVA Research Centre, Ludwig Boltzmann Institute for Experimental and Clinical Traumatology, 1200 Vienna, Austria

[3] Competence Center MechanoBiology, 1200 Vienna, Austria

[4] Austrian Cluster for Tissue Regeneration, 1200 Vienna, Austria

[5] Institute of Chemical, Environmental and Bioscience Engineering - Fluid Dynamics Simulation, University of Technology, Getreidemarkt 9/166-2, 1060 Vienna, Austria

[6] Institute of Solid State Electronics, Vienna University of Technology, Vienna, 1040, Austria

***Correspondence:**

Peter Ertl - peter.ertl@tuwien.ac.at

Keywords: Vascularization, Sprouting, Lymphatic System, Organ-on-a-Chip, Mechanobiology

ABSTRACT

After decades of simply being referred to as the body's sewage system, the lymphatic system has recently been recognized as a key player in numerous physiological and pathological processes. As an essential site of immune cell interactions, the lymphatic system is a potential target for next-generation drug delivery approaches in treatments for cancer, infections, and inflammatory diseases. However, the lack of cell-based assays capable of recapitulating the required biological complexity and unreliable *in vivo* animal models currently hamper scientific progress in lymph-targeted drug delivery. To gain more in-depth insight into the blood-lymph interface, we established an advanced chip-based microvascular model to study mechanical stimulation's importance on lymphatic sprout formation. Our microvascular model's key feature is the co-cultivation of spatially separated 3D blood and lymphatic vessels under controlled, unidirectional interstitial fluid flow while allowing signaling molecule exchange similar to the *in vivo* situation. We demonstrate that our microphysiological model recreates biomimetic interstitial fluid flow similar to the route of fluid *in vivo*, where shear stress within blood vessels expels fluid into the interstitial space, which is subsequently transported to the nearby lymphatic capillaries. Results of our cell culture optimization study clearly point at an increased vessel sprouting number, length, and morphological characteristics under dynamic cultivation conditions and physiological relevant mechanobiological stimulation. For the first time, a microvascular on-chip system incorporating microcapillaries of both blood and lymphatic origin *in vitro* recapitulates the interstitial blood-lymph interface.

INTRODUCTION

The lymphatic system absorbs, transports, and recirculates excess interstitial fluid via initial lymphatic capillaries, collecting lymphatic vessels, lymph nodes, and the thoracic duct. Even though this process is essential for physiologic fluid homeostasis, the historical view of the lymphatic system as a simple fluid conduit has needed reconsideration in the last decade following discoveries of its vital function in immune surveillance,[1] inflammation,[2] and cancer metastasis.[3] Aside from its role as a significant component of the immune system, playing a crucial part in autoimmune disease and infection,[4,5] the lymphatic system is the preferential site for cancer metastasis,[6] facilitated by decreased fluid stress and lymph nodes as holding reservoirs.[7] With the growing understanding of lymphatic physiology and disease, the interest in targeting the lymphatic system for drug delivery for potency enhancement of anti-inflammatory drugs, vaccines, or chemotherapeutics has risen accordingly. During physiological fluid homeostasis, interstitial fluid flow pushes excess fluid and molecules towards lymphatic capillaries. Within the initial lymphatics, lymph formation and molecule uptake occur via passive transport through endothelial cell junctions. The fate of molecules within interstitial tissue predominantly depends on their size. Small molecules preferentially reenter into blood capillaries, while lymphatic capillaries drain larger molecules such as proteins, pathogens, or immune cells.[8] Current methods in lymphatics research to study these transport phenomena, however, rely heavily on animal models.[9] While valuable to determine the influence of specific genes on lymphatic function *in vivo*, these models often lack the spatiotemporal resolution to track single-cell and molecule movement under controlled and reproducible measurement conditions.

Traditional *in vitro* models of vascular biology, in contrast, often involve endothelial monolayers, Transwell cultures, or pseudo-capillary structures on hydrogels and simplify biology to a point where effective translation to *in vivo* phenomena becomes questionable. Alternatively, organ-on-a-chip technology provides the opportunity to engineer microphysiological systems within an *in vivo*-like microenvironment optimally tailored to the individual research question, overcoming traditional in vitro models' limitations.[10–12] In particular, microfluidic vascular cell culture systems demonstrate successful vascularization to form interconnected, perfusable three-dimensional vascular networks between two medium

channels.[13] To provide a brief overview, Table 1 lists recent publications on 3D microvascular systems and highlights how microfluidic approaches are preferentially used to study the vascular microenvironment.

Table 1: Recent reports and applications of microfluidics for 3d-vascular biology

VASCULATURE TYPE	CULTIVATION SETUP	MICROFLUIDIC	APPLICATION	REF
BLOOD	Vascular network	Yes	Vasculogenesis and growth factor gradients	14
BLOOD	Sprouting	Yes	IF magnitude and direction	15
BLOOD	Vascular network	Yes	Endothelial paracellular and transcellular permeability	16
BLOOD	Vascular network	Yes	Measurement of trans-capillary solute flux	17
LYMPH	Sprouting	Yes	Influence of IF on sprouting lymphangiogenesis	18
LYMPH	LEC in hydrogel	Yes	Contribution of lymphatic endothelium on colorectal cancer cell growth	19
BLOOD/LYMPH	Single Vessel	Yes	Anti-angiogenic drug screening	20
BLOOD/LYMPH	Vascular network	No	Integration of blood and lymph capillaries in tissue-engineered constructs	21
BLOOD/LYMPH	2D separated by a membrane	Yes	Blood- and lymphatic-vessel permeability Assay	22

Among these, self-assembled and autologously formed vascular networks in hydrogel-laden microfluidic channels have proven ideal for studying fundamental biological processes, diseases, and exposure to drugs or toxic compounds.[16,23,24] The success of vasculature-on-chip systems is inherently linked to the unique capability to adjust physiological flow conditions,[15] shear forces,[25] nutrient gradients,[14] and biomechanical cues.[11,26] Additionally, the inherent design flexibility of microfluidics technology has led to the generation of a variety of customized cultivation chamber geometries capable of precisely controlling cell-cell, cell-matrix, and cell-molecule interactions.[11,12,27]

Vessel formation *in vivo* occurs either via vascularization from single cells or via sprouting angiogenesis from preexisting vasculature. Sprouting angiogenesis relies on cues from the surrounding tissue signaling nutrient demand or excess fluid accumulation. In other words, endothelial cells can sense mechanobiological stimuli arising from fluid flow irregularities in the interstitial tissue and respond by forming new vessels to regain fluid homeostasis.

Similarly, both blood[15] and lymphatic[18] endothelial cells *in vitro* respond sensitively to flow magnitude and direction dependent on their physiologic function. Despite recent advances in mimicking cardiovasculature, models of the lymphatic system remain scarce. To date, only one study demonstrates the cultivation of three-dimensional (3D) blood and lymphatic vessels on a microfluidic platform,[20] even though such systems could investigate immune cell chemotaxis or lymphedema progression.[28] As an example, mechanobiological stimulation via directional interstitial fluid flow increases tumor cell entry into lymphatic capillaries and stimulates lymphatic sprouting.[29,18] Emulating the mechanobiological environment regarding matrix elasticity,[30] fluid flow,[31] or nutrient gradients[32–34] is crucial for developing reliable and accurate *in vitro* systems. We have previously shown that mechanobiological control over shear stress and growth factor gradients allows manipulation of vascular network formation and nanoparticle uptake by endothelial cells.[14,31]. The lessons learned from mimicking the cardiovascular endothelium in microphysiological systems provide an excellent opportunity to establish, for the first time, an interstitial blood-lymph interface featuring 3D microcapillaries of both blood and lymphatic origin.[35] Building on our previous knowledge, we now developed a microfluidic system containing two adjacent and locally separated hydrogel-embedded microvascular systems to study the impact of interstitial fluid flow regimes and mechanobiological stimulation on lymphatic vessel formation. A hydrostatic pressure-driven fluid flow inside the microvasculature-on-chip system accomplishes mechanobiological stimulation resulting in a unidirectional, interstitial-like fluid flow. Within our optimized blood-lymph interface, primary microvascular blood and lymphatic endothelial cells are co-cultured in the presence of adipose-derived stem cells under static and dynamic conditions. Consequently, our study sets out to investigate the impact of directional interstitial fluid flow regimes on vascularization and sprouting angiogenesis, which leads to the formation of a microvascular blood-lymph interface.

MATERIALS AND METHODS

Microfabrication

Microfluidic devices were manufactured using soft-lithography techniques to generate hybrid poly-dimethylsiloxane (PDMS) / glass microdevices. Photolithographic molds were produced using Ordyl SY 300 dry-film photoresist (Elga Europe) on silicon wafers to generate 100 µm high replicas of the microdevice design. Microfluidic structures were attained by liquid PDMS (Sylgard® 184, Dow Corning) casting and subsequent polymerization at 80°C for 90 minutes. After generating hydrogel inlet ports and medium reservoirs using biopsy punches, microfluidic chambers were bonded to clean glass slides using oxygen plasma. Three microfluidic chambers are featured on one object slide-sized microchip for facilitated replica cultivation as visible in a microfluidic device rendered in Figure 1A. These vascularization chambers feature two individually loadable hydrogel chambers separated by an array of pillar structures 100 µm in diameter. Before cell loading, microfluidic devices were sterilized using 70% Ethanol and dried for at least 24h to ensure the restoration of hydrophobic properties.

Computational fluid dynamic (CFD) simulations

Commercial general-purpose CFD code Ansys Fluent 6.3.26 has been utilized for simulating fluid flow and concentrations within the device. The fluid flow in a micro-hip can be characterized as laminar (Re << 1), for the fluid-wall interaction a no-slip boundary condition has been applied. Given the low species concentrations and, assuming Newtonian behaviour, the fluid properties of water have been used in the model (density 998 kg/m³, dynamic viscosity 1 mPa.s). Hydrogels have been modelled using an isotropic porous medium approach with a fixed porosity and a constant viscous resistance (0.99 and 6.67 10-12/m, respectively). Diffusion coefficients have been used from literature data. A fixed ambient temperature (25 °C) and constant atmospheric pressure (1 atm = 101325 Pa) have been used for the reference conditions. At the inlet and outlet boundary zones of the flow geometry, constant velocity and/or pressure boundary conditions have been derived from the experimental setups. For transient simulation runs, grid cell size and time steps have been matched to meet the Courant stability criterion to ensure physically valid results. To speed up simulation run time, gravity

forces can be replaced by equivalent pressure on the boundaries for steady state snapshot simulations. The simulation results ("virtual experiments") can also be utilized to derive more generic correlations to describe e.g. a function describing the fluid flow rate depending on the filling level for a given chip geometry and physical parameter set. From multiple steady state CFD calculations, flow fields, concentration gradients and accumulation or depletion of reservoir fluids as well as dissolved species in defined fluid regions have been monitored and illustrated.

Cell culture

Primary human umbilical vein endothelial cells (HUVEC) and adipose-derived stem cells (ASC) were isolated and cultivated as previously described[21,36] after approval by the local ethics committees of Upper Austria and the AUVA and written donor consent. Telomerase-immortalized lymphatic endothelial cells (LEC-tert) were purchased from Evercyte, and primary microvascular blood endothelial cells (BEC) and lymphatic endothelial cells (LEC) were obtained from PromoCell. All cells were cultivated in a fully supplemented EGM-2 medium with 5% FCS (Promocell), if not recommended otherwise by the supplier, and used for on-chip experiments before passage 10. HUVEC and LEC-tert were retrovirally transfected with GFP or mCherry as previously published.[37]

Microchip loading and vessel generation

For microchip loading of hydrogel-embedded cell suspensions, bovine fibrinogen (Sigma Aldrich) was resuspended in $PBS^{-/-}$ at 6 mg/mL and dissolved by incubation at 37°C for three hours before sterile filtering. Cells were washed with PBS, detached from cell culture flasks, and resuspended in an FCS-free endothelial cell medium before the addition of bovine thrombin (Sigma Aldrich). Fibrinogen and cell/thrombin solutions were subsequently mixed and injected into the hydrogel region using 8 µL cell suspension/chamber to yield final concentrations of 3 mg/mL fibrinogen, 1 U/mL Thrombin, $5*10^6$ endothelial cells/mL, and $2.5*10^6$ ASC/mL. Fibrin hydrogels were polymerized for 10 minutes at room temperature in humidity chambers as previously described[38] before the second hydrogel chamber was filled following either the procedure mentioned above or with cell-free fibrin hydrogel. Subsequently, hydrogels were polymerized for 20 minutes at 37°C before supplying cell

culture medium via the fluid reservoirs. For lymphatic sprouting experiments, medium channels were coated with 1 µg/mL fibronectin for 1h before adding 5 µL LEC suspension at $5*10^6$ cells/mL, and devices were tilted by 90° to ensure cell attachment to the hydrogel interface. Microvascular cultures were maintained in EGM-2 or a mixture of EGM-MV (PromoCell) and EGM-MV2 (Promocell), depending on cultured cell types, with daily medium changes for five days. Primary lymphatic endothelial cell cultures were supplied with vascular endothelial growth factor C (VEGF-C, CoaChrom Diagnostica) at 25 ng/mL, 50 ng/mL, or 100 ng/mL and stimulated with 100 ng/mL Phorbol 12-Myristate 13-Acetate (PMA) as described. Selected devices were perfused using 70 kDa TRITC-dextran (Sigma Aldrich) via hydrostatic pressure-driven flow.

Immunofluorescent staining

For immunofluorescent staining, microvascular devices were washed twice in HBSS, fixed in 4% paraformaldehyde (PFA) for 30 minutes, and permeabilized using 0.1% Triton-X100 for 15 minutes. Specimens were blocked overnight in a blocking buffer of 2% goat serum in HBSS, incubated with rabbit anti-VE-cadherin antibody (Abcam) for 72h, washed, and incubated with goat anti-rabbit secondary antibody (Abcam) for 48h. Nuclei were stained using DAPI at 1 µg/mL, and F-actin fibers were visualized using a 1x phalloidin solution (Abcam). Images were obtained on an Olympus IX83 epifluorescent microscope using lasers at appropriate wavelengths.

Image and data analysis

Image analysis of microvascular networks and lymphatic sprouting behavior was performed using Image J and AngioTool software.[39] Data were visualized and analyzed using GraphPad Prism. Where applicable, outliers were excluded using a Grubbs Outlier test at $\alpha = 0.05$, and statistical significance was determined at p-value < 0.05 using Student's t-tests or two-way ANOVA.

RESULTS AND DISCUSSION

Microfluidic device supports spatially separated cultivation and generates interstitial flow

Directional flow conditions are vital for maintaining the blood-lymph interface *in vivo,* where blood endothelial cells sprout in flow direction, and lymphatic endothelial cells need to sprout against the fluid flow.[15,18] We integrated two separately loadable hydrogel compartments for blood and lymphatic vasculature to investigate whether unidirectional flow also guides endothelial cell sprouting inside a microfluidic biochip. These compartments are in close proximity and downstream from each other to allow reciprocal cell signaling and cell to cell interactions. In total, the microvasculature-on-chip device, depicted in Figure 1A, contains three individually addressable µLymph units on a single device to enable twelve measurements in parallel using a microwell plate-sized chip holder. Each of the individual µLymph units, shown in Figure 1B, further consists of two cell culture chambers, two medium channels, and four medium reservoirs. Equidistant circular micropillars separate the individual hydrogel-laden chambers from each other and the respective medium channels ensuring (1) reproducibility of hydrogel injection, (2) individual nutrient and growth factor supply to each of the cultures, (3) reciprocal signaling between the cell types, and (4) establishment of a directional fluid flow across both hydrogel regions. Controlling fluid column height within the reservoirs enables a directional fluid flow from the reservoir across the adjacent hydrogel chambers containing the blood and lymphatic vasculatures. For instance, a fluid column difference of 4 mm between blood and lymphatic fluid reservoirs creates a pressure drop of 40 Pa across the hydrogel region, as confirmed by CFD simulation illustrated in Figure 1C. This pressure difference results in a mean unidirectional fluid flow across the hydrogel region of 2 µm/s, thus mimicking the pressure gradient in the interstitial capillary bed. Detailed CFD simulation data depicting column height and fluid flow velocities over four days of culture, shown in Figure S1, describe peak fluid flow velocities of 3 µm/s after the medium change and a decrease until column equilibration at day 4. These results correlate well with interstitial fluid flow velocities found *in vivo* ranging between 0.1 and 4 µm/s, depending on tissue type, location, and activity level.[40] By simply adjusting reservoir fill height every 24 h, our microvasculature-on-chip device can maintain physiologic interstitial flow velocities between

1 – 3 µm/s for mechanobiological stimulation of endothelial cell behavior over extended cultivation periods (e.g., weeks).

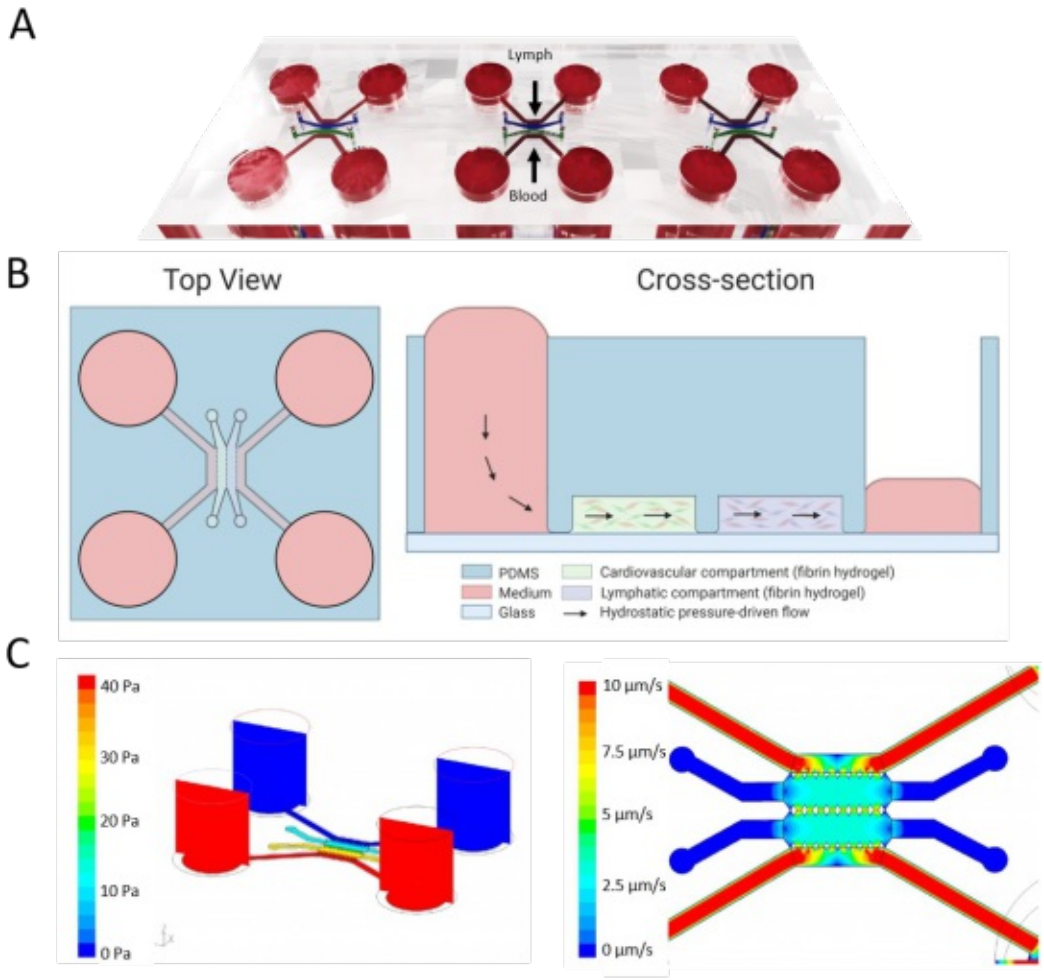

Figure 1: A) Render of Microvessel-on-chip device housing three seperately adressable cell cultivation chambers on one object-slide sized microchip. (B) Schematics of top view and cross section of one cell cultivation chamber designed for side-by-side cultivation of blood and lymphatic endothelial vasculature stimulated via unidirectional hydrostatic pressure-driven flow. (C) CFD simulation of hydrostatic pressure-driven flow in microvessel-on-chip device controlled by medium reservoir fluid level. Pressure-driven flow within hydrogel area represent interstitial flow-like velocities ranging between 1 – 3 µm/s.

Lymphatic sprouting setup determines flow-induced sprouting variations

The suitability of our microvasculature-on-chip device to mimic the blood-lymph interface was investigated in subsequent experiments. Initially, a cell culture optimization study was performed in the presence and absence of interstitial fluid flow using blood endothelial cells (HUVEC) and lymphatic endothelial cells (LEC-tert) in co-culture with adipose-derived stem cells (ASC), as a replacement of vessel supporting cells such as pericytes.[21] Figure 2A shows a schematic drawing of the dual vascularization setup (left) and the lymphatic sprouting setup (right). HUVEC and ASC are seeded as a cell suspension in fibrin hydrogel within the left hydrogel chamber in both cultivation setups. The main difference between dual vascularization and the lymphatic sprouting set up is that in the lymphatic sprouting configuration, LEC-tert are not mixed into the fibrin hydrogel but instead added via the exit channels to allow the formation of an endothelial cell monolayer at the hydrogel interface by tilting the microfluidic device during cell attachment. In other words, LEC-tert need to sprout into the hydrogel to form vessels that reach and interact with the blood vasculature. Results of our cell culture optimization study, shown in Figure 2B and S2A, revealed the stable and reproducible formation of blood vasculature and endothelial sprouting within a five-day cultivation period. Additional perfusion studies using 70 kDa TRITC-dextran (see also Figure S3) confirmed functionality and structural integrity of the on-chip generated blood vascular networks. A direct comparison of the intertwined blood-lymphatic capillaries generated in the absence (static) and presence of fluid flow (dynamic) using the dual vascularization setup showed no discernible impact of interstitial flow conditions on vascularization behavior. In turn, the presence of unidirectional interstitial fluid flow positively impacted lymphatic endothelial sprouting as early as day 3 of culture. In other words, mechanobiological stimulation initiated sprouting activity early on, leading to endothelial sprout elongation under dynamic growth conditions and pointing at the activation of sprouting behavior by shear stress perpendicular to the endothelial cell surface. White arrows in Figure 2B (right lower panel) further highlight lymphatic sprout formation at day 5 of culture, thus highlighting our microvessel-on-chip's ability to achieve an *in vitro* blood-lymphatic capillary interface using both cultivation approaches.

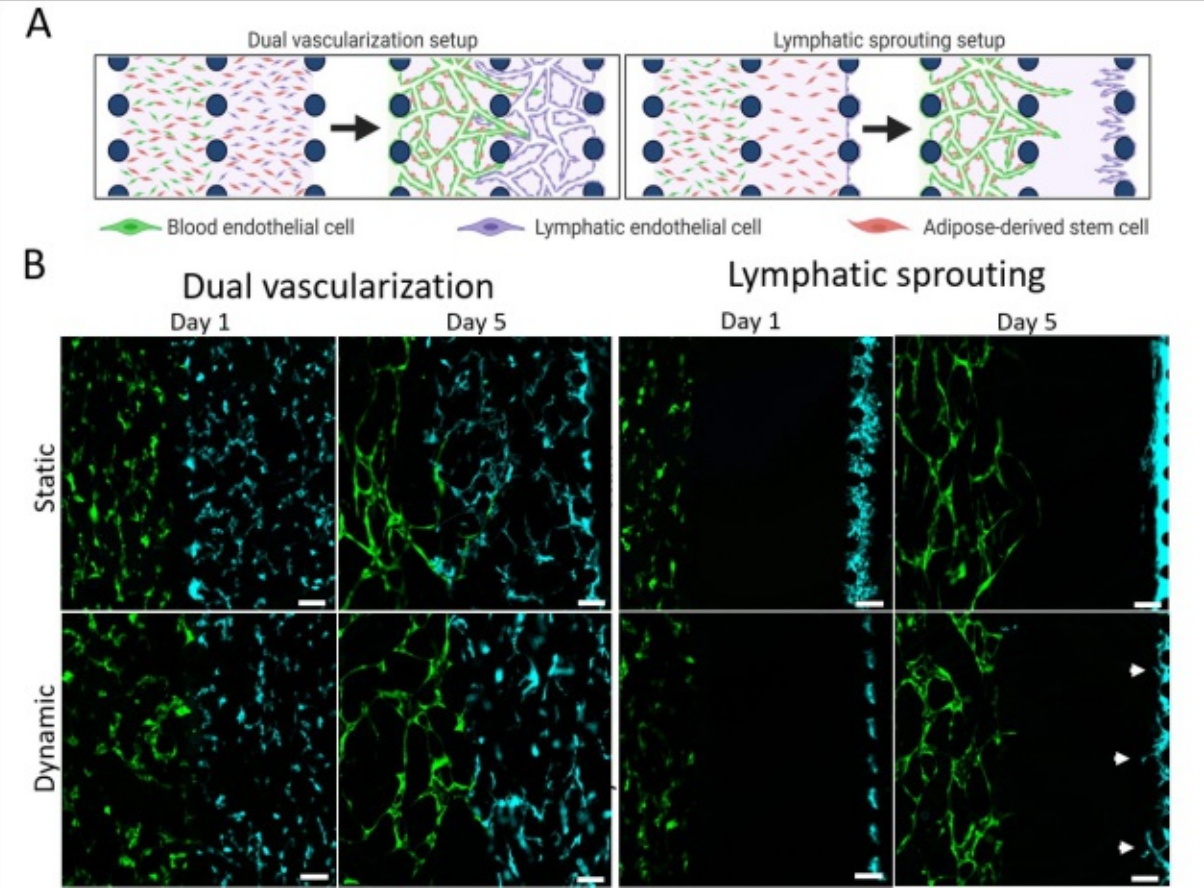

Figure 2: Cultivation strategies performed using the MechanoLymph device depicted as a sketch (A) and with fluorescent endothelial cell (B). Blood endothelial cells (HUVEC-GFP) form vascular networks in co-culture with adipose-derived stem cells (ASC, not labeled) are seeded within fibrin hydrogel within the left chamber of the device. Lymphatic endothelial cells (mCherry LEC-tert, shown in cyan) are seeded within the right compartment either as hydrogel-embedded culture (dual vascularization setup) or as cell monolayer adherent to the hydrogel at the medium interface (lymphatic sprouting setup) and form lymphatic vasculature via vasculogenesis or sprouting into the hydrogel within five days of culture. Dynamic cultivation has no discernible effect in the dual vascularization setup but enhances lymphatic sprouting. Scale Bar 100 µm.

Primary microvascular LEC respond to the cooperative effect of VEGF-C and PMA

In the next set of experiments, primary microvascular lymphatic endothelial cells (LEC) replaced LEC-tert as a model system to attain a more physiologically relevant chip-based lymphatic model. For optimal culture conditions, the effect growth factor concentration on lymphatic sprouting was determined in exclusively static conditions using the lymphatic sprouting set up described above using increasing vascular endothelial growth factor C (VEGF-C)[41] without or with additional stimulation via phorbol 12-myristate 13-acetate (PMA)[42]. The growth factor optimization study results in respective sprout number and sprout length changes, both key quality parameters, as shown in Figure 3. Interestingly, primary LECs highly

rely on PMA stimulation to form lymphatic sprouts in the static culture since very limited sprouting occurred only in 25 ng/mL VEGF-C non-PMA stimulated cultures. A combination of PMA (100 ng/mL) and VEGF-C (25 ng/mL) stimulation, however, resulted in consistent lymphatic endothelial sprout formation (see Figure 3A). Moreover, when increasing the VEGF-C concentration from 25 to 50 and 100 ng/mL, the mean sprout number rose from 7 to 24 sprouts per device in the presence of 100 ng/mL VEGF C (see Figure 3A). It is important to note that a similar sprout length of approx. 200 µm (e.g., 242 µm, 193 µm, and 185 µm) was obtained independent of the applied VEGF-C concentration in PMA-stimulated cultures, while sprout morphology deviated slightly. For instance, LEC treated with 25 ng/mL or 50 ng/mL formed fine capillaries often reconnecting to lumenized vessels after initial sprout growth and featuring single tip cell protrusions that extend into the cell-free hydrogel as visualized by nuclei and F-actin staining in Figure 3B. In contrast, cultures stimulated with 100 ng/mL VEGF-C emanated from the gel interface directly as single, lumenized vessels. In turn, non-PMA-stimulated cultures formed an endothelial cell monolayer circumferentially lining the medium channel as visible in Figure 3B irrespective of VEGF-C concentration. In summary, results of our growth factor optimization study revealed a striking morphological similarity of our PMA (100 ng/mL) and VEGF-C (100 ng/mL) co-stimulated vascular networks to blind-ended lymphatic capillaries found *in vivo.*[7] Consequently, all following experiments are conducted using this co-stimulation protocol to investigate sprouting behavior under dynamic flow conditions.

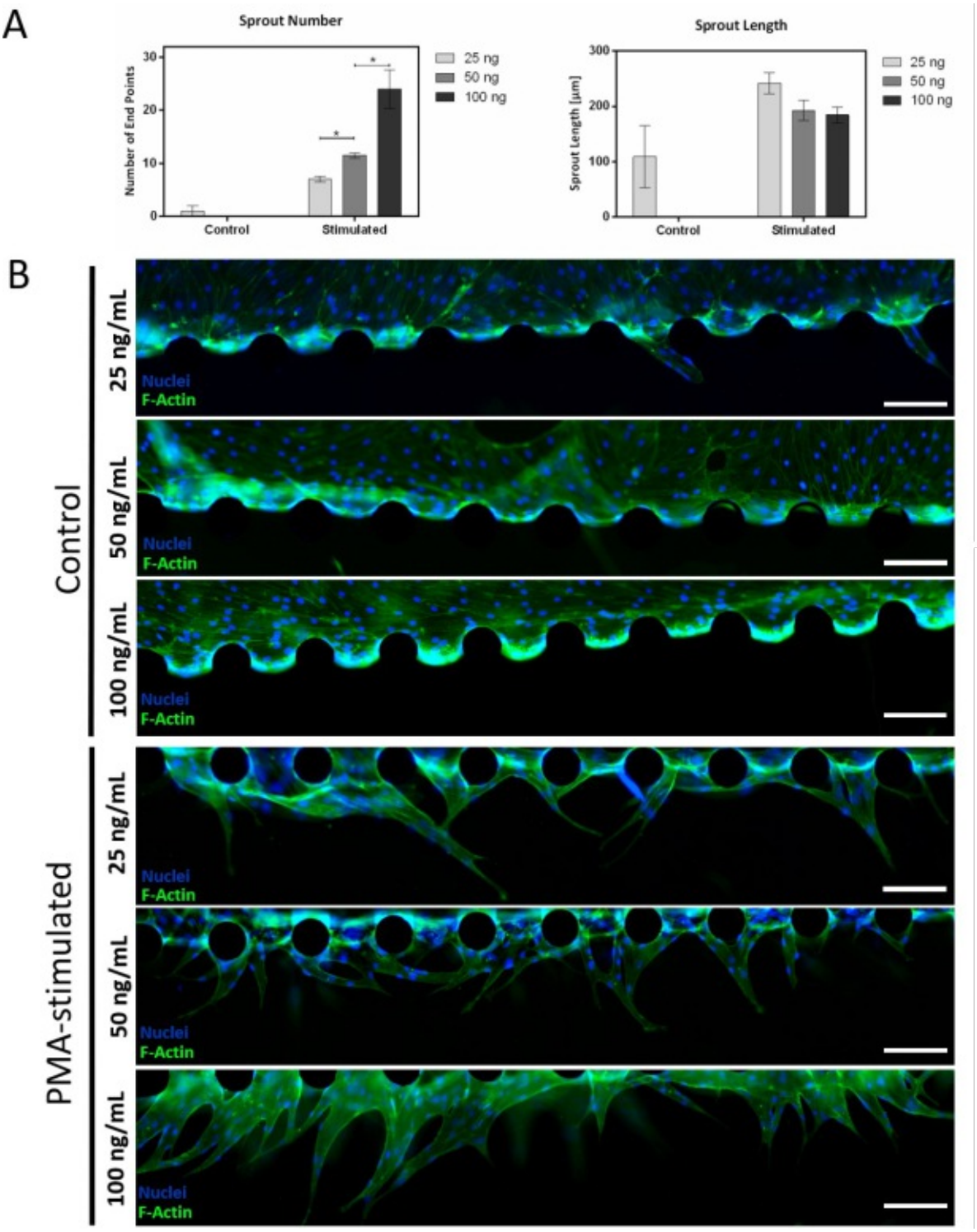

Figure 3: (A) Increase of lymphatic sprout number with VEGF-C concentration in culture medium and addition of PMA and differences in sprout length with VEGF-C concentration. (B) Epifluorescent images of LEC in culture with varied VEGF-C concentration and PMA stimulation. Stimulated LEC show increased sprouting behavior and morphological differences dependent on VEGF-C concentration. Scale Bar 200 µm.

Dynamic cultivation initiates sprouting and enhances lymphatic capillary length

Since lymphatic capillaries are highly sensitive to interstitial fluid flow *in vivo*, lymphangiogenesis usually occurs in response to fluid flow irregularities and associated tension variations caused by, e.g., wound healing processes or tumor growth.[43] To evaluate the impact on LEC sprouting and BEC network formation under unidirectional interstitial fluid flow (e.g., 1 – 3 µm/s) across the hydrogel compartments, the lymphatic sprouting setup (shown in Figure 2A) is used in subsequent experiments. Results shown in Figure 4 clearly demonstrate the impact of dynamic culture conditions on lymphatic sprouting behavior, which led to significantly elevated sprouting activities in both PMA-stimulated and control cultures. Interestingly, dynamic cultivation prompted lymphatic capillary formation even without auxiliary stimulation via PMA and elevated sprouting activity in PMA-stimulated cultures, visible in representative images of capillaries in all conditions in Figure 4A. While PMA-stimulated cultures exhibited a higher number of lymphatic sprouts before fusing into larger capillary structures, unstimulated LEC predominantly formed larger and single capillaries originating from the endothelial monolayer at the hydrogel interface. A detailed quantitative analysis of sprouting activity is shown in Figure 4B, further indicating the generation of elevated sprouting lengths in the presence of dynamic culture conditions. In other words, the presence of unidirectional interstitial flow leads to sprouting length increase by 1.7-fold from 180 µm in static PMA-stimulated cultures to 313 µm in dynamic controls, thus highlighting the beneficial impact of physiologically relevant directional interstitial fluid flow conditions on lymphatic sprouting activity.

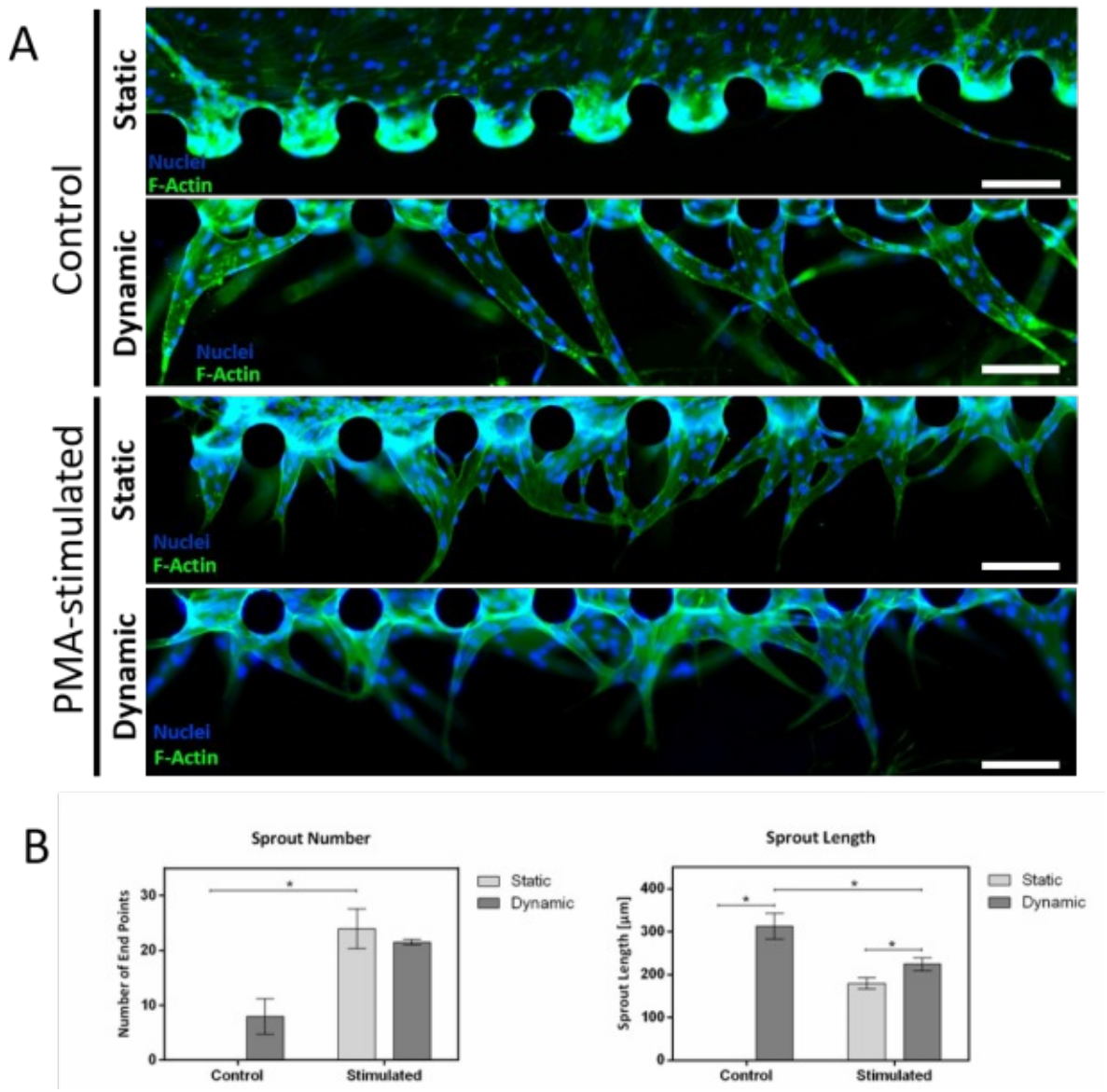

Figure 4: Mechanobiological effect of interstital fluid flow on LEC sprouting (A) Increase in LEC sprouting activity under dynamic cultivation conditions mimicking interstitial flow. (B) Lymphatic sprout morphology under static and dynamic cultivation conditions under control and in PMA-stimulated cultures. Scale Bar 200 µm.

Next, we focused on the influence of directional interstitial fluid flow on vascularization behavior of primary blood endothelial cells (BEC) located upstream of the LEC sprouting compartment and cellular outgrowth from the BEC vascularization chamber towards the lymphatic capillaries as illustrated in Figure 5. A comparative analysis of vessel area coverage, junction number, and average vessel length in the absence and presence of flow using stimulated and non-stimulated BEC cultures is conducted. Figure S4 demonstrates the marginal impact of fluid flow and cell culture stimulation on experimental vascularization

parameters. For instance, neither PMA stimulation nor dynamic cultivation significantly impacted vessel area coverages (e.g., 42% and 45%), where BEC and ASC co-cultures reliably formed stable networks exhibiting 97 – 114 junctions per network and device. However, average vessel length decreased from an average network length of 10156 µm in statically cultivated control cultures to 5500 µm in dynamically cultivated unstimulated cultures (statistically not relevant). In comparison, PMA-stimulated cultures yielded an increased average vessel length of approximately 1000 µm (e.g., 3230 µm to 4466 µm) under dynamic cultivation. In other words, BEC may react to the constant supply of PMA molecules resulting in increased cell migration and proliferation. Another intriguing effect of the directed interstitial flow conditions was the occurrence of cellular ingrowth from the blood endothelial compartment into the cell-free lymphatic sprouting compartment. Quantitative analyses of cellular protrusion length and nuclei number are shown in Figures 5 and S4, respectively, and demonstrate cell outgrowth predominantly in non-PMA-stimulated cultures, despite supposed migratory stimulation via PMA.

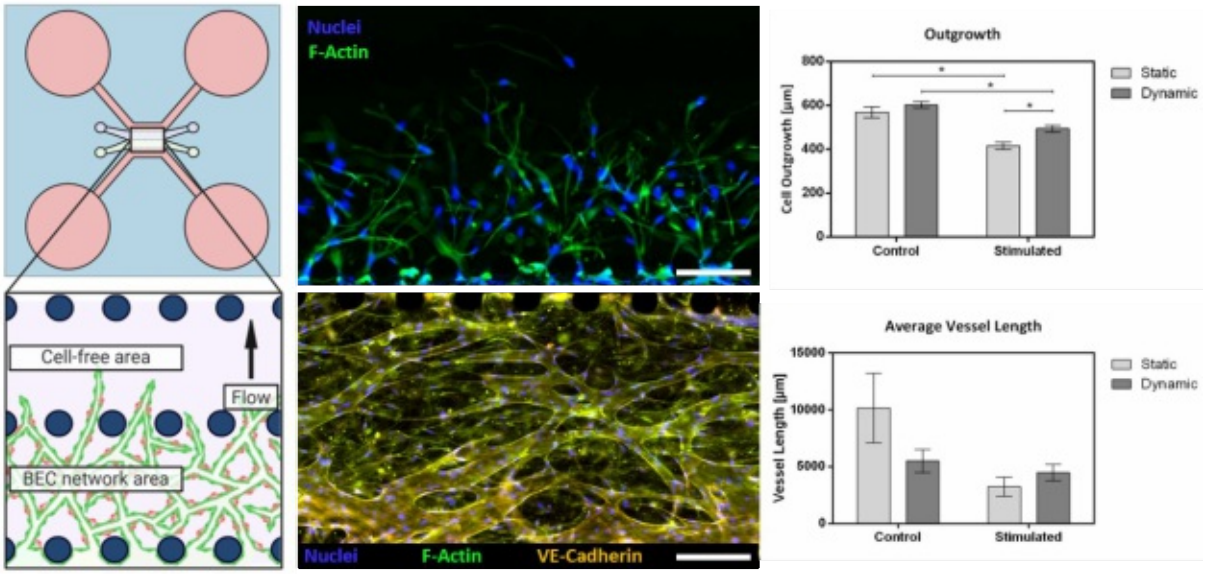

Figure 5: Effect of dynamic cultivation on cell outgrowth from the blood vascular compartment and blood vessel vascularization. Non-PMA stimulated cultures grow into gel-free area irrespective of dynamic cultivation while PMA-stimulated cultures show significantly increased outgrowth under directional fluid flow. BECs from blood vascular networks through vascularization irrespective of flow condition. Scale bar 200 µm.

In summary, Figure 6 shows the successful establishment of lumenized vessels from blood and lymphatic vascular origin within one cell cultivation unit on-chip. The device supports the formation of vasculatures of both origins by using our optimized cultivation method and the described lymphatic sprouting setup. Both vasculatures form viable, lumenized vessels expressing endothelial cell-cell junctions and show distinct differences similar to their *in vivo* morphology. In other words, lymphatic sprouts form thicker blind-ended vessels while blood endothelial cells vascularize the fibrin hydrogel with a thinner, continuous blood vascular network. The microvasculature-on-chip system recreates the interstitial niche by mimicking interstitial fluid flow velocities via hydrostatic pressure-driven flow resulting in enhanced lymphatic sprouting and establishing the blood-lymph interstitial interface within a microfluidic device.

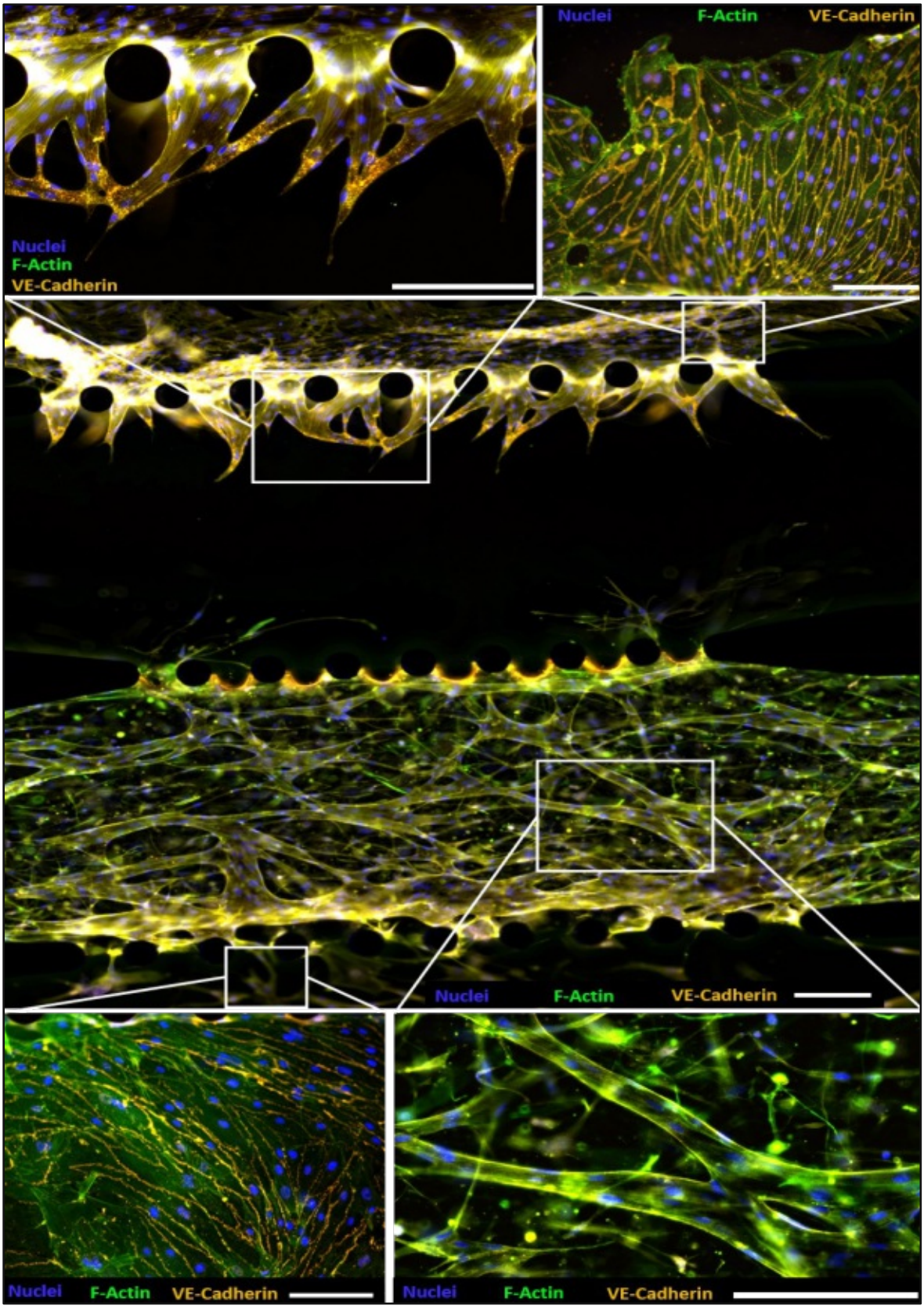

Figure 6: Overview of one cell cultivation unit highlighting successful lymphatic endothelial sprouting and blood endothelial network formation to generate a blood-lymph capillary bed in a microfluidic device. Scale bars 200 µm.

CONCLUSION

In the present work, we investigated the suitability of our novel microvasculature-on-chip device to establish a blood-lymphatic interface i*n vitro*. The device harnesses microfluidic technology's advantages to tailor the *in vitro* microenvironment by spatial separation of two hydrogel compartments and utilization of hydrostatic pressure-driven flow. Creating hydrostatic pressure via fluid reservoirs allows the generation of interstitial fluid flow of 1 – 3 µm/s to mimic the path of fluid expelled from the blood vasculature traveling through interstitial tissue into the lymphatics. VEGF-C is crucial for the first steps in lymphatic development. Without it, embryonic endothelial cells commit to the lymphatic lineage but do not form sprouts to develop functioning lymphatic vasculature[41]. We thus utilized our microvessel-on-a-chip platform to evaluate sprouting induction via varied VEGF-C concentrations individually and as a combined effect with PMA, which, too, acts as a potent inducer of endothelial sprouting[42]. We then demonstrated the effect of mechanobiological stimulated cultivation on spatially separated cultures of blood and lymphatic endothelial cell populations. While vascularization of blood endothelial cells was not affected by dynamic cultivation conditions, dynamic cultivation conditions recreating the interstitial microenvironment enhanced lymphatic endothelial sprout formation. In short, dynamically cultivated lymphatic cultures formed significantly longer lymphatic vessels than their static counterparts. We report the successful formation of both vascular systems within one device, exemplifying the first step towards engineering novel *in vitro* tools to bridge the gap between animal models and conventional monolayer cultures. The establishment of such models will be an essential step to expand our knowledge of the human body in general and the lymphatic system in particular. Our microvasculature-on-chip model will help develop drug delivery strategies into the lymphatic system that can revolutionize modern vaccines and chemotherapeutics.

CONFLICT OF INTEREST

The authors declare that the research was conducted without commercial or financial relationships that could be construed as a potential conflict of interest.

AUTHOR CONTRIBUTIONS

BB, WH, and PE designed the study. BB executed experiments and analysis with assistance from SS. CJ, BH, and MH performed computational fluid dynamic simulations. BB, SS, HR, WH, and PE interpreted the data. BB drafted the manuscript with contributions from SS, PE, and CJ. All authors revised and approved the final manuscript.

FUNDING

This work was partly funded by the European Union's INTERREG V-A AT-CZ program (ATCZ133).

ACKNOWLEDGMENTS

The authors acknowledge BioRender.com for facilitating the generation of schematics for visual representation of the work.

DATA AVAILABILITY STATEMENT

The raw data supporting this manuscript's conclusions will be made available by the authors, without undue reservation, to any qualified researcher.

REFERENCES

1. Liao, S. & von der Weid, P. Y. Lymphatic system: An active pathway for immune protection. *Seminars in Cell and Developmental Biology* (2015). doi:10.1016/j.semcdb.2014.11.012
2. Angeli, V. & Randolph, G. J. Inflammation, lymphatic function, and dendritic cell migration. *Lymphatic Research and Biology* (2006). doi:10.1089/lrb.2006.4406
3. Hampton, H. R. & Chtanova, T. Lymphatic migration of immune cells. *Frontiers in Immunology* (2019). doi:10.3389/fimmu.2019.01168
4. Schwartz, N. *et al.* Lymphatic Function in Autoimmune Diseases. *Front. Immunol.* **10**, 519 (2019).
5. Friedrich, S. K. *et al.* Mechanisms of lymphatic system-specific viral replication and its potential role in autoimmune disease. *Clinical and Experimental Immunology* (2019). doi:10.1111/cei.13241
6. Griffith, L. G. & Swartz, M. A. Capturing complex 3D tissue physiology in vitro. *Nature Reviews Molecular*

Cell Biology **7**, 211–224 (2006).

7. Swartz, M. A. The physiology of the lymphatic system. *Advanced Drug Delivery Reviews* (2001). doi:10.1016/S0169-409X(01)00150-8

8. Trevaskis, N. L., Kaminskas, L. M. & Porter, C. J. H. From sewer to saviour-targeting the lymphatic system to promote drug exposure and activity. *Nature Reviews Drug Discovery* (2015). doi:10.1038/nrd4608

9. O'Melia, M. J., Lund, A. W. & Thomas, S. N. The Biophysics of Lymphatic Transport: Engineering Tools and Immunological Consequences. *iScience* (2019). doi:10.1016/j.isci.2019.11.005

10. Haase, K. & Kamm, R. D. Advances in on-chip vascularization. *Regen. Med.* (2017). doi:10.2217/rme-2016-0152

11. Ergir, E., Bachmann, B., Redl, H., Forte, G. & Ertl, P. Small force, big impact: Next generation organ-on-a-chip systems incorporating biomechanical cues. *Frontiers in Physiology* (2018). doi:10.3389/fphys.2018.01417

12. Rothbauer, M., Rosser, J. M., Zirath, H. & Ertl, P. Tomorrow today: organ-on-a-chip advances towards clinically relevant pharmaceutical and medical in vitro models. *Current Opinion in Biotechnology* (2019). doi:10.1016/j.copbio.2018.08.009

13. Jeon, J. S. *et al.* Generation of 3D functional microvascular networks with mural cell-differentiated human mesenchymal stem cells in microfluidic vasculogenesis systems. *Integr Biol* **6**, 555–563 (2014).

14. Bachmann, B. *et al.* Engineering of three-dimensional pre-vascular networks within fibrin hydrogel constructs by microfluidic control over reciprocal cell signaling. *Biomicrofluidics* **12**, (2018).

15. Abe, Y. *et al.* Balance of interstitial flow magnitude and vascular endothelial growth factor concentration modulates three-dimensional microvascular network formation. *APL Bioeng.* (2019). doi:10.1063/1.5094735

16. Offeddu, G. S. *et al.* An on-chip model of protein paracellular and transcellular permeability in the microcirculation. *Biomaterials* (2019). doi:10.1016/j.biomaterials.2019.05.022

17. Offeddu, G. S. *et al.* Microcirculation-on-Chip: Application of Transmural Flow Across In Vitro Microvasculature Enables Direct Sampling of Interstitial Therapeutic Molecule Distribution (Small 46/2019). *Small* (2019). doi:10.1002/smll.201970247

18. Kim, S., Chung, M. & Jeon, N. L. Three-dimensional biomimetic model to reconstitute sprouting lymphangiogenesis in vitro. *Biomaterials* (2016). doi:10.1016/j.biomaterials.2015.11.019

19. Ungaro, F. *et al.* Lymphatic endothelium contributes to colorectal cancer growth via the soluble matrisome component GDF11. *Int. J. Cancer* (2019). doi:10.1002/ijc.32286

20. Osaki, T., Serrano, J. C. & Kamm, R. D. Cooperative Effects of Vascular Angiogenesis and Lymphangiogenesis. *Regen. Eng. Transl. Med.* (2018). doi:10.1007/s40883-018-0054-2

21. Knezevic, L. *et al.* Engineering Blood and Lymphatic Microvascular Networks in Fibrin Matrices. *Front. Bioeng. Biotechnol.* (2017). doi:10.3389/fbioe.2017.00025

22. Sato, M. *et al.* Microcirculation-on-a-chip: A microfluidic platform for assaying blood-and lymphatic-vessel permeability. *PLoS One* (2015). doi:10.1371/journal.pone.0137301

23. Jeon, J. S. *et al.* Human 3D vascularized organotypic microfluidic assays to study breast cancer cell extravasation. *Proc. Natl. Acad. Sci.* (2015). doi:10.1073/pnas.1417115112

24. Kim, S., Kim, W., Lim, S. & Jeon, J. Vasculature-On-A-Chip for In Vitro Disease Models. *Bioengineering* (2017). doi:10.3390/bioengineering4010008

25. Charwat, V. *et al.* Combinatorial in Vitro and in Silico Approach To Describe Shear-Force Dependent Uptake of Nanoparticles in Microfluidic Vascular Models. *Anal. Chem.* acs.analchem.7b04788 (2018). doi:10.1021/acs.analchem.7b04788

26. Ugolini, G. S. *et al.* On-chip assessment of human primary cardiac fibroblasts proliferative responses to

uniaxial cyclic mechanical strain. *Biotechnol. Bioeng.* (2016). doi:10.1002/bit.25847

27. Rothbauer, M., Zirath, H. & Ertl, P. Recent advances in microfluidic technologies for cell-to-cell interaction studies. *Lab on a Chip* (2018). doi:10.1039/c7lc00815e

28. Henderson, A. R., Choi, H. & Lee, E. Blood and lymphatic vasculatures on-chip platforms and their applications for organ-specific in vitro modeling. *Micromachines* (2020). doi:10.3390/mi11020147

29. Pisano, M., Triacca, V., Barbee, K. A. & Swartz, M. A. An in vitro model of the tumor–lymphatic microenvironment with simultaneous transendothelial and luminal flows reveals mechanisms of flow enhanced invasion. *Integr. Biol.* (2015). doi:10.1039/C5IB00085H

30. Bachmann, B. *et al.* Stiffness Matters: Fine-Tuned Hydrogel Elasticity Alters Chondrogenic Redifferentiation. *Front. Bioeng. Biotechnol.* (2020). doi:10.3389/fbioe.2020.00373

31. Charwat, V. *et al.* Combinatorial in Vitro and in Silico Approach to Describe Shear-Force Dependent Uptake of Nanoparticles in Microfluidic Vascular Models. *Anal. Chem.* (2018). doi:10.1021/acs.analchem.7b04788

32. Zirath, H. *et al.* Every breath you take: Non-invasive real-time oxygen biosensing in two- and three-dimensional microfluidic cell models. *Front. Physiol.* **9**, (2018).

33. Bachmann, B. *et al.* Engineering of three-dimensional pre-vascular networks within fibrin hydrogel constructs by microfluidic control over reciprocal cell signaling. *Biomicrofluidics* (2018). doi:10.1063/1.5027054

34. Rosser, J. *et al.* Microfluidic nutrient gradient–based three-dimensional chondrocyte culture-on-a-chip as an in vitro equine arthritis model. *Mater. Today Bio* (2019). doi:10.1016/j.mtbio.2019.100023

35. Chen, H. *et al.* Microfluidic models of physiological or pathological flow shear stress for cell biology, disease modeling and drug development. *TrAC - Trends in Analytical Chemistry* (2019). doi:10.1016/j.trac.2019.06.023

36. Wolbank, S. *et al.* Dose-dependent immunomodulatory effect of human stem cells from amniotic membrane: A comparison with human mesenchymal stem cells from adipose tissue. *Tissue Eng.* (2007). doi:10.1089/ten.2006.0313

37. Hasenberg, T. *et al.* Emulating human microcapillaries in a multi-organ-chip platform. *J. Biotechnol.* (2015). doi:10.1016/j.jbiotec.2015.09.038

38. Chen, M. B. *et al.* On-chip human microvasculature assay for visualization and quantification of tumor cell extravasation dynamics. *Nat. Protoc.* (2017). doi:10.1038/nprot.2017.018

39. Zudaire, E., Gambardella, L., Kurcz, C. & Vermeren, S. A computational tool for quantitative analysis of vascular networks. *PLoS One* (2011). doi:10.1371/journal.pone.0027385

40. Rutkowski, J. M. & Swartz, M. A. A driving force for change: interstitial flow as a morphoregulator. *Trends in Cell Biology* (2007). doi:10.1016/j.tcb.2006.11.007

41. Karkkainen, M. J. *et al.* Vascular endothelial growth factor C is required for sprouting of the first lymphatic vessels from embryonic veins. *Nat. Immunol.* (2004). doi:10.1038/ni1013

42. Montesano, R. & Orci, L. Phorbol esters induce angiogenesis in vitro from large-vessel endothelial cells. *J. Cell. Physiol.* (1987). doi:10.1002/jcp.1041300215

43. Helm, C.-L. E., Fleury, M. E., Zisch, A. H., Boschetti, F. & Swartz, M. A. Synergy between interstitial flow and VEGF directs capillary morphogenesis in vitro through a gradient amplification mechanism.

MANUSCRIPT #4

ENGINEERING OF THREE-DIMENSIONAL PRE-VASCULAR NETWORKS WITHIN FIBRIN HYDROGEL CONSTRUCTS BY MICROFLUIDIC CONTROL OVER RECIPROCAL CELL SIGNALING

Barbara Bachmann, Sarah Spitz, Mario Rothbauer, Christian Jorden, Michaela Purtscher, Helene Zirath, Patrick Schuller, Christoph Eilenberger, Syed Faheem Ali, Severin Mühleder, Eleni Priglinger, Michael Harasek, Heinz Redl, Wolfgang Holnthoner, and Peter Ertl

BIOMICROFLUIDICS **12**, 042216 (2018)

Engineering of three-dimensional pre-vascular networks within fibrin hydrogel constructs by microfluidic control over reciprocal cell signaling

Barbara Bachmann,[1,2,3,4,a)] Sarah Spitz,[1,4,5,a)] Mario Rothbauer,[1,a)] Christian Jordan,[1] Michaela Purtscher,[6] Helene Zirath,[1] Patrick Schuller,[1] Christoph Eilenberger,[1] Syed Faheem Ali,[1,3,4] Severin Mühleder,[2,3,4] Eleni Priglinger,[2,4] Michael Harasek,[1] Heinz Redl,[2,3,4,5] Wolfgang Holnthoner,[2,3,4] and Peter Ertl[1,3,4,b)]

[1]*Faculty of Technical Chemistry, Institute of Applied Synthetic Chemistry, Institute of Chemical Technologies and Analytics, Vienna University of Technology, 1060 Vienna, Austria*
[2]*AUVA Research Centre, Ludwig Boltzmann Institute for Experimental and Clinical Traumatology, 1200 Vienna, Austria*
[3]*Kompetenzzentrum für MechanoBiologie (INTERREG V-A AT-CZ ATCZ133), 1200 Vienna, Austria*
[4]*Austrian Cluster for Tissue Regeneration, 1200 Vienna, Austria*
[5]*Trauma Care Consult GmbH, Vienna, 1200 Vienna, Austria*
[6]*Department of Biochemical Engineering, University of Applied Sciences Technikum Wien, 1060 Vienna, Austria*

(Received 27 February 2018; accepted 6 June 2018; published online 20 June 2018)

Reengineering functional vascular networks *in vitro* remains an integral part in tissue engineering, since the incorporation of non-perfused tissues results in restricted nutrient supply and limited waste removal. Microfluidic devices are routinely used to mimic both physiological and pathological vascular microenvironments. Current procedures either involve the investigation of growth factor gradients and interstitial flow on endothelial cell sprouting alone or on the heterotypic cell-cell interactions between endothelial and mural cells. However, limited research has been conducted on the influence of flow on co-cultures of these cells. Here, we exploited the ability of microfluidics to create and monitor spatiotemporal gradients to investigate the influence of growth factor supply and elution on vascularization using static as well as indirect and direct flow setups. Co-cultures of human adipose-derived stem/stromal cells and human umbilical vein endothelial cells embedded in fibrin hydrogels were found to be severely affected by diffusion limited growth factor gradients as well as by elution of reciprocal signaling molecules during both static and flow conditions. Static cultures formed pre-vascular networks up to a depth of 4 mm into the construct with subsequent decline due to diffusion limitation. In contrast, indirect flow conditions enhanced endothelial cell sprouting but failed to form vascular networks. Additionally, complete inhibition of pre-vascular network formation was observable for direct application of flow through the hydrogel with decline of endothelial cell viability after seven days. Using finite volume CFD simulations of different sized molecules vital for pre-vascular network formation into and out of the hydrogel constructs, we found that interstitial flow enhances growth factor supply to the cells in the bulk of the chamber but elutes cellular secretome, resulting in truncated, premature vascularization. *Published by AIP Publishing.* https://doi.org/10.1063/1.5027054

[a)]B. Bachmann, S. Spitz, and M. Rothbauer contributed equally to this work.
[b)]Author to whom correspondence should be addressed: peter.ertl@tuwien.ac.at

INTRODUCTION

A major issue in tissue engineering is the formation of necrotic cores inside biological structures due to limited diffusion of oxygen and nutrients to tissue regions beyond 200–400 μm. One promising strategy to overcome apparent oxygen and nutrient deficiencies is based on the integration of lumenized and perfused vessels to promote long-term viability of tissue-engineered constructs.[1] Over the last decade, generation of vascularized tissues has steadily improved enabling controlled nutrient supply and waste removal to and from the engineered construct through blood vessel-like networks.[2,3] From a physiological point of view, blood vessels are generally formed by two distinct mechanisms being vasculo- and angiogenesis.[4] While vasculogenesis refers to the *de novo* formation of blood vessels during embryonic development, angiogenesis requires a pre-existing vasculature, which can be extended by sprouting endothelial cells.[5] Additionally, mural cells such as vascular smooth muscle cells and pericytes actively take part in vessel maturation and stabilization.[6] While smooth muscle cells form concentric layers around arteries and veins, pericytes partially envelope smaller sized structures including arterioles, capillaries, and venules.[7] Coordination of endothelial cell sprouting is therefore guided by both reciprocal cell signaling events and heterotypic cell-to-cell contact. Similar sprouting behavior has also been observed in the presence of adipose and bone-marrow derived mesenchymal stem cells, which are known to mimic mural cells through heterotypic cell-cell interactions with endothelial cells.[6,8,9] Mesenchymal stem cells secrete numerous factors including vascular-endothelial growth factor (VEGF) and hepatocyte growth factor (HGF) that not only contribute to endothelial cell survival and proliferation but also promote the formation of pre-vascular structures *in vitro*.[8,10,11] Although the importance of reciprocal cell signaling on endothelial cell sprouting has been extensively studied over the years,[6] little is still known on the influence of growth factor gradients, which are inherently present in any natural and engineered tissue construct.

To gain a deeper understanding of the modulating effect of spatio-temporal gradients on the formation of pre-vascular networks, we have developed three different microfluidic devices that allow precise control over nutrient supply from predefined entry points to a 3D-hydrogel based co-culture system. Microfluidic cell culture systems are ideally suited to study vascular biology due to the inherent ability to control the respective microenvironment.[12–17] For instance, 2D microfluidic endothelial cell cultures systems have been used to elucidate the impact of growth factor gradients in intra- and extravasation of cancer cells[18–20] as well as VEGF[21,22] and angiopoietin-1 (ANG-1) gradients in endothelial cell sprouting.[21] In addition to demonstrating the importance of VEGF gradients for the formation of blood vessels,[23,24] microfluidic devices are routinely employed to provide physiologically relevant shear and interstitial flow regimes.[25] As an example, changes in endothelial cell morphology, phenotype, and proliferative capacity have been reported for increasing shear conditions ranging up to 130 dyn cm^{-2}.[26] While under physiological shear stress of 0.1 dyn cm^{-2} to 3 dyn cm^{-2}, a decrease in endothelial sprouting has been reported,[23] shear restriction and the presence of interstitial flow velocities between 1 μm/s and 35 μm s^{-1}, in turn, have shown to positively affect vasculo- and angiogenesis.[23,27,28] Although, in the absence of supporting cells, these microfluidic endothelial cell culture systems failed to recapitulate the physiological architecture of microvessels in interstitial tissues, these studies still demonstrated that growth factor gradients may influence sprouting. Interestingly, all existing perfused microvascular networks based on co-culture of endothelial cells and mural cells did not consider apparent wash out effects and gradients of soluble growth factors during interstitial flow conditions.[20,29,30] While current microfluidic strategies mainly focus on engineering perfusable vascular networks in tumor models[20,31] and investigating endothelial barrier functions,[32] we aim at utilizing microfluidics to fine tune vascular network formation by controlling growth factor gradients and flow profiles. In contrast to previously reported vascularization on chip models, which focus on perfusable networks anastomosed to the microfluidic channel, the goal of this study is to establish enlarged tissue constructs for potential applications in tissue engineering. This means that our microfluidic

chamber geometries greatly vary from previously published vasculature-on-chip work in terms of chamber size as well as hydrogel boundary surface.

To close this knowledge gap and to gain a deeper understanding of the relationship between heterotypic cell-to-cell interactions and reciprocal cell signaling during initial endothelial cell sprouting, a dual *in vitro* and *in silico* strategy is employed to describe the effects of spatial depletion of growth factors on the formation of a vascular network. In our experimental approach, three microfluidic 3D co-culture systems, which contain adipose-derived stem cells as supporting cells and human umbilical vein endothelial cells embedded in a fibrin matrix, are used to evaluate vascular network area coverage and average microvessel length over a seven day cultivation period. Similar to recent publications in the field,[25,31] an initial vascular network formed after five days of culture with a mature vascular network after seven days. The microfluidic biochips are designed either for indirect and lateral perfusion or direct flow conditions to establish various gradients in 1, 3, and 8 mm thick 3D vascular co-culture systems. Additional finite volume CFD simulations are performed to characterize transport phenomena and distance-relationships of signaling molecules and growth factors of increasing sizes ranging from 10 kDa, 20 kDa, 40 kDa, to 500 kDa in the absence and presence of varying interstitial flow conditions. Since the individual and combinatorial biophysical constraints such as interstitial flow, size-dependent gradients, and tissue dimension are keys in vascular network formation, a better understanding of their modulating effects may provide new insight into angiogenesis, tissue regeneration, and cancer biology.

MATERIALS AND METHODS

Device fabrication

Three microfluidic devices were used for characterization of tube formation under static or fluid flow conditions. Two of the devices had a circular chamber adjacent to a medium channel (see Fig. 1 and supplementary material Fig. 1). Microstructures were fabricated using polydimethylsiloxane (PDMS, Sylgard® 184 Silicone Elastomer Kit, Down Corning) by soft lithography from 3D-printed molds (i.materialise). After polymerization, the PDMS was bonded to glass slides using air plasma (Harrick Plasma, High Power, 2 min) and sterilized with 70% ethanol

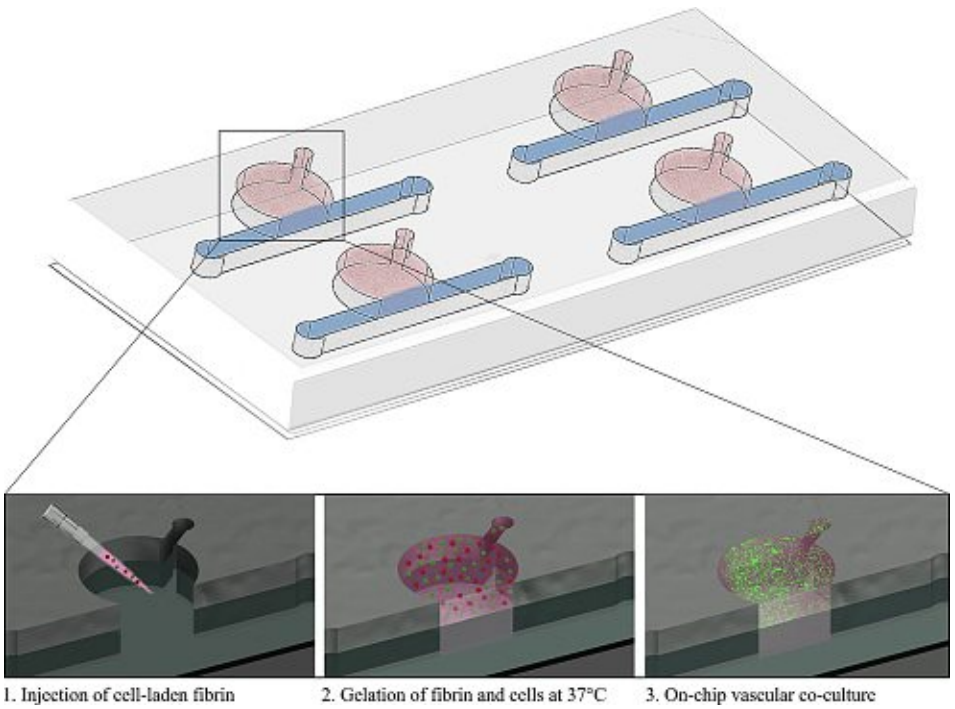

FIG. 1. Schematic overview of the microfluidic device and cell loading procedure.

before use. In turn, the microfluidic biochip designed for direct perfusion through hydrogel [see Fig. 4(a)] was manufactured using a PDMS-sheet cutter (CAMM-1 GS-24, Roland DGA). After cutting the microchannel network into PDMS membranes, the fluidic layer was sandwiched between two glass slides, sealed via air plasma activation, and treated with 3% (3-Aminopropyl) triethoxysilane (APTES; Sigma Aldrich) solution for 1 h. The assembled microfluidic biochips were sterilized (70% ethanol), rinsed with de-ionized (DI) water for a period of 30 min, and coated with 10 mg/ml fibrinogen solution overnight.

Cell culture and device seeding

Isolation of human adipose-derived stem cells (ASC) as well as human umbilical vein endothelial cells (HUVEC) was carried out as previously described[33,34] following the approval of the ethics committees (state of Upper Austria and the AUVA) and written donor consent. Harvested cells were maintained in fully supplemented endothelial cell growth medium 2 (EGM-2, PromoCell) with 5% fetal calf serum until passage 5 to 9. Retroviral infection of GFP-HUVECs was carried out as previously published.[35,36] Prior to cell seeding into microfluidic devices, fibrin hydrogel (TISSEEL®, Baxter) with a final concentrations of 2.5 mg/ml fibrinogen, 1 U/ml thrombin, and 5×10^5 cells/ml per cell type was loaded into the hydrogel chambers and polymerized for 45 min. Cell cultivation was carried out in the presence of fully supplemented EGM-2 medium under static conditions (exchange of medium every other day) and constant perfusion over a period of 7 days with four replicas per condition. Adipose-derived stem cell conditioned medium was generated by seeding 3500 cells/cm^2 and collecting secretome after three days of incubation. Non-treated controls were similarly incubated in culture flasks without cells. For experiments using a temporal adjustment of flow, co-cultures were statically cultivated for three days before initiation of flow using fresh culture medium for five days.

Finite volume CFD simulation

A multipurpose finite volume CFD code was used for solving the flow problems. The geometries were split in hexahedral control volumes, an example grid is presented in supplementary Fig. 2A. Second or higher order discretization was selected for all flow variables as well as for the species equations. To ensure physically correct transient solutions, the time step size was selected to guarantee a maximum Courant number Co < 1 within the flow domain over the whole run time of up to 18 h. Wall boundaries were treated as ideally smooth, no slip boundary conditions were selected for all surfaces. The inlet of the flow geometry was set to mass flow inlet with a plug flow velocity profile, and the outlet was set to pressure outlet at a standard pressure of 1 atm (101325 Pa) with the flow considered to be isothermal. For simplicity, Newtonian fluid behavior was assumed with a constant dynamic viscosity and constant density. As the concentrations of the dissolved species in the fluid are low, the properties of the solvent, water, have been used for the simulation ($\rho = 998\,\text{kg/m}^3$, $\eta = 0.001003\,\text{Pa s}$). The diffusion coefficients for the tracer components have been set according to measurements or literature values, assuming a dilute solution. Tracers at the flow inlet were added as step functions at the initial time $T = 0$ s, and at the same time a constant tracer saturation of the hydrogel zones were set as starting values for the simulation runs. In addition to the tracer species, a non-diffusing scalar was tracked for calculation of the residence time distributions—an example can be found in S1B. The maximum Reynolds number Re within the geometry was $\ll 1$; therefore, laminar flow was assumed with no boundary layer grid. The hydrogel regions were approximated as porous zones with constant porosities of $\varepsilon = 0.99$ and isotropic viscous resistances of $R = 6.67 \times 10^{-12}\,\text{m}^{-2}$.

Data analysis

All microfluidic devices were analyzed on day 7 based on green fluorescence intensities obtained from transfected HUVECs using AngioTool64 software [Version 0.6a (02.18.14)] to determine network parameters as described elsewhere.[37]

RESULTS AND DISCUSSION

Impact of hydrogel volume and diffusion distances on reciprocal signaling during pre-vascular network formation

Microfluidic devices similar in design but consisting of differently sized hydrogel chambers ($Ø_1 = 3$ mm and $Ø_2 = 8$ mm) are used to investigate tube formation, vessel length, and area covered throughout the hydrogel in the presence of growth factor gradients. Figure 2 shows the impact of growth factor depletion on vascular network formation caused by diffusion-distance limitation and the elution of molecules produced by stem cells as well as endothelial cells during medium replacement. Results shown in Fig. 2(a) and supplementary material Fig. 3 revealed that vascular network formation occurred homogeneously throughout the smaller cultivation chamber ($Ø_1 = 3$ mm, $V = 7.5\ \mu$l), covering approximately 9% of the entire growth volume with 15–20 junctions per mm^2. Since the average vessel length increased from $297 \pm 26\ \mu$m within the first 1 mm to 439 ± 60 over a 3 mm distance into the cultivation chambers, sufficient supply of nutrients is provided throughout the whole cultivation chamber. In turn, results shown in Fig. 2(b) point at the presence of a biochemical gradient, since vascular network parameters varied greatly throughout the 8 mm long ($V = 100\ \mu$l) fibrin hydrogel construct. Within the first 3 mm distance from the medium supply channel, peak values for vessel area coverage of $40.4 \pm 5.9\%$, an average vessel length of 2.05 ± 0.94 mm and 22 ± 2 junctions per mm^2 are found. Between 3 and 8 mm distance, however, the quality of pre-vascular network formation declined gradually resulting in an average reduction in vessel area of $2.5 \pm 2.2\%$, a vessel length of 0.18 ± 0.25 mm and of 2.19 ± 0.1 junctions per mm^2.

To gain a better understanding of the underlying mechanisms responsible for the distance-dependent decline in the quality of pre-vascular network, fluorescently labelled dextran similar in size as proangiogenic molecules including a 10 kDa dextran (e.g., EGF and IGF), a 20 kDa dextran (e.g., ß-FGF and PDGF), and a 40 kDa dextran (e.g., VEGF and Ang-1/-2) as well as FITC-dextran with 500 kDa in size was chosen as a reference molecule to visualize gradient formation inside the fibrin hydrogel constructs under static conditions; for representative images of the dextran diffusion and a comparison of *in vitro* to *in silico* results, see supplementary material Figs. 4 and 5. Based on these results, finite volume CFD simulations were performed to determine the distribution of differently sized biomolecules inside the hydrogel volume. Figure 3(a) shows that approximately 30% of proangiogenic biomolecules with 40 kDa in size and 50% of smaller molecules are readily delivered within 12 h to cells residing up to 3 mm inside the hydrogel construct (for three dimensional graphs see also supplementary material Fig. 6). This is followed by the formation of a steep gradient starting around 3 mm hydrogel distance where only 10% of 20 kDa biomolecules but hardly any 40 kDa sized proangiogenic

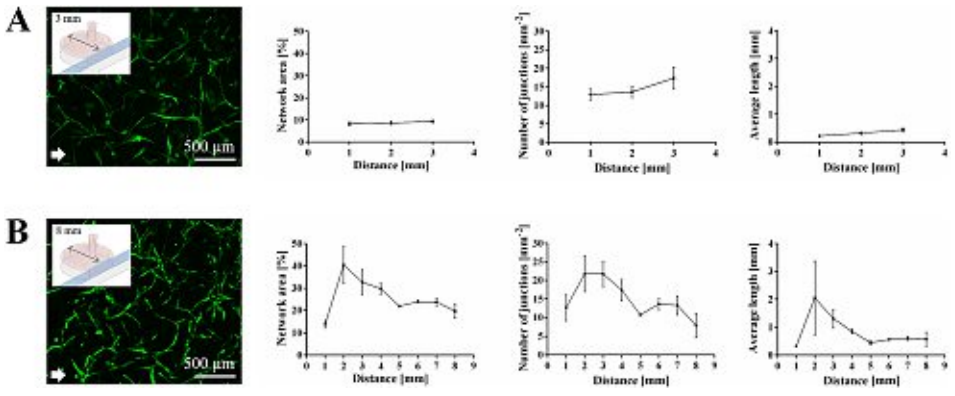

FIG. 2. Fluorescence images of pre-vascular networks with quality parameters in fibrin-based hydrogel constructs seeded with adipose-derived stem cells and green-fluorescent endothelial cells for (a) 3 mm and (b) 8 mm hydrogel chamber diameter day 7 post seeding.

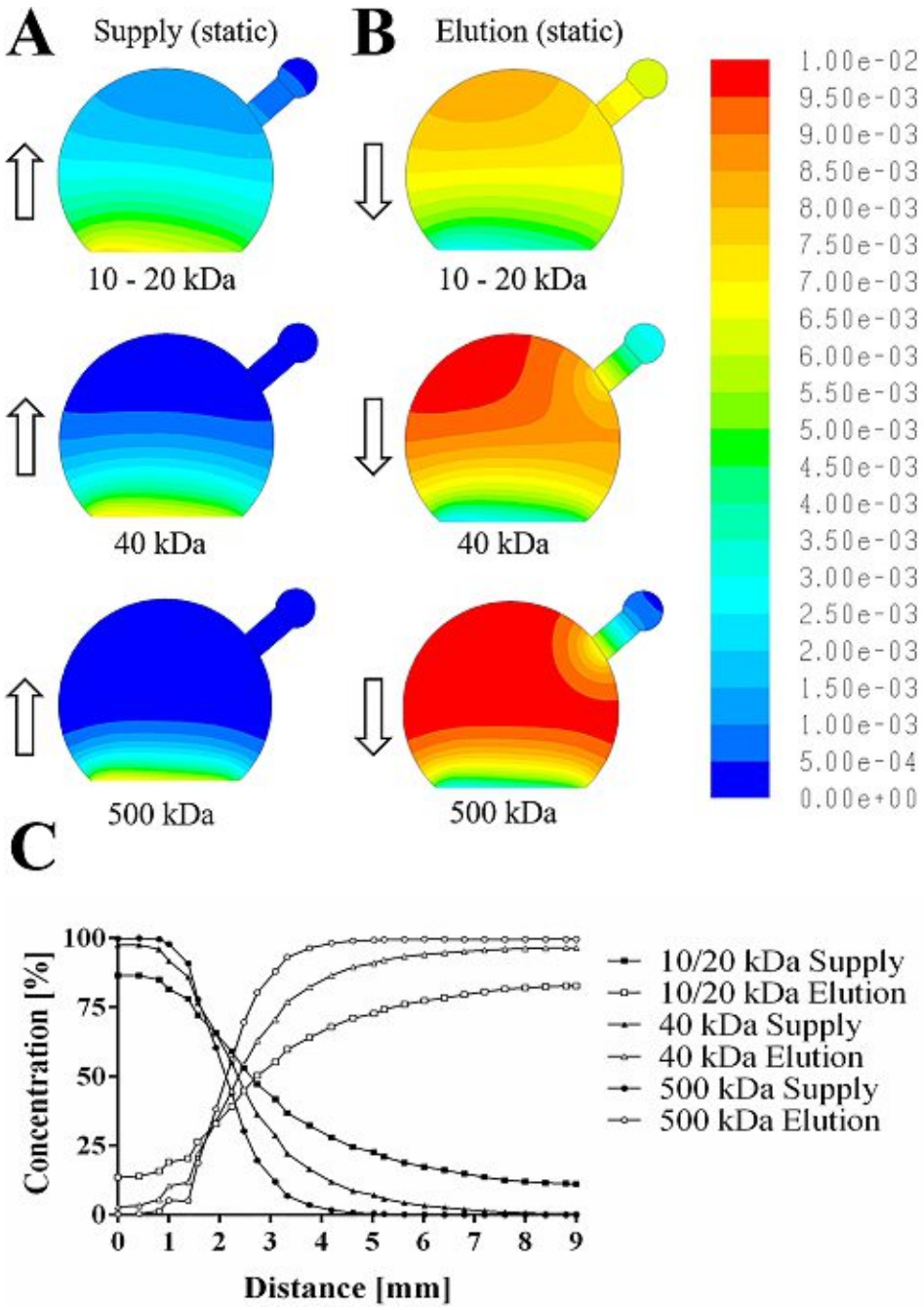

FIG. 3. Finite volume CFD simulations of size-dependent molecule diffusion (a) and elution (b) for static cell culture conditions and (c) concentration profile of molecules with distance.

factors can reach deeper regions of the fibrin hydrogel. Any larger biomolecules only diffuse up to a distance of 2 mm reaching approximately 5% of mass after a 12 h period. Additionally, the removal of secreted biomolecules and elution into the medium supply channel was simulated to estimate the distribution of cell signaling molecules within the fibrin hydrogel construct. Results shown in Fig. 3(b) indicate that over 80% of secreted biomolecules are eluted from the first millimeter and 50% are still eluted from up to 3 mm inside the fibrin construct. In other words, small hydrogel volumes are prone to elution of proangiogenic factors, thus severely impeding reciprocal cell-cell signaling events.

Overall, our simulation results correlate well with experimental differences observed in vascular network formation using microfluidic co-cultures of adipose-derived stem cells with endothelial cells, indicating that distance between 2 to 3 mm inside the hydrogel reaches optimum equilibrium between nutrient supply and elution of metabolites for pre-vascular network formation in static culture conditions. Since the 8 mm diameter hydrogel chamber design displayed gradient-dependent network formation, it was selected for subsequent flow experiments.

Impact of direct and indirect interstitial fluid flow on pre-vascular network formation

In addition to diffusion-limited supply of nutrients, interstitial flow conditions can also influence vascular network formation due to the increased elution of secreted biomolecules. To study the effects of direct and indirect fluid flow on pre-vascular network formation, two different microfluidic geometries shown in Fig. 4 are employed in subsequent experiments. In the first microfluidic configuration (right panel of Fig. 4) indirect interstitial flow conditions are established by directing the medium flow alongside the hydrogel interface at a velocity of 3 μm/s, whereas the second microchip design (left panel of Fig. 4) was adjusted to reduce hydrogel resistance and increase hydrogel anchorage to enable direct flow through the hydrogel. Results of our lateral flow direction study revealed that microfluidic ASCs/HUVEC co-cultures embedded in 8 mm fibrin hydrogel constructs started to form vascular connections already at day 3. Since apparent vascular network morphologies improved over the following 4 days in culture, sufficient supply of reciprocal signaling of proangiogenic growth factors is provided during indirect medium perfusion. In contrast, fluid flow forced through the fibrin hydrogel

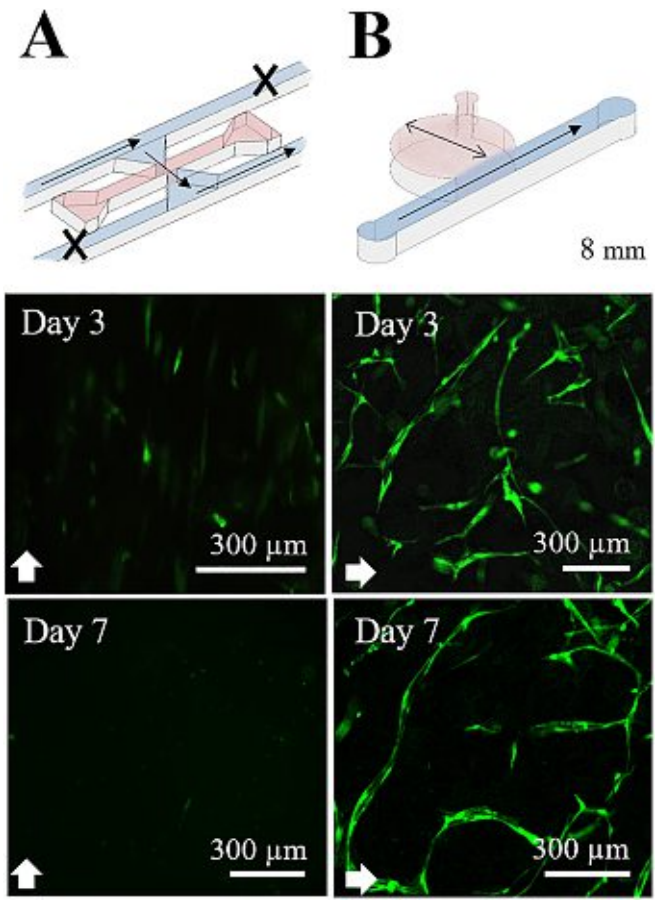

FIG. 4. Influence of direct compared to orthogonal interstitial fluid flow on pre-vascular network formation.

construct using our second microfluidic configuration (left panel of Fig. 4) resulted in endothelial cell alignment in the direction of the fluid flow with no evidence of pre-vascular network formation at day 3. Even more striking, complete loss of endothelial cell viability occurred by day 7 under direct interstitial fluid flow conditions. Additionally, finite volume CFD simulations (see supplementary video 1) revealed that direct fluid flow through a hydrogel results in complete elution of pro-angiogenic growth factors from the perfused region already after 120 s, thus eliminating reciprocal cell signaling and the formation of vascular structures. In other words, secretion of proangiogenic growth factors from the adipose-derived stem cells plays a key role in the initial phase of vascular network formation, while forced fluid flow through a hydrogel construct may be beneficial in maturation of preformed lumenized vessels.

Interstitial flow enhances sprouting but lessens network maturation

Since reciprocal cell-cell signaling is an important part during the onset and formation of pre-vascular networks, additional finite volume CFD simulations were performed to assess the distribution of proangiogenic growth factors in fibrin hydrogel constructs. *In silico* results shown in Fig. 5 indicate that during indirect lateral flow conditions sufficient growth factors are present over the complete hydrogel distance, where 50% of 20 kDa sized molecules reach 4 mm and 40% diffuse up to 6 mm into the hydrogel within a period of 12 h. Additionally, Fig. 5(a) shows that approximately 50% of biomolecules ranging from 10 to 20 kDa in size are delivered in a similarly fashion to static cultures. It is important to note, however, that slightly higher biomolecule concentrations in the deeper regions of the hydrogel construct could be achieved in the presence of lateral fluid flow. Interestingly, lateral fluid flow did not increase the penetration depth of 40 and 500 kDa biomolecules after 12 h of perfusion. Furthermore, elution of proangiogenic growth factors from the fibrin hydrogel construct is significantly enhanced for smaller biomolecules sizes with complete removal from the first millimeter distance [see Fig. 5(b)], while bigger sized molecules displayed similar distribution as static cultivation.

In a next set of experiments, network area coverage, vessel length, and number of junctions of microfluidic *in vitro* co-cultures of stem cells and endothelial cells were evaluated to assess the quality of vascular network formation in the presence of physiologically relevant fluid flow rates that resemble interstitial flow regimes. Figure 6(a) shows a cross-section analysis of the 3D-cultivation chambers where images of endothelial tube formation are compared, revealing good agreement with above *in silico* results. While endothelial cell alignment along the flow direction is found within the first millimeter where highest flow rates are present, premature vascular connections started to form 2 mm inside the hydrogel exhibiting a vessel area coverage of $5.11 \pm 1.42\%$, 51 ± 12 junctions mm^{-2}, and an average vessel length of 0.066 ± 0.008 mm. In turn, within deeper regions around 4 mm inside of the hydrogel construct, vascular network formation improved markedly featuring a vessel area of $12.07 \pm 1.21\%$, 155 ± 16 junctions mm^{-2}, and an average vessel length of 0.16 ± 0.02 mm. This improved vascular structure quality suggests efficient nutrient delivery to the entire hydrogel volume, while simultaneously retaining secreted cell signaling molecules, thus promoting homogenous vascular network formation.

In a final comparative analysis, vascular network formation in the presence of varying concentration gradients was investigated to assess the impact of size-depended growth factor distribution inside the hydrogel construct. Additionally, we investigated whether preconditioning of culture medium in stem cell secretome or application of a stop-flow regime alters vascular network formation. Results of our comparative study are summarized in Fig. 7 where size-dependent biomolecule distribution and vascular network formation of ASC and HUVEC co-cultures embedded in fibrin hydrogels are analyzed. Results in Fig. 7(a) illustrate that the distribution of biomolecules in the range of 10 and 20 kDa differs between 20% to 40% over a distance of 1, 3, and 6 mm inside the hydrogel construct in the presence of indirect perfusion. These phenomena can mainly be attributed to the elution and removal of smaller molecules from the hydrogel during lateral flow conditions. The evaluation of the quality of the vascular structures over the distance in the absence and presence of interstitial flow is shown in

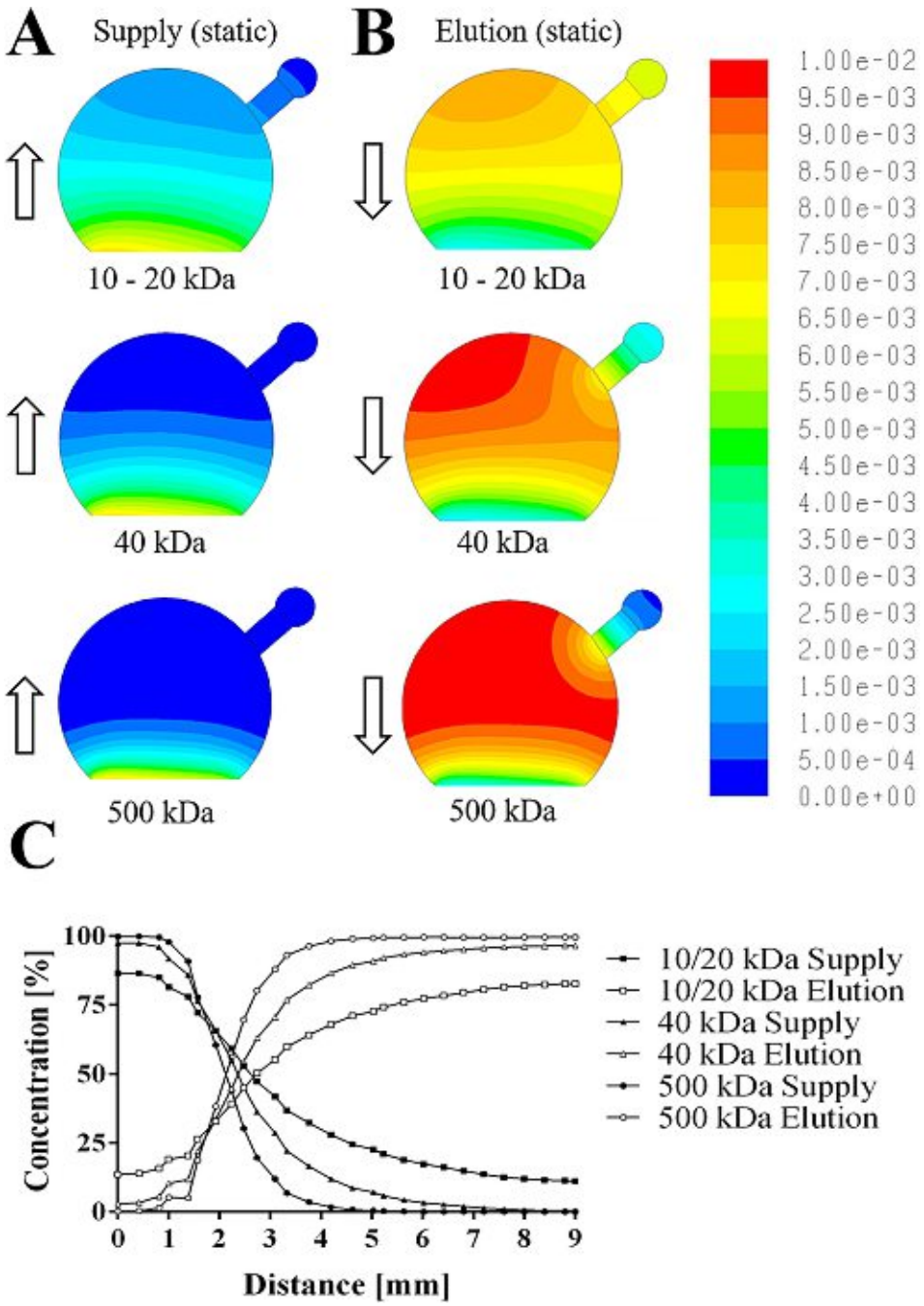

FIG. 5. Finite volume CFD simulations of size-dependent molecule diffusion (a) and elution (b) for indirect interstitial fluid flow and (c) concentration profile of molecules with distance.

Fig. 7(b). While lateral perfusion of the fibrin-hydrogel construct led to improved endothelial sprouting events, reduced vessel length and network area coverage, particularly inside deeper regions (< 4 mm), are found compared to static conditions. Although dynamic culture conditions resulted in overall lower vascular network quality values, the obtained vascular morphology displayed a higher degree uniformity and regularity throughout the fibrin hydrogel construct. These results point at the mitigating effect of local concentration of proangiogenic biomolecules, which is governed by supply of nutrients, maintenance of secretome, and elution of metabolic waste products. In a final set of experiments, we investigated the possibility to

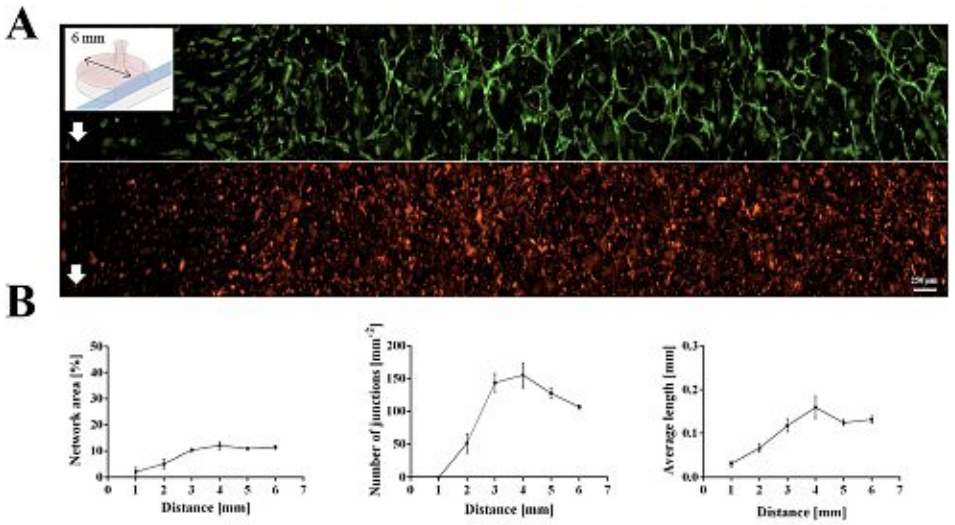

FIG. 6. (a) Fluorescence images pre-vascular networks and (b) quality parameters of adipose-derived stem cells (red) and umbilical vein endothelial cells (green) at interstitial fluid flow day 7 post seeding.

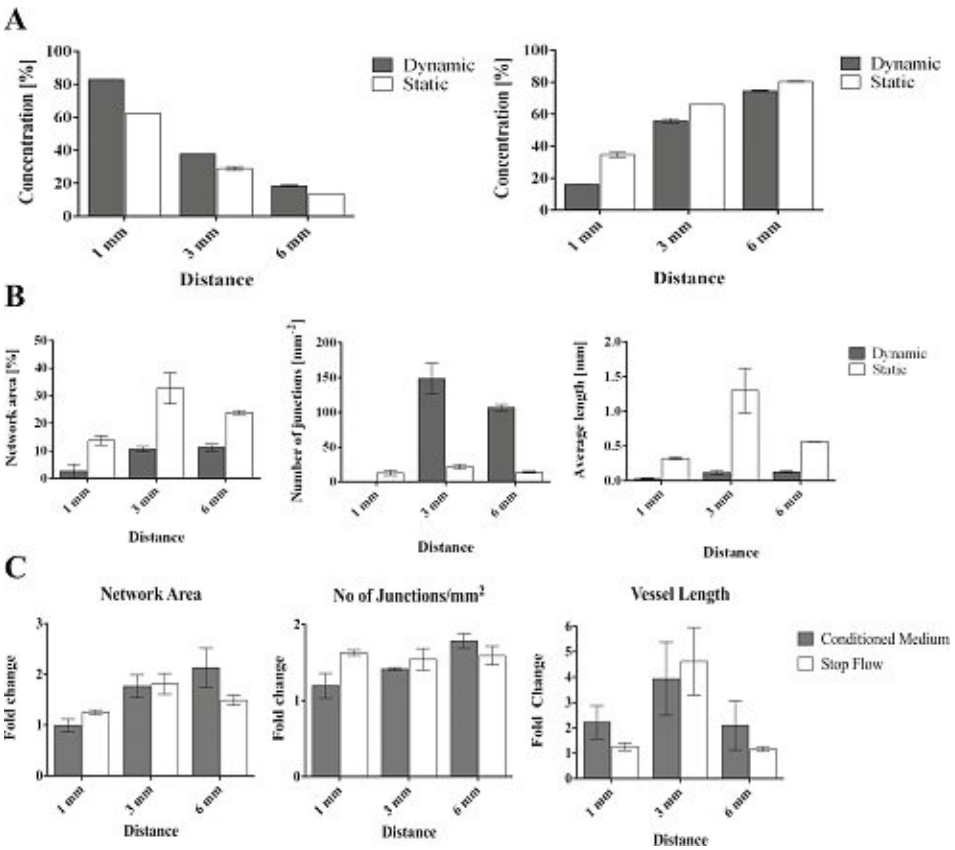

FIG. 7. (a) Finite volume CFD simulations of biomolecule diffusion in static compared to dynamic cell culture conditions. (b) Comparison of pre-vascular network formation for static and dynamic culture conditions using microfluidic devices day 7 post seeding. (c) Fold changes of network characteristics during cultivation with ASC conditioned medium (grey) and temporal adjustment of flow regime (white) compared to the initial flow setup.

improve vessel parameters by either employing a setup with temporal adjustment of flow or stem cell conditioned culture medium in the initial setup in the presence of continuous flow directly after cell seeding. In the "temporal adjustment of flow setup" (Stop-Flow), the co-cultures were cultivated statically for three days to allow establishment of preliminary vascular connections before application of flow for the final five days of culture. Results of both setups are displayed in Fig. 7(c) and show a minor improvement of network area and number of junctions/mm^2 within the first millimeter of the construct. However, both parameters were visibly increased at distances of 3 and 6 mm into the construct. Interestingly, temporal adjustment of flow resulted in 4.6-times longer vessels at 3 mm from the medium channel but only slight improvement at the other distances while the stem cell conditioned medium enhanced the vessel length at all distances.

CONCLUSION

In this work, we have investigated the influence of concentration gradients on the formation of vascular networks inside fibrin-hydrogel constructs containing human umbilical vein endothelial cells and adipose-derived stem cells. Using three different microfluidic 3D vascular co-culture models, the importance of biochemical gradients and reciprocal cell signaling events on endothelial sprouting was demonstrated in the absence and presence of indirect as well as direct flow conditions. Starting with single elongated cells at the edges of the hydrogel construct, pre-vascular network formation started within 0.5–1 mm distance inside the fibrin hydrogel for all devices. In the absence of fluid flow, pre-vascular microvessels formation occurred predominantly inside 2–3 mm inside the fibrin construct followed by subsequent decline of vascular network quality. The observed asymmetry in endothelial sprouting events can be attributed to diffusional transport limitations of nutrients into deeper zones of the vascular co-culture model. In turn, direct perfusion through the fibrin construct resulted in endothelial cell alignment in flow direction during the first three days of culture; however, no tube formation was obtained after 7 days. Indirect perfusion based on the lateral flow direction showed significantly higher sprouting activity and uniformity throughout the hydrogel construct, but also exhibited a reduced vascular network area coverage and decreased average microvessel length. To gain deeper insights into gradient-mediated endothelial sprouting within a 3D matrix, an *in silico* assessment of size-dependent biomolecule distribution was performed. Our finite volume CFD simulations are based on experimental data derived from differently sized and fluorescently labeled dextrans. The selected size range of 10, 20, 40, and 500 kDa soluble molecules correspond to the size of major signaling molecules and growth factors present during vascular network formation. Results from the finite volume CFD simulations on the distribution profiles of differently sized proangiogenic molecules suggest that at least a 1:1 ratio between fresh nutrient supply and elution of reciprocal signaling molecules, produced locally within the hydrogel construct by the co-culture, is best suited to ensure efficient vascular network formation. This ratio corresponds to a balance of delivery of 50% fresh medium supplements and retention of 50% of reciprocal signaling molecules inside the fibrin hydrogel, a comparative graph of supply and elution in both static and dynamic conditions can be found in Fig. 7(a). In summary, we found that the establishment of growth factor gradients via lateral fluid flow on the order of micrometers per second enhances endothelial cell sprouting and heterotypic cell-cell interactions facilitate initial network formation. However, after vessel maturation, spatio-temporal control of direct perfusion in microvascular systems is of utmost importance to ensure proper endothelial phenotype. In other words, direct flow through a hydrogel construct is only beneficial in the presence of mature lumenized microvessels, since adipose-derived stem cell secretome plays a key role in the initial phase of vascular network formation.

SUPPLEMENTARY MATERIAL

See supplementary material for additional information on microchip geometries, finite volume CFD simulations, and FITC-dextran diffusion experiments.

ACKNOWLEDGMENTS

This work was funded by the European Union's INTERREG V-A AT-CZ programme (ATCZ133), the European Union's Horizon 2020 research and innovation programme (685817), the City of Vienna Tissue Engineering International Project (MA 23, #14–06), and the Austrian Research Promotion Agency (FFG; 849791). The authors also thank Carina Huber-Gries for fruitful discussions.

[1]R. Costa-Almeida, P. L. Granja, R. Soares, and S. G. Guerreiro, Eur. Cell Mater. **28**, 51–66 (2014).
[2]M. Lovett, K. Lee, A. Edwards, and D. L. Kaplan, Tissue Eng. Part B, Rev. **15**(3), 353–370 (2009).
[3]E. A. Phelps and A. J. Garcia, Curr. Opin. Biotechnol. **21**(5), 704–709 (2010).
[4]G. D. Yancopoulos, S. Davis, N. W. Gale, J. S. Rudge, S. J. Wiegand, and J. Holash, Nature **407**(6801), 242–248 (2000).
[5]W. Risau, Nature **386**(6626), 671–674 (1997).
[6]K. Pill, S. Hofmann, H. Redl, and W. Holnthoner, Cell Regener. (Lond) **4**, 8 (2015).
[7]K. Gaengel, G. Genove, A. Armulik, and C. Betsholtz, Arterioscler., Thromb., Vasc. Biol. **29**(5), 630–638 (2009).
[8]F. Verseijden, S. J. Posthumus-van Sluijs, P. Pavljasevic, S. O. Hofer, G. J. van Osch, and E. Farrell, Tissue Eng. Part A **16**(1), 101–114 (2010).
[9]S. Merfeld-Clauss, N. Gollahalli, K. L. March, and D. O. Traktuev, Tissue Eng. Part A **16**(9), 2953–2966 (2010).
[10]J. Rehman, D. Traktuev, J. Li, S. Merfeld-Clauss, C. J. Temm-Grove, J. E. Bovenkerk, C. L. Pell, B. H. Johnstone, R. V. Considine, and K. L. March, Circulation **109**(10), 1292–1298 (2004).
[11]S. Rohringer, P. Hofbauer, K. H. Schneider, A. M. Husa, G. Feichtinger, A. Peterbauer-Scherb, H. Redl, and W. Holnthoner, Angiogenesis **17**(4), 921–933 (2014).
[12]D. Wartmann, M. Rothbauer, O. Kuten, C. Barresi, C. Visus, T. Felzmann, and P. Ertl, Front. Mater. **2**, 60 (2015).
[13]D. Sticker, S. Lechner, C. Jungreuthmayer, J. Zanghellini, and P. Ertl, Anal. Chem. **89**(4), 2326–2333 (2017).
[14]M. Rothbauer, H. Zirath, and P. Ertl, Lab Chip **18**(2), 249–270 (2018).
[15]M. Rothbauer, D. Wartmann, V. Charwat, and P. Ertl, Biotechnol. Adv. **33**(6 Pt 1), 948–961 (2015).
[16]M. Rothbauer, I. Praisler, D. Docter, R. H. Stauber, and P. Ertl, Biosensors (Basel) **5**(4), 736–749 (2015).
[17]J. M. Rosser, I. Olmos-Calvo, M. Schlager, M. Purtscher, F. Jenner, and P. Ertl, J. Cell Biol. Cell Metab. **2**, 005 (2015).
[18]K. Aizel, A. G. Clark, A. Simon, S. Geraldo, A. Funfak, P. Vargas, J. Bibette, D. M. Vignjevic, and N. Bremond, Lab Chip **17**(22), 3851–3861 (2017).
[19]I. K. Zervantonakis, S. K. Hughes-Alford, J. L. Charest, J. S. Condeelis, F. B. Gertler, and R. D. Kamm, Proc. Natl. Acad. Sci. U. S. A. **109**(34), 13515–13520 (2012).
[20]J. S. Jeon, S. Bersini, M. Gilardi, G. Dubini, J. L. Charest, M. Moretti, and R. D. Kamm, Proc. Natl. Acad. Sci. U. S. A. **112**(1), 214–219 (2015).
[21]Y. Shin, J. S. Jeon, S. Han, G. S. Jung, S. Shin, S. H. Lee, R. Sudo, R. D. Kamm, and S. Chung, Lab Chip **11**(13), 2175–2181 (2011).
[22]W. A. Farahat, L. B. Wood, I. K. Zervantonakis, A. Schor, S. Ong, D. Neal, R. D. Kamm, and H. H. Asada, PLoS One **7**(5), e37333 (2012).
[23]J. W. Song and L. L. Munn, Proc. Natl. Acad. Sci. U. S. A. **108**(37), 15342–15347 (2011).
[24]C. L. Helm, M. E. Fleury, A. H. Zisch, F. Boschetti, and M. A. Swartz, Proc. Natl. Acad. Sci. U. S. A. **102**(44), 15779–15784 (2005).
[25]K. Haase and R. D. Kamm, Regener. Med. **12**(3), 285–302 (2017).
[26]Q. Smith and S. Gerecht, Curr. Opin. Chem. Eng. **3**, 42–50 (2014).
[27]Y. H. Hsu, M. L. Moya, C. C. Hughes, S. C. George, and A. P. Lee, Lab Chip **13**(15), 2990–2998 (2013).
[28]C. Bonvin, J. Overney, A. C. Shieh, J. B. Dixon, and M. A. Swartz, Biotechnol. Bioeng. **105**(5), 982–991 (2010).
[29]J. S. Jeon, S. Bersini, J. A. Whisler, M. B. Chen, G. Dubini, J. L. Charest, M. Moretti, and R. D. Kamm, Integr. Biol. (Camb) **6**(5), 555–563 (2014).
[30]S. Kim, H. Lee, M. Chung, and N. L. Jeon, Lab Chip **13**(8), 1489–1500 (2013).
[31]A. Sobrino, D. T. T. Phan, R. Datta, X. Wang, S. J. Hachey, M. Romero-López, E. Gratton, A. P. Lee, S. C. George, and C. C. W. Hughes, Sci. Rep. **6**, 31589 (2016).
[32]W. J. Polacheck, M. L. Kutys, J. Yang, J. Eyckmans, Y. Wu, H. Vasavada, K. K. Hirschi, and C. S. Chen, Nature **552**, 258 (2017).
[33]S. Wolbank, A. Peterbauer, M. Fahrner, S. Hennerbichler, M. van Griensven, G. Stadler, H. Redl, and C. Gabriel, Tissue Eng. **13**(6), 1173–1183 (2007).
[34]P. Petzelbauer, J. R. Bender, J. Wilson, and J. S. Pober, J. Immunol. **151**(9), 5062–5072 (1993), available at https://www.ncbi.nlm.nih.gov/pubmed/7691964.
[35]S. Muhleder, K. Pill, M. Schaupper, K. Labuda, E. Priglinger, P. Hofbauer, V. Charwat, U. Marx, H. Redl, and W. Holnthoner, Stem Cell Res. Ther. **9**(1), 35 (2018).
[36]L. Knezevic, M. Schaupper, S. Muhleder, K. Schimek, T. Hasenberg, U. Marx, E. Priglinger, H. Redl, and W. Holnthoner, Front. Bioeng. Biotechnol. **5**, 25 (2017).
[37]E. Zudaire, L. Gambardella, C. Kurcz, and S. Vermeren, PLoS One **6**(11), e27385 (2011).

MANUSCRIPT #5

STIFFNESS MATTERS: FINE-TUNED HYDROGEL ELASTICITY ALTERS CHONDROGENIC REDIFFERENTIATION

Barbara Bachmann, Sarah Spitz, Barbara Schädl, Andreas Teuschl, Heinz Redl, Sylvia Nürnberger, and Peter Ertl

frontiers in Bioengineering and Biotechnology

ORIGINAL RESEARCH
published: 30 April 2020
doi: 10.3389/fbioe.2020.00373

Stiffness Matters: Fine-Tuned Hydrogel Elasticity Alters Chondrogenic Redifferentiation

Barbara Bachmann[1,2,3,4†], Sarah Spitz[1,4†], Barbara Schädl[2,4,5], Andreas H. Teuschl[4,6], Heinz Redl[2,4], Sylvia Nürnberger[2,4,7] and Peter Ertl[1,4*]*

[1] Faculty of Technical Chemistry, Institute of Applied Synthetic Chemistry and Institute of Chemical Technologies and Analytics, Vienna University of Technology, Vienna, Austria, [2] AUVA Research Centre, Ludwig Boltzmann Institute for Experimental and Clinical Traumatology, Vienna, Austria, [3] Competence Center MechanoBiology, Vienna, Austria, [4] Austrian Cluster for Tissue Regeneration, Vienna, Austria, [5] University Clinic of Dentistry, Medical University of Vienna, Vienna, Austria, [6] Department Life Science Engineering, University of Applied Sciences Technikum Wien, Vienna, Austria, [7] Division of Trauma-Surgery, Department of Orthopedics and Trauma-Surgery, Medical University of Vienna, Vienna, Austria

Edited by:
Miloslav Pekař, Brno University of Technology, Czechia

Reviewed by:
Khoon Lim, University of Otago, Christchurch, New Zealand
Felix B. Engel, University Hospital Erlangen, Germany

***Correspondence:**
Sylvia Nürnberger
sylvia.nuernberger@meduniwien.ac.at
Peter Ertl
peter.ertl@tuwien.ac.at

† These authors have contributed equally to this work

Specialty section:
This article was submitted to Biomaterials, a section of the journal Frontiers in Bioengineering and Biotechnology

Received: *22 October 2019*
Accepted: *03 April 2020*
Published: *30 April 2020*

Citation:
Bachmann B, Spitz S, Schädl B, Teuschl AH, Redl H, Nürnberger S and Ertl P (2020) Stiffness Matters: Fine-Tuned Hydrogel Elasticity Alters Chondrogenic Redifferentiation. Front. Bioeng. Biotechnol. 8:373. doi: 10.3389/fbioe.2020.00373

Biomechanical cues such as shear stress, stretching, compression, and matrix elasticity are vital in the establishment of next generation physiological *in vitro* tissue models. Matrix elasticity, for instance, is known to guide stem cell differentiation, influence healing processes and modulate extracellular matrix (ECM) deposition needed for tissue development and maintenance. To better understand the biomechanical effect of matrix elasticity on the formation of articular cartilage analogs *in vitro*, this study aims at assessing the redifferentiation capacity of primary human chondrocytes in three different hydrogel matrices of predefined matrix elasticities. The hydrogel elasticities were chosen to represent a broad spectrum of tissue stiffness ranging from very soft tissues with a Young's modulus of 1 kPa up to elasticities of 30 kPa, representative of the perichondral-space. In addition, the interplay of matrix elasticity and transforming growth factor beta-3 (TGF-β3) on the redifferentiation of primary human articular chondrocytes was studied by analyzing both qualitative (viability, morphology, histology) and quantitative (RT-qPCR, sGAG, DNA) parameters, crucial to the chondrotypic phenotype. Results show that fibrin hydrogels of 30 kPa Young's modulus best guide chondrocyte redifferentiation resulting in a native-like morphology as well as induces the synthesis of physiologic ECM constituents such as glycosaminoglycans (sGAG) and collagen type II. This comprehensive study sheds light onto the mechanobiological impact of matrix elasticity on formation and maintenance of articular cartilage and thus represents a major step toward meeting the need for advanced *in vitro* tissue models to study both re- and degeneration of articular cartilage.

Keywords: cartilage, chondrocytes, 3D cell culture, extracellular matrix, hydrogel, Young's modulus

INTRODUCTION

Articular cartilage is a specialized load-bearing tissue providing the ability of frictionless movement within synovial joints such as the knee, hip or shoulder. Generated by its single resident cell type, the chondrocyte, during embryogenesis the tissue is rearranged to withstand increasing mechanical forces until early adulthood (Carter et al., 2004). Upon reaching musculoskeletal maturity, the

chondrocytes are embedded in a thick interwoven mesh of glycosaminoglycans and collagen type II. Adult articular cartilage is a relatively simple tissue with the extracellular matrix (ECM) forming up to 99% of the tissue while the chondrocytes cease their proliferative activity and acquire a metabolically quiescent state (Camarero-Espinosa et al., 2016). This characteristic simplicity, however, poses a major conundrum: given the absence of vascularization or innervation and the quiescent nature of chondrocytes, cartilage fails to regenerate if damaged by trauma or degenerative diseases (Hunziker et al., 2015). The relatively simple anatomy of cartilage – inhabitation by a single cell type and lack of vascular or nervous system – has led to the assumption that cartilage would be one of the first tissues to be successfully engineered (Temenoff and Mikos, 2000). Instead, primary chondrocyte isolation and cultivation proved to be inherently difficult, with a phenotype switch of primary chondrocytes during *in vitro* expansion posing a central challenge (Schnabel et al., 2002). The main indicators of this loss of differentiated phenotype are (i) an elongated morphology in contrast to chondrotypic sphericity, (ii) a switch from production of articular cartilage-specific collagen type II to fibrous tissue collagen type I and (iii) increased proliferative activity. The reversion into a differentiated phenotype can be achieved, by transferring chondrocytes into a three-dimensional (3D) culture setup within the first couple of passages after isolation (Caron et al., 2012). In other words, chondrocytes need to be cultivated as pellet, on a scaffold or suspended in a hydrogel to achieve chondrogenic behavior *in vitro*. Hydrogels, in particular, are ideally suited for 3D *in vitro* cultures owing to their ease of use, variety and flexibility. Hydrogels are hydrophilic polymeric networks capable of absorbing aqueous solutions multiple times their dry weight and thus present an ideal 3D cellular microenvironment emulating the native ECM characteristics of articular cartilage (Liu et al., 2017). These ECM-mimicking properties can further be exploited by the addition of chondrogenic molecules as well as by fine-tuning matrix elasticity. The elasticity of a matrix describes the resistance that cells feel in response to substrate deformation. Even though the elasticity of bodily tissues ranges from soft brain matter (1 kPa) to stiff collagenous, pre-calcified bone (100 kPa), its implication for *in vitro* tissue modeling is still widely unknown (Discher et al., 2009). While pilot studies in 2D culture substantiate the importance of matrix elasticity on cellular behavior (Engler et al., 2006), comprehensive studies conducted in a 3D environment remain scarce. Especially literature highlighting the influence of matrix elasticity on chondrocyte behavior is heterogenous and inconclusive. While some studies using monolayer cultures suggest that more compliant substrates foster the occurrence and maintenance of chondrogenic phenotypes (Schuh et al., 2010; Park et al., 2011), others mention surfaces exhibiting a cartilage-mimicking elasticity to provide chondroinductive effects (Allen et al., 2012; Du et al., 2016). In turn, the few comprehensive studies using 3D culture systems are challenging to interpret, since they lack comparability due to (a) the different methods used in determining and reporting matrix elasticity, (b) the choice of hydrogel type and elasticity ranges employed, and (c) used different chondrocyte passages, cultivation methods and cell sources (Schuh et al., 2012a; Vonwil et al., 2012). As a consequence of these methodological differences, beneficial effects of both soft, compliant substrates and stiff scaffolds emulating a chondrotypic matrix elasticity have been reported (Schuh et al., 2012b; Wang L. S. et al., 2014; Wang T. et al., 2014; Li et al., 2016). A short overview of current 3D studies investigating the interplay between matrix elasticity and chondrocyte behavior is provided in **Table 1**, further highlighting the heterogenicity of the state of the art.

In this work, the influence of matrix elasticity on primary human chondrocyte redifferentiation embedded in three different hydrogels was investigated in a comprehensive manner to determine the link between matrix elasticity and chondrogenic responses and close the knowledge gap associated with heterogenous prior reports. As visible in the graphical abstract in **Figure 1**, this was accomplished by embedding dedifferentiated human articular chondrocytes (hACs) in two natural hydrogels, fibrin and silk/fibrin, and one synthetic hydrogel, PEG-dextran. Silk fibroin has been added to further modulate matrix degradation and improve chondrogenic properties of fibrin hydrogels (Hofmann et al., 2006). While fibrin is an abundantly used (Hunter et al., 2004) protein-based biopolymer of natural origin that allows for cellular degradation and motility, PEG-dextran, in turn, is a chemically well-defined, highly biocompatible hydrogel that cannot be degraded by chondrocytes. In other words, bioinert PEG-dextran encapsulates chondrocytes resulting in physiologic shape control and movement restriction. Using oscillatory rheology, the matrix elasticity was adjusted to 1 kPa, 15 kPa, and 30 kPa Young's modulus. The three chosen elasticity values represent the values of brain tissue, muscle fibers and that of the matrix surrounding each chondrocyte, the perichondral space, respectively (Guilak et al., 2005; Engler et al., 2006; Discher et al., 2009; Stolz et al., 2009). In addition to varying matrix type and elasticity, primary hACs were stimulated using TGF-β3 to gain insight into potential synergistic effects of matrix elasticity and growth factor presence. In summary, the aim of this study was the establishment of an improved articular cartilage *in vitro* model featuring spherical cell morphology, physiological gene expression as well as cartilaginous matrix deposition. It is envisioned that our improved *in vitro* model integrating biomechanics of articular cartilage can be employed in multiple cultivation systems including microbioreactors and organ-on-a-chip systems to study both re- and degenerative processes of the synovial joint.

MATERIALS AND METHODS

Rheology

To assure that rheological characterization was performed within the linear-viscoelastic regime of each hydrogel as well as within the hydrogel's respective low frequency plateau, rheometer settings were chosen in accordance with published protocols specifically designed for the rheological characterization of hydrogels (Zuidema et al., 2014). For the determination of Young's Moduli, polymeric networks were assumed to display affine behavior. Affine models assume that within the

TABLE 1 | Overview of currently existing 3D chondrocyte models discussing matrix elasticity responses.

Cell source	Passage	Endpoint	Hydrogel	Matrix stiffness	Modulus	Cell density	Outcome	References
Porcine	P2	2 weeks	Agarose	0.75% (3.7 ± 1.9 kPa) 3.5% (53.2 ± 14.64 kPa)	Equilibrium	$6*10^5$/mL	Increased proliferation in softer hydrogels No effect on chondrogenic phenotype	Schuh et al. (2012a)
Rabbit	P2	2 weeks	Gelatin-hydroxyphenylpropionic acid	570 Pa 1000 Pa 2750 Pa	Storage	$1*10^6$/mL	Medium stiffness hydrogel exhibited superior 3D environment	Wang L. S. et al. (2014)
Rabbit	P2–P4	4 weeks	Chitosan-hyaluronic acid dialdehyde	130.78 ± 19.83 kPa 199.35 ± 81.57 kPa 181.47 ± 19.77 kPa	Young's	$5*10^6$/mL	Stiffer gels show spherical morphology and increased matrix synthesis	Thomas et al. (2017)
Bovine	P3	2 weeks	Gelatin- methacryloyl	3.8 ± 0.3 17.1 ± 2.4 29.9 ± 3.4 kPa	Young's	$2*10^7$/mL	Spherical morphology and enhanced matrix synthesis in highest stiffness	Li et al. (2016)
Human	P5	3 weeks	Gelatin - ethyl lysine diisocyanate	450 Pa 850 Pa	Shear	$1*10^6$/construct	Softer gel more efficiently promoted chondrogenic differentiation	Sarem et al. (2018)
Human	P2	3 weeks	Fibrin Silk/Fibrin PEG-dextran	1 kPa 15 kPa 30 kPa	Young's	$1*10^6$/mL	High stiffness fibrin hydrogel induces spherical morphology and chondrogenic matrix synthesis	This study

deformation of the polymeric network the macroscopic strain equals the strain of each individual fiber (Wufsus et al., 2015). Rheological measurements were performed until desired hydrogel compositions displaying designated Young's modulus values of 1 kPa, 15 kPa, and 30 kPa were ascertained.

Hydrogel-dependent gelation kinetics were studied using an MCR 302 WESP rheometer (Anton Paar, Austria), employing a parallel plate geometry (d = 25 mm, stainless steel) at 0.3 mm measuring gap distance. Hydrogel components were mixed thoroughly before injecting and subsequently recording dynamic oscillatory time sweeps [0.1% strain for fibrin (Zuidema et al., 2014) and 10% strain for PEG-dextran as determined by strain sweep shown in S1; 1 Hz] at 37°C. Hydrogel mixtures were applied to the precooled rheometer plate (4°C) to prevent premature polymerization and the measurement gap was sealed using paraffin oil to avoid sample evaporation. To guarantee reproducible data analysis, a simple mathematical evaluation protocol was established. Recorded data was analyzed by generating the first derivative thereof, calculating 10% of the curves slope, followed by averaging the Young's modulus from the first 100 values were the slope falls below 10% of the peak value. The Young's modulus was calculated by the following formula:

$$E = 2G(1 + \nu)$$

where E is the Young's modulus, G is the complex modulus, and ν is the Poisson's Ratio, accounting for the response in the directions orthogonal to the uniaxial stress. An affine network dominated by stretching modes was assumed and therefore a Poisson's ratio of 0.5 was employed for the calculation of the Young's modulus. Each measurement was performed in triplicates and the data represents the average thereof with the corresponding standard deviations.

Primary Human Chondrocyte Isolation

Human articular chondrocytes were collected from the femoral head of three patients undergoing hip replacement, with patient's consent and the approval of the ethical board of the Medical University of Vienna (No 1741/2018). Articular chondrocytes were isolated by 1 h incubation in 0.1% hyaluronidase solution (Sigma-Aldrich, Austria), 0.5 h in 0.1% pronase solution (Roche, Switzerland) followed by overnight incubation in a mixture of 200 U/mL collagenase (Gibco, United States) and 1 U/mL papain (Sigma-Aldrich, Austria). HAC were expanded in monolayer culture until passage two prior to hydrogel embedding. Medium was exchanged twice a week using chondrogenic expansion medium consisting of DMEM high glucose with 10% FCS, 1% antibiotic antimycotic solution, 10 mM HEPES, 6 mM L-glutamine, 5 μg/mL insulin, 50 μg/mL L-ascorbate-2-phosphate (all from Sigma-Aldrich, Austria).

Hydrogel Embedding and 3D Chondrocyte Culture

For hydrogel embedding, primary human chondrocytes in passage 2 were detached from the culture flasks, pelleted and resuspended using a concentration of $4*10^6$ cells/mL. Hydrogel clots were prepared according to compositions given in **Table 2**

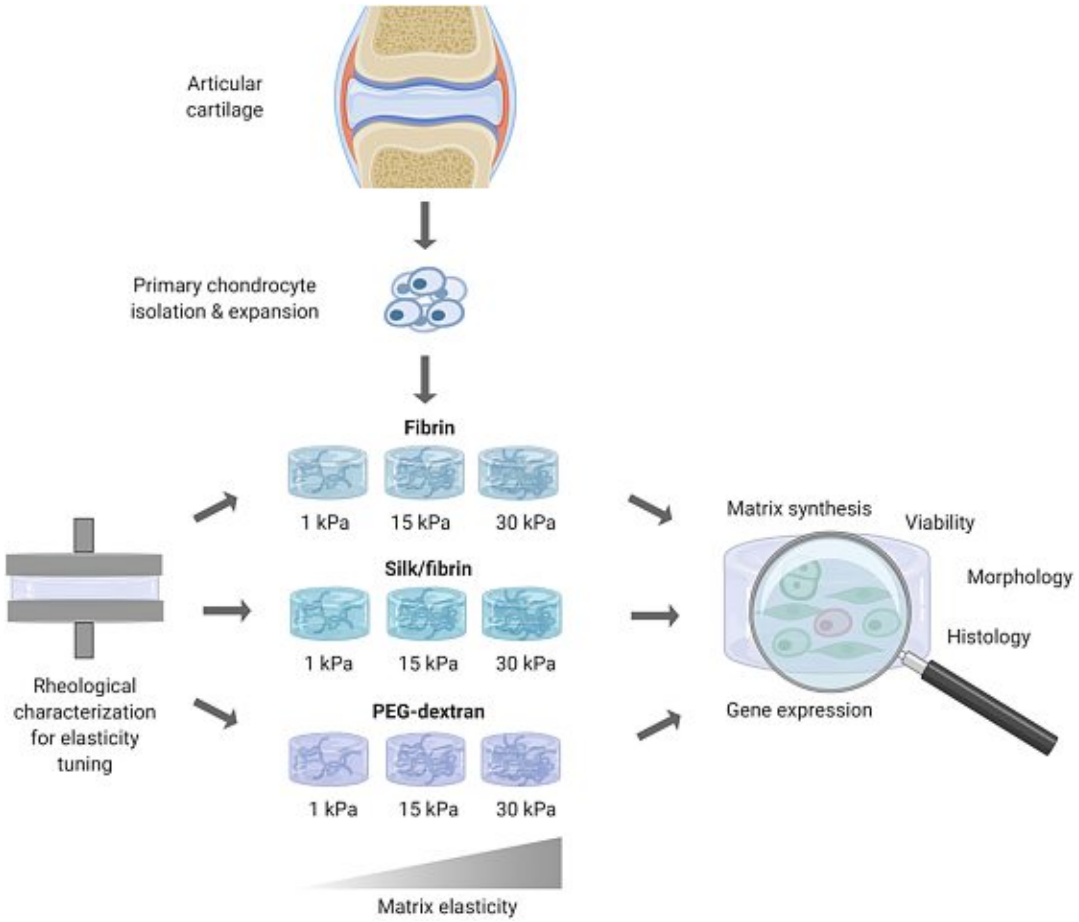

FIGURE 1 | Overview of workflow for redifferentiation analysis of primary human chondrocytes in hydrogels of different elasticities. After rheological measurements for obtaining hydrogels of defined elasticities of 1 kPa, 15 kPa, and 30 kPa Youngs's modulus, primary human chondrocytes where embedded and cultivated for 3 weeks. Chondrogenic redifferentiation was subsequently assessed by viability, histology and quantitative analysis of cartilage matrix components by GAG Assay and RT-qPCR.

TABLE 2 | Rheologically determined loss moduli, storage moduli as well as complex moduli, calculated Young's Moduli and concentrations of respective hydrogel components for fibrin and PEG-dextran hydrogels to achieve predefined elasticities of 1 kPa, 15 kPa and 30 kPa Young's modulus.

Hydrogel	Loss modulus [kPa]	Storage modulus [kPa]	Complex modulus [kPa]	Young's modulus [kPa]	Average gelation time [h]	Component 1	Component 2
Fibrin	0.0182 ± 0.0067	0.37 ± 0.1	0.37 ± 0.1	1.1 ± 0.3	0.87	15 mg/mL Fibrinogen	1 U/mL Thrombin
	0.158 ± 0.095	4.6 ± 0.4	4.6 ± 0.4	13.8 ± 1.3	1.50	27 mg/mL Fibrinogen	1 U/mL Thrombin
	0.307 ± 0.0279	10.6 ± 1	10.6 ± 1	31.8 ± 2.8	1.67	50 mg/mL Fibrinogen	1 U/mL Thrombin
PEG-Dextran	0.0007 ± 0.0002	0.35 ± 0.1	0.35 ± 0.1	1.0 ± 0.3	5.1	2.3 mM PEG-Linker	3 mM SG-Dextran
	0.0018 ± 0.0032	5.4 ± 0.6	5.4 ± 0.6	16.2 ± 1.8	1.6	5 mM PEG-Linker	5.8 mM SG-Dextran
	0.0076 ± 0.0067	9.9 ± 1.0	9.9 ± 1.0	29.6 ± 3	1.5	7.5 mM PEG-Linker	8.2 mM SG-Dextran

and as per manufacturer's instructions. Briefly, fibrin hydrogels were mixed to achieve final concentrations of 15 mg/mL, 27 mg/mL or 50 mg/mL fibrinogen (Tisseel, Baxter, Austria) and 1 U/mL thrombin (Tisseel, Baxter, Austria). Silk/fibrin hydrogels were prepared using the same fibrinogen and thrombin concentrations with the addition of 25% silk fibroin solution isolated from *Bombyx mori* as previously described (Teuschl et al., 2014). Silk fibroin was vortexed for 10 min at 3,000 rpm to induce β-sheet formation (Yucel et al., 2009) prior to mixing with cell suspension and fibrin hydrogel components. PEG-dextran hydrogels (Cellendes, Germany) were generated using 2.3 mM, 5 mM or 7.5 mM PEG-linker and 3 mM, 5.8 mM or 8.2 mM SG-dextran. All hydrogels were prepared in clots with 50 μL volume and a final cell concentration of 1,000 cells/μL hydrogel. Depending on the type of hydrogel, clots polymerized for 30 min up to 1 h before addition of cell culture

medium. Hydrogel clots were cultivated over a period of 21 days with medium changes two times a week. The experiments were conducted using three individually prepared clots per analysis using chondrogenic differentiation medium consisting of DMEM with 1% antibiotic antimycotic solution, 1% L-glutamine, 1% HSA/linoleic acid mixture, 14 µg/mL L-ascorbate-2-phosphate, 1% ITS premix, 1 mM dexamethasone (all from Sigma-Aldrich, Austria) without or with the addition of 10 ng/mL TGF-b3 (R&D Systems, United Kingdom).

Live/Dead Assay

To obtain information on cellular vitality, a viability assay using calcein-AM and ethidium-H1 (Invitrogen, Austria) was performed according to the manufacturer's instructions after a cultivation period of 21 days. Viability was assessed by comparing the number of live cells to total cell count.

Histology

For paraffin histology, the samples were fixed in 4% buffered formalin for 24 h and subsequently rinsed in running tap water for 1 h. Afterward, the samples were transferred to 50% ethanol for 1 h and then stored in 70% ethanol until further processing. For paraffin embedding, the samples were first dehydrated in an uprising series of ethanol and then embedded in paraffin. The samples were cut with a Microm S in 4 µm sections and dried overnight in an incubator at 37°C. After removing the paraffin with xylene and rehydration the slides were stained histochemically with H&E or alcian blue at pH 2.5, which is ideal for the proof of glycosaminoglycans. For staining of collagen type II via immunohistochemistry, the slides were pretreated with pepsin (Sigma-Aldrich, Austria) for 10 min in a humidity chamber at 37°C. Subsequently, endogenous peroxidase and alkaline phosphatase were blocked using the ready-to-use BloxAll (Vector Laboratories, United States) solution for 10 min. Afterward, the slides were blocked with 2.5% normal horse serum (Vector Laboratories, United States). Then the slides were incubated with collagen type II antibody (Neomarkers, United States), 1:100 for 1 h in the Labvision Autostainer 360 (Thermo Scientific, United States). The secondary HRP-anti-mouse antibody (ImmunoLogic, Netherlands) was incubated for 30 min and then the sections were treated with the ImmPACT NovaRed (Vector Laboratories, United States) peroxidase substrate for 6 min. After rinsing the slides in water they were counterstained with hematoxylin, dehydrated and permanently embedded with Consul-mount (Thermo Scientific, Waltham, United States).

RT-qPCR

For gene expression analysis, hydrogel clots were enzymatically digested by adding either 100 U/mL nattokinase solution (Japan Bio Science Laboratory Co., Ltd., Osaka, Japan) for fibrin and silk/fibrin hydrogels (Heher et al., 2015) or a 1:20 dilution of dextranase (Cellendes, Germany) for PEG-dextran hydrogels as per the manufacturer's instructions and subsequently incubated at 37°C for 1 h. Thereafter the digested clots were snap frozen by submersion into liquid nitrogen and stored at −80°C up to the point of analysis. RNA was extracted using TRIzol reagent (Invitrogen, Austria). Total extracted RNA was quantified using a NanoDrop ND-1000 spectrophotometer (Thermo Fisher Scientific Inc., United States) at 260/280 nm and DNA was removed by employing the RQ1 RNAse-Free DNAse Kit (Promega, Austria). Next, complementary DNA (cDNA) was synthesized from 2 µg total RNA employing the OneScript™ cDNA Synthesis Kit (ABM) according to the manufacturers' instructions. Finally, RT-qPCR analysis was accomplished using a Bio-Rad C1000/CFX Cycler as well as the KAPA SYBR Fast Kit (VWR, Austria). To assess both primer quality (see **Table 3**) and required primer concentration an initial standardization was performed using purified total RNA of primary hACs. Fold change in gene expression was calculated by the $2^{-\Delta\Delta CT}$ formula relative to the housekeeping gene B2M and referenced to same-passage chondrocytes cultivated in monolayer.

Glycosaminoglycan Quantification

For quantification of glycosaminoglycans, a standard protocol based on dimethyl-methylene blue (DMMB) precipitation was performed. Prior to the assay, PEG-dextran hydrogels were digested using dextranase (Cellendes, Germany) while no pretreatment was necessary for fibrin and silk/fibrin hydrogels. Briefly, samples were digested using 30 U/mL proteinase K (Sigma-Aldrich, Austria) at 56°C overnight before addition of DMMB (Sigma-Aldrich, Austria) reagent. Precipitates were centrifuged and the pellet was dissociated using decomplexion solution. Subsequently, absorption was measured at 560 nm within a PerkinElmer Ensight™ multimode plate reader. A standard curve was prepared by the dilution of chondroitin sulfate (Sigma-Aldrich, Austria) in phosphate buffered EDTA/cysteine solution.

DNA Quantification

Sample DNA was quantified using a DNA Quantitation Kit Fluorescence Assay (Sigma-Aldrich, Austria) as per the manufacturers' instructions. Briefly, 10 µL of the proteinase K digest was mixed with 200 µL of bisbenzimide H33258 dye. Samples were measured in triplicates using a PerkinElmer Ensight™ multimode plate reader.

Data Analysis

Data was analyzed using GraphPad Prism software. ROUT outlier test was performed on all data sets and significant outliers (Q = 1%) were removed if applicable. Two-way ANOVA as well as Tukey's multiple comparisons test were performed to compare the data sets.

RESULTS AND DISCUSSION

Rheological Characterization of Hydrogels

Fine-tuning of matrix elasticity toward the desired Young's moduli of 1 kPa, 15 kPa, and 30 kPa for fibrin and PEG-dextran

TABLE 3 | Primers employed in gene expression analysis with RT-qPCR.

Gene	Denotation	Characteristics	Forward primer	Reverse primer
ACAN	Aggrecan	ECM component	TCSGAGGACA GCSGAGGCC	TCSGAGGGTGTA GCGTGTASGAGA
Col1	Collagen type I	Dedifferentiation	AGGTGCTGA TGGCTCTCCT	GGACCACTTT CACCCTTGT
Col2	Collagen type II	ECM component	CCACGCTCAA GTCCCTCAAC	AGTCACCGCT CTTCCACTCG
B2M	Beta micro-globulin 2	Housekeeping gene	ACTGAATTCA CCCCCACTGA	CCTCCATGAT GCTGCTTACA

was achieved using oscillatory rheology. Intended elasticity values represent a broad spectrum of matrix stiffness ranging from very soft tissues (e.g., brain tissue), to tissues with medium elasticity (e.g., muscle tissue) up to matrices with high elasticities which mimic the native pericellular microenvironment of the human chondrocyte (Discher et al., 2009). Results of rheological characterization of fibrin and PEG-dextran are listed in **Table 2** featuring loss, storage and complex as well as Young's moduli at the determined hydrogel compositions. Since preliminary rheological assessment of silk fibroin revealed a Young's Modulus below 1 kPa (data not shown), the impact on matrix elasticity of 25% silk fibroin addition to fibrin hydrogels was considered negligible. For fibrin hydrogels, an increase in both storage and loss modulus as well as in Young's modulus was achieved when incrementing total fibrinogen concentration at a constant thrombin concentration of 1 U/mL. Exemplary graphs of hydrogel gelation in **Supplementary Figures S1, S2** show that the storage modulus contributes to a much higher extent to the complex modulus in comparison to the loss modulus, a characteristic behavior for hydrogels suggesting high intrinsic solidity. All examined parameters display linearity along the range of increasing stiffness with Young's moduli ranging from 1.1 ± 0.3 kPa for hydrogels with 15 mg/mL fibrinogen to 13.8 ± 1.3 kPa for hydrogels with 27 mg/mL fibrinogen up to 31.8 ± 2.8 kPa for hydrogels using 50 mg/mL fibrinogen. Overall, hydrogel polymerization was completed within 1–2 h, depending on the hydrogel's stiffness. Similar to the results obtained for fibrin hydrogels, an increase in the Young's moduli of PEG-dextran hydrogels was achieved when increasing both dextran and PEG-linker concentration accordingly, as depicted in **Table 2**. Concentrations of the PEG-linker and dextran ranged from 2.3 mM and 3 mM to attain a PEG-dextran hydrogel of 1.0 ± 0.3 kPa Young's modulus to 5 mM and 5.8 mM for hydrogels of 16.2 ± 1.8 kPa Young's modulus up to 7.5 mM and 8.2 mM for the highest elasticity hydrogels of 29.6 ± 3 kPa Young's modulus. As visible in the gelation plots shown in **Supplementary Figure S1A**, PEG-dextran hydrogels displayed low loss moduli ranging from 0.7 ± 0.2 to 7.6 ± 6.7 Pa coupled with long gelation times of up to 5.1 h. Overall, both fibrin and PEG-dextran hydrogels proved to be well suited for fine-tuning of matrix elasticity.

Hydrogel Type and Elasticity Affect Cell Viability and Morphology

As a first qualitative evaluation of hydrogel-embedded chondrocyte behavior, cellular viability, and morphology were assessed using a calcein-AM-based viability assay after a cultivation time of three weeks. Images depicted in **Figure 2** and **Supplementary Figure S3** showing epifluorescence pictures of the whole hydrogel clot reveal that chondrocyte cultivation in both fibrin and silk/fibrin hydrogels resulted in high cell viabilities irrespective of hydrogel elasticity and growth factor presence. Despite high cell survival in both hydrogels, variations in cell density indicate a both hydrogel and matrix elasticity-dependent response in cell proliferation. For fibrin hydrogels, viability was consistently high with values ranging from 92 ± 6% in 1 kPa hydrogels with TGF-β3 to 99% ± 1% in 30 kPa hydrogels with TGF-β3. Similarly, high viabilities were observed in silk/fibrin hydrogels with values ranging from 89 ± 9% in hydrogels with 1 kPa elasticity with TGF-β3 to 98 ± 1% in 30 kPa hydrogels with TGF-β3. In contrast to these observations, chondrocytes embedded in PEG-dextran hydrogels showed significantly reduced viability as shown in the right panel of **Figure 2**. The viability values steeply declined from 67 ± 1% in 1 kPa hydrogels to no measurable viability in PEG-dextran hydrogels with an elasticity of 30 kPa Young's modulus. This decline in viability may be a result of (a) a decrease in pore size (below 10 nm) with increasing crosslinking density and/or (b) increased cellular encapsulation restricting any cellular motility. The lower panel of **Figure 2** shows exemplary images of chondrocytes embedded in fibrin, silk/fibrin and PEG-dextran hydrogel of 15 kPa Young's modulus without growth factor addition. For a more comprehensive analysis on morphological changes induced by matrix elasticity, **Supplementary Figure S3** shows images of live/dead stained chondrocytes in all three hydrogels of 1 kPa, 15 kPa, and 30 kPa matrix elasticity without and with growth factor supplementation. Comparable trends in cellular morphology were observed in both fibrin and silk/fibrin hydrogels, as visible in the upper panels of **Supplementary Figures S3A,B**. Importantly, chondrocyte sphericity increased while overall cell density decreased with increasing matrix elasticity, indicating a redifferentiated chondrogenic phenotype. Growth factor stimulation with 10 ng/mL TGF-β3 resulted in a more elongated morphology of embedded chondrocytes compared to their non-stimulated counterparts irrespective of matrix elasticity as also described by Lin et al. (2006). While chondrocytes cultivated in all matrix elasticities formed cellular protrusions, the general cell morphology was more elongated in hydrogels of 1 kPa and 15 kPa Young's modulus compared to hydrogels of 30 kPa Young's modulus, where chondrocytes retained a chondrotypic sphericity. In silk/fibrin hydrogels, however, the morphological changes with increasing elasticity were less distinct. In the presence of TGF-β3 stimulation

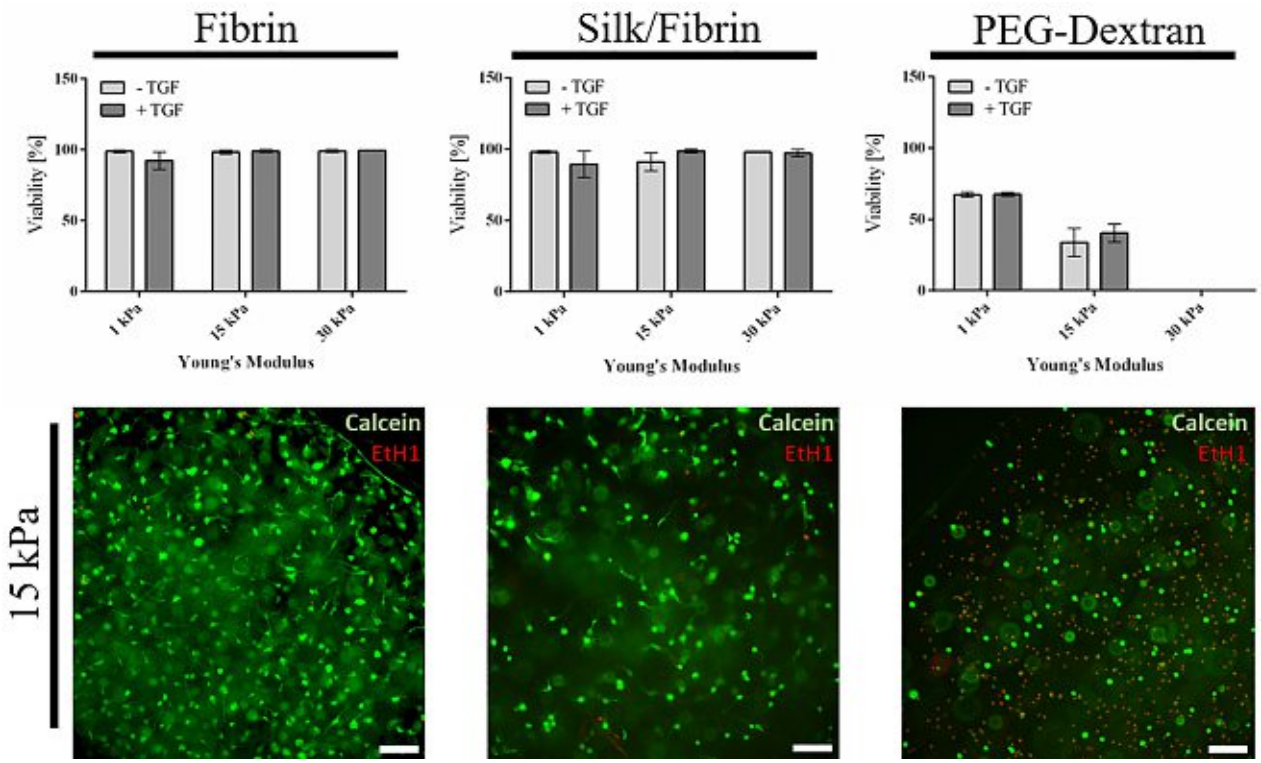

FIGURE 2 | Viability of primary chondrocytes in fibrin, silk fibrin and PEG-dextran hydrogels depicted as mean with SD (n = 9). Fibrin and silk/fibrin hydrogels display high viabilities irrespective of stiffness while viability in PEG-dextran hydrogels declines rapidly with increasing elasticity. Epifluorescent exemplary images of Live(Calcein-AM)/Dead staining (Ethidium-H1) in 15 kPa hydrogels without growth factor addition (below). Scale bar 100 μm.

chondrocytes organized into clusters, predominantly observed in 30 kPa hydrogels as could additionally be observed in histological analysis discussed in section "Increasing Matrix Elasticity Modulates Chondrotypic Morphology and Matrix Deposition." This cluster formation can be explained by a combination of growth factor induced proliferation with a stiffness dependent restriction in cell motility. PEG-dextran hydrogels were specifically chosen to emulate chondrocyte encapsulation similar to widely used agarose and alginate hydrogels while providing matrix tunability and ease-of-use. Even though RGD-peptide was added to PEG-dextran hydrogel to increase hydrogel comparability and ameliorate a possible negative impact of lacking adhesion sites on cell behavior as recommended by the supplier, PEG-dextran hydrogel impaired cellular viability as depicted in **Supplementary Figure S3C**. Interestingly, chondrocytes encapsulated in 15 kPa and 30 kPa hydrogels exhibited a duality in live/dead staining in addition to low cell viabilities as shown in **Figure 2** and **Supplementary Figure S3C**. This behavior, characterized by a red-stained nucleus and green-stained cytoplasm, suggests a hydrogel-inflicted permeability of the cellular membrane. These observations reveal the negative effect of PEG-dextran hydrogels with increasing elasticity on cell behavior. In conclusion, while chondrogenic morphology was supported by high matrix elasticity in the case of both fibrin-based hydrogels, undegradable PEG-dextran hydrogels promoted a spherical morphology in all elasticities but negatively affected cell vitality.

Increasing Matrix Elasticity Modulates Chondrotypic Morphology and Matrix Deposition

To gain deeper insights into morphological changes and ECM synthesis in response to increasing matrix elasticity, histological analysis of 4 μm thin sections was conducted. While H&E staining allows for the assessment of cellular morphology, alcian blue and collagen type II staining were performed to identify *de novo* synthesis of GAG and collagen type II by the embedded chondrocytes. Representative images of histological sections are shown in **Figure 3** for fibrin hydrogel, **Figure 4** for silk/fibrin hydrogel as well as in **Supplementary Figure S4** for PEG-dextran hydrogels. Overall, results of histological analysis demonstrate a morphological trend toward increased number of fully spherical chondrocytes in the presence of high matrix elasticities. H&E staining of fibrin hydrogels, depicted in **Figure 3A**, shows that while a large fraction of chondrocytes exhibited a dedifferentiated elongated or polygonal morphology in hydrogels of 1 kPa and 15 kPa elasticity, almost all chondrocytes displayed a physiologic round morphology in 30 kPa hydrogels. Furthermore, stimulation with TGF-β3 seems to result in an increased cell density in all hydrogels, suggesting

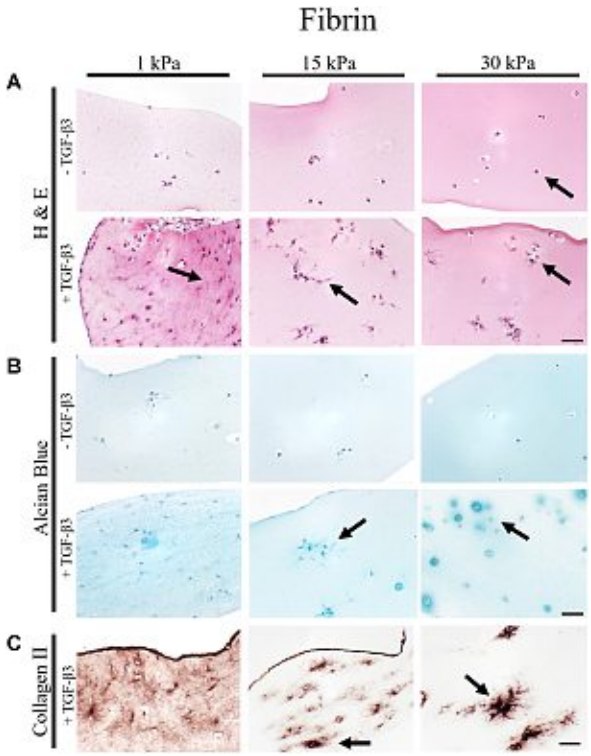

FIGURE 3 | Histological images of 4 μm thick sections of primary chondrocytes in fibrin hydrogels of 1 kPa, 15 kPa, and 30 kPa elasticity stained with **(A)** H&E for morphology, **(B)** alcian blue for sGAG and **(C)** collagen II. Scale bar 50 μm. Arrows highlight visible morphological differences in the presence of increasing matrix elasticity and growth factor stimulation, where elongated, fibroblastic morphology is found in softer hydrogels, and chondrotypic spherical morphology in 30 kPa hydrogels. Growth factor stimulation resulted in an overall increase in cell numbers with stiffness-depended cell distribution including cellular cluster formations in 30 kPa hydrogels.

an elevated proliferation rate. While this growth-factor induced proliferation resulted in an even distribution of chondrocytes with dedifferentiated fibroblastic morphology in hydrogels with the lowest elasticity, chondrocytes embedded in 15 kPa and 30 kPa hydrogels formed small cellular clusters. Especially, chondrocytes in 30 kPa hydrogels were found to be densely packed and formed circular clusters, underlining a restricted cellular motility at increased matrix stiffness.

To assess the effect of hydrogel elasticity on matrix deposition, histological sections were stained with alcian blue to highlight sulfated sGAG, one of the key components of the native ECM. **Figure 3B** shows an increased presence of sGAG with increasing matrix stiffness only when stimulated with TGF-β3. Differences in sGAG deposition between hydrogels of low, medium and high elasticities can be associated with varying matrix distributions. Particularly striking was the formation of small alcian blue-positive halos around many spherical chondrocytes in fibrin hydrogels of the highest matrix elasticity. The presence of these halos resembles the pericellular and interterritorial matrix in chondrons, a characteristic feature of native cartilage tissue. In contrast to this chondrotypic behavior in 30 kPa hydrogels, sGAG staining was evenly spread throughout the hydrogel in fibrin hydrogels with the lowest matrix elasticity of 1 kPa Young's modulus. To confirm physiological behavior within hydrogels of increasing matrix elasticity, immunohistochemical staining of the most common cartilaginous matrix protein, collagen type II, was performed. Results in **Figure 3C** reveal fibrillar collagen type II staining loosely distributed throughout the whole hydrogel at 1 kPa Young's modulus and in-between cell clusters in 15 kPa hydrogels. In 30 kPa hydrogels collagen type II fibrils are co-localized with the alcian blue staining and densely packed around the chondrocyte clusters. In other words, chondrocytes embed themselves within a thick, native ECM-enriched microenvironment only when exposed to physiologic matrix elasticities.

In the case of silk modified fibrin hydrogels, shown in **Figure 4**, similar trends in chondrogenic morphology and native ECM deposition were observed with increasing matrix elasticity. Remarkably, the formation of small, chondron-like halos around each spherical chondrocyte in hydrogels with an elasticity of 30 kPa was also visible in this blended fibrin hydrogel (arrow **Figure 4A**). SGAG distribution in higher elasticity matrices shows striking similarity to *in vivo* cartilage, highlighting the positive effect of perichondral space-like matrix stiffness mimicked by 30kPa silk/fibrin hydrogels. Similar to observations in fibrin hydrogels, chondrocytes stimulated with TGF-β3 in 1 kPa silk/fibrin hydrogels exhibited a dedifferentiated fibroblastic morphology. The beneficial effect of TGF-β3 stimulation on ECM synthesis is demonstrated in **Figures 4B,C**, where sGAG and collagen type II production are clearly visible. Location of sGAGs as well as collagen type II again coincided with cellular distribution. In 1 kPa Young's modulus hydrogels, both chondrocytes and ECM molecules were evenly distributed throughout the whole hydrogel clot. In contrast, sGAG secretion was mainly allocated with single spherical chondrocytes in silk/fibrin hydrogels of 15 kPa Young's modulus or with chondrocyte clusters in 30 kPa Young's modulus hydrogels. Overall, collagen type II was most pronounced in 30 kPa silk/fibrin hydrogels where chondrocytes generated a thick collagen type II matrix. Final histological analysis of chondrocytes embedded in PEG-dextran hydrogels showed no obvious differences in morphology as the synthetic, undegradable hydrogel encapsulates the cells in a spherical morphology. Additionally, **Supplementary Figure S4** shows no increase in cell number despite TGF-β3 stimulation pointing at a hydrogel-associated restriction disenabling cellular motility. Confirming previous findings of reduced cellular viability, histological sections depict cellular debris and empty hydrogel pockets.

In summary, fibrin and silk/fibrin hydrogels with elasticities of 30 kPa resembling the stiffness of the perichondral space most effectively support chondrogenic redifferentiation based on spherical morphology and synthesis of native sulfated glycosaminoglycans as well as collagen type II. In contrast, chondrocytes embedded in elasticities resembling brain tissue exhibited a dedifferentiated elongated morphology but still synthesized cartilage-associated ECM molecules.

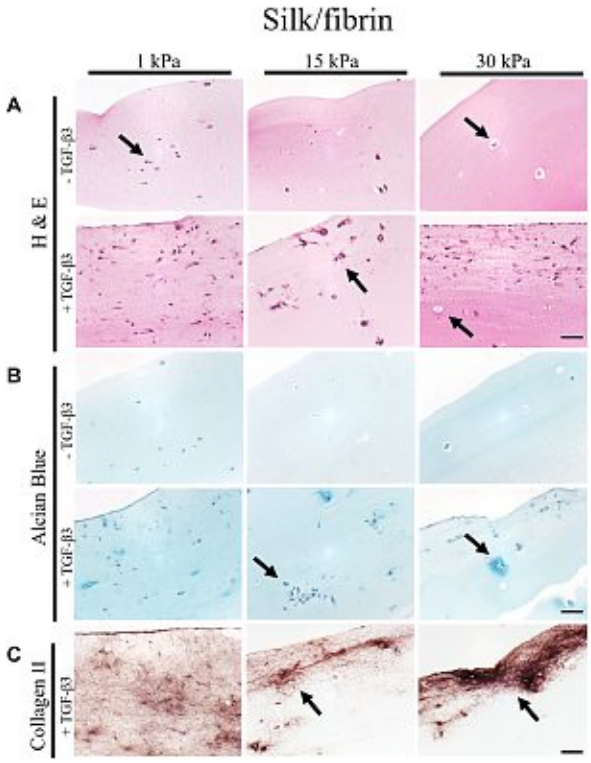

FIGURE 4 | Histological images of 4 μm thick sections primary chondrocytes in silk/fibrin hydrogels of 1 kPa, 15 kPa and 30 kPa elasticity stained with **(A)** H&E for morphology, **(B)** alcian blue for sGAG and **(C)** collagen II. Scale bar 50 μm. Arrows highlight visible in the presence of increasing matrix elasticity and growth factor stimulation, resulting in enhanced chondrotypic sphericity with increasing hydrogel stiffness and cell cluster formation at 30 kPa hydrogels. Additional stimulation with growth factor resulted in massive formation of cartilage matrix collagen II around the clusters.

Quantitative Analysis of Matrix Components

To emphasize the qualitative observations from histological analysis, redifferentiation of primary human chondrocytes was assessed quantitatively using both RT-qPCR of collagen type I, collagen type II as well as aggrecan and glycosaminoglycan quantification. Redifferentiation indices in **Figure 5** were calculated using the expression profiles of cartilaginous collagen type II in relation to dedifferentiated collagen type I. Individual gene expression changes are displayed in **Supplementary Figure S5**. Additionally, redifferentiation was evaluated based on the expression of aggrecan, an integral part of the cartilaginous matrix. In unstimulated fibrin hydrogels (left panel of **Figure 5A**) a minor increase in the redifferentiation index from 0.71 ± 0.05 in the softest hydrogels of 1 kPa Young's modulus to 1.75 ± 1.15 in fibrin hydrogels of 30 kPa Young's modulus was observed. A more prominent difference, however, was discernible in TGF-β3 stimulated cultures, where chondrocyte redifferentiation significantly increased with incremental changes in matrix elasticity. Here, redifferentiation indices ranged from 324 ± 88 for fibrin hydrogels of 1 kPa Young's modulus to 470 ± 177 for 15 kPa hydrogels up to 1051 ± 212 for 30 kPa hydrogels resembling the elasticity of the native perichondral environment. It is important to note that the addition of TGF-β3 resulted in a 600-fold increase in the redifferentiation index, confirming the synergistic effects of growth factor TGF-β3 and native elasticity. In turn, the observed upregulation of collagen type I (see **Supplementary Figure S5**) in soft hydrogels clearly points at an undesired fibrocartilaginous response. The outcome that fibrin hydrogels of 30 kPa elasticity ideally support the differentiation process of primary human chondrocytes is additionally supported by an increase in aggrecan expression in TGF-ß3-unstimulated as well as in stimulated cultures as displayed in **Figure 5A** (lower panel). Fold change values were slightly elevated from 18.5 ± 4.4 in 1 kPa hydrogels to 28.6 ± 13.0 in 30 kPa hydrogels for unstimulated cultures and significantly increased from 20.5 ± 4.5 in 15 kPa hydrogels to 49.0 ± 7.0 in 30 kPa hydrogels following TGF-β3 stimulation. A similar correlation was observed for sGAG synthesis as results shown in **Figure 5B** (left panel) revealed the highest sGAG content of 1.55 ± 0.19 μg sGAG/μg DNA for TGF-β3 treated fibrin hydrogels of 30 kPa matrix elasticity. In comparison, 1.21 ± 0.08 μg sGAG/μg DNA was detected in 1 kPa hydrogels and 1.16 ± 0.1 μg sGAG were synthesized per μg DNA in hydrogels of 15 kPa matrix elasticity. Interestingly, the addition of 25% silk fibroin to the fibrin hydrogel negatively affected the expression of cartilaginous proteins as visible in the middle panel of **Figure 5**. While collagen type II expression in hydrogels without growth factor stimulation remained below the limit of detection, collagen type I expression was downregulated in the absence and presence of TGF-β3 with increasing matrix elasticity as depicted in the middle panel of **Figure 5A** and **Supplementary Figure S5** (middle panel). For the remaining elasticities (e.g., 1 kPa and 15 kPa), the redifferentiation indices were almost 10-fold decreased compared to pure fibrin hydrogels with values of 40.2 ± 19.6 and 32.9 ± 3.6 for 1 kPa and 15 kPa hydrogels, respectively. Remarkably, a reverse trend was observed for aggrecan expression and sGAG synthesis, where ECM production was lowest with highest hydrogel elasticity. For aggrecan synthesis, this relates to a fold change of 21.3 ± 7.9 in 1 kPa hydrogels and 4.2 ± 0.4 in 15 kPa hydrogels. This upregulation in aggrecan expression and increased synthesis of sulfated glycosaminoglycans in the softest 1 kPa silk/fibrin hydrogels as shown in **Figure 5B** may be attributed to miscibility issues in higher stiffness hydrogels. The right panel in **Figure 5** displays gene expression and sGAG synthesis profiles in PEG-dextran hydrogels. Despite limited cellular viability, redifferentiation indices incrementally increased with increasing matrix elasticity for TGF-β3 supplemented hydrogels, with mean index values of 35.5 ± 12.0, 65.6 ± 14.6 for 1 kPa and 15 kPa hydrogels, respectively. For PEG-dextran hydrogels of 30 kPa elasticity, however, no gene expression activity of collagen type I or collagen type II could be detected, probably owed to the limited chondrocyte viability in these hydrogels. Correspondingly, gene expression results related to 15 kPa and 30 kPa hydrogels must be interpreted with caution due to the small amounts of surviving cells within said hydrogels. Similar trends of declining ECM synthesis with the loss of cell vitality

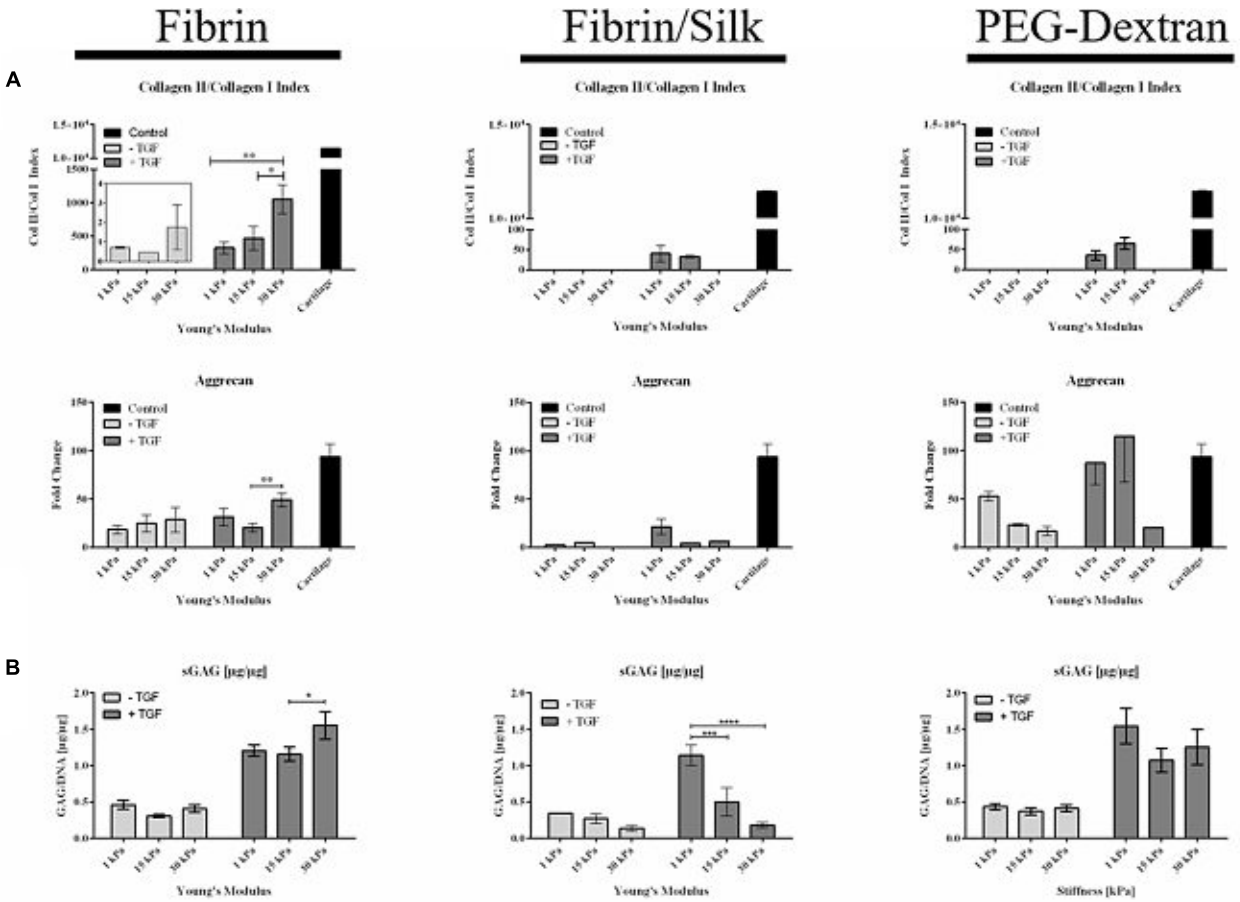

FIGURE 5 | (A) Gene expression of redifferentiation indices and aggrecan expression in the presence of increasing hydrogel stiffness, resulting in incremental increases of collagen type II and aggrecan synthesis using fibrin hydrogels. In turn, in the presence of PEG-dextran hydrogels native amount of aggrecan synthesis was observed (results should be interpreted with caution due to low cell vitality). **(B)** Quantification of synthesized sGAG per µg DNA in fibrin, silk/fibrin and PEG-dextran hydrogel of varied elasticity again showed an improved redifferentiation behavior in fibrin hydrogels with increasing matrix elasticity. All results depicted as mean with SEM. $n = 9$; $^{*}p < 0.1$; $^{**}p < 0.05$; $^{***}p < 0.01$; $^{****}p < 0.001$.

were seen in gene expression levels of aggrecan as well as sGAG content. However, aggrecan expression was slightly elevated in TGF-β3 stimulated PEG-dextran hydrogels of 15 kPa elasticity with a value of 115 ± 47 compared to 87.3 ± 22.3 in 1 kPa hydrogels. This means that the gene expression of aggrecan is comparable to levels in native cartilage controls, pointing at a positive chondrogenic effect of the PEG-dextran encapsulation. Additional quantification of sulfated glycosaminoglycans, visible in the right panel of **Figure 5B**, similarly revealed a significant decline in sGAG synthesis with increasing matrix elasticity and decreasing cell viability. As an example, values in PEG-dextran hydrogels with TGF-β3 stimulated chondrocytes declined from 1.14 ± 0.14 µg sGAG/µg DNA in 1 kPa hydrogels to 0.50 ± 0.19 µg sGAG/µg DNA in 15 kPa hydrogels down to 0.18 ± 0.04 µg sGAG/µg DNA in 30 kPa hydrogels. In contrast to observations in fibrin and silk/fibrin hydrogels, where DNA content, depicted in **Supplementary Figure S6**, increased twofold in all hydrogels upon growth factor stimulation, TGF-β3 failed to elicit proliferative activity in PEG-dextran hydrogels as corroborated by matching DNA quantities in both unstimulated and stimulated cultures.

CONCLUSION

This study was aimed at elucidating the effect of matrix elasticity on the redifferentiation of primary human chondrocytes to obtain an optimized *in vitro* model for articular cartilage trauma and disease. Three well known hydrogels, fibrin, silk/fibrin and PEG-dextran were selected based on stiffness-tunability and characterized using oscillatory rheology. Hydrogel composition was adjusted to achieve defined matrix elasticities representing the stiffness of a wide range of bodily tissues including the elasticity of the perichondral space ($E = 30$ kPa). Rheological assessment revealed the suitability of both fibrin and PEG-dextran hydrogels for fine-tuning of matrix elasticity up to 30 kPa Young's modulus. Results of this study clearly demonstrate the superior chondrogenic properties of pure

fibrin over both silk-modified fibrin and PEG-dextran. In more detail, fibrin hydrogel supported high cell viabilities and chondrotypic behavior with increasing matrix stiffness associated with the hallmarks of redifferentiation, spherical morphologies, and especially matrix synthesis (Caron et al., 2012). Matrices mimicking the perichondral space guided chondrocytes not only to form small halos, resembling native cartilage chondrons, but also to generate a thick cartilaginous matrix composed of sGAGs and collagen type II. In other words, chondrocytes cultivated in pure fibrin hydrogels embedded themselves within a native ECM-enriched microenvironment under physiologic matrix elasticity, especially upon stimulation with TGF-β3. Additional beneficial effects of perichondral space-like matrix elasticity were further corroborated by elevated redifferentiation indices of collagen type II versus collagen type I and sGAG synthesis. Although the addition of 25% silk fibroin, intended to support chondrogenic differentiation, showed high viability and increased chondrotypic morphology with increasing matrix stiffness, it adversely affected redifferentiation capacity of embedded chondrocytes. As a result, we do not recommend the addition of silk fibroin to improve chondrogenic behavior of primary chondrocytes without additional assessment. In the case of PEG-dextran, physiologic morphologies were induced irrespective of matrix elasticity, but chondrocytes failed to remain viable especially in matrices of high stiffness, probably due to pore sizes below 10 nm restricting cell motility, proliferation and nutrient supply. Although dextran-based hydrogels generally seem to support chondrogenic redifferentiation based on elevated aggrecan gene expression, cell vitality becomes the key limiting factor.

In summary, we report the interplay between biomechanical cues, matrix composition and biochemical factors as a key aspect modulating chondrogenic phenotype. Only redifferentiated chondrocytes are capable of generating an *in vitro* cartilage analog, which is crucial for reliably generating functional tissue models of the synovial joint. In the last decade, conflicting information on the effect of matrix stiffness on chondrocytic behavior has been published and reliable knowledge of 3D biomechanical cues is still in its infancy. Consequently, our detailed study represents an important step in elucidating physiologically relevant matrix elasticity on cellular behavior.

DATA AVAILABILITY STATEMENT

The raw data supporting the conclusions of this article will be made available by the authors, without undue reservation, to any qualified researcher.

AUTHOR CONTRIBUTIONS

BB, SN, and PE designed the study. BB and SS executed experiments, performed RT-qPCR and sGAG quantification and analyzed the data. BS conducted histological sectioning and staining of the specimens. BB, SS, AT, SN, and HR interpreted the data. BB, SS, and PE drafted the manuscript with section contributions from BS, SN, and AT. All authors revised and approved the final manuscript.

FUNDING

This work was partly funded by the European Union's INTERREG V-A AT-CZ programme (ATCZ133). The authors acknowledge TU Wien University Library for financial support through its Open Access Funding Program.

ACKNOWLEDGMENTS

The authors want to acknowledge Marian Fürsatz for primary human chondrocyte isolation and cultivation and Michaela Stainer for assisting in RNA isolation and RT-qPCR execution and analysis. Additionally, the authors want to recognize Stefan Baudis for assistance in oscillatory rheology and Elias Salzer for silk fibroin isolation. The graphical abstract (**Figure 1**) was created using BioRender.com.

SUPPLEMENTARY MATERIAL

The Supplementary Material for this article can be found online at: https://www.frontiersin.org/articles/10.3389/fbioe.2020.00373/full#supplementary-material

FIGURE S1 | Loss, storage, and complex modulus as well as Young's Modulus development of PEG-dextran hydrogels during gelation (n = 3). Frequency sweep and strain sweep of polymerized PEG-dextran hydrogels for the adequate selection of rheological parameters.

FIGURE S2 | Loss modulus, storage, and complex modulus as well as Young's Modulus development of fibrin hydrogels during gelation (n = 3).

FIGURE S3 | Viability of primary chondrocytes determined by Live (Calein-AM)/Dead (Ethidium-H1) staining in **(A)** fibrin, **(B)** silk fibrin and **(C)** PEG-dextran hydrogels of 1 kPa, 15 kPa and 30 kPa elasticity without and with addition of TGF-β3. Pictures show epifluorescence images of whole hydrogel clots. (Scale bar: 100 μm).

FIGURE S4 | Histological images of primary chondrocytes in PEG-dextran hydrogels of 1 kPa, 15 kPa, and 30 kPa elasticity stained with **(A)** H & E for morphology, **(B)** alcian blue for sGAG and **(C)** collagen type II antibodies. (Scale bar: 50 μm).

FIGURE S5 | Gene expression of collagen type I and collagen type II in fibrin, silk/fibrin and PEG-dextran hydrogels of different elasticities. Depicted as mean with SEM (n = 9). *p < 0.1; **p < 0.05; ***p < 0.01; ****p < 0.001.

FIGURE S6 | Quantification of total sGAG and total DNA amount per hydrogel for fibrin, silk/fibrin and PEG-dextran. Depicted as mean with SEM (n = 9). *p < 0.1; **p < 0.05; ***p < 0.01; ****p < 0.001.

REFERENCES

Allen, J. L., Cooke, M. E., and Alliston, T. (2012). ECM stiffness primes the TGFbeta pathway to promote chondrocyte differentiation. *Mol. Biol. Cell.* 23, 3731–3742. doi: 10.1091/mbc.e12-03-0172

Camarero-Espinosa, S., Rothen-Rutishauser, B., Foster, E. J., and Weder, C. (2016). Articular cartilage: from formation to tissue engineering. *Biomater. Sci.* 4, 734–767. doi: 10.1039/c6bm00068a

Caron, M. M., Emans, P. J., Coolsen, M. M., Voss, L., Surtel, D. A., Cremers, A., et al. (2012). Redifferentiation of dedifferentiated human articular chondrocytes: comparison of 2D and 3D cultures. *Osteoarthritis Cartilage* 20, 1170–1178. doi: 10.1016/j.joca.2012.06.016

Carter, D. R., Beaupre, G. S., Wong, M., Smith, R. L., Andriacchi, T. P., and Schurman, D. J. (2004). The mechanobiology of articular cartilage development and degeneration. *Clin. Orthop. Relat. Res.* 427, S69–S77.

Discher, D. E., Mooney, D. J., and Zandstra, P. W. (2009). Growth factors, matrices, and forces combine and control stem cells. *Science* 324, 1673–1677. doi: 10.1126/science.1171643

Du, J., Zu, Y., Li, J., Du, S., Xu, Y., Zhang, L., et al. (2016). Extracellular matrix stiffness dictates Wnt expression through integrin pathway. *Sci. Rep.* 6:20395. doi: 10.1038/srep20395

Engler, A. J., Sen, S., Sweeney, H. L., and Discher, D. E. (2006). Matrix elasticity directs stem cell lineage specification. *Cell* 126, 677–689. doi: 10.1016/j.cell.2006.06.044

Guilak, F., Alexopoulos, L. G., Haider, M. A., Ting-Beall, H. P., and Setton, L. A. (2005). Zonal uniformity in mechanical properties of the chondrocyte pericellular matrix: micropipette aspiration of canine chondrons isolated by cartilage homogenization. *Ann. Biomed. Eng.* 1, 1312–1318. doi: 10.1007/s10439-005-4479-7

Heher, P., Maleiner, B., Pruller, J., Teuschl, A. H., Kollmitzer, J., Monforte, X., et al. (2015). A novel bioreactor for the generation of highly aligned 3D skeletal muscle-like constructs through orientation of fibrin via application of static strain. *Acta Biomater.* 24, 251–265. doi: 10.1016/j.actbio.2015.06.033

Hofmann, S., Knecht, S., Langer, R., Kaplan, D. L., Vunjak-Novakovic, G., Merkle, H. P., et al. (2006). Cartilage-like tissue engineering using silk scaffolds and mesenchymal stem cells. *Tissue Eng.* 12, 2729–2738. doi: 10.1089/ten.2006.12.2729

Hunter, C. J., Mouw, J. K., and Levenston, M. E. (2004). Dynamic compression of chondrocyte-seeded fibrin gels: effects on matrix accumulation and mechanical stiffness. *Osteoarthritis Cartilage* 12, 117–130. doi: 10.1016/j.joca.2003.08.009

Hunziker, E. B., Lippuner, K., Keel, M. J., and Shintani, N. (2015). An educational review of cartilage repair: precepts & practice–myths & misconceptions–progress & prospects. *Osteoarthritis Cartilage* 23, 334–350. doi: 10.1016/j.joca.2014.12.011

Li, X., Chen, S., Li, J., Wang, X., Zhang, J., Kawazoe, N., et al. (2016). 3D culture of chondrocytes in gelatin hydrogels with different stiffness. *Polymers* 8:269. doi: 10.3390/polym8080269

Lin, Z., Willers, C., Xu, J., and Zheng, M. H. (2006). The chondrocyte: biology and clinical application. *Tissue Eng.* 12, 1971–1984. doi: 10.1089/ten.2006.12.1971

Liu, M., Zeng, X., Ma, C., Yi, H., Ali, Z., Mou, X., et al. (2017). Injectable hydrogels for cartilage and bone tissue engineering. *Bone Res.* 5:17014. doi: 10.1038/boneres.2017.14

Park, J. S., Chu, J. S., Tsou, A. D., Diop, R., Tang, Z., Wang, A., et al. (2011). The effect of matrix stiffness on the differentiation of mesenchymal stem cells in response to TGF-beta. *Biomaterials* 32, 3921–3930. doi: 10.1016/j.biomaterials.2011.02.019

Sarem, M., Arya, N., Heizmann, M., Neffe, A. T., Barbero, A., Gebauer, T. P., et al. (2018). Interplay between stiffness and degradation of architectured gelatin hydrogels leads to differential modulation of chondrogenesis in vitro and in vivo. *Acta Biomater.* 69, 83–94. doi: 10.1016/j.actbio.2018.01.025

Schnabel, M., Marlovits, S., Eckhoff, G., Fichtel, I., Gotzen, L., Vecsei, V., et al. (2002). Dedifferentiation-associated changes in morphology and gene expression in primary human articular chondrocytes in cell culture. *Osteoarthritis Cartilage* 10, 62–70. doi: 10.1053/joca.2001.0482

Schuh, E., Hofmann, S., Stok, K., Notbohm, H., Muller, R., and Rotter, N. (2012a). Chondrocyte redifferentiation in 3D: the effect of adhesion site density and substrate elasticity. *J. Biomed. Mater. Res. A* 100, 38–47. doi: 10.1002/jbm.a.33226

Schuh, E., Hofmann, S., Stok, K. S., Notbohm, H., Muller, R., and Rotter, N. (2012b). The influence of matrix elasticity on chondrocyte behavior in 3D. *J. Tissue Eng. Regen. Med.* 6, e31–e42. doi: 10.1002/term.501

Schuh, E., Kramer, J., Rohwedel, J., Notbohm, H., Muller, R., Gutsmann, T., et al. (2010). Effect of matrix elasticity on the maintenance of the chondrogenic phenotype. *Tissue Eng. Part A* 16, 1281–1290. doi: 10.1089/ten.tea.2009.0614

Stolz, M., Gottardi, R., Raiteri, R., Miot, S., Martin, I., Imer, R., et al. (2009). Early detection of aging cartilage and osteoarthritis in mice and patient samples using atomic force microscopy. *Nat. Nanotechnol.* 4, 186–192. doi: 10.1038/nnano.2008.410

Temenoff, J. S., and Mikos, A. G. (2000). Review: tissue engineering for regeneration of articular cartilage. *Biomaterials* 21, 431–440. doi: 10.1016/s0142-9612(99)00213-6

Teuschl, A. H., Neutsch, L., Monforte, X., Runzler, D., van Griensven, M., Gabor, F., et al. (2014). Enhanced cell adhesion on silk fibroin via lectin surface modification. *Acta Biomater.* 10, 2506–2517. doi: 10.1016/j.actbio.2014.02.012

Thomas, L. V., Vg, R., and Nair, P. D. (2017). Effect of stiffness of chitosan-hyaluronic acid dialdehyde hydrogels on the viability and growth of encapsulated chondrocytes. *Int. J. Biol. Macromol.* 104, 1925–1935. doi: 10.1016/j.ijbiomac.2017.05.116

Vonwil, D., Trussel, A., Haupt, O., Gobaa, S., Barbero, A., Shastri, V. P., et al. (2012). Substrate elasticity modulates TGF beta stimulated re-differentiation of expanded human articular chondrocytes. *Drug Deliv. Transl. Res.* 2, 351–362. doi: 10.1007/s13346-012-0080-4

Wang, L. S., Du, C., Toh, W. S., Wan, A. C., Gao, S. J., and Kurisawa, M. (2014). Modulation of chondrocyte functions and stiffness-dependent cartilage repair using an injectable enzymatically crosslinked hydrogel with tunable mechanical properties. *Biomaterials* 35, 2207–2217. doi: 10.1016/j.biomaterials.2013.11.070

Wang, T., Lai, J. H., Han, L. H., Tong, X., and Yang, F. (2014). Chondrogenic differentiation of adipose-derived stromal cells in combinatorial hydrogels containing cartilage matrix proteins with decoupled mechanical stiffness. *Tissue Eng. Part A* 20, 2131–2139. doi: 10.1089/ten.tea.2013.0531

Wufsus, A. R., Rana, K., Brown, A., Dorgan, J. R., Liberatore, M. W., and Neeves, K. B. (2015). Elastic behavior and platelet retraction in low- and high-density fibrin gels. *Biophys. J.* 108, 173–183. doi: 10.1016/j.bpj.2014.11.007

Yucel, T., Cebe, P., and Kaplan, D. L. (2009). Vortex-induced injectable silk fibroin hydrogels. *Biophys. J.* 97, 2044–2050. doi: 10.1016/j.bpj.2009.07.028

Zuidema, J. M., Rivet, C. J., Gilbert, R. J., and Morrison, F. A. (2014). A protocol for rheological characterization of hydrogels for tissue engineering strategies. *J. Biomed. Mater. Res. B Appl. Biomater.* 102, 1063–1073. doi: 10.1002/jbm.b.33088

Conflict of Interest: The authors declare that the research was conducted in the absence of any commercial or financial relationships that could be construed as a potential conflict of interest.

MANUSCRIPT #6

MICROFLUIDIC NUTRIENT GRADIENT-BASED THREE-DIMENSIONAL CHONDROCYTE CULTURE-ON-A-CHIP AS AN IN VITRO EQUINE ARTHRITIS MODEL

Julie Rosser, Barbara Bachmann, Christian Jordan, Iris Ribitsch, Eva Haltmayer, Sinan Gültekin, Sini Junttila, Bence Galik, Attila Gyenesei, Bahram Haddadi, Michael Harasek, Monika Egerbacher, Peter Ertl, and Florien Jenner

Materials Today Bio 4 (2019) 100023

Contents lists available at ScienceDirect

Materials Today Bio

journal homepage: www.journals.elsevier.com/materials-today-bio

Microfluidic nutrient gradient–based three-dimensional chondrocyte culture-on-a-chip as an in vitro equine arthritis model

J. Rosser [c,d], B. Bachmann [c,d], C. Jordan [c], I. Ribitsch [a], E. Haltmayer [a], S. Gueltekin [a], S. Junttila [b], B. Galik [b], A. Gyenesei [b], B. Haddadi [c], M. Harasek [c], M. Egerbacher [a], P. Ertl [c,*], F. Jenner [a]

[a] Department of Equine Surgery, University of Veterinary Medicine, Veterinärplatz 1, 1210 Vienna, Austria
[b] BIOCOMP, Bioinformatics & Scientific Computing VBCF, Vienna Biocenter Core Facilities GmbH, GmbH, Dr. Bohr Gasse 3, 1030 Vienna, Austria
[c] Faculty of Technical Chemistry, Vienna University of Technology, Getreidemarkt 9, 1060 Vienna, Austria

ARTICLE INFO

Keywords:
Organ-on-a-Chip
Cartilage
Primary cells
Tissue-on-a-Chip

ABSTRACT

In this work, we describe a microfluidic three-dimensional (3D) chondrocyte culture mimicking *in vivo* articular chondrocyte morphology, cell distribution, metabolism, and gene expression. This has been accomplished by establishing a physiologic nutrient diffusion gradient across the simulated matrix, while geometric design constraints of the microchambers drive native-like cellular behavior. Primary equine chondrocytes remained viable for the extended culture time of 3 weeks and maintained the low metabolic activity and high Sox9, aggrecan, and Col2 expression typical of articular chondrocytes. Our microfluidic 3D chondrocyte microtissues were further exposed to inflammatory cytokines to establish an animal-free, *in vitro* osteoarthritis model. Results of our study indicate that our microtissue model emulates the basic characteristics of native cartilage and responds to biochemical injury, thus providing a new foundation for exploration of osteoarthritis pathophysiology in both human and veterinary patients.

1. Introduction

Articular cartilage is exposed to high loads and stresses during joint loading and has limited regenerative capacity. Hence, damage to articular cartilage commonly leads to osteoarthritis, the most common joint disease, which affects 10–12% of the adult population [1]. Despite the high incidence of osteoarthritis, currently no disease-modifying treatments are available, motivating large-scale research efforts. Animal models including sheep, goats, mice, rabbits, dogs, and horses are validated for cartilage research. Among these, the horse, which also suffers from naturally occurring osteoarthritis, provides the closest approximation to human articular cartilage and subchondral bone thicknesses [2]. However, animal trials are expensive and controversial because of ethical considerations, creating the demand for alternative, ethically responsible, and economic research methods. Among others [3], one promising alternative is organ-on-a-chip technology, where the recreation of physiological conditions promotes the formation of tissue-like structures on a microchip platform [4,5]. Another benefit of organ-on-a-chip technology is the inherent flexibility in design, which allows for relevant concentration gradients and shear force conditions [6], both vital to cartilage physiology and function. For instance, an integrated microfluidic device was used to investigate the effects of growth factor gradients on morphology and proliferation of rabbit articular chondrocytes embedded in Matrigel [7]. A microphysiological cartilage-on-a-chip model that applied strain-controlled compression to three-dimensional (3D) articular cartilage microtissues demonstrated that a 30% confined compression recapitulates the mechanical factors involved in osteoarthritis pathogenesis [8]. Another example integrated a microfluidic base in a multichamber bioreactor containing human bone marrow stem cell (hBMSC)–derived constructs to create tissue-specific microenvironments in which chondral and osseous tissues develop and mature [9]. Despite these recent advances, existing microfluidic technologies are either not scalable and/or do not fully recapitulate the physiological cartilage niche in terms of its *in vivo* physical dimensions, nutrient availability, and time-dependent

* Corresponding author.
E-mail address: peter.ertl@tuwien.ac.at (P. Ertl).
[d] contributed equally.

https://doi.org/10.1016/j.mtbio.2019.100023
Received 23 April 2019; Received in revised form 30 July 2019; Accepted 31 July 2019
Available online 19 August 2019

diffusion gradients inside the matrix, as well as shear forces. It is also important to note that articular cartilage is an avascular and relatively acellular tissue with the single-cell population, chondrocytes, only being nourished by the synovial fluid through diffusion. The chondrocytes contribute significantly to the stability and integrity of the tissue by synthesizing a strong extracellular matrix (ECM) mainly consisting of collagen type II and proteoglycans [10]. In addition, the functional role of articular cartilage is reflected by its unique organization into three different zones including (a) the superficial zone toward the synovial cavity of the joint, where chondrocytes show a flattened morphology [11]; (b) the middle zone with chondrocytes exhibiting a more typical, spherical morphology surrounded by more randomly arranged collagen fibers and high amounts of aggrecan, a glucosaminoglycan (GAG) typical for articular cartilage; and (c) the deep zone that has the lowest cell density but high contents of aggrecan and collagen fibrils [12].

To combine the need for device scalability, ease of use, and proper tissue functionality, the premise of our work was to recreate an approximate 1:1 articular cartilage model in a single step by inducing chondrocyte redifferentiation that promotes spontaneous self-organization into cartilaginous tissue structures such as the superficial zone [13]. This is achieved by loading hydrogel-embedded primary (equine) chondrocytes into a 3-mm-long and 1-mm-high semicircular tissue chamber designed to establish defined, unidirectional, and reproducible nutrient concentration gradients across the *in vitro* tissue constructs. Additional regular media exchanges provide cyclic shear stress on chondrocytes residing at the hydrogel to media interface, thus mimicking joint movement resulting in fresh nutrient supply. In this work, we show that our microfluidic 3D chondrocyte culture-on-a-chip array features a number of relevant cartilage characteristics including structural organization, cellular morphologies, and gene expression patterns, as well as limited proliferative capacity and low metabolic activity of resident chondrocytes. Furthermore, we demonstrate that on-chip–established equine cartilage microtissues strongly react to biochemical injury using inflammatory mediators and also respond to triamcinolone steroid treatment, a well-known veterinary therapy option.

2. Results and discussion

2.1. Organ-on-a-chip specifications and design characterization

Owing to articular cartilage's avascular nature, nutrient transport in native tissue is mainly accomplished by joint movement and subsequent diffusion from the synovial cavity into the cartilage tissue [3]. In other words, nutrient gradients are present across the cartilage thickness which drive cellular behavior [14] and need to be accounted for in the design of the biological niche on chip. Fig. 1A shows the optimized tissue chamber geometry emulating the *in vivo* cartilage thickness of the equine stifle joint featuring a 3-mm-wide and 1-mm-high semispherical cultivation chamber adjacent to a rectangular medium supply channel. It is important to highlight that although simple, the present device configuration supports the main tissue requirements including (i) formation of nutrient gradients across the tissue construct without perfusion, (ii) application of periodic shear stress and fresh nutrient supply to the chondrocytes residing at the matrix to fluid interface, and (iii) reliable loading of cell-laden hydrogel to establish reproducible 3D environments for chondrocyte redifferentiation, cultivation, and maturation (Fig. 1). Using our simple chamber design, high cellular viability of chondrocytes was maintained over a period of 28 days as shown by live cell staining in Fig. 1B and S1A. Staining primary chondrocytes with 5-chloromethylfluorescein diacetate (CMFDA Cell Tracker Green™ Dye), a cytoplasmic dye that only persists in viable cells [15], also allowed for morphology assessment inside the turbid fibrin hydrogel. Chondrocyte morphologies are distinct and change from elongated at the superficial layer and round in the middle and deep layers, as shown in Fig. 1C and E. In addition, sectioning and histological evaluation as well as gene expression analysis are accomplished after extracting the complete 3D chondrocyte constructs (Fig. 1D) from the microarray. For instance, Fig. 1D shows hematoxylin and eosin (H&E) staining of the superficial layer, indicating a clear alignment along the medium channel featuring elongated cells. Elongation is most likely caused by medium exchange resulting in a nutrient-rich zone at the biointerface, which promotes cell migration and proliferation from the deeper zones of the hydrogel. Cell migration from the middle and deeper zones strongly points at the

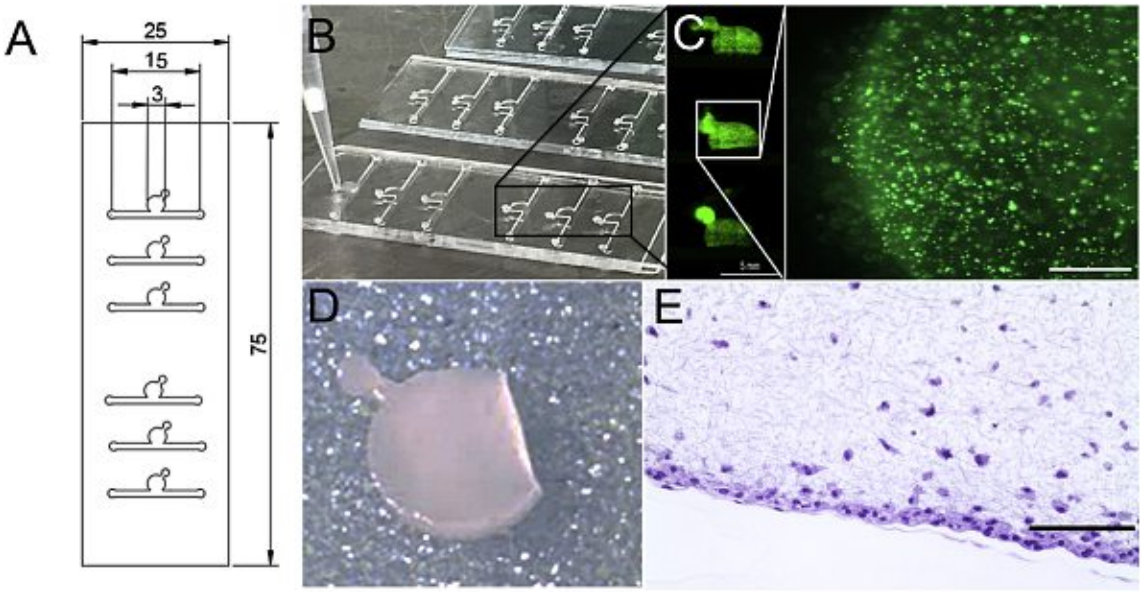

Fig. 1. (A) CAD design of cartilage-on-a-chip device featuring six individually addressable circular chambers on one object slide, enabling multiplexing of experiments. (B) Photograph of an actual cartilage-on-a-chip device with glass slide as the top layer and PDMS slab with microstructures as the bottom layer showing loading of cell-laden hydrogel in the top chamber using a pipette tip. (C) Lift side showing overview picture of three cell culture chambers and right side showing one individual culture chamber featuring CMFDA-stained primary equine chondrocytes cultivated on-chip for 21 days. Scale bars 5 mm and 500 μm. (D) Intact cell-laden fibrin hydrogel clot released from the device before downstream analyses and (E) histological section of chondrocytes-on-a-chip. Scale bar 100 μm. CMFDA, 5-chloromethylfluorescein diacetate

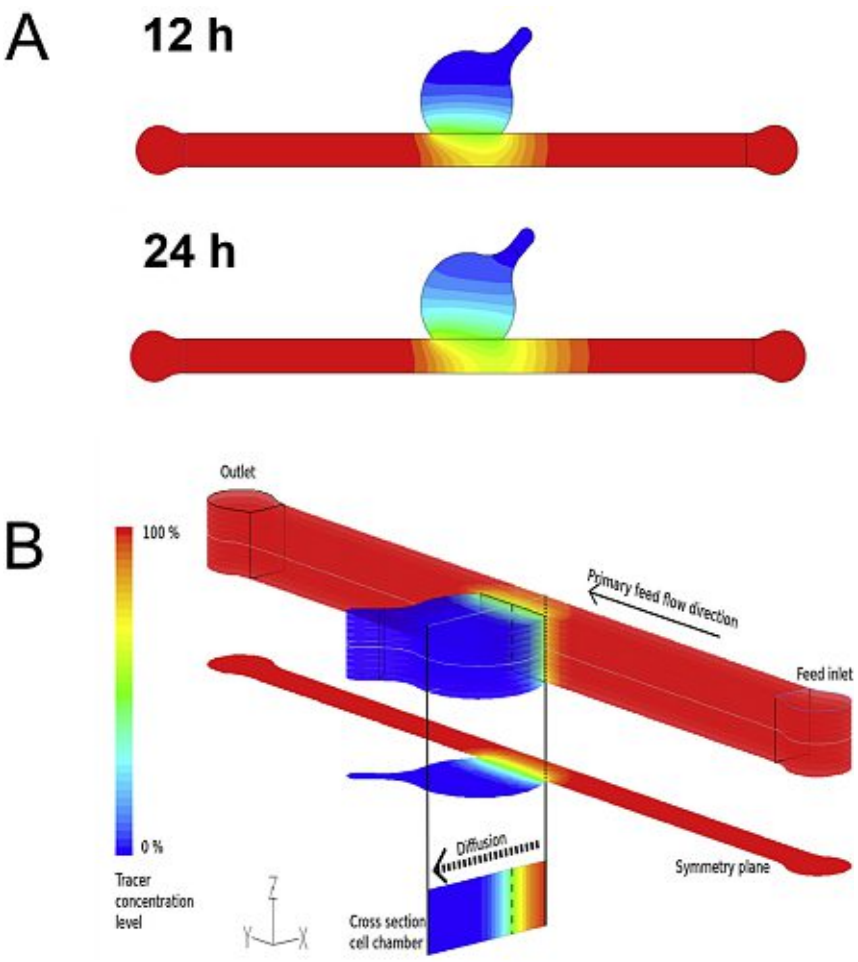

Fig. 2. (A) Finite volume (CFD) simulation of diffusion distance of a 40-kDa-sized biomolecule 12 h and 24 h after addition and (B) 3D representation of a 40-kDa-sized biomolecule 12 h after addition, demonstrating the establishment of a diffusion gradient. CFD, computational fluid dynamics.

presence of a nutrient gradient across the 3D hydrogel construct. To gain a deeper understanding of gradient formation across the 20-mg mL^{-1} fibrin hydrogel construct, a series of CFD-finite volume simulations were performed to portray small (0.3 kDa) and large (40 kDa) molecule diffusion [6], as well as glucose (0.18 kDa) consumption, using a previously reported consumption rate of 1.28 × 10−7 mol/(L·s) [16]. Results of the first computational fluid dynamics (CFD) calculation are shown in Fig. 2A describing the time-dependent formation of a nutrient gradient based on an average protein of 40 kDa after 12 h and 24 h. Interestingly, even after 24 h of cultivation, a defined and stable nutrient gradient is still present across the 3-mm tissue chamber. A 3D representation of the established nutrient gradient is shown in Fig. 2B, further highlighting the diffusion-based nutrient supply in the present device configuration. In other words, the geometric features of the tissue chamber provide optimized conditions to cultivate chondrocyte tissue constructs inside a microfluidic device. In an attempt to investigate the established gradients in more detail, diffusion distance and speed were calculated for a large (40 kDa) protein and small (0.3 kDa) biomolecules to gain a deeper insight into the nutrient distributions within the hydrogel construct. Fig. 3A shows distance-concentration profiles of a 40-kDa protein over time. Results of the simulation demonstrate that at a distance larger than 2 mm from the fluid interface, only 10% of large molecules reach the deeper zone of the chondrocyte construct within 24 h. The constant nutrient limitation beyond the threshold of 2 mm represents similar conditions as found in deep-zone cartilage [17]. While at the bio-interface, a constant nutrient supply of at least 50% is present, at a distance of 1 mm, a time-dependent protein gradient is established ranging from 15% to 23% after 12 h and 24 h, respectively. In turn, Fig. 3B shows that small molecules (0.3 kDa) are rapidly distributed across the entire hydrogel chamber after medium exchange, resulting in a 50% and 75% concentration after 6 h and 24 h, respectively. In addition, simulations including the consumption rate of chondrocytes, shown in Fig S2A, confirm constant supply of glucose to all cells within the hydrogel construct. Time-resolved representations of all conditions can be found in the supplementary video 1. Overall, a reproducible and reliable gradient-based nutrient supply offer optimal cell culture conditions for 3D hydrogel-based chondrocytes.

Supplementary video related to this article can be found at https://doi.org/10.1016/j.mtbio.2019.100023.

2.2. Development of gradient-based microfluidic chondrocyte culture

The biological impact of the gradient-based 3D cell culture condition within our microfluidic device was investigated in subsequent experiments to determine (a) cell morphology, (b) cellular metabolism, (c) gene expression, and (d) histology. All microfluidic cultures (3000 cells/mm^3) were compared with same-passage, same-donor monolayer chondrocyte cultures (2500 cells/cm^2) as controls. Results of our cell morphology experiments are shown in Fig. 4A revealing spherical cell morphologies, a hallmark of articular chondrocytes, which increased from day one to day 8 from 84% to 99% of round cells, remaining at this level throughout prolonged gradient-based 3D culture. In addition to spherical cellular

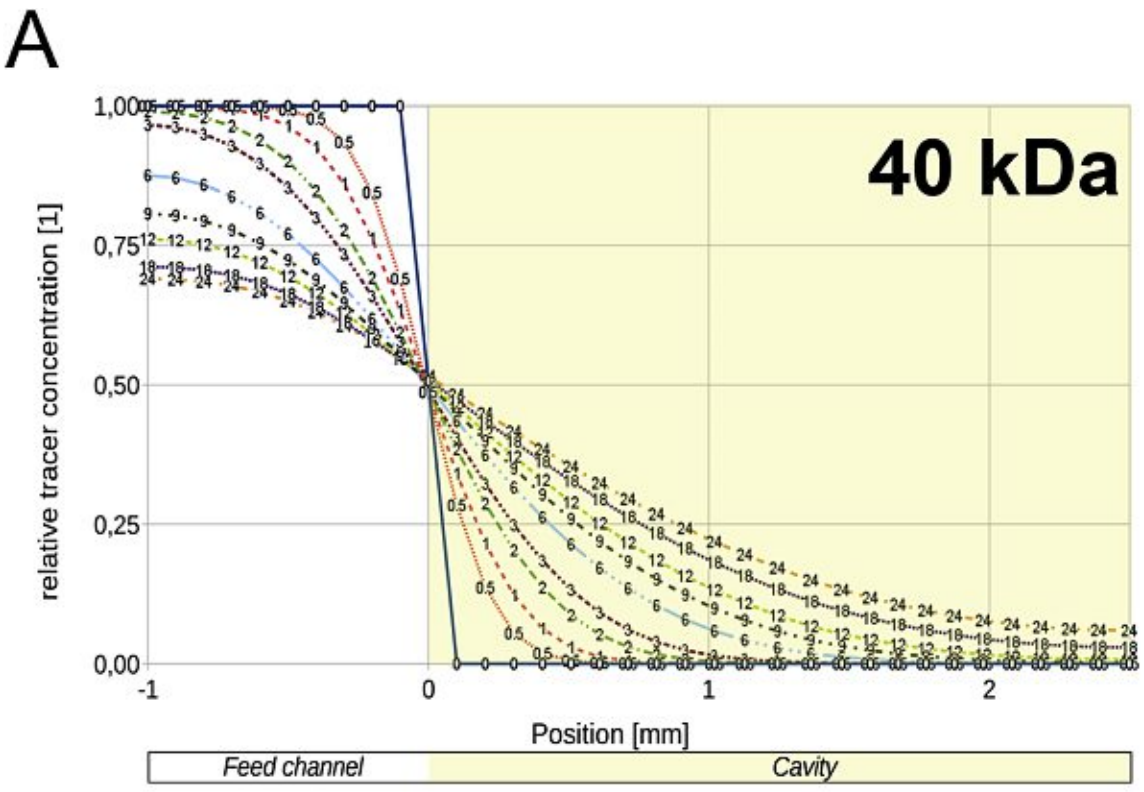

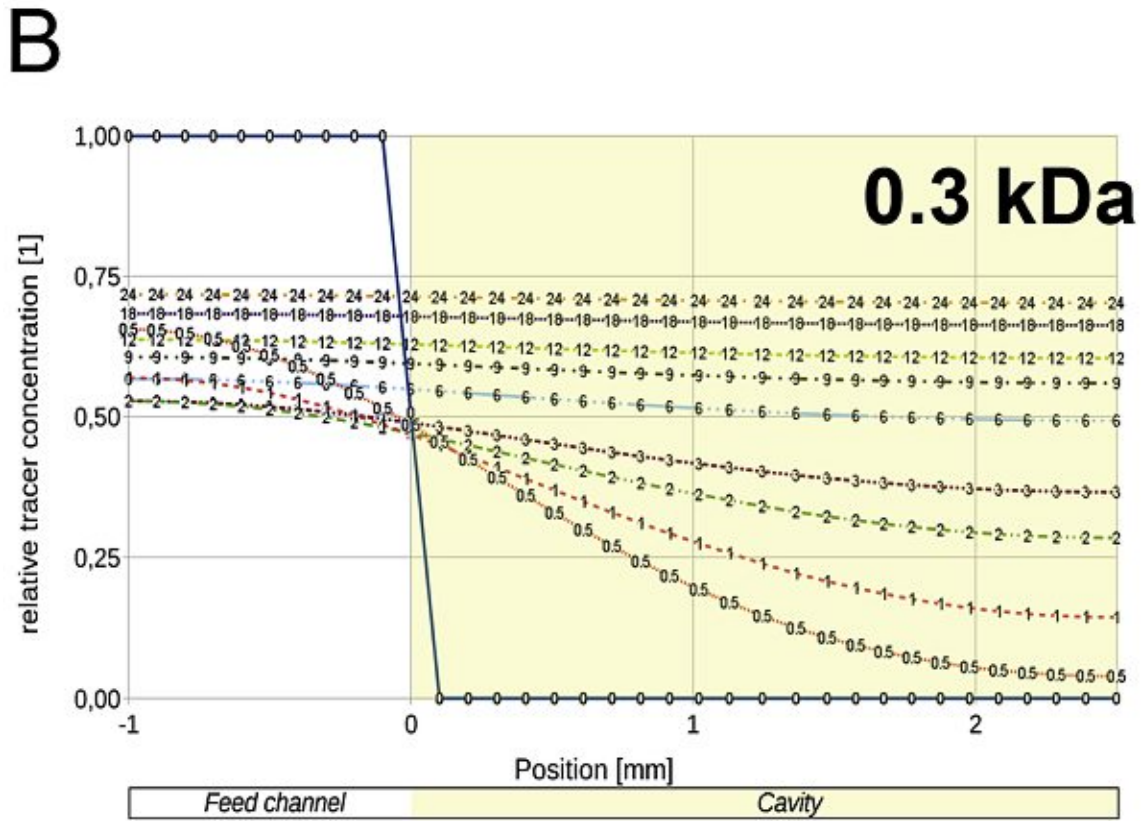

Fig. 3. Comparison of diffusion distance and speed of (A) 40-kDa-sized and (B) 0.3-kDa-sized biomolecules into the fibrin hydrogel at various time points up to 24 h. A nutrient gradient is formed for the 40-kDa-sized molecule, stabilizing in the time frame of 12 h–24 h, while the 0.3-kDa-sized molecule diffuses rapidly into the culture chamber and levels out at 75% of feed concentration.

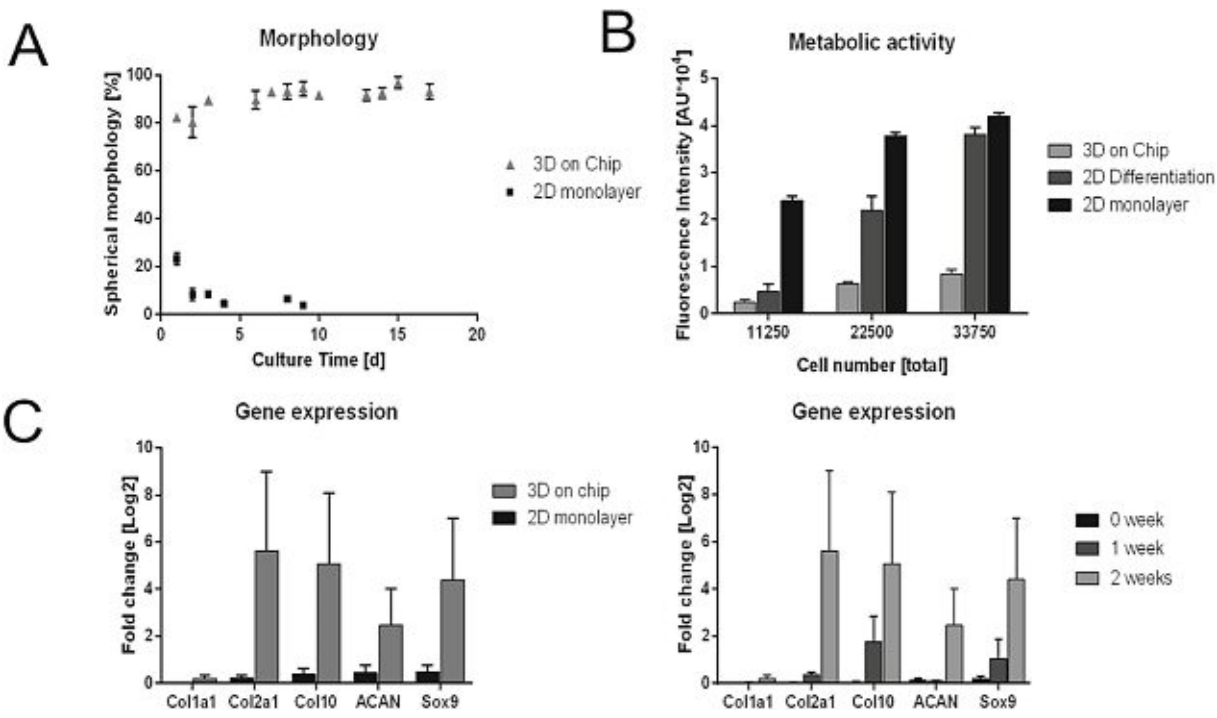

Fig. 4. (A) Comparison of cell morphologies between 3D chondrocyte cultures and monolayer cultures. (B) Metabolic activities of 2D chondrocytes in the presence of Ham's F12 medium chondrogenic differentiation medium as well as 3D chondrocytes. (C) Gene expression patterns of 3D chondrocyte cultures compared with monolayer cultivation after 2 weeks of cultivation (left) and changes in gene expression during cultivation (right).

morphologies, low metabolic activities are an important indicator of physiological behavior of mature native articular chondrocytes. Metabolic activity was compared between 2D monolayer and 3D hydrogel primary chondrocyte cultures via Resazurin-based TOX8 Assay. Results in Fig. 4B display lowest metabolic activities by chondrocytes cultivated in 3D hydrogels on chip, while highest metabolic rates are present in chondrocytes in 2D culture. The resulting sevenfold reduction in metabolic activity under gradient-based microfluidic 3D culture conditions highlights the redifferentiated status of the chondrocytes-on-chip. To verify that the redifferentiation seen on chip was due to the 3D gradient-based conditions and not associated with factors in the medium, a comparison of chondrogenic differentiation medium with Ham's F12 was performed in monolayer cultures. As evidenced by the 40% reduction in metabolic rates when chondrocytes were cultured in chondrogenic differentiation medium vs. Ham's F12 medium, an influence toward phenotypic behavior is noted. Further reduction in the metabolic rate was observed under microfluidic 3D culture conditions, demonstrating that the metabolism of on-chip–cultivated 3D chondrocytes resembles the low metabolic activity seen *in vivo* [18]. Although limited metabolic activity is an indicator of articular chondrocyte behavior, gene expression analysis is needed to substantiate chondrocytic phenotype. To compare expression of cartilage matrix proteins aggrecan (Acan), collagen type 2 (Col2), and a marker for chondrogenic differentiation (Sox9), real-time quantative PCR (RT-qPCR) analysis was performed on the microtissues. Fig. 4C (left panel) highlights the differences in gene expression between 3D and 2D chondrocyte cultures after a period of two weeks in culture. All relevant chondrogenic markers including Col2 and Acan are upregulated within the 3D hydrogel-based chondrocyte constructs. In addition, expression of Col1 is downregulated, thus pointing at the establishment of a stable chondrogenic phenotype. Fig. 4C (right panel) demonstrates time-dependent upregulation in 3D hydrogel chondrocyte constructs of Sox9, Acan, and Col2 chondrogenesis markers, supporting the earlier observations of successful redifferentiation of chondrocytes-on-chip. To further investigate whether discernible tissue remodeling also took place on chip in the presence of gradient-based cultivation conditions, a series of histological investigations were performed. After 3 weeks of culture, 3D chondrocyte microtissues were fixed in formalin, harvested, and subsequently analyzed after sectioning under H&E, Safranin O, and Ki67 staining to visualize chondrocyte organization and morphology, proteoglycan deposition, and cell proliferation. Histology results (shown in S1B) revealed the absence of cell proliferation and little to no appreciable proteoglycan secretion. Although some indication of the formation of cartilage-relevant extracellular matrix was present, the cultivation period of 3 weeks was not sufficient for substantial accumulation of proteoglycans in the matrix. Overall, these results support the redifferentiation capacity of primary chondrocytes inside our microfluidic device including (a) spherical morphologies, (b) low metabolic activity, (c) cartilage-related phenotype, and (d) limited proliferation.

2.3. *Evidence of osteoarthritis-mimicking response to inflammation and treatment*

In a final set of experiments, established chip-based 3D chondrocyte constructs were exposed to an inflammatory environment to induce a biochemical injury associated with osteoarthritis. Inflammation of the microtissue was incited after 1 week of culture via biochemical stimulation using 50 pg/mL of tumor necrosis factor (TNF)-α and interleukin (IL)-1β [19], and cellular responses were analyzed by RT-qPCR. A comparison between healthy control and biochemically injured microtissues is shown in Fig. 5A. After 24 h of stimulation, all inflammatory mediators aggrecanase (ADAMTS5), interleukin (IL-6), matrixmetalloproteinases (MMP-1, MMP-3, and MMP-13), as well as ColX, were significantly upregulated (black bars). These results point at an inflammatory phenotype and beginning hypertrophic differentiation in stimulated cultures, thus supporting the onset of an osteoarthritic

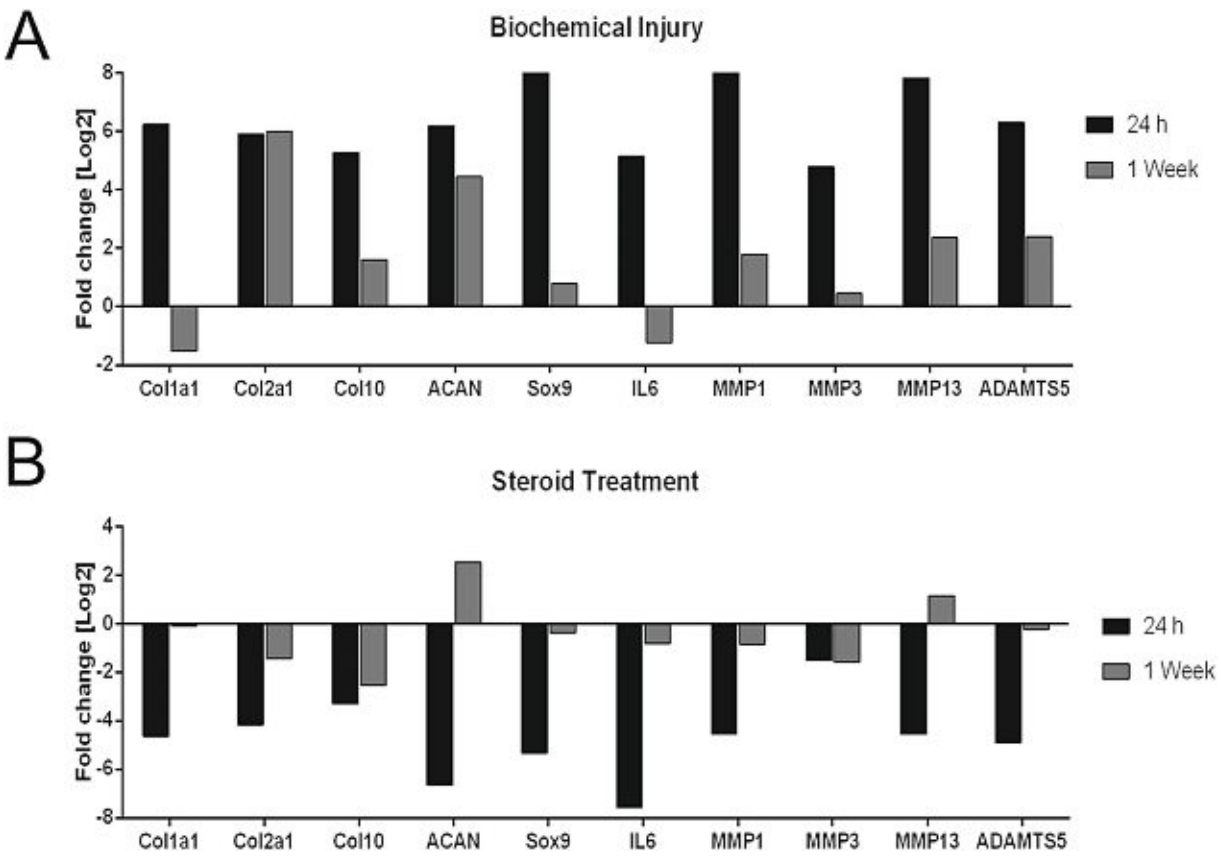

Fig. 5. (A) Gene expression levels of biochemically inflamed microtissues after 1 week of culture and 24-h exposure with 50 pg/mL of TNF-α and IL-1β at day 7 and 2 weeks after stimulation. (B) Gene expression levels of biochemically inflamed microtissues in the presence of 60 μg/mL of triamcinolone, an inflammation inhibiting steroid. TNF-α, tumor necrosis factor-α; IL-1β, interleukin-1β.

microenvironment. However, two weeks after biochemical stimulation (gray bars), a number of inflammatory mediators including ADAMTS5, IL-6, MMP-1, MMP-3, and MMP-13, as well as ColX, were downregulated, indicating subsiding inflammatory processes and a cellular rescue. Verification of the microtissue as a potential disease model was conducted by simulating a current clinical osteoarthritis therapy, intra-articular injection of the corticosteroid triamcinolone. Here, inflammation of our microtissues was treated using 60 μg/mL of triamcinolone [20] to mitigate the inflammatory effects of TNF-α and IL-1β. After 24 h of stimulation with TNF-α and IL-1β in the presence of the corticosteroid triamcinolone, a substantial decrease in expression of inflammatory markers was revealed, as shown in Fig. 5B (black bars). In addition, decreased expression of ADAMTS5, IL-6, MMP-1 and MMP-3, as well as ColX, at 1 week after treatment was observed (gray bars). The fact that discernible effects after treatment were demonstrated further indicates the suitability of our microfluidic 3D chondrocyte culture as a simple disease model for osteoarthritis.

3. Conclusion

In conclusion, the nutrient gradient–based microfluidic 3D cell cultivation method provides an improved *in vitro* environment for primary chondrocytes that fosters (a) redifferentiation including chondrocytic morphology and phenotype, (b) biochemical osteoarthritis-like inflammatory responses, and (c) the ability to evaluate osteoarthritic treatment options. In addition, in contrast to previous reports of engineered cartilage that separately assembled the distinctly different zones of cartilage [21] or used biphasic constructs [22], in the present study, chondrocytes were seeded in a homogenous distribution in fibrin gel and migrated to the gel-medium interface, approximating the superficial zone of cartilage. The observed increased cell density of the resident chondrocytes at the medium-hydrogel interface and their orientation along the microchannel points at a shear force induced cellular orientation similar to native cartilage. Some limitations in the present study remain and include the number of biological replicates (e.g. 4 horses used in the study) and difficulties in obtaining physiologically relevant cell densities of primary cells in low passage to avoid cellular senescence and dedifferentiation. Furthermore, the lack of biomechanical stimulation and absence of corresponding synovial fluid constitute additional limitations not yet addressed in the current work. However, we postulate that the presented microfluid-based chondrocyte culture technique may offer a new platform for future investigations in the behavior of differentiated chondrocytes and subsequently how the cells respond differently in pathophysiological states.

4. Methods

4.1. Microfluidic 3D hydrogel chondrocyte culture-on-a-chip

4.1.1. Microfluidic device and microfabrication

The device consists of two layers, a glass top layer with inlets and a polydimethylsiloxane (PDMS) bottom layer with the microfluidic structures. The device comprises a cell chamber of 3 mm diameter, with a chamber volume of 7.5 μL, a medium channel of 21.5 mm length × 1.0 mm width, and a chamber height of 1 mm. One chip hosts six of these chamber-medium channel complexes. The PDMS bottom can be opened to release intact cell-laden fibrin matrices for histological analysis. Molds for soft lithography of PDMS were designed using AutoCAD software and

manufactured by stereolithography (i.materialise). The soft lithography mold was cleaned using 99% isopropanol and dried at 70 °C. PDMS (Sylgard® 184 Silicone Elastomer Kit; Down Corning) polymer was then mixed in a 1:10 ratio of curing agent and base, distributed evenly on the surface of the mold and polymerized at 70 °C for 1 h. Inlets on the glass cover slides were drilled using a 1-mm spheroid diamond drill bit to form the top layer. Before plasma activation, both layers were again cleaned with isopropanol and dried at 70 °C. After drying, substrates were plasma activated for 45 s each using a handheld corona plasma discharge system to create excess hydroxyl groups on both surfaces and ensure stable adhesive bonding. The two layers were then aligned with one another, and gentle pressure was applied before overnight incubation. All devices were sterilized with 70% ethanol and subsequently baked overnight at 70 °C before cell loading.

4.1.2. Isolation of primary equine chondrocytes

Primary chondrocytes were isolated with written owner consent and under strict sterile technique from the knee joints of 4 horses (4 biological replicates) euthanized for reasons unrelated to osteoarthritis and unrelated to this study. After harvest, the cartilage was minced into small pieces (1 mm^3), digested in a 1-mg mL^{-1} collagenase (Type I; Sigma-Aldrich, St. Louis, MO, USA) solution for 6–8 h under constant stirring at 37 °C and filtered through a cell strainer (100 μm; Greiner Bio-One). The obtained chondrocytes were washed twice in Dulbecco's phosphate buffered saline (DPBS + Ca/Mg) and centrifuged at 400*g* for 5 min. The resulting cell pellet was resuspended in standard culture medium consisting of Ham's (low glucose, with L-Glutamine, [Lonza]), 10% fetal calf serum (FCS) [low endotoxin; Sigma-Aldrich], 1% Pen/Strep [100×; Sigma-Aldrich], and 1% amphotericin B [250 μg/ml; Biochrom]). Chondrocytes were seeded in polystyrene tissue culture flasks (Sarstedt) and cultured in a humidified atmosphere at 37 °C and 5% CO_2. The following day, the cells were washed to remove non-adherent cells and tissue debris. Medium was changed twice weekly. Passaging was performed upon colony confluence for the first passage and later upon 80–90% confluence by trypsinization (trypsin 0.05%, Ethylenediaminetetraacetic acid (EDTA) 0.02% [Biochrom]). Chondrocytes were frozen and stored in liquid nitrogen until further processing.

4.1.3. Microfluidic device loading

Primary equine chondrocytes were used for cultivation in passage two or passage three. Immediately before loading, cells were washed twice with phosphate-buffered saline (PBS) and stained for 45 min using 1 μM cytoplasmic Cell Tracker Green™ CMFDA Dye (Thermo Fisher Scientific, Waltham, MA, USA) in pure Ham's F12 medium per the manufacturer's instructions. After staining, the cells were washed twice with PBS, detached using 0.25% trypsin-EDTA solution, and centrifuged at 450 rpm for 5 min. Cell concentration and viability were determined via Trypan blue exclusion using Countess™ automated cell counter (Invitrogen). Microfluidic devices were subsequently loaded with chondrocytes encapsulated in fibrin hydrogel (Tisseel Fibrinkleber, Baxter, Germany/Austria. https://www.baxter.com/healthcare-professionals/surgical-care/tisseel-fibrin-sealant-surgical-care), yielding final concentrations of 3×10^6 cells/mL, 20 mg mL^{-1} of fibrinogen, and 5 U/mL of thrombin. The fibrin hydrogel was polymerized at 37 °C in a cell culture incubator before adding Ham's F12 complete chondrocyte medium into the medium channel and sealing the microfluidic inlets with clear, self-adhesive foil (Polyolefin StarSeal Xtra-Clear; StarLab). Medium in the microfluidic devices was exchanged by manual pipetting every other day. Chondrocyte-on-chips were harvested for further analysis on day 7 and 21. All experiments and assays were carried out in 3 technical replicates/biological replicates.

4.1.4. Finite volume simulation

A multipurpose finite volume CFD code (e.g. Ansys Fluent 6.3) was used for analyzing diffusion distance and velocity into the hydrogel. The geometry consisting of the hydrogel cavity and the feed channel was split into about 26400 hexahedral control volumes (Supplementary Fig. 2B). Second-order or higher order discretization was selected for all flow variables (momentum, mass) and for the species equations. To ensure physically correct transient solutions, the time step size was selected to guarantee a maximum Courant number Co < 1 within the flow domain over the whole run time of up to 24 h physical time. Wall boundaries were treated as ideally smooth, no-slip boundary conditions were selected for all surfaces. Stagnant flow was assumed in the flow channel – for numerical stability, a small non-zero flow velocity had to be applied (mass flow inlet with plug flow velocity profile, maximum Reynolds number Re << 10-8→ laminar; diffusion-based Peclet number $Pe < 0.1$ → diffusion dominated transport inside the hydrogel zone). The outlet was set to pressure outlet at a standard pressure of p = 1 atm (101325 Pa). The hydrogel regions were approximated as porous zones with constant porosities of $\varepsilon = 0.99$ and isotropic viscous resistances of R = 6.67.10–12 $1/m^2$. The flow was considered isothermal; no temperature or energy field was solved. For simplicity, Newtonian fluid behavior was assumed with a constant dynamic viscosity and constant density. As the concentrations of the dissolved species in the fluid are low, the properties of the solvent, water, have been used for the simulation ($\rho = 998$ kg/m^3, $\eta = 0.001003$ Pa s). The diffusion coefficients for the tracer components have been determined previously [6] or based on literature values (generic tracers with 0.3 kDa–4.10^{-10} m [2]/s and 40 kDa–1.10^{-11} m [2]/s, and glucose with 0.18 kDa 4.10^{-10} m [2]/s), assuming a dilute solution. Tracers in the flow channel (reservoir zone) were added with constant concentration at the initial time T = 0 s; at the same time, a constant zero tracer saturation of the hydrogel zone was set as starting values for the simulation runs. For glucose, the actual concentration levels from experiments were used (1.35 g/l initial concentration in the hydrogel; 4.5 g/l in the feed channel). Simulations were carried out on cae.zserv.tuwien.ac.at.

4.1.5. Live cell imaging and on-chip morphology assessment

Chondrocytes cultivated in fibrin hydrogels and in conventional cell culture were imaged via brightfield, phase contrast, and fluorescent microscopy throughout the entire culture period of 21 days using an EVOS cell imaging system (Thermo Fisher Scientific). Cell viability was assessed by means of Cell Tracker Green™ CMFDA Dye, cell morphology was recorded, and the cells cultured in Ham's F12 chondrocyte medium were counted manually under fluorescent microscopy every day in multiple microfluidic chambers and culture flasks to compare the morphological redifferentiation process of the chondrocytes during the culture period [23]. Chondrocytes were considered redifferentiated when they displayed a round, spherical morphology and fibroblastic when their length was twice their width. If the morphology differed from these specifications, the differentiation status was listed as not assigned [24].

4.1.6. Metabolic activity

A Resazurin-based in vitro toxicology assay (TOX8; Sigma-Aldrich) was performed to determine differences in metabolic activity between microfluidic and monolayer cultures. To study the metabolic changes during chondrogenic differentiation, cells were cultured with the standard cultivation method using Ham's F12 or StemPro™ Chondrogenesis Differentiation Kit (Gibco). Cells were cultured in either monolayer culture or on a microfluidic device for 6 days. To standardize the fluid volume and cell number between the different culture methods, 11250 cells, 22500 cells, or 33750 cells were transferred into a 24-well plate either in continued monolayer culture or embedded in fibrin gel (microfluidic device group). For the metabolic assay, 40 μL of TOX8 reagent (Sigma-Aldrich) was added to 400 μL of medium and incubated for 8 h at 37 °C inside a cell culture incubator. The analysis was performed by aliquoting 100 μL of supernatant per technical triplicate in a flat-bottom 96-well plate and measured fluorometrically at a wavelength of 590 nm with excitation at 560 nm.

4.1.7. Gene expression analysis

Isolation of RNA. Fibrin hydrogel clots were released from the microfluidic device using a scalpel and tweezers before homogenization using a Biopulverizer (Biospec, USA). In detail, the BioPulverizer was cooled thoroughly by submerging in liquid nitrogen for 1 min. Each fibrin hydrogel to be analyzed was placed in a shallow container of the Biopulverizer and pulverized for 1 min by blowing the hammer to the pestle. Powdered contents were transferred to an Eppendorf tube. Total RNA was extracted from both 3D and 2D cultures using peqGOLD Total RNA isolation Kit (Peqlab) per the provided protocol.

4.1.7.2. Quantitative PCR. One nanogram of RNA of each sample was used for quantitative PCR (qPCR) reaction. RevTrans QPCR One-Step EvaGreen kit (Bio&Sell, Germany) was used first for cDNA synthesis and subsequently for qPCR reaction. The reaction mixtures were incubated for 15 min at 50 °C for cDNA generation, followed by qPCR reaction; 95 °C for 5 min, 95 °C for 15 s, 55 °C for 20 s, and 72 °C for 30 s. For each gene, a reaction mixture with water instead of the total RNA template was run at the same time as a PCR negative control. The transcript data were analyzed using the Agilent AriaMx 1.1 software (Agilent Technologies, USA). The transcript level of genes of interest was normalized to the transcriptional level of GAPDH and represented as a relative transcript level relative to GAPDH.

4.1.8. Histology

Histological sections of cell-laden fibrin hydrogels cultured inside the microfluidic device were performed to analyze cell morphology and distribution. After cultivation, the hydrogels were fixed overnight using 4% buffered formalin, released from the microfluidic device using a scalpel and tweezers, and kept in histology cassettes in 70% ethanol until embedding. The hydrogels were dehydrated, embedded in paraffin using a Shandon Tissue Excelsior (Thermo Fisher Scientific) and cut into 2-μm slices. The sections were mounted onto glass slides using dibutylphthalate polystyrene xylene (DPX) (Sigma-Aldrich) and stained with hematoxylin (Richard Allan Scientific, Waltham, MA, USA), eosin (Carl Roth, Karlsruhe, Germany), and Safranin O/Fast Green (counterstain). Immunohistochemical staining for Ki67 (Cell Signaling, clone 8D5, mouse mc, dilution 1:400) was performed after 30 min of antigen retrieval in a steamer with citrate buffer at pH 6.

4.1.9. Biochemical injury and steroid treatment

Chip-based 3D chondrocyte constructs were exposed to an inflammatory environment using 50 pg/mL of TNF-α and IL-1β (Sigma-Aldrich), as previously described [19]. Chondrocyte cultures were subjected to biochemical stimulation after one week in culture for a time of 24 h, after which chondrocyte constructs were either released from the device for RT-qPCR or cultivated in standard medium for another six days before analysis. For steroid treatment, 60 μg/mL of triamcinolone [20] was added simultaneously with inflammatory factors.

Conflict of interest

The authors declare that they have no known competing financial interests or personal relationships that could have appeared to influence the work reported in this paper.

Appendix A. Supplementary data

Supplementary data to this article can be found online at https://doi.org/10.1016/j.mtbio.2019.100023.

References

[1] D.J. Hunter, et al., Nat. Rev. Rheumatol. 10 (7) (2014) 437.
[2] D.D. Frisbie, et al., Vet. Comp. Orthop. Traumatol. 19 (3) (2006) 142.
[3] S. Camarero-Espinosa, et al., Biomater Sci. 4 (5) (2016) 734.
[4] D. Sticker, et al., Lab Chip 15 (24) (2015) 4542.
[5] M. Rothbauer, et al., Lab Chip 18 (2) (2018) 249.
[6] B. Bachmann, et al., Biomicrofluidics 12 (4) (2018), 042216.
[7] Y. Li, et al., Exp. Ther. Med. 14 (3) (2017) 2657.
[8] P. Occhetta, et al., Nat. Biomed. Eng. 3 (7) (2019) 545.
[9] H. Lin, et al., Mol. Pharm. 11 (7) (2014) 2203.
[10] A.M. Bhosale, J.B. Richardson, Br. Med. Bull. 87 (2008) 77.
[11] A.R. Poole, et al., Clin. Orthop. Relat. Res. (2001) S26, 391 Suppl.
[12] A.J. Sophia Fox, et al., Sport Health 1 (6) (2009) 461.
[13] H. Lee, et al., Connect. Tissue Res. 55 (5–6) (2014) 339.
[14] A. Maroudas, J. Anat. 122 (Pt 2) (1976) 335.
[15] I. Johnson, Histochem. J. 30 (3) (1998) 123.
[16] T.W.G.M. Spitters, et al., Tissue Eng. A 20 (23–24) (2014) 3270.
[17] A. Jackson, W. Gu, Curr. Rheumatol. Rev. 5 (1) (2009) 40.
[18] T. Aigner, et al., Arthritis Rheum. 44 (6) (2001) 1304.
[19] L. Sun, et al., Biomaterials 32 (24) (2011) 5581.
[20] J.E. Dechant, et al., Equine Vet. J. 35 (5) (2003) 444.
[21] W. Schuurman, et al., J. Tissue Eng. Regenerat. Med. 10 (4) (2016) 315.
[22] H. Paetzold, et al., Eur. Cells Mater. 23 (2012) 209.
[23] R. Dorotka, et al., Biomaterials 26 (17) (2005) 3617.
[24] R.A. Stockwell, J. Anat. 101 (Pt 4) (1967) 753.

CHAPTER 4

SUPPLEMENTARY INFORMATION

MANUSCRIPT #1

EVERY BREATH YOU TAKE: NON-INVASIVE REAL-TIME OXYGEN BIOSENSING IN TWO- AND THREE-DIMENSIONAL MICROFLUIDIC CELL MODELS

Helene Zirath, Mario Rothbauer, Sarah Spitz, Barbara Bachmann, Christian Jordan, Bernhard Müller, Josef Ehgartner, Eleni Priglinger, Severin Mühleder, Heinz Redl, Wolfgang Holnthoner, Michael Harasek, Thorsten Mayr, and Peter Ertl

frontiers

Supplementary information

Every breath you take: Non-invasive real-time oxygen biosensing in two- and three-dimensional microfluidic cell models

Helene Zirath[1,4,£,*], Mario Rothbauer[1,4,£,*], Sarah Spitz[1,4,£], Barbara Bachmann[1,2,4,£], Christian Jordan[1], Bernhard Müller[3], Josef Ehgartner[3], Eleni Priglinger[2], Severin Mühleder[2], Heinz Redl[2], Wolfgang Holnthoner[2], Michael Harasek[1], Torsten Mayr[3] and Peter Ertl[1,4]

[1] Institute of Applied Synthetic Chemistry, Institute of Chemical Technologies & Analytics, and Institute of Chemical, Environmental and Bioscience Engineering, Vienna University of Technology, Vienna, Austria

[2] Ludwig Boltzmann Institute for Experimental and Clinical Traumatology, AUVA Research Centre, Vienna, Austria

[3] Institute of Analytical Chemistry and Food Chemistry, Graz University of Technology, NAWI Graz, Graz, Austria

[4] Austrian Cluster for Tissue Regeneration, Vienna, Austria

[£] These authors contributed equally

[*] Correspondence:
Helene Zirath, helene.zirath@tuwien.ac.at

Mario Rothbauer, mario.rothbauer@tuwien.ac.at

Keywords: Microfluidics, 3D Culture, Biosensor, Oxygen, Oxygen gradient, Organ-on-a-Chip, Lab-on-a-Chip, Hydrogel

Number of words: 4416

Number of figures: 7 (+3 Supplementary)

SI1: Images of microfluidic devices. (A) Microfluidic glass chip (76x26x2.3 mm) for monolayer culture containing 8 chambers with a sensor spot centralized in each chamber. (B) Microfluidic glass chip (76x26x4.4 mm) for three-dimensional (3D) hydrogel cultures with 4 sensor spots in each chamber. Scale bar represent 10 mm.

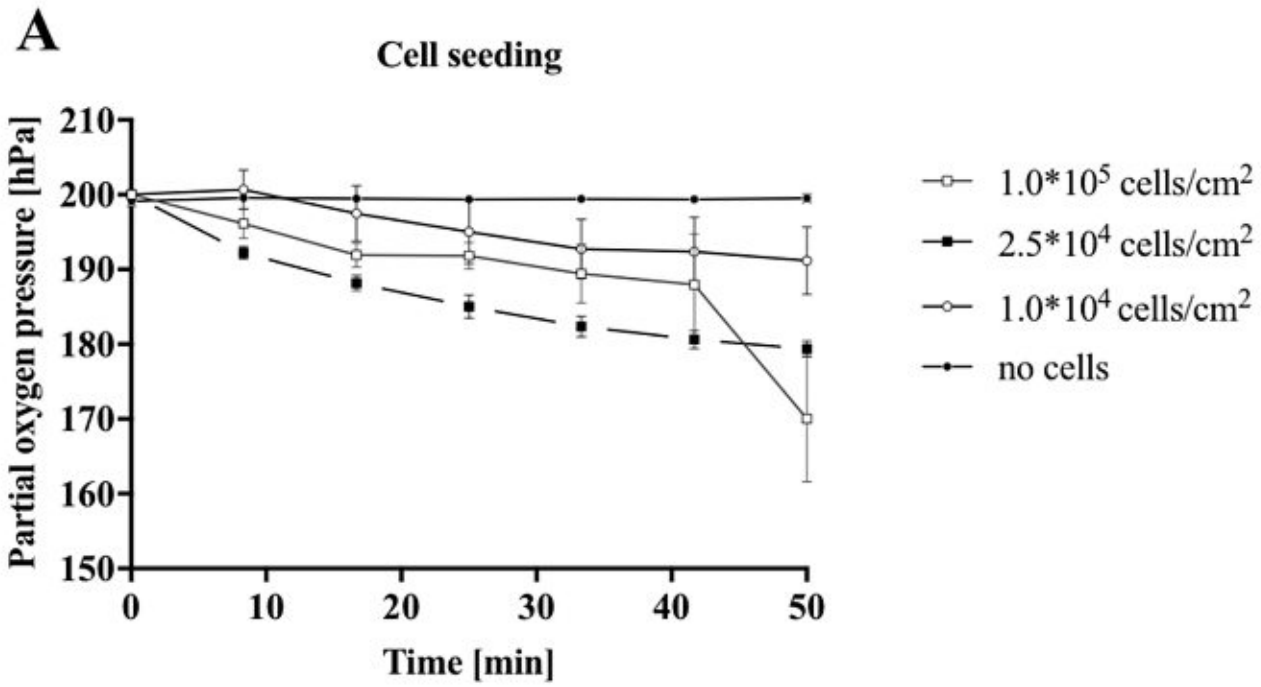

SI2: Partial oxygen pressure recorded during 3 hours of cell seeding zoomed in to the first 50 min of oxygen monitoring.

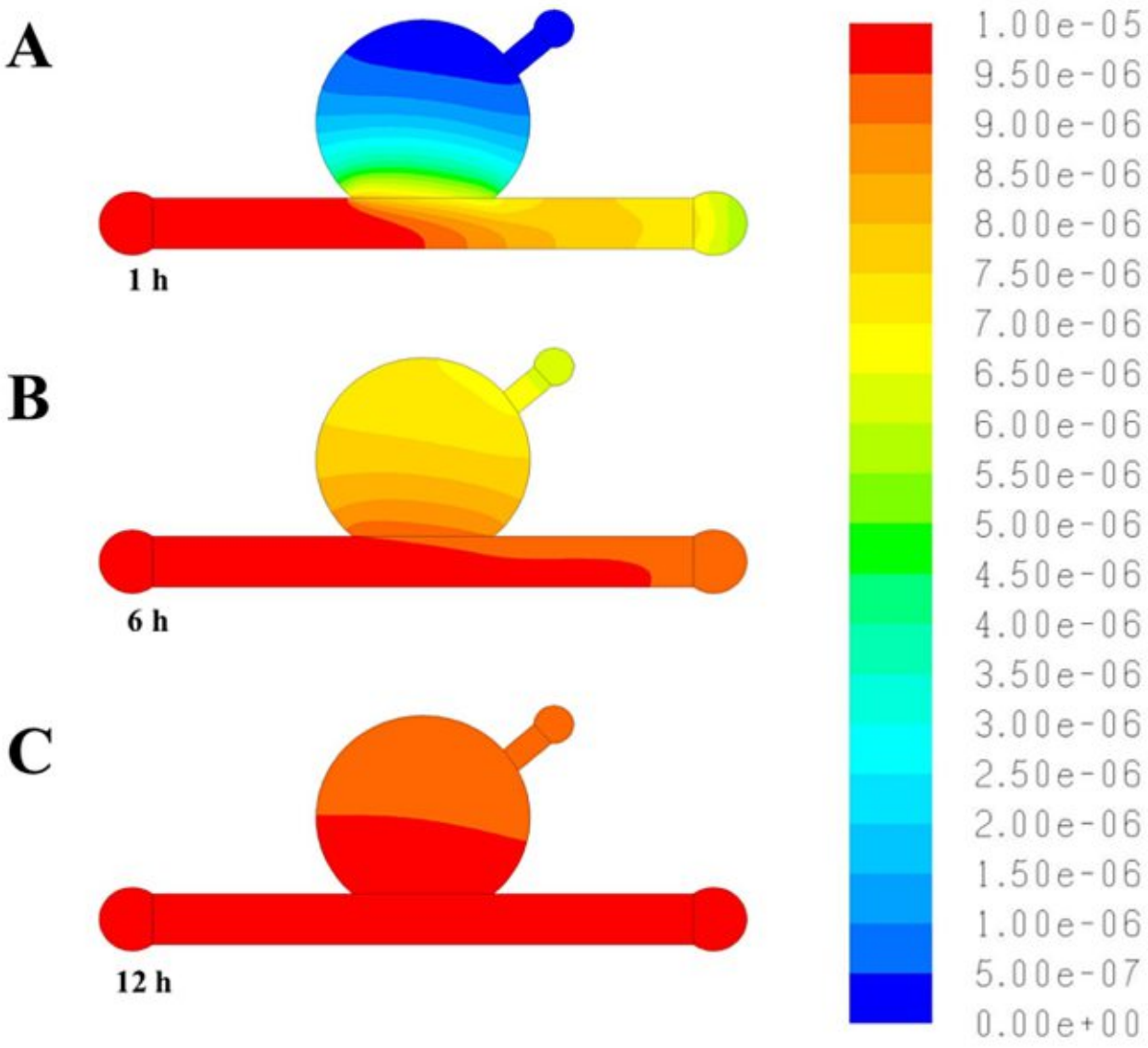

SI3: Finite volume simulation of oxygen distribution in 3D hydrogel after (A) 1 hour, (B) 6 hours and (C) 12 hours of medium perfusion without cells showing complete saturation of hydrogel with oxygen within 12 hours.

MANUSCRIPT #3

MICROVASCULATURE-ON-A-CHIP: BRIDGING THE INTERSTITIAL BLOOD-LYMPH INTERFACE VIA MECHANOBIOLOGICAL STIMULI

Barbara Bachmann, Sarah Spitz, Christian Jordan, Patrick Schuller, Heinz Wanzenböck, Bahram Haddadi, Michael Harasek, Heinz Redl, Wolfgang Holnthoner, and Peter Ertl

Supplementary information

Microvasculature-on-a-Chip: Bridging the interstitial blood-lymph interface via mechanobiological stimuli

Barbara Bachmann[1,2,3,4], Sarah Spitz[1,4], Christian Jordan[5], Patrick Schuller[6], Heinz Wanzenböck[6], Bahram Haddadi[5], Michael Harasek[5], Heinz Redl[2,3,4], Wolfgang Holnthoner[2,3,4] and Peter Ertl[* 1,3,4]

[1] Faculty of Technical Chemistry, Institute of Applied Synthetic Chemistry and Institute of Chemical Technologies & Analytics, Vienna University of Technology, 1060 Vienna, Austria

[2] AUVA Research Centre, Ludwig Boltzmann Institute for Experimental and Clinical Traumatology, 1200 Vienna, Austria

[3] Competence Center MechanoBiology, 1200 Vienna, Austria

[4] Austrian Cluster for Tissue Regeneration, 1200 Vienna, Austria

[5] Institute of Chemical, Environmental and Bioscience Engineering - Fluid Dynamics Simulation, University of Technology, Getreidemarkt 9/166-2, 1060 Vienna, Austria

[6] Institute of Solid State Electronics, Vienna University of Technology, Vienna, 1040, Austria

***Correspondence:**

Peter Ertl - peter.ertl@tuwien.ac.at

Keywords: Vascularization, Sprouting, Lymphatic System, Organ-on-a-Chip, Mechanobiology

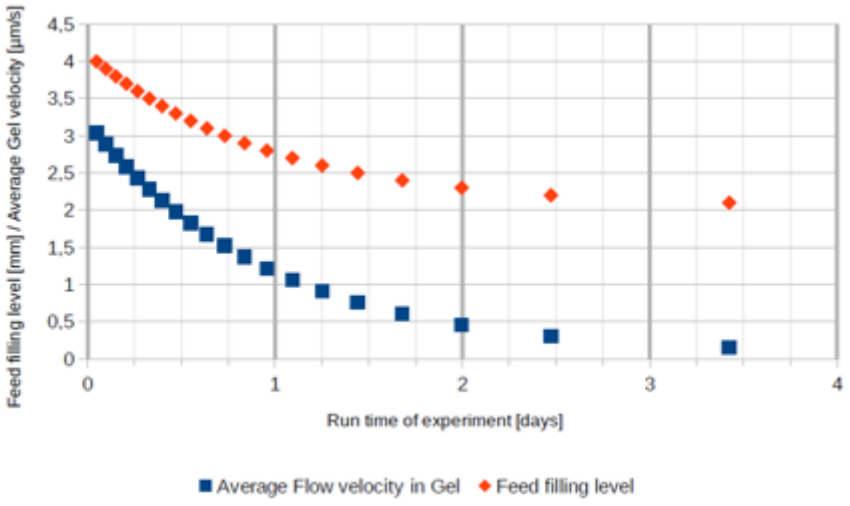

Supplementary Figure 1: Feed filling level and averagy velocity in hydrogel over time as determined by CFD simulation.

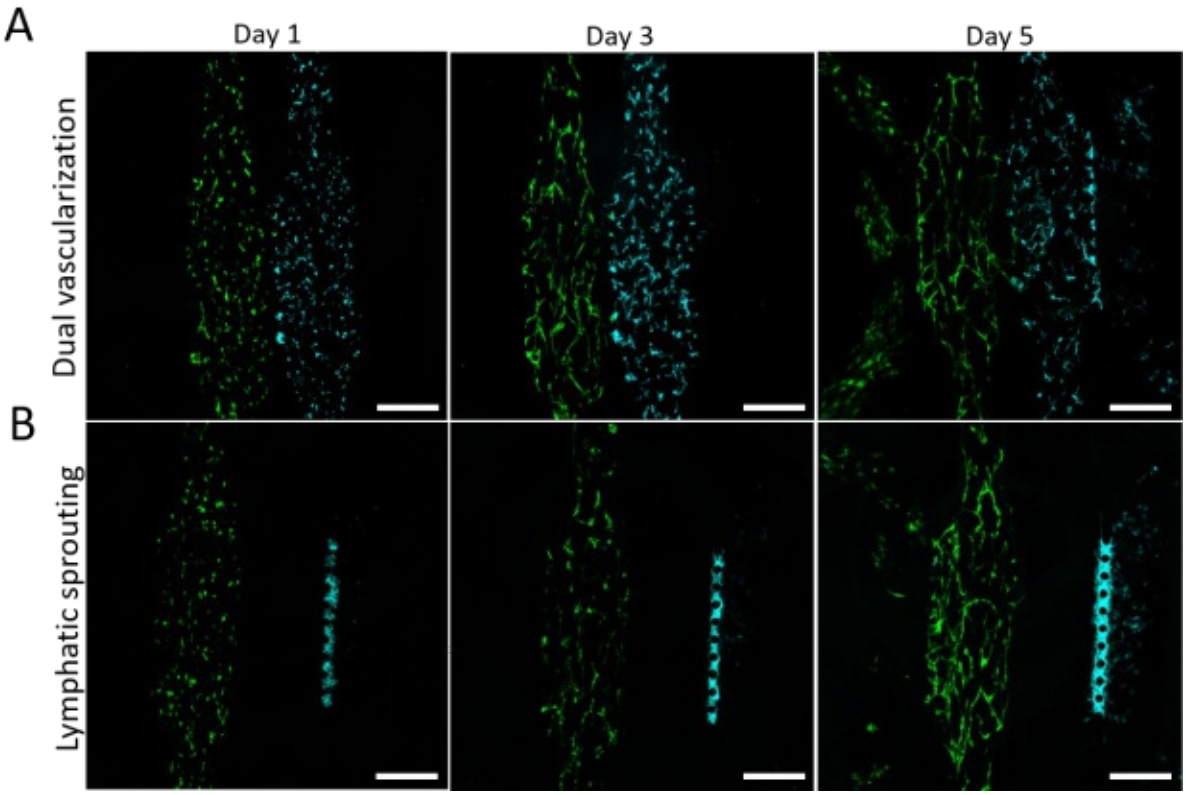

Supplementary Figure 2: Development of blood-lymphatic interstitial interface over five days of culture time. (A) Dual vascularization setup and (B) Lymphatic sprouting setup. Scale Bar 400 µm.

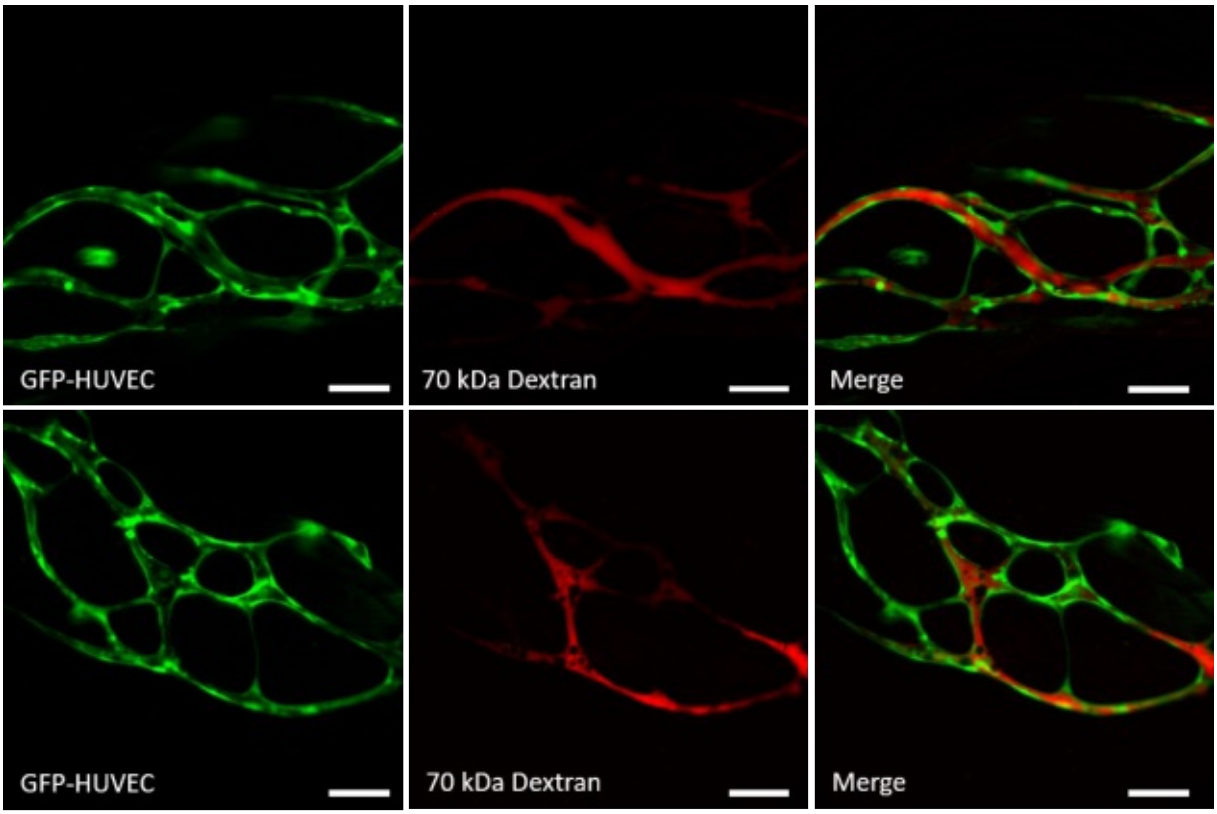

Supplementary Figure 3: Perfusion of blood vessels (GFP-HUVEC, green) with 70 kDa TRITC-dextran (red) demonstrating lumen formation and vessel functionality. Scale bar 100 µm.

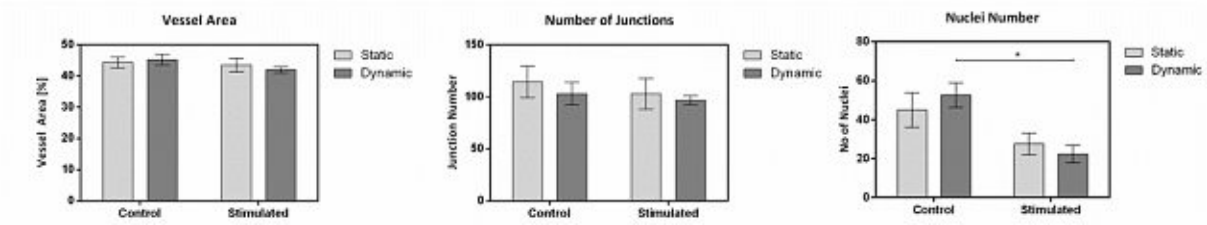

Supplementary Figure 4: Influence of dynamic cultivation on blood vascular network and nuclei number within the cell-free compartment. The blood vascular network is unaffected by dynamic cultivation showing consistent vessel area coverage and junction number irrespective of cultivation conditions. Cell outgrowth is significantly enhanced in non-PMA-stimulated cultures.

MANUSCRIPT #4

ENGINEERING OF THREE-DIMENSIONAL PRE-VASCULAR NETWORKS WITHIN FIBRIN HYDROGEL CONSTRUCTS BY MICROFLUIDIC CONTROL OVER RECIPROCAL CELL SIGNALING

Barbara Bachmann, Sarah Spitz, Mario Rothbauer, Christian Jorden, Michaela Purtscher, Helene Zirath, Patrick Schuller, Christoph Eilenberger, Syed Faheem Ali, Severin Mühleder, Eleni Priglinger, Michael Harasek, Heinz Redl, Wolfgang Holnthoner, and Peter Ertl

Supplementary Information

Engineering of three-dimensional pre-vascular networks within fibrin hydrogel constructs by microfluidic control over reciprocal cell signaling

Barbara Bachmann [⊥,1, 2, 3, 4], Sarah Spitz [⊥,1, 4, 5], Mario Rothbauer [⊥,1], Christian Jordan[1], Michaela Purtscher[6], Helene Zirath[1], Patrick Schuller[1], Christoph Eilenberger[1], Syed Faheem Ali[1,3,4], Severin Mühleder[2,3,4], Eleni Priglinger[2,4], Michael Harasek[1], Heinz Redl[2,3,4,5], Wolfgang Holnthoner[2,3,4] and Peter Ertl[*1,3,4]

[1] Faculty of Technical Chemistry, Institute of Applied Synthetic Chemistry, Institute of Chemical Technologies & Analytics, Vienna University of Technology, 1060 Vienna, Austria

[2] AUVA Research Centre, Ludwig Boltzmann Institute for Experimental and Clinical Traumatology, 1200 Vienna, Austria

[3] Kompetenzzentrum für MechanoBiologie (INTERREG V-A AT-CZ ATCZ133), 1200 Vienna, Austria

[4] Austrian Cluster for Tissue Regeneration, 1200 Vienna, Austria

[5] Trauma Care Consult GmbH, Vienna, 1200 Vienna, Austria

[6] Department of Biochemical Engineering, University of Applied Sciences Technikum Wien, 1060 Vienna, Austria

[⊥]These authors contributed equally to the present work

[*]Correspondence: peter.ertl@tuwien.ac.at

Supplementary Information

SI Figure 1: Dimensions of the indirect flow (A) and direct flow (B) chip geometry.

SI Figure 2: Representative image showing mesh quality employed in *in silico* experiments (A). Non-diffusing scalar used for calculation of the residence time distributions (B).

SI Figure 3: Fluorescence images of pre-vascular networks after 7 days of cultivation in the 8 mm (A) and 3 mm (B) indirect flow chip geometry.

SI Figure 4: Size-dependent diffusion behavior of FITC labelled dextrans throughout the hydrogel at 0h (A) and after 12h (B).

SI Figure 5: Distance-dependent concentration profiles of 10/20 kDa (A) and 40 kDa (B) molecules using in silico and in vitro methods.

SI Figure 6: Cross section of finite element simulations of 10/20 kDA molecule diffusion and elution for static (A) and dynamic (B) conditions.

SI Video 1: Finite volume CFD simulations of direct flow device showing complete elution of pro-angiogenic growth factors from the perfused region already after 120 s.

SI Video 2: Finite volume CFD simulations of indirect flow device showing distribution of different sized molecules in the fibrin hydrogel.

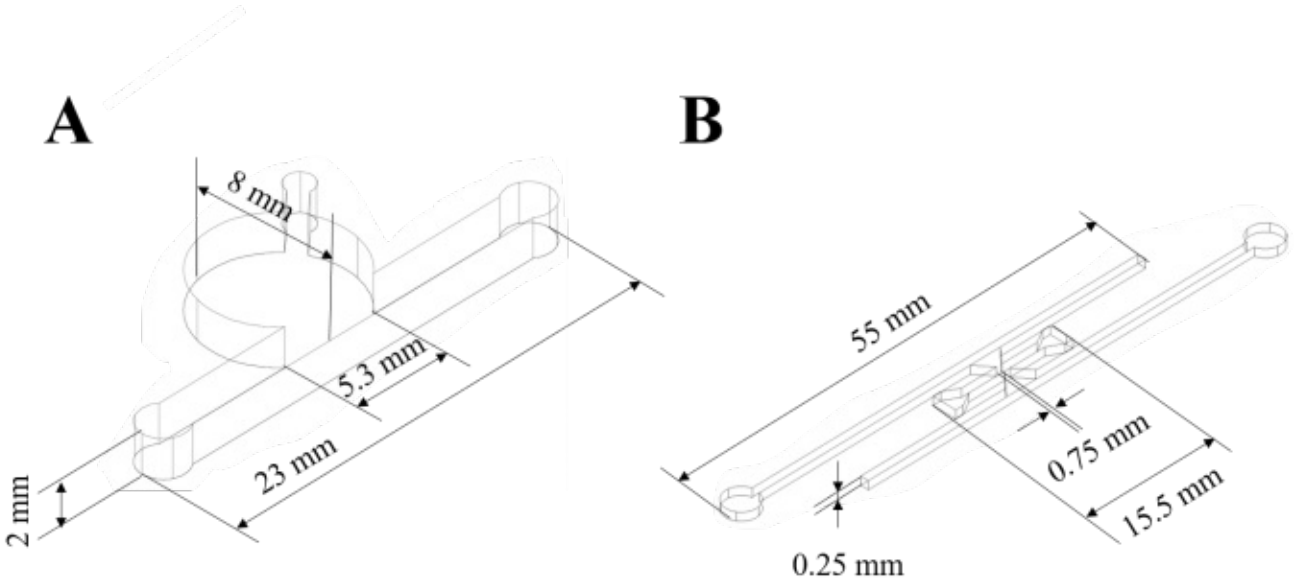

SI Figure 1

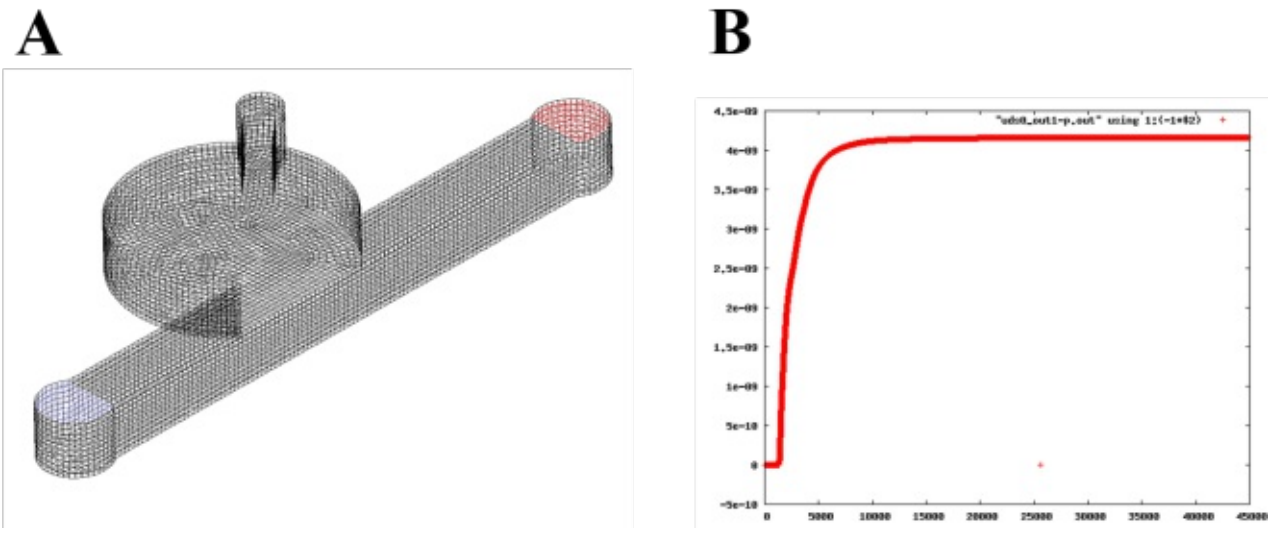

SI Figure 2

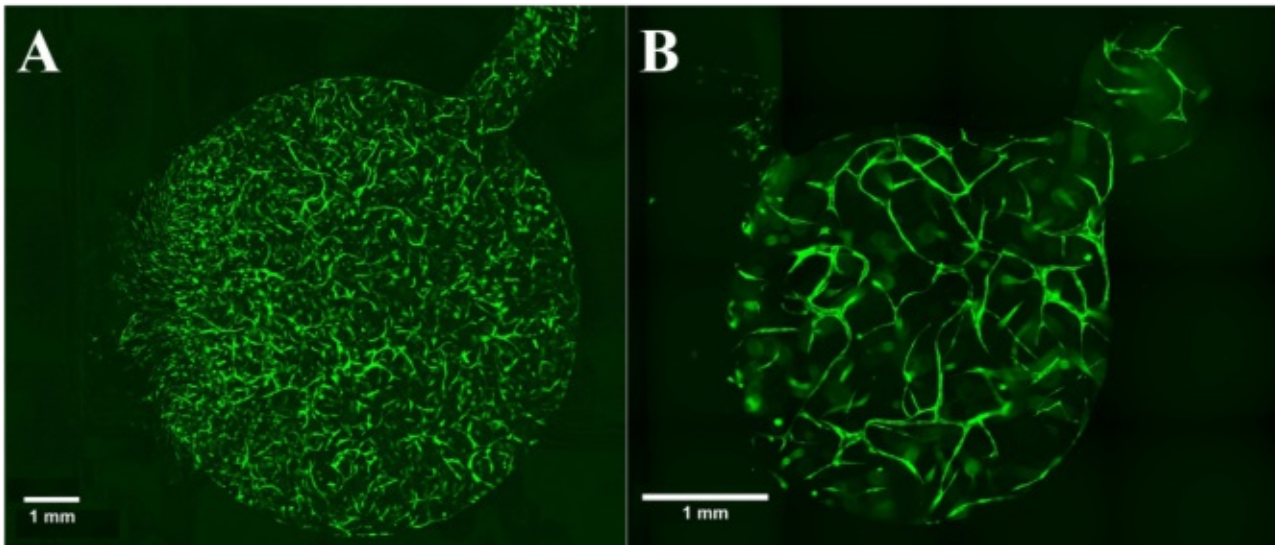

SI Figure 3

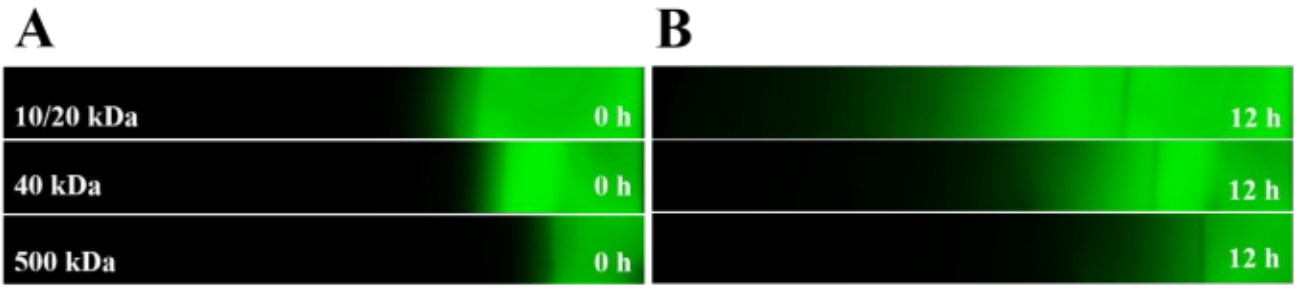

SI Figure 4

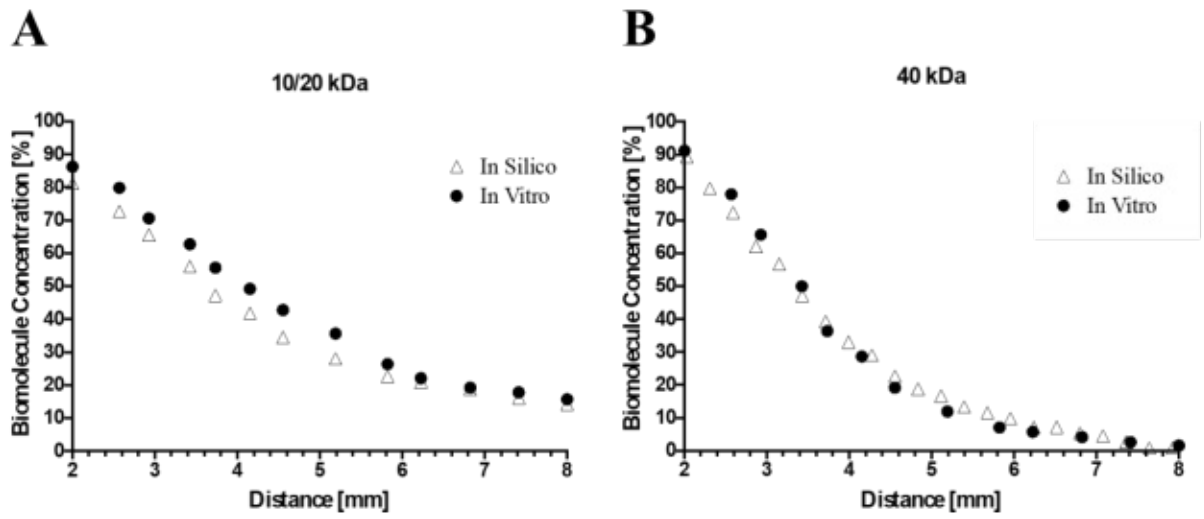

SI Figure 5

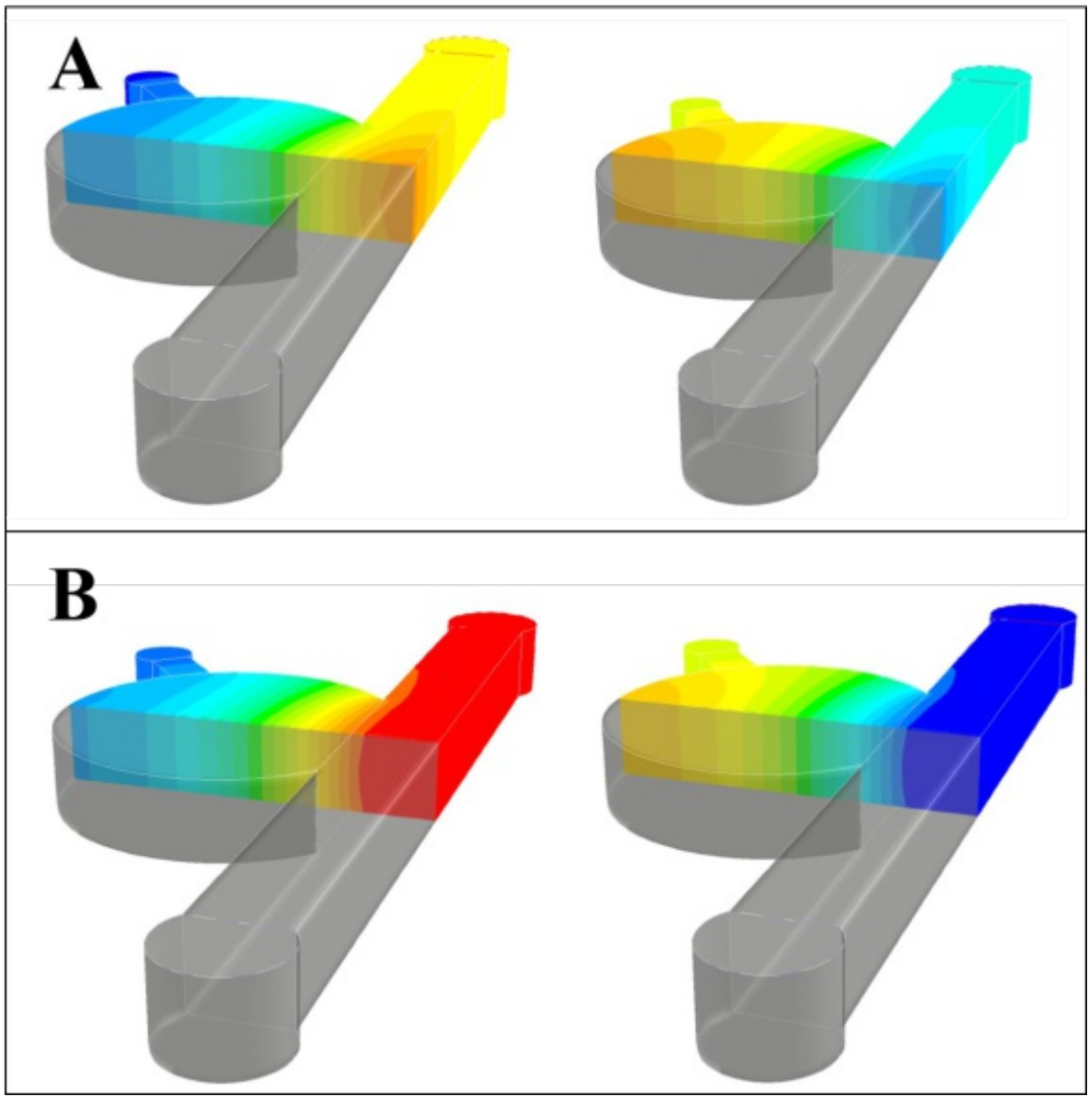

SI Figure 6

MANUSCRIPT #5

STIFFNESS MATTERS: FINE-TUNED HYDROGEL ELASTICITY ALTERS CHONDROGENIC REDIFFERENTIATION

Barbara Bachmann, Sarah Spitz, Barbara Schädl, Andreas Teuschl, Heinz Redl, Sylvia Nürnberger, and Peter Ertl

frontiers

Supplementary Material

Stiffness matters: Fine-tuned hydrogel elasticity alters chondrogenic redifferentiation

Barbara Bachmann[§ 1,2,3,5], Sarah Spitz[§ 1,5], Barbara Schädl[2,5,6], Andreas Herbert Teuschl[5,4], Heinz Redl[2,5], Sylvia Nürnberger[*2,5,7], and Peter Ertl[* 1,5]

[1] Faculty of Technical Chemistry, Institute of Applied Synthetic Chemistry and Institute of Chemical Technologies & Analytics, Vienna University of Technology, 1060 Vienna, Austria

[2] AUVA Research Centre, Ludwig Boltzmann Institute for Experimental and Clinical Traumatology, 1200 Vienna, Austria

[3] Competence Center MechanoBiology, 1200 Vienna, Austria

[4] Department of Biochemical Engineering, UAS Technikum Wien, 1200 Vienna, Austria

[5] Austrian Cluster for Tissue Regeneration, 1200 Vienna, Austria

[6] University Clinic of Dentistry, Medical University of Vienna, 1090 Vienna, Austria

[7] Department of Orthopedics and Trauma-Surgery, Division of Trauma-Surgery, Medical University of Vienna, 1090 Vienna, Austria

***Correspondence:**

Sylvia Nürnberger
sylvia.nuernberger@meduni.ac.at

Peter Ertl
peter.ertl@tuwien.ac.at

§ These authors contributed equally

Keywords: cartilage, chondrocytes, 3D cell culture, extracellular matrix, hydrogel, Young's modulus

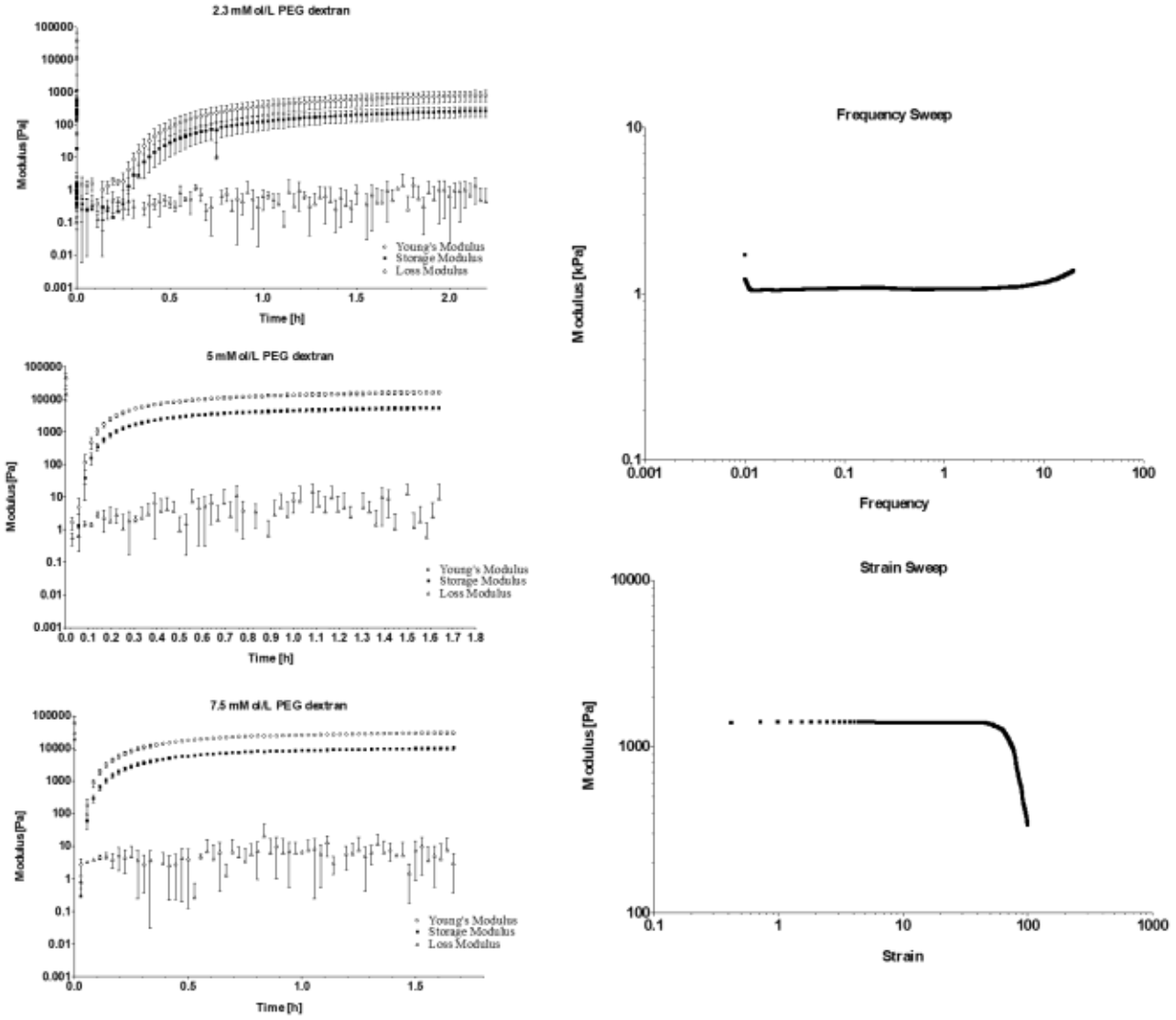

Supplementary Figure 1: Loss, storage, and complex modulus as well as Young's Modulus development of PEG-dextran hydrogels during gelation (n = 3). Frequency sweep and strain sweep of polymerized PEG-dextran hydrogels for the adequate selection of rheological parameters.

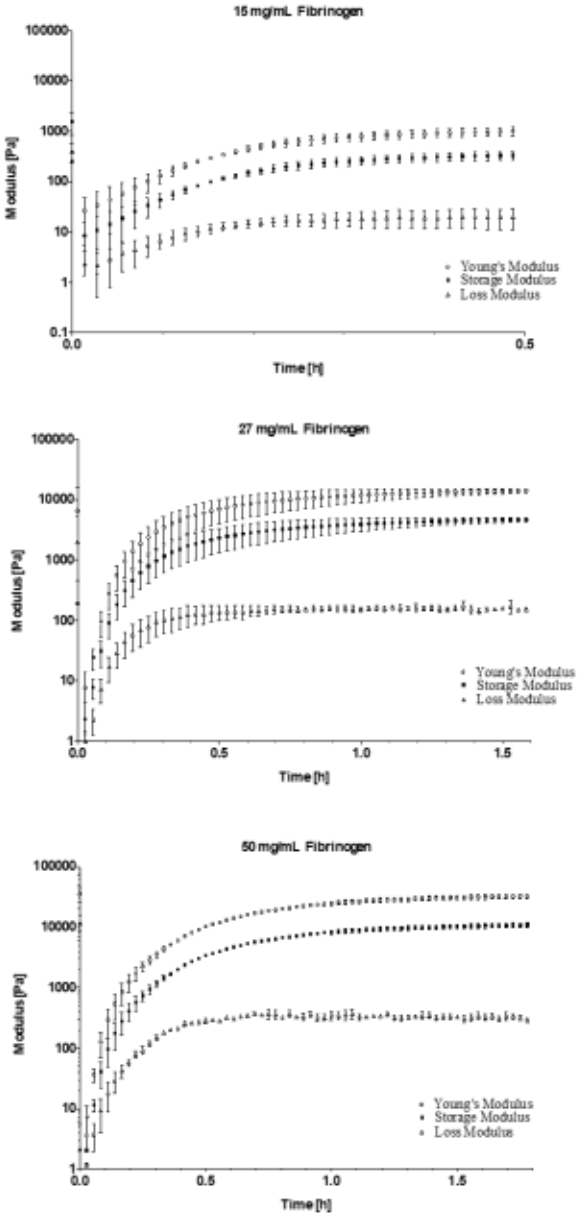

Supplementary Figure 2: Loss modulus, storage, and complex modulus as well as Young‘s Modulus development of fibrin hydrogels during gelation (n = 3).

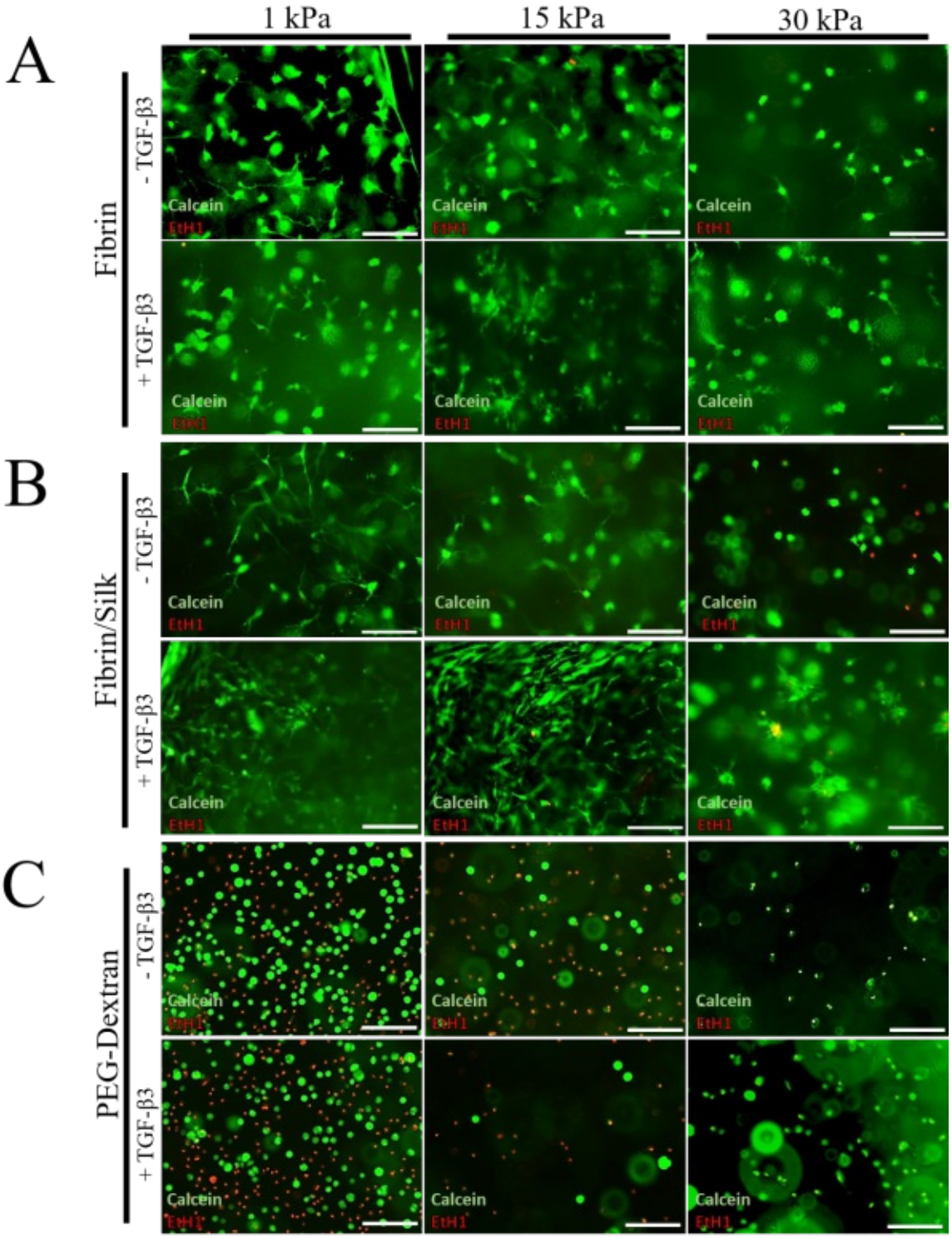

Supplementary Figure 3: Viability of primary chondrocytes determined by Live (Calein-AM)/Dead (Ethidium-H1) staining in (A) fibrin, (B) silk fibrin and (C) PEG-dextran hydrogels of 1 kPa, 15 kPa

and 30 kPa elasticity without and with addition of TGF-β3. Pictures show epifluorescence images of whole hydrogel clots. (Scale bar:100 µm)

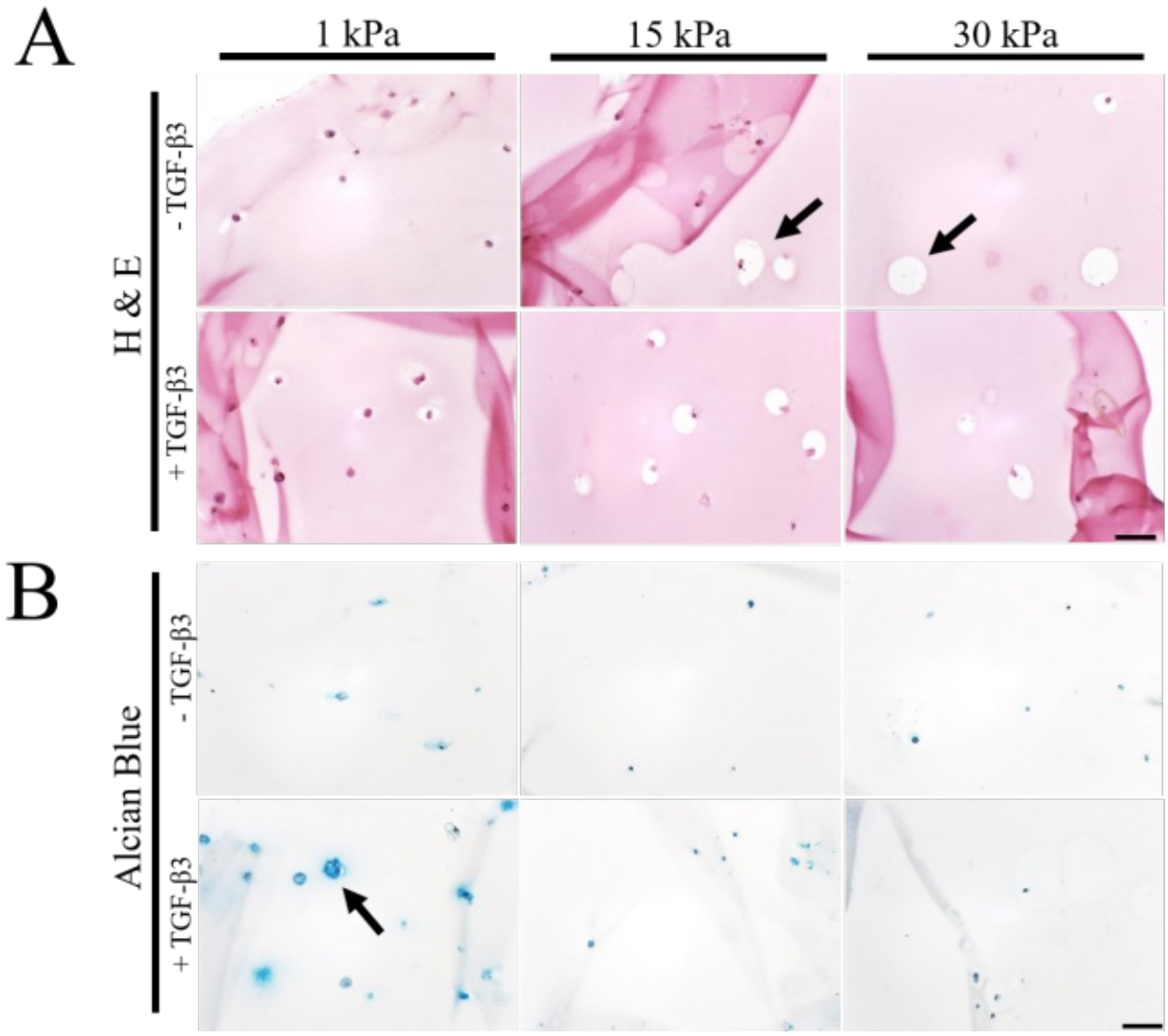

Supplementary Figure 4: Histological images of primary chondrocytes in PEG-dextran hydrogels of 1 kPa, 15 kPa and 30 kPa elasticity stained with (A) H & E for morphology, (B) alcian blue for sGAG and (C) collagen type II antibodies. (Scale bar: 50 µm)

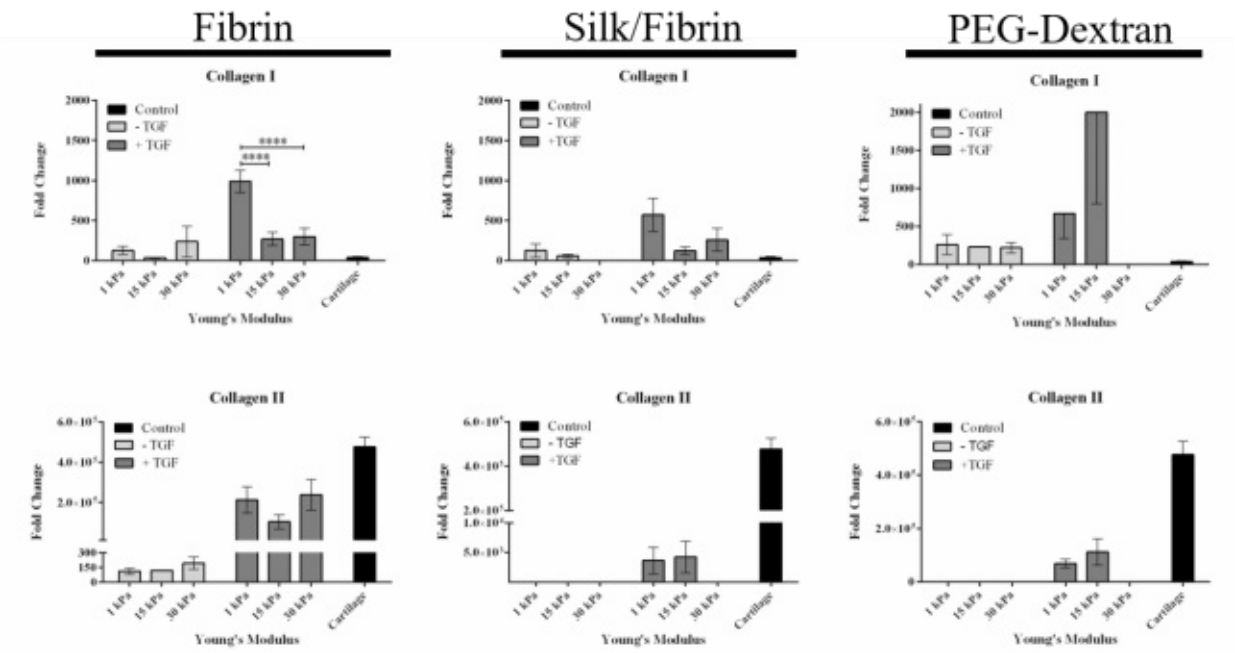

Supplementary Figure 5: Gene expression of collagen type I and collagen type II in fibrin, silk/fibrin and PEG-dextran hydrogels of different elasticities. Depicted as mean with SEM (n = 9). p-value: * < 0.1; **<0.05; *** < 0.01; **** < 0.001

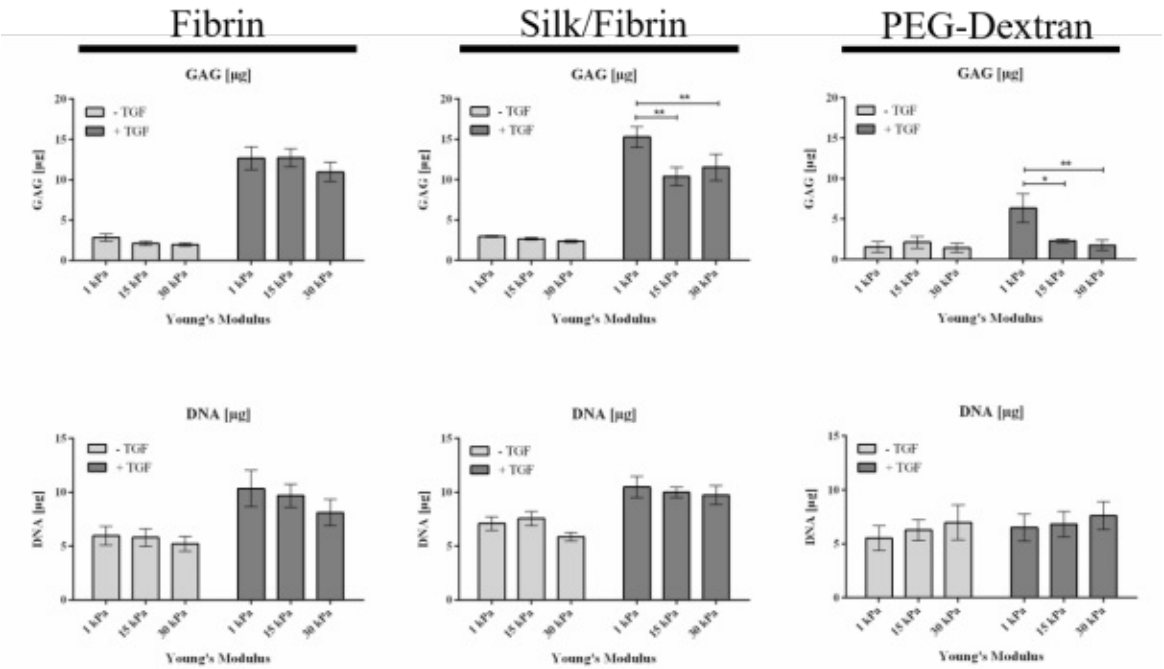

Supplementary Figure 6: Quantification of total sGAG and total DNA amount per hydrogel for fibrin, silk/fibrin and PEG-dextran. Depicted as mean with SEM (n = 9). p-value: * < 0.1; **<0.05; *** < 0.01; **** < 0.001

MANUSCRIPT #6

MICROFLUIDIC NUTRIENT GRADIENT-BASED THREE-DIMENSIONAL CHONDROCYTE CULTURE-ON-A-CHIP AS AN IN VITRO EQUINE ARTHRITIS MODEL

Julie Rosser, Barbara Bachmann, Christian Jordan, Iris Ribitsch, Eva Haltmayer, Sinan Gültekin, Sini Junttila, Bence Galik, Attila Gyenesei, Bahram Haddadi, Michael Harasek, Monika Egerbacher, Peter Ertl, and Florien Jenner

Supplementary Information

Microfluidic Nutrient Gradient-based 3D Chondrocyte Culture-on-a-Chip as in vitro Equine Arthritis Model

Julie Rosser,[†⌉] Barbara Bachmann,[†⌉] Christian Jordan,[†] Iris Ribitsch,[⊥] Eva Haltmayer,[⊥] Sinan Gueltekin,[⊥] Sini Junttila,[‡] Bence Galik,[‡] Attila Gyenesei,[‡] Bahram Haddadi,[†] Michael Harasek,[†] Monika Egerbacher,[⊥] Peter Ertl,[†*] and Florien Jenner[⊥]

[⊥] Department of Equine Surgery, University of Veterinary Medicine, Veterinärplatz 1, 1210 Vienna, Austria

[‡] BIOCOMP, Bioinformatics & Scientific Computing VBCF - Vienna Biocenter Core Facilities GmbH, GmbH, Dr. Bohr Gasse 3, 1030 Vienna, Austria

[†] Faculty of Technical Chemistry, Vienna University of Technology, Getreidemarkt 9 1060 Vienna, Austria

*Corresponding authors: peter.ertl@tuwien.ac.at

[⌉] contributed equally

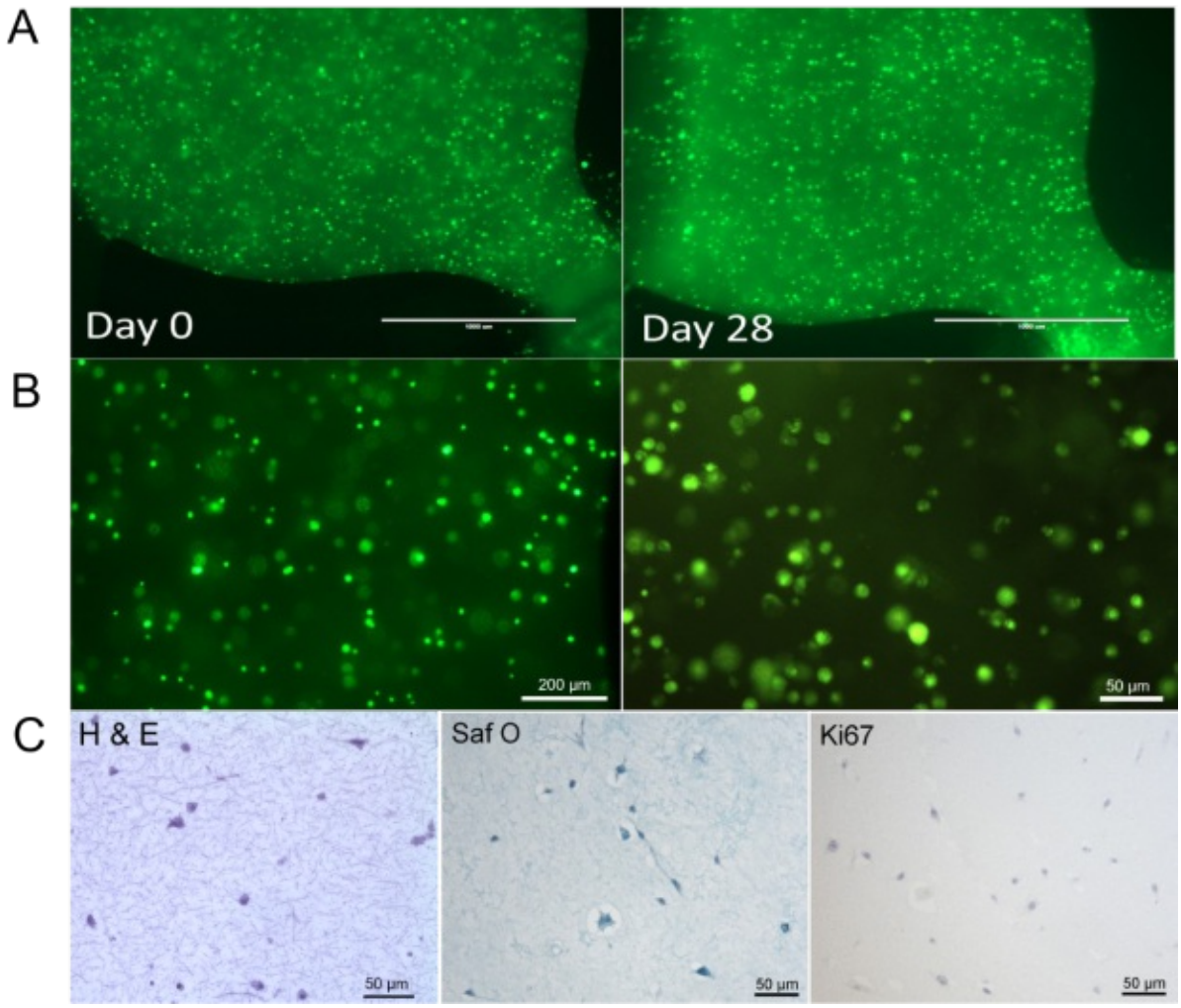

S1: A) Live staining of chondrocytes on-chip directly after loading (left) and after 28 of cultivation (right), confirming high viabilities throughout the cultivation time. (B) CMFDA-stained chondrocytes in the cultivation chamber exhibiting spherical morphology. (B) Histological staining of chondrocyte-on-chip cultures with H & E (left), Safranin O (middle) and Ki67 (right).

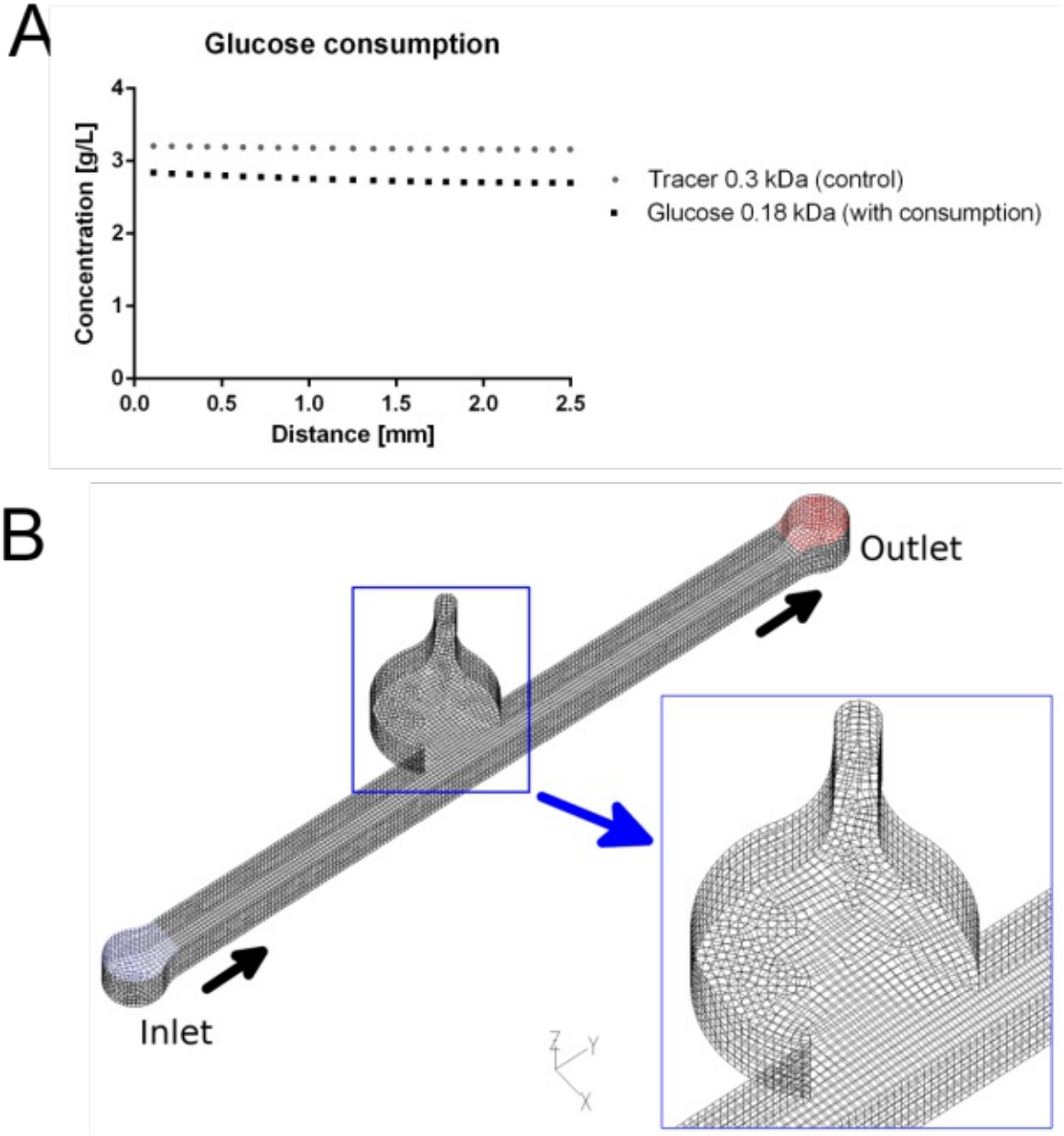

S2: (A) Levels of tracer molecule compared to glucose levels including glucose consumption after 24 h and (B) Representative image showing mesh quality employed in *in silico* experiments.